Manchester Metropolitan University

Development of Novel Methods for the Determination of Antimicrobial Capabilities of Photocatalytic Titania Coatings

ANTONY DAMIEN SCIMONE

A thesis submitted in partial fulfilment of the requirements of

Manchester Metropolitan University

for the Degree of Doctor of Philosophy

School of Healthcare Science

Faculty of Science and Engineering

Manchester Metropolitan University

2018

Abstract

Pathogenic and food spoilage organisms can survive on surfaces for extended periods of time and must be removed or inactivated to avoid product spoilage and disease. Current interventions include chemical and physical cleaning protocols, which can be costly and environmentally unsustainable.

Coating surfaces with photocatalytic titanium dioxide may represent a solution to these issues, due to its stability, sustainability, low cost and significant self-cleaning and antimicrobial properties. However, only UV can activate the photocatalyst, making the technology impractical for many desired applications. By doping the titania with other materials, it is possible to achieve activation using visible light. The focus of this thesis was to produce visible light-activated photocatalytic coatings and assess their antimicrobial efficacy. Furthermore, the current tests used to assess antimicrobial efficacy are complex, time-consuming and unattractive for non-specialists. Therefore, this work also aimed to develop simple, rapid tests for the antimicrobial potential of photocatalytic coatings.

Titanium dioxide films doped with molybdenum or niobium at a range of concentrations were produced on stainless steel and glass substrates using magnetron sputtering techniques, annealed at a range of times and temperatures and characterised via EDX, SEM, XRD and optical profiling. The photocatalytic activity of the films was measured via the degradation of methylene blue while the photocatalytic-antimicrobial properties were determined using an adaptation of the BS ISO 27447:2009 test. It was found that $Mo\text{-}TiO_2$ had improved visible light activity and photocatalytic-antimicrobial properties; antimicrobial activity was also present in the absence of irradiation, while $Nb\text{-}TiO_2$ did not show improved activity compared to undoped TiO_2. The substrate greatly affected the antimicrobial activity of $Mo\text{-}TiO_2$ and this was ascribed to differences in roughness and surface area; substrates with lower surfaces areas consistently had reduced antimicrobial activity.

Two existing methods were identified in the literature and redeveloped as assays for photocatalytic-antimicrobial efficacy. The first method was based on real time *in situ* light absorbance of bacteria in suspension using inexpensive spectrophotometric equipment. This method showed promise, approximating the viability dynamics of a planktonic suspension well. However, assessment of decreases in viability could not be made. The second method was based on the time taken to detect changes in the colour of resazurin dye to indicate the viability of bacteria after a period of irradiation. The time to detect a colour change was inversely proportional to the viable population size and thus represents a rapid alternative for enumeration of viable cells following photocatalytic treatment. Furthermore, the test was stratified into three tiers of sensitivity and complexity and so can be used as a first-stage screening for putative photocatalytic-antimicrobial properties, or a fully quantitive enumeration technique. It is hoped that that this alternative test will enable non-specialists to further develop their photocatalytic coatings for antimicrobial use.

Declaration

This is to certify that the material contained in this thesis has been produced by the author, has not been accepted in substance for any other degree and is not currently submitted in candidature for any other academic award.

Conference presentations have been given as follows:

<u>Oral presentation</u>

"Novel Methods for Determining the Antimicrobial Potential of Photocatalytic Surface Coatings". New Photocatalytic Materials for Environment, Energy and Sustainability (Göttingen, Germany) – June 2016.

Acknowledgements

My name appears on the cover of this thesis, but without the support of my friends, family and colleagues, this work would not have been possible.

I would like to first give utmost thanks to my Director of Studies, Professor Jo Verran, for giving me the opportunity to fulfil this PhD. Her continued support, guidance, constant encouragement and *extensive patience* is gratefully acknowledged. Sincere thanks are also given to Professor Pete Kelly, for his knowledge and insightful comments and for welcoming me into a supportive and friendly research group.

I also thank Dr James Redfern, who has been a constant source of guidance and inspiration, not just in terms of this project and thesis, but as a scientist and person. His big-picture attitude has had a major impact on my outlook and personality in the time I have known him and I will be forever grateful for his patience, approachability and willingness to help.

Thanks are also given to Dr Leanne Fisher for sharing her *good laboratory practice* and to Dr Lisa Simmons for her contributions to this thesis and guidance with the materials characterisation experiments.

Acknowledgments are also given industrial partners Teer Coatings Ltd., specifically to Dr Kevin Cooke and Dr Parnia Navabpour, for graciously inviting me to their facility and for the part-funding of this project.

Sincere and heartfelt thanks are extended to the Microbiology Technical Team at Manchester Met, especially Dr Paul Benson-White, for their endless patience and keeping their sense of humour when I had lost mine. Special thanks also go to Natalie Callaghan and Gill Collier.

I would also like to acknowledge Dr Hayley Andrews, Dr Gary Miller and Lee Harman for their training and technical expertise. I thank Dr Marina Ratova and Dr Glen West their guidance and approachability with the surface engineering and magnetron sputtering aspects of this work.

I would also like to acknowledge Dr David Sawtell, for his numerous key contributions and extensive mentorship. Similarly, gratitude is given to Dr Jonathan Butler, for his encouragement and insightful comments.

Gratitude is expressed to Dr Iduma Devine Akhidime and my colleagues in E231, for their support and encouragement. Additional thanks are given to the fellow PhD students I have shared this journey with, especially Lewis Mattin and Chris Broughton, for their friendship, assistance and support.

I would now like to thank my most excellent friends Aidan Dunkerley, Mathew Raftery, David O'Donnell and Kyle Dignan, for their incredible support. Thank you for lending me your strength.

To Elisha, I also thank from the bottom of my heart. Thank you so much for your love, emotional support and patience with me during this project.

Finally, I dedicate this thesis to Adele and Vince, my mum and dad. You have made all this possible. Thank you for believing in me when I stopped believing in myself, again and again.

Table of Contents

List of Figures

List of Tables

List of Equations

List of Abbreviations

Abbreviation	Full name
AFM	Atomic force microscopy
CFUMS	Closed-field unbalanced magnetron sputtering
CVD	Chemical vapour deposition
EDX	Energy-dispersive X-ray spectroscopy
$FADH_2$	Reduced flavin adenine dinucleotide
FISH	Fluorescent *in situ* hybridisation
LMB	Leucomethylene blue
MB	Methylene blue
MFP	Mean free path
NADH	Reduced nicotinamide adenine dinucleotide
NADHP	Reduced nicotinamide adenine dinucleotide phosphate
OEM	Optical emission monitoring
PU	Polyurethane
PVD	Physical vapour deposition
Ra	Profile average roughness
ROS	Reactive oxygen species
Rz	Profile peak-to-valley distance
Sa	Area average roughness
TTD	Time to detection
UV	Ultraviolet
UVA	Ultraviolet A
UVB	Ultraviolet B
UVC	Ultraviolet C
UV-VIS	Ultraviolet - Visible
XPS	X-ray photoelectron spectroscopy
XRD	X-ray diffraction

INTRODUCTION

1.0 - Introduction

Microorganisms are ubiquitous. Many species can exist in a viable state for long periods of time, from several hours to several weeks on surfaces and up to several years when suspended in liquid (Verran, 2002; Kusumaningrum *et al.*, 2003; Liao and Shollenberger, 2003; Wilks *et al.*, 2005; Fuster-Valls *et al.*, 2008; Møretrø *et al.*, 2010). Pathogenic species with low infectious doses can be transferred from these surfaces many hours after initial contamination, contributing to the spread of disease (Wilks *et al.*, 2006; Gerhardts *et al.*, 2012; Pérez-Rodríguez *et al.*, 2013). Furthermore, with access to nutrients, microorganisms can colonise the environment and form biofilms (Matz *et al.*, 2004; Codd *et al.*, 2005; Driscoll *et al.*, 2007; Banat *et al.*, 2010; Møretrø *et al.*, 2010). This has major implications in certain domains where the hygienic status of the environment is paramount. Industries such as food, beverage, pharmaceutical, biomedical and wastewater remediation all require that microbial populations are controlled to prevent the spread of infectious disease, avoid product spoilage and reduce operating costs (Choi *et al.*, 2007; Simões *et al.*, 2010; Bruscolini *et al.*, 2015; Priha *et al.*, 2015). Application of photocatalytic thin film coatings to surfaces may go some way to ameliorating these problems (Foster *et al.*, 2011) and are the focus of this study.

Advances made in coating fabrication methods in recent years have led to improvements in the reliability and cost-effectiveness of previously under-utilised technologies. Innovations in physical vapour deposition (PVD) techniques have enabled complex coating processes to be simplified and have greatly increased the versatility and ubiquity of thin film coatings (Kelly and Arnell, 2000; Yu *et al.*, 2006; Bräuer *et al.*, 2010). These techniques are now routinely employed to produce coatings with many and varied properties - hardwearing, corrosion resistance, low friction, coatings with highly specific technical properties (such as a specific electrical conductance) and even decorative coatings (Kelly and Arnell, 2000). Another area where PVD lends itself is the deposition of photocatalytic coatings. There has been renewed interest in photocatalytic semiconductor coatings in recent years. The

concept of a functional coating, wherein the properties can be controlled by application of a light source, is highly desirable – low operating costs and passive mode of action make these coatings highly suited to the industries mentioned.

One of the most versatile and commonly used photocatalytic materials is titanium dioxide, or titania. Titanium dioxide has several crystalline phases, the most photoactive of which is the anatase phase (Fujishima *et al.*, 2000). Other less active phases include rutile and brookite. Titania has been used in many applications as a surface coating, for example as self-cleaning windows and tiles, anti-fogging screens, water splitting fuel cells, water and air purification and antimicrobial applications (Farahani *et al.*, 2011).

However, a significant drawback of this material is that ultraviolet light (UV) must be used to activate the material. While sunlight does contain a portion of UV, it comprises less than 5% of total photons, rendering the photocatalyst relatively inefficient (Dalrymple *et al.*, 2010). Additionally, it is likely that only outdoor coatings would be activated by sunlight at all, as indoor fluorescent lighting contains few UV photons. Indoor coatings may be activated by UV lamps, but this might be impractical in many of the domains where the coating would be beneficial. Therefore, a significant amount of current research into titania is aimed at activating the material using visible light; a common strategy employed throughout the literature is the addition of dopant materials (Allen *et al.*, 2008). This is explored further in *section 1.4.*

Of all the properties of titania semiconductors, the antimicrobial properties are of primary importance to this work. As mentioned, many sectors would benefit from such a coating – medical applications, industrial food preparation areas and commercial kitchens, along with hygienic domains such as bathroom fixtures and fittings (Fernández-Ibáñez *et al.*, 2009; Page *et al.*, 2009; Foster *et al.*, 2011). In order to develop coatings with higher activity, comparisons with existing coatings must be made. However, evaluation and comparison of photocatalytic-antimicrobial activity between different coating compositions can be difficult for several reasons. For example, different coating production methods can lead to non-controlled variation in the coatings. Furthermore, variability in testing methods between

authors, or perhaps a lack of microbiological technical expertise, can lead to discrepancies and artefactual results. The test most commonly used, the BS ISO 27447:2009 (British Standards Institution, 2009), would benefit from modification, as it is time-consuming and prone to user error and variation. In addition, it requires extensive repeat testing for statistical validation and is relatively expensive (*section 1.3.2).* An improved test, that would require less technical expertise, be quicker and/or act as a first-stage screen, would be useful in the development of highly active functional photocatalytic coatings (Kelly *et al.*, 2014).

1.1 - Titania as a photocatalyst

1.1.1 - Definition and principles

Photocatalysis can be defined as "the acceleration of a reaction by light" (Oxford English Dictionary, 2017). This broad definition encompasses many processes that are of interest. By understanding the process by which the catalyst accelerates the reaction, the process can be optimised by novel and more efficient catalyst design.

There are two main types of photocatalysis: homogenous and heterogeneous. In homogenous photocatalysis, the catalyst is in the same physical phase as the reactants. For example, in a process known as the Fenton system, iron ions dissolved in a strong acid react with hydrogen peroxide to form hydroxyl radicals (Peternel *et al.*, 2007) (1).

$$Fe^{2+} + H_2O_2 \rightarrow HO \cdot + Fe^{3+} + OH^-$$

$$Fe^{3+} + H_2O_2 \rightarrow Fe^{2+} + HO_2 \cdot + H^+$$

$$Fe^{2+} + HO \cdot \rightarrow Fe^{3+} + OH^-$$

(1)
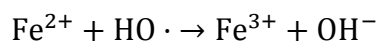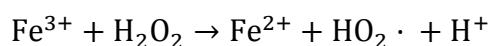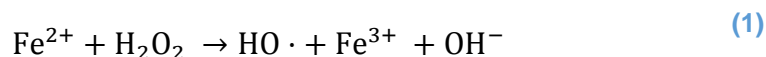
When this system is irradiated with light of wavelength, $\lambda \leq 450$ nm, additional hydroxyl radicals are produced (Feng and Le-cheng, 2004). This is the photo-Fenton system (2).

$$H_2O_2 + light\ energy \rightarrow HO \cdot + HO \cdot$$

$$Fe^{3+} + H_2O + light\ energy \rightarrow Fe^{2+} + HO \cdot + H^+$$

(2)
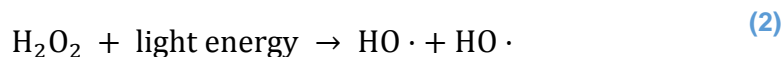
The hydroxyl radicals react with target compounds, converting them into less harmful substances; a common application is the breakdown of substances such as phenol and organic dyes in wastewater treatment facilities (Monteagudo *et al.*, 2014).

In heterogeneous photocatalysis, the catalyst is in a different phase than the reactants; this is most commonly encountered as either a gas-solid or a

liquid-solid system. Heterogeneous photocatalysis has a wider range of application than homogenous; this type of catalyst is employed in self-cleaning materials, wastewater treatment facilities, air purification systems and hydrogen fuel cells. Hygienic and medical domains are also key areas in which heterogeneous photocatalysts may be used, as the products of photocatalysis are lethal to a range of microorganisms (Allen *et al.*, 2008; Caballero *et al.*, 2014; Cao *et al.*, 2014; Fisher *et al.*, 2014; Byrne *et al.*, 2015; Robertson *et al.*, 2015).

The photocatalytic effects of titanium dioxide have been known for many years (Jacobsen, 1949). These photocatalysts received renewed interest due to Fujishima's discovery of the photocatalytic splitting of water by titanium dioxide (Fujishima and Honda, 1972). Since then, there has been extensive study and development of titanium dioxide photocatalysts (Fox and Dulay, 1993; Hoffmann *et al.*, 1995; Diebold, 2002; Verran, 2002; Allen *et al.*, 2008; Fujishima *et al.*, 2008; Caballero *et al.*, 2009; Foster *et al.*, 2011; Nakata and Fujishima, 2012; Lang *et al.*, 2014; Low *et al.*, 2017). Research has been focused here for several reasons; titanium dioxide has a high stability and activity compared to similar semiconductors, in addition to a low cost (Carp *et al.*, 2004). It is also commonly said to have a low toxicity (Sharifi *et al.*, 2012), although occupational exposure to TiO_2 nanoparticles has been tied to upper respiratory tract inflammation - inhalation is the primary route of entry. In addition, lung tumours have been detected in rats that were exposed to high doses of titanium dioxide nanoparticles two years after exposure (Shi *et al.*, 2013). For these reasons, titanium dioxide is classified as a Group 2B carcinogen (possibly carcinogenic to humans) by the WHO (The IARC Monographs Working Group on the Evaluation of Carcinogenic Risks to Humans, 2010). It should be noted that these toxicity studies have only found harm when the titania was in a nanoparticle form and inhaled – these conditions would be unlikely to be found in standard applications for photocatalysts, especially when immobilised.

1.1.2 - Mechanism of titania photocatalysis

Photocatalysis and similar terms are somewhat of a misnomer when applied to titania; the implication is that the desired reaction is accelerated by light itself, which is then consumed in the reaction and regenerated without undergoing permanent change (Kaleji *et al.*, 2013). Rather, the reaction is accelerated by a light-activated (or photoinduced) catalyst. Therefore, in order to accelerate reactions, titanium dioxide must first be activated (Mills and LeHunte, 1997).

Anatase titania has a band gap of 3.2 eV – this is the energy difference between the highest valence band and lowest conduction band within a crystal. An electron can be given this energy by a photon with $\lambda \leq 385$ nm, according to the Plank-Einstein equation (3), where E is energy, h is Planck's constant 4.14×10^{-15} eV and v is the incident photon frequency. This equation can also be expressed in terms of wavelength λ and the speed of light in a vacuum c, 3×10^8 ms^{-1} (4).

$$E = hv$$

(3)

$$E = \frac{hc}{\lambda}$$

(4)

An electron cannot exist between bands, or energy states and so when 3.2 eV is applied to a valence band electron it becomes excited and 'jumps' to the conduction band, leaving a positively-charged electron hole. Thus, an electron (e^-) – hole (h^+) pair is formed (Figure 1).
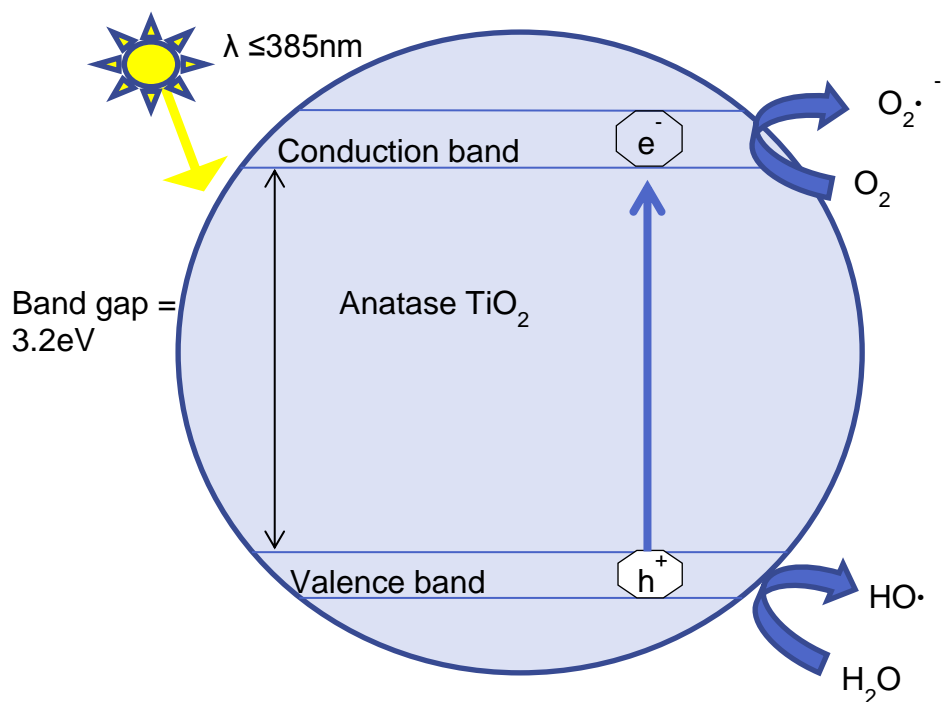
Figure 1: Diagram of the formation of reactive oxygen species. A photon of wavelength ≤385 nm interacts with an electron in the valence band of titanium dioxide. The electron jumps to the conduction band, forming an electron-hole pair. These reactive species react with adsorbed O_2 and H_2O to form the reactive oxygen species $O_2 \cdot^-$ and HO· respectively. Adapted from Angelo *et al.* (2013).

The electron-hole pair (commonly notated as e-h) reacts with adsorbed water and oxygen – the primary products are thus superoxide ($O_2 \cdot^-$) and hydroxyl radicals (HO·), with the secondary product hydrogen peroxide (H_2O_2) also being formed. The mechanism for this reaction, as described by Fujishima *et al.* (2008), is shown below (5-8).

$$hv \rightarrow e^- + h^+ \tag{5}$$

$$2H_2O + 4h^+ \rightarrow O_2 + 4H^+$$
$$O_2 + 2e^- + 2H^+ \rightarrow H_2O_2 \tag{6}$$

$$O_2 + e^- \rightarrow O \cdot_2^- \tag{7}$$

$$H_2O_2 + e^- \rightarrow \cdot OH + OH^-$$
$$H_2O_2 + O \cdot_2^- \rightarrow \cdot OH + OH^- + O_2$$
$$H_2O_2 + hv \rightarrow \cdot OH + OH^- \tag{8}$$
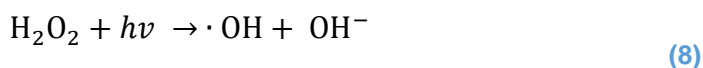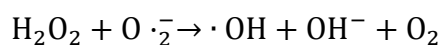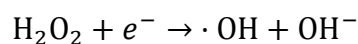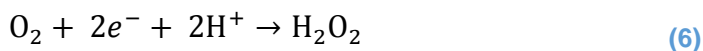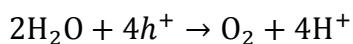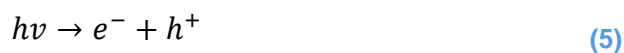
It is these highly reactive products, known as reactive oxygen species (ROS), in addition to the electrons and holes, which are responsible for the further oxidation and reduction of target compounds. However, the e-h pair are typically only separated for a very short period; studies vary, but suggest that recombination occurs between 10 picoseconds (Pelaez *et al.*, 2012) and 200 nanoseconds (Ozawa *et al.*, 2014). If no reactants are encountered within this separation time, the pair will 'recombine' with the electron falling back to the ground state. After recombination, an electron must once again be excited by an appropriate photon to jump to the conduction band; one of the key areas of research into titanium dioxide is developing strategies to extend the separation time, delaying recombination so that the e-h pair have more time to encounter reactants.

The purpose of a catalyst is to accelerate a reaction without being consumed in the process. Titanium dioxide photocatalysts achieve this purpose by continually recycling the e-h pair. Recombination of the e-h pair will inherently regenerate the photocatalyst if no reactants are encountered in the separation period, but if reactants are encountered, the vacant hole in the valence band is filled by an electron from the electron donor reactant, therefore regenerating the catalyst (Fujishima and Zhang, 2006).

1.1.3 – Non-antimicrobial applications for titania surface coatings

As mentioned, applications for photoactive coatings are many and varied. In addition to causing the inactivation of microorganisms, titania photocatalysts produce ROS that can degrade target compounds. This has applications in wastewater remediation and processing industries, as harmful pollutants such as endocrine disrupting compounds, pesticides and volatile organic compounds can be degraded (Pelaez *et al.*, 2012).

Another useful property of photocatalytic titania coatings, is the superhydrophilic properties that are exhibited when illuminated. Illumination of the photocatalytic surface generates oxygen vacancies – in the presence of water, these vacancies can be replaced by water molecules on the surface, leaving adsorbed hydroxyl groups. The hydroxyl groups make the surface hydrophilic, reducing the contact angle of liquids on the surface (Fujishima *et al.*, 2000). This makes liquids spread much further on the surface and occupy a greater surface area – the result of this is a phenomenon called sheeting, where the liquid may roll off the surface in a continuous body as opposed to singular droplets. This sheeting carries away dirt and debris, cleaning the surface in the process.

The self-cleaning property lends itself to incorporation in building materials such as glass and concrete, where regular chemical cleaning may be an economic and environmental burden (Carp *et al.*, 2004; Chen and Poon, 2009; Smits *et al.*, 2014). This property also allows liquids on the surface to evaporate more easily, facilitating antifogging coatings; these coatings minimise the effect of fogging and misting on optical surfaces. The applications for these coatings are anywhere where fogging occurs and is not desired, for example on mirrors, lenses and windows (Fujishima *et al.*, 2000).

In addition to self-cleaning and anti-fogging coatings, titanium dioxide coatings can also improve air quality. In many urban environments, air quality is poor – this can be ascribed to high concentrations of harmful compounds, usually caused by combustion of fuel in vehicle engines. Two of

these compounds are nitric oxide and nitrogen dioxide – collectively known as NO_x (Roy *et al.*, 2009). These gases have raised human health concerns, in addition to causing acid rain (Wang *et al.*, 2007). Titanium dioxide removes these compounds from the air by a process called NO_x abatement. Nitric oxide in the air may adsorb to the surface of the photocatalyst and react with photocatalytically generated ROS (or excited electrons in the valence band directly), forming nitrogen dioxide, which can then further react with additional ROS or excited electrons to form the less-harmful nitrate (Lasek *et al.*, 2013). The nitrate species may then be washed from the surface of the photocatalyst via the self-cleaning mechanisms discussed previously (Hüsken *et al.*, 2009).

Globally, there are several instances of incorporating titania photocatalysts into building materials for the purpose of air purification. Some notable buildings are the Philharmonie 2 in Chambéry, France, *Dives in Misericordia* Church in Rome, Italy, National Opera Hall in Beijing, China and the Dubai International Stadium, United Arab Emirates (Cassar, 2011; Banerjee *et al.*, 2015). In addition to buildings, titania photocatalysts may also be incorporated into roads and pavements. This has proved very effective in the reduction of NO_x particles in the air, with reductions from 25% (Umberto I Tunnel, Rome, Italy) to 90% (Vinci Car Park, Paris, France) have been observed (Angelo *et al.*, 2013).

Complementary to the work described in this thesis, a series of long-term experiments were performed; this involved coating various materials with photocatalytic titania coatings on a west-facing outdoor wall of a 1970's Manchester building and investigating their long-term self-cleaning, NOx abatement and antimicrobial effects. This served as a vehicle for public displays of the benefits and applications of photocatalytic technologies. These experiments and details of the public engagement are detailed in *Appendix A.*

1.1.4 – Mechanism of photocatalytic inactivation of microorganisms

An additional property of photoactive coatings is that they can kill microorganisms, including potentially pathogenic bacteria. When hydroxyl radicals encounter a bacterium, a reaction takes place. Although a bacterium may have several intracellular targets for ROS such as enzymes, co-enzymes and nucleic material (Carp *et al.*, 2004; Dalrymple *et al.*, 2010), the cell envelope provides an initial line of defence, repelling ROS. Indeed, it could be argued that the cell envelope is an equally critical target, as destabilisation of the membrane leads to loss of function and leakage of intracellular components, resulting in cell death (Sirelkhatim *et al.*, 2015).

The cell envelopes of bacteria are dynamic, complex structures that facilitate many functions such as nutrient and waste exchange, ion transport, oxidative phosphorylation and respiration. The specific components and functions of the cell envelope vary between species but can be placed into one of two classifications. Gram-positive species have a two-layer envelope, containing an inner cytoplasmic membrane, attached to many surrounding layers of peptidoglycan forming a rigid cell wall for strength and structure. The peptidoglycan layer is interspersed with functionalised polymers such as teichoic acid, which assist in providing structure and regulating cell division, as well as playing a role in inherent antibiotic resistance. These polymers also contribute to the physicochemical properties of the cell; by tailoring their cation content, the surface charge can be adjusted, protecting the cell from cationic antimicrobial molecules and influencing adhesion behaviour (Saar-Dover *et al.*, 2012; Brown *et al.*, 2013).

In contrast, Gram-negative species have three layers – the inner cytoplasmic membrane, a thin peptidoglycan layer within the periplasmic space and an additional outer membrane. The outer membrane is asymmetrical, consisting of an in-facing phospholipid layer and an out-facing glycolipid layer, more commonly called the lipopolysaccharide (LPS) layer. Transmembrane protein channels known as porins allow diffusion of specific molecules into the cell, acting as a selective permeability barrier. This action can improve the

survival of the organism in certain adverse conditions. Furthermore, if antimicrobial or harmful compounds do enter the cell via porins, efflux pumps on the outer membrane may remove such compounds from the periplasm before any intracellular damage occurs, contributing to inherent antimicrobial resistance (Delcour, 2009; Silhavy *et al.*, 2010).

Despite protecting intracellular components from attack, these cell envelope components can provide targets for ROS attack. Both the LPS and phospholipid layers can be destabilised by ROS (Sunada *et al.*, 2003), although perhaps due to the properties of the cell envelopes discussed, Gram-negative cells are thought to be more susceptible to photocatalytic inactivation than Gram-positive cells (Bogdan *et al.*, 2015). It is thought that this is because these layers contain high amounts of lipid material; when a hydroxyl radical encounters a lipid (specifically an unsaturated lipid), a lipid propagation reaction occurs. The reaction of an unsaturated lipid with a hydroxyl radical in the presence of oxygen leads to the production of water and a lipid radical, which in turn can react with other nearby lipid molecules to generate additional lipid radicals. The newly formed lipid radicals can react with oxygen to form lipid peroxide radicals. Finally, lipid peroxide radicals can react with unsaturated lipids to form a lipid peroxide molecule and as lipid radical (Figure 2).
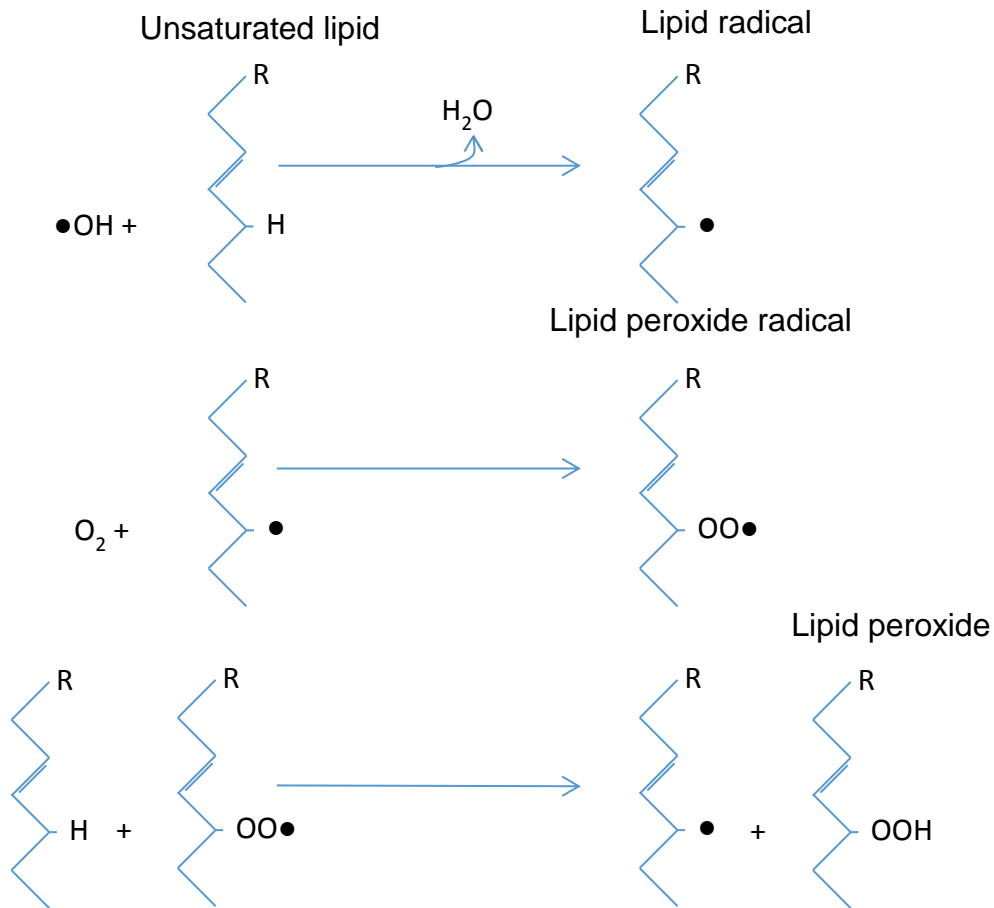
Figure 2: Schematic of lipid peroxidation propagation. Hydroxyl radicals react with unsaturated lipid molecules in bacterial membranes, forming water and lipid radicals. Lipid radicals react with local molecular oxygen to form lipid peroxide radicals. These lipid peroxide radicals react with other unsaturated lipids, forming lipid peroxides and lipid radicals. These lipid radicals undergo further reactions with local molecular oxygen, propagating the reaction. Adapted from Dalrymple *et al.* (2010).

Because these layers are composed of repeating patterns of lipids, a radical chain reaction initiated by ROS disrupts normal membrane processes such as ion transport. The cell dies due to the disrupted membrane; it is thought this is due to a combination of cessation of oxidative phosphorylation, leakage of intracellular components and eventual internal oxidative damage caused by influx of ROS though the cell wall breach (Fernández-Ibáñez *et al.*, 2009; Dalrymple *et al.*, 2010).

While the above reaction is true for Gram-negative organisms, the outermost component of the cell envelope in Gram-positive cells is the thick peptidoglycan layer; hydroxyl radicals would have to first penetrate this layer

in order to destabilise the inner membrane (Pal *et al.*, 2007). The peptidoglycan layer has a permeability of around 2 nm, so ROS can pass through and attack the inner membrane, but due to the high reactivity of ROS, they are likely to react with the components peptidoglycan layer before approaching the inner membrane (Dalrymple *et al.*, 2010).

The actual effect of the peptidoglycan layer in the photoinactivation of bacteria is disputed. As with Gram-negative species, the killing mechanism has been suggested to be related to oxidation of the membrane leading to gross disruption of the main permeability barrier, causing rapid leakage of potassium ions and slower leakage of RNA and proteins (Hu *et al.*, 2007).

The work of Saito *et al.* (1992) showed a similar mechanism, although destruction of the peptidoglycan layer was also observed. However, it was proposed that even though the peptidoglycan layer was destroyed by ROS in the Gram-positive organism *Streptococcus sobrinus*, it may not be essentially concerned with loss of cell viability – rather, it may be a secondary phenomenon. In their experiment, they indicated a reduction in cell viability after one minute of irradiation whereas destruction of the peptidoglycan was observed after thirty minutes. This implies that the presence of the peptidoglycan layer did not impede the ROS attacks on the inner membrane or improve resistance to ROS; the destruction of the cell wall was not necessary to reduce the viability of the cells. This was also seen by van Grieken *et al.* (2010), who observed similar inactivation dynamics for both Gram-positive (*Enterococcus faecalis*) and Gram-negative (*Escherichia coli*) species. Indeed, they propose that due to the similar inactivation kinetics, photocatalytic trials against *E. coli* may be extrapolated to other types of bacteria, leading to this organism not only being used as an indicator of faecal contamination (Beerens, 1998), but also as a model organism for photocatalytic applications.

The Gram status of the bacterial cell can also influence the adhesion between the cell and photocatalyst surface; the two cell envelope types can have differences in electrostatic charge, affecting the hydrophobicity of the cells and leading to differences in cell-catalyst adhesion. Adhesion of the cell to the surface of the photocatalyst is critical to efficient photoinactivation on

immobilised titania surfaces; ROS generated at the surface of the photocatalyst have less distance to travel if the cell is adhered to the surface, yielding a more rapid inactivation and decreasing the chance of reacting with a non-target reactant.

The importance of cell adhesion is reduced when the catalyst and bacteria are in suspension, as it is well known that immobilised titania has lower activity than titania in suspension (Foster *et al.*, 2011); as discussed in *section 1.2.1*, this greatly increases the number of active sites for reaction and reduces the importance of cell-catalyst adhesion.

It is worth noting that the experiments of both Saito *et al.* (1992) and van Grieken *et al.* (2010) were performed with the bacteria in suspension with the photocatalyst, which may help to explain why the presence of the peptidoglycan layer had seemingly little effect on viability. Indeed, in a separate study, van Grieken *et al.* (2009b) observed no differences in kill rate between Gram-positive and Gram-negative when cells were in suspension along with titania nanoparticles, but Gram-positive cells had an improved survival rate and took longer to kill on immobilised, surface-bound titania. Other authors have also observed a similar effect, where Gram-positive organisms exhibit lower inactivation levels when on immobilised photocatalysts (Kühn *et al.*, 2003; Pal *et al.*, 2007). This suggests that the differences in inactivation rates between Gram type may be due to the way the cell envelope influences the contact and adhesion between cell and photocatalyst (Foster *et al.*, 2011).

Due to the differences in susceptibility, it has been suggested that there may in fact be different photokilling mechanisms for Gram-positive and Gram-negative organisms (Liu and Yang, 2003), although data to support this are scarce. Overall, Gram-negative organisms are generally observed to have a greater loss of viability than Gram-positive organisms (Bogdan *et al.*, 2015) and it has been suggested that this could be due to the thick peptidoglycan layer absorbing ROS radicals without fatal effects (Pal *et al.*, 2007), or differences in cell envelope charge causing differences in photocatalyst contact and adhesion (Foster *et al.*, 2011; Saar-Dover *et al.*, 2012). In other words, Gram-positive organisms are less affected than Gram-negative

organisms and so care must be taken when considering the application of photocatalytic surfaces.

1.2 - Factors affecting photocatalytic activity

The purpose of any catalyst is to accelerate a desired reaction. Therefore, the efficacy of the catalyst is proportional to the rate at which the target reactant becomes product, compared to the reaction without the catalyst i.e., the increase in reaction rate that is attributable to the catalyst is proportional to the efficacy of the catalyst.

It follows that improving the efficacy of a catalyst requires insight into factors affecting catalysis. The rate of non-photocatalytic, catalyst-mediated reactions can be influenced by factors such as heat, pressure and the relative concentrations of reactant, catalyst and product. While these may also influence the rate of a photocatalyst-mediated reaction, there are many other factors that are to be considered. The factors affecting the rate of a photocatalytic reaction can be classified as either extrinsic or intrinsic. Intrinsic factors relate to the photocatalyst, whereas extrinsic factors pertain to that specific reaction.

1.2.1 – Extrinsic factors

The properties of available light are important to consider for a given reaction. As discussed in *section 1.1.2*, photon energy is the most important property of light relating to activating the photocatalyst – if the photon contains insufficient energy upon collision with an electron in the valence band, the electron will not excite into the conduction band, therefore no further reaction will take place. In addition to this, light intensity, or photon flux, must also be considered. Photon flux can be considered the number of photons that strike a defined surface area in a defined time – usually expressed in watts per square meter and derivatives thereof. Interestingly, it has been found that even with only a few photons of the correct energy, titania photocatalysts may still activate – high flux is not explicitly required (Fujishima *et al.*, 2000). Indeed, it has been found that ordinary room lighting is sufficient to activate pure anatase titania (albeit inefficiently), even though this kind of light is likely to contain very few photons with wavelength $\lambda \leq 385$

nm. Given appropriate wavelengths, low fluxes (0-20 mW cm^{-2}) have been shown to exhibit 1st order rate dependence (indicating a linear increase in rate with increasing flux), intermediate fluxes (up to 25 mW cm^{-2}) have shown ½ order rate dependence and high fluxes (above 25 mW cm^{-2}) have exhibited no rate dependence (Herrmann, 1999; Sauer *et al.*, 2002; Carp *et al.*, 2004; Li Puma *et al.*, 2009; Puddu *et al.*, 2010). An idealised schematic of this behaviour is shown in Figure 3.
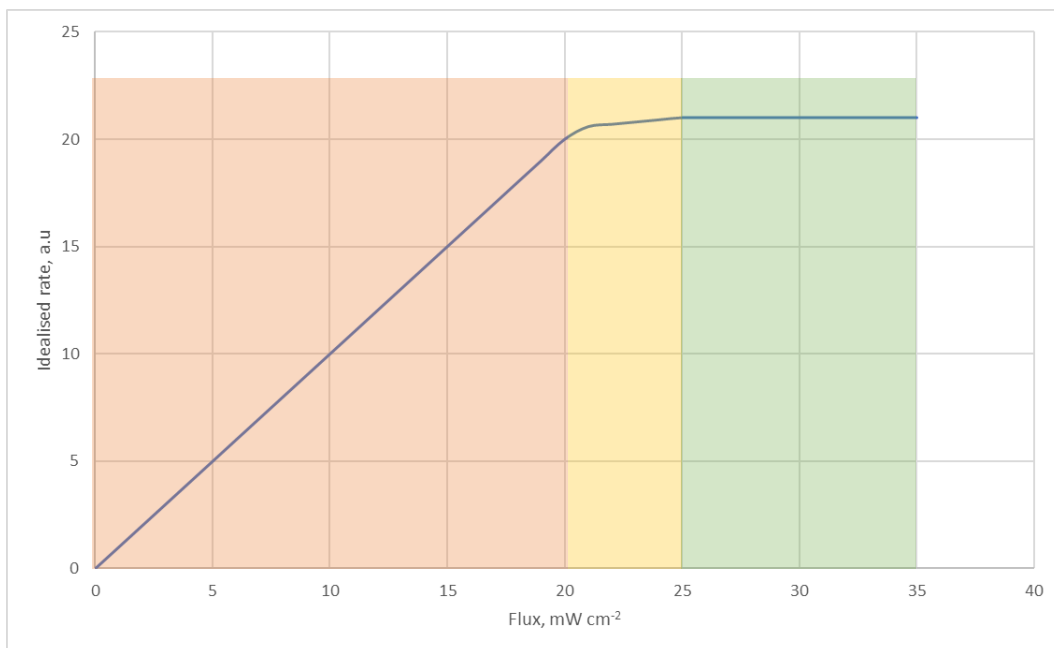
Figure 3: Schematic representation of idealised reaction rate by flux intensity. At lower fluxes (up to 20mW cm^{-2}), increasing the flux increases the rate with first order dependence (orange region, left). Between 20-25 mW cm^{-2}, increasing the flux increases the rate with half-order dependence (yellow region, middle). At high fluxes above 25 mW cm^{-2}, increasing the flux does not increase the rate, signifying zero-order dependence (green region, right).

Several mechanisms are thought to be responsible for this. At low flux, each incident photon has a chance to excite a valence electron. However, as flux increases, the number of available valence electrons decreases, limiting the rate increase. Concurrently, the e-h recombination rate increases as flux increases, resulting in a reduced effect on rate. This is due to the increase in heat of the catalyst caused by energy transfer by the photons; higher temperatures encourage recombination of e-h pairs (Herrmann, 2010). Therefore, it must not be assumed that increasing the light intensity will increase the photocatalytic activity.

Like many catalytic reactions, photocatalytic reactions are influenced by the amount of catalyst compared to reactant in a given system. This important property is termed the catalyst load. When considering slurry-type reactors, the photocatalyst is suspended in a liquid with the reactant and are typically used as small beads (Li *et al.*, 2014), zeolites (Shankar *et al.*, 2004) or nanoparticles (Sauer *et al.*, 2002). The amount of catalyst has an optimum value; increasing the amount of catalyst in the system will increase the number of adsorption sites, therefore increasing the rate. However, too much catalyst can reduce the transmission of light through the system, reducing the total amount of catalyst activated. Additionally, at high catalyst load, aggregation effects can occur, reducing available sites for photon interaction (Mengyue *et al.*, 1995; Shankar *et al.*, 2004; Verran *et al.*, 2007). In stationary, immobile, or thin film systems, the 'amount' of photocatalyst is more related to the surface area of the film and so will be explored along with other intrinsic properties (*section 1.2.2*).

Reports on the effect of temperature on photocatalytic reactions are conflicting. It is commonly accepted that minor changes in temperature do not influence photocatalysis, similar to many photoreactions. This is because photoreactions tend to have very low activation energies and are thus less rate-dependent on temperature than other reactions (Atkins and de Paula, 2014). However, as temperature increases, so does the rate of adsorption and desorption. This leads to a higher rate of transfer of catalytic products, increasing activity (Carp *et al.*, 2004). In addition, it seems that the effect of temperature changes with the reactant; it was found that the decomposition rate for aliphatic alcohols did not change with temperature, but the rate exhibited a first-order dependence (linear relationship) with temperature for chloroform and second-order dependence (exponential relationship) was reported for phenol and salicylic acid (Fox and Dulay, 1993). This also highlights that different reactants are likely to have different degradation rates, as different chemical bonds have different bond energies. Therefore, when designing and testing a photocatalyst, the application must always be considered.

The medium that the reaction takes place in is also an important factor. If the reaction is in a liquid, photocatalytic degradation can occur up to 500 μm away from the film surface (Fujishima *et al.*, 2000; Cai *et al.*, 2014). This 'remote photocatalysis' indicates that some ROS can diffuse this distance through the medium and collide with target reactants. However, it is generally observed that reaction rates increase with increasing proximity of the reactant to the photocatalyst; at distances of 50 μm from the photocatalyst, reaction rates can be two orders of magnitude lower than at the interface of the photocatalyst (Fujishima *et al.*, 2008). In addition, if the medium is viscous, the rates of diffusion of the ROS and reactants will decrease, therefore limiting the reaction to areas very close to the photocatalyst. The medium may also contain other non-target oxidisable material or preferential reactants, which compete with the target reactant for ROS. This can also be the case if the reaction does not occur in a liquid, but rather on a surface. For example, when considering self-sterilizing contact surfaces, a person's fingers may deposit oil, grease and other material, in addition to target reactants such as bacteria. This additional material could significantly reduce the rate and so should be considered when designing photocatalytic systems for these applications.

The pH that the reaction takes place at can affect the efficiency of photocatalytic processes in solution. This can be attributed to several factors: surface charge of the catalyst substrate, net charge of the reactants and net production of hydroxyl radicals (Carp *et al.*, 2004). Photocatalytic reactions are most efficient at a pH of six or lower and therefore favour acidic conditions. This is due to the surface charge of titanium dioxide and its relation to the acid dissociation constant of the reactants (Sauer *et al.*, 2002). Indeed, changes in pH from basic to acidic can increase the rate of reaction by up to one order of magnitude. Nevertheless, it has been shown that higher reaction rates for various compounds exist at both low and high pH, indicating the process is at least somewhat reactant-dependent (Fox and Dulay, 1993).

Clearly, there are many factors pertaining to the reaction conditions that can influence the rate of reaction. While some of these factors are common,

some considerations are unique to photochemistry/photocatalysis disciplines. Optimum conditions exist for each factor and by considering these, increases in photocatalytic efficacy can be affected. However, an increase in photocatalytic efficacy is not necessarily proportional to an increase in overall reaction rate; as discussed, factors such as diffusion of species through the medium and availability of target reactants also influence the overall conversion of target reactant to product. The influence of each of these factors must always be considered when designing and testing novel photocatalysts, as test conditions should match the intended application as closely as possible.

1.2.2 – Intrinsic factors

Titania only exhibits semiconductor behaviour when crystalline; the titanium dioxide units must be in a repeating ordered structure, i.e. crystals, to facilitate transfer of electrons from valence to conduction bands and delay the electrons from recombining with the hole. The phase, size and orientation of the crystals can be collectively referred to as the crystallinity.

The crystallinity of the photocatalyst is a crucial parameter in the photocatalytic activity and can significantly affect the reaction rate. Firstly, the phase; if the photocatalyst is amorphous then no electron transfer can occur – only crystalline titania has the structure to facilitate the generation of e-h pairs. Of the two relevant crystal phases of titanium dioxide, anatase is commonly acknowledged as more photoactive than rutile (Allen *et al.*, 2005; Luttrell *et al.*, 2014). While the reason for this is unclear, it has been suggested that the improved response of anatase may be due to the larger band gap it exhibits compared to the rutile crystal phase (the second most-active crystal phase). Although the larger band gap could lead to lower photonic efficiency (as fewer incident photons will have the required energy to excite an electron to the conduction band), the electrons that do become excited and jump to the conduction band possess a higher oxidation power, facilitating electron transfer from the titania to an adsorbed reactant (Batzill, 2011). Additionally, transient photoconductivity measurements have shown that anatase crystals can hold the e-h pairs apart for longer before recombination; this increases the likelihood of further reactions, increasing efficiency and activity (Xu *et al.*, 2011).

Despite this consensus, some authors dispute the superior photoactivity attained using pure anatase titania. These authors suggest that an anatase – rutile mixed phase has synergistic effects and yields better activity; differences in energy levels may contribute to greater charge separation capabilities (Ohno *et al.*, 2001). Research into anatase-rutile mixed photocatalysts has attempted to identify an ideal ratio between the phases, typically using weight-fraction analysis (Spurr and Myers, 1957; Mahalingam *et al.*, 2017). Such ratios have varied from 75 % anatase – 25 % rutile (Kaleji

et al., 2017), to rutile fractions as high as 50-70 %, with accompanying anatase 50-30 % (McEvoy *et al.*, 2013). Indeed, commercially available photocatalyst powders such as Degussa-25 have been found to contain anatase-rutile mixtures, around 78 % anatase,14 % rutile, and 8 % amorphous (Ohtani *et al.*, 2010). It is clear that despite the considerable research into this area, unifying claims cannot yet be made.

Other aspects of crystallinity influence generation and continued separation of e-h pairs. Films with good crystallinity can facilitate the conduction of photoelectrons away from the interface into the bulk, preventing the rapid recombination of e-h pairs, therefore improving overall efficiency (Ismail and Bahnemann, 2011). If the film has poor crystallinity – few ordered repeating structures, differing orientations, high number of grain boundaries – then efficiency will decrease. Poor crystallinity is often caused by incorrect thermal treatment and annealing conditions, addition of certain dopants or too much dopant, or film stresses/defects during fabrication (such as arcing during magnetron sputter deposition).

One of the most important factors relating to the photocatalyst itself is the catalyst load. While this is considered an extrinsic factor in a slurry-type reactor, it is considered an intrinsic factor in thin-film and immobile systems. As in slurry-systems, the catalyst load is ultimately analogous to available reaction sites and so in thin film systems this can be considered as the surface area. However, several additional considerations must be considered in relation to immobilised photocatalysts that are absent in slurry-systems, such as electron exchange through the bulk and photon attenuation. Several authors (Chen and Dionysiou, 2006; Camera-Roda and Santarelli, 2007; Cao *et al.*, 2014; Luttrell *et al.*, 2014) have reported a positive correlation between film thickness and photoactivity. One explanation for this is due to increasing number of potential collisions between incident photons and TiO_2 valence electrons.

It is this property that makes thicker films less transparent – more photons interact with the titania and fewer pass through the film. Therefore, more titania interacts with the present photons and can produce e-h pairs.

However, as the e-h pair recombines rapidly, the probability of the electron or hole being conducted from the bulk to the surface and undergoing further oxidation reactions is low in films greater than a few tens of nanometres. Additionally, the effect of light flux must be considered with film thickness. Specifically, for films thicker than 100 nm, increase in flux does not result in an increase in reaction rate (Fujishima *et al.*, 2000). This is likely due to rapid attenuation and absorption of the UV component of the light in the first 100 nm of the film.

A more likely explanation is that, when films are not fully dense, increasing thickness leads to an increase in surface area, increasing the number of reaction sites and increasing activity. Therefore, increasing the thickness of these films appears to increase the activity, but actually, it is the corresponding increase in surface area that improves the activity. Interestingly, it follows then that the magnitude of the effect of thickness can vary, depending on fabrication method. For example, films produced via sol-gel techniques tend to be porous; a thicker coating can have deeper pores, thus more surface area and adsorption/reaction sites. However, as the pores become deeper, it becomes more difficult for the reactants and ROS to diffuse along the pore and collide, leading to a reduction in the reaction rate. Furthermore, if the film forms strong crystal facets with thickness, then increasing the thickness will have an effect. However, films produced using other methods, such as magnetron sputtering, do not tend to have a porous structure and tend to produce fully dense films without crystal facets that increase with thickness (*section 2.3*) and therefore the magnitude of the effect of thickness on activity is reduced. (Carp *et al.*, 2004).

Another important parameter is roughness of the photocatalyst, as it can directly inform the surface area; a smooth surface has less surface area than a rough surface for the same apparent area. This is significant because increasing the surface area increases the number of available adsorption sites for oxygen and water, therefore facilitating more exchange between e-h pairs and molecular species that convert into reactive oxygen species; the overall effect is an increased rate of generation of radical oxygen species. However, films with high roughness and surface area can have poor

crystallinity. This is because ideal crystallinity is considered to be crystals in the same orientation with few grain boundaries. Indeed, it has been found that it is more beneficial to have high-quality crystals than to have a high surface area (Verran *et al.*, 2007; Puddu *et al.*, 2010).

In contrast to photocatalytic reactions in suspensions, or slurry-type reactions, thin film photocatalysts require a substrate. The substrate is important, as it can have direct and indirect effects on several other efficacy-affecting properties. The chemical composition of the substrate can have an effect on the efficacy of the photocatalyst, as there is the potential for substrate material to diffuse or leach into the photocatalyst. For example, if a soda-based glass is used as the substrate, then the sodium present could enter the bulk of the film during annealing stages, thus influencing crystallite growth and activity. Indeed, high sodium concentrations can suppress the formation of the anatase phase completely and even at low concentrations, can form charge recombination centres (Paz and Heller, 1997). Similarly, this can also happen when stainless steel substrates are used – the various metals in the substrate can diffuse into the film and influence electron behaviour, reducing activity. This is likely because the diffused material acts as a defect point, becoming a charge recombination centre (Chen and Dionysiou, 2006). In films fabricated using sol-gel methods, the roughness of the substrate can affect how much sol is retained, therefore influencing the thickness of the film.

Another important property of the substrate is the coefficient of thermal expansion – a measure of how the substrate expands and contracts with heating and cooling respectively. During the annealing process, if there is a significant mismatch in the coefficient of thermal expansion between the substrate and the film, they will expand at different rates; this can cause structural stress to the film, increasing the likelihood of the film cracking. The result of this is poor crystallinity and non-uniform coatings, which aid e-h recombination therefore reducing efficacy. The effects of stresses on film structure are explored thoroughly in *section 2.3.2*. Additionally, as films are generally conformal to the substrate, the roughness of the substrate will

directly influence the roughness of the film, in turn modifying the surface area (Lopez *et al.*, 2013).

Finally, the chemical composition of a photocatalyst is also of vital importance in improving photocatalytic efficiency for visible-light applications. Changing the composition by adding dopants can have a drastic effect on the rate of the reaction, either improving the photoactivity under visible light illumination, or reducing it – this is explored in *section 1.4.*

As can be seen, there are several key properties that influence the photoactivity of the photocatalyst, independent of reaction conditions. The most vital parameter initially is the crystallinity, because if the titania is not crystalline then no photocatalytic activity will be observed. Indeed, given two photocatalysts with identical properties, the one with a lower surface area but improved crystalline structure, with few grain boundaries and few orientations will generally yield higher activity than the photocatalyst with a higher surface area, but poorer crystallinity. One caveat to this argument is when dopants are used; this may negatively affect the crystallinity but can improve the photocatalytic response under visible light illumination. As mentioned, this is discussed further in *section 1.4.*

1.3 – Assessing photocatalytic activity

In order to develop high-performance photocatalysts that can degrade target reactants *in situ*, the activity of the photocatalyst must first be determined *in vitro*. While various properties of the photocatalyst can be measured and characterised, these properties ultimately inform the activity. Therefore, it is necessary to determine the photocatalytic activity in test conditions that approximate the conditions of the intended application. In addition, as discussed in *section 1.2.1*, the target reactant used to determine efficacy should be as close to the target reactant in the intended application as possible. To this end, several 'model' or 'probe' reactants are used throughout the literature in order to determine the photocatalytic activity of photocatalysts.

1.3.1 – Photoactivity against chemical pollutants

The photocatalytic activity of a photocatalyst can be thought of as an indication of the influence it has on the rate of a reaction – the higher the photocatalytic activity, the greater the increase in reaction rate. There are several ways to measure the photocatalytic activity of a photocatalyst *in vitro*. These tests generally involve measuring the breakdown of an organic compound or dye over a period of time. Commonly used substances include

- Volatile organic compounds such as acetone (Mattsson *et al.*, 2006) and formaldehyde (Akbarzadeh *et al.*, 2010)

- Specific probe reactants such as stearic acid (Kafizas *et al.*, 2009), 4-nitrophenol (Di Paola *et al.*, 2002), 4-chlorophenol (Bakardjieva *et al.*, 2005) and nitrous oxide/dioxide degradation (Chen and Chu, 2011).

- An array of industrially relevant dyes, such as rhodamine B (Wilke and Breuer, 1999) methyl orange (Yao *et al.*, 2009; Wang *et al.*, 2013), resazurin (Mills *et al.*, 2017), malachite green (Sayılkan *et al.*, 2008) and methylene blue (Hirano and Matsushima, 2006; Breault and Bartlett, 2012; Kaleji *et al.*, 2012; Gutbrod and Zollfrank, 2013; Khan and Berk, 2014; Fisher *et al.*, 2014).

One of the most commonly performed *in vitro* tests is the degradation of the organic dye methylene blue. This test is preferred for several reasons: it is relatively inexpensive, simple and easy to interpret. Specifically, when dissolved in distilled water at a concentration 1 µM, methylene blue strongly absorbs light with at a wavelength of λ=665 nm. As the dye is photocatalytically degraded to leucomethylene blue, the solution turns clear and the absorption at this wavelength decreases. By plotting the reduction in absorbance against time and measuring the gradient, a reaction rate constant can be determined; this is a comparable measure of the photoactivity. The methods pertaining to the methylene blue test are discussed further in *section 3.3.1.*

1.3.2 – Photoactivity against bacteria

As can be seen, there are a plethora of appropriate tests available to measure degradation of pollutants. The probe compounds allow the photoactivity of a sample to be determined in relatively similar conditions to the desired application. While measuring the photoactivity of a sample in this way is relatively straightforward, determining the effect of a photocatalyst on microorganisms is much more complex. Currently, a British standard (British Standards Institution, 2009) is commonly used. There are several shortcomings of this test; in order to discuss these, an overview of the method is detailed below.

Specifically, the test involves inoculating a test sample with a known number of microorganisms (a volume of 0.15 mL of pre-prepared bacterial suspension, at a concentration of between 6.7×10^5 cells mL^{-1} and 2.6×10^6 cells mL^{-1}, suspended in 1:500 dilution of nutrient broth) and covering the sample with a clear plastic or glass cover to ensure even distribution of microorganism across the surface. The sample is then placed into a petri dish, the bottom of which contains a moisture-saturated paper filter (the purpose of which is to ensure high humidity throughout the experiment – otherwise the microorganisms may die due to drying out, therefore invalidating the test). Between the paper filter and photocatalyst is a glass stick or rod bent into a 'u' or 'v' shape, used to eliminate contact between the photocatalyst and paper filter. Finally, a glass lid of thickness ≤1.1 mm, with a transparency over 85 % in the λ=340 nm-380 nm range is placed on top of the petri dish, in order to preserve moisture within the petri dish. This 'test cell' should be prepared for each test and control sample and for each time point. The protocol calls for one time point at zero hours (to ascertain initial inoculum and recovery) and one time point at eight hours, although it does then specify that this can be changed to four hours in order to more closely emulate applications *in situ*.

After preparation, the zero-hour samples are immediately immersed in washout solution consisting of peptone, salts and glucose mixed with a surfactant, such as TWEEN 80. The purpose of the washout fluid is to act as

preferential reactants for any remaining active radical oxygen species on the photocatalyst. The test samples for the other time point (either four or eight hours), along with non-photocatalytic 'light' controls, are placed in a UV-irradiated chamber. The UV flux intensity must be able to be measured from the test sample position and should be no greater than 0.25 mW cm^{-2} – at intensities greater than this the bactericidal action of UV light could become the predominant mode of inactivation, as opposed to the photocatalytic inactivation, leading to unclear and obfuscated test results. Photocatalytic and non-photocatalytic controls are also prepared in the manner described and placed in a dark chamber; this is done to determine whether any bacterial reduction seen is due to photocatalytic reactions, or other means.

After the prescribed time, the samples are removed and immersed in the washout solution. A volume of 1 mL of this washout solution-bacterial suspension is pipetted into a volume of 9 mL sterile saline; this is repeated to obtain a series of dilutions. A volume of 1 mL of each dilution factor is pipetted into two sterile petri dishes. A volume of 15-20 mL of fresh sterile nutrient agar is then added to the petri dishes. Once the agar has solidified, they are incubated at 37°C for 40-48 hours. The number of colonies are then counted for the dilution factor at which the plates contain between 30 and 300 colonies.

Using these values, the bacterial concentration of the initial washout solution can be determined (9).

$$P = ZR \tag{9}$$

Where P is the bacterial concentration in colony forming units per ml solution (CFUml^{-1}), Z is the average number of colonies in two petri dishes of the same dilution factor and R is the dilution factor.

From this, considering the dark controls and the non-photocatalytic light controls, a value for photokilling efficacy can be calculated (10).

$$\Delta R = log\left[{}^{B_L}/_{C_L}\right] - log\left[{}^{B_D}/_{C_D}\right] \tag{10}$$

Where:

- ΔR is the photokilling efficacy value with UV irradiation

- B_L is the average number of viable bacteria recovered from a non-photocatalytic sample after UV irradiation intensity L

- C_L is the average number of viable bacteria recovered from a photocatalytic test sample after UV irradiation intensity L.

- B_D and C_D are the same as B_L and C_L, except these were the samples kept in a dark place as opposed to being irradiated.

While this method is highly specific, it has been modified for use in individual laboratories; disparity in methods have led to difficulty in comparing the work done by different research groups. Indeed, even small changes to the method can affect the results. Foster *et al.* (2010) determined the differences in activity reported for a photocatalyst using the BS ISO described above and a well-documented similar in-house method (Brook *et al.*, 2007; Ditta *et al.*, 2008). They found that the photocatalyst investigated reduced the number of viable cells by around 2 Log10 cfu mL^{-1} within 4 hours, determined using the BS ISO. However, the reduction was reported as 6 Log10 cfu mL^{-1} within 4 hours using the in-house method.

It is thought that differences in the inoculation medium (1:500 nutrient broth for the BS ISO, sterile distilled water for the in-house method) had a profound effect on the activity reported, as the 1:500 nutrient broth had more oxidizable material than distilled water, which then acts as a preferential reactant for ROS, reducing the effect on the bacteria. Additionally, distilled water can osmotically stress bacterial cells, potentially increasing the susceptibility of the cells to the ROS (Sperelakis, 2012). In addition, Foster ascribed the difference in activity to a 10-fold difference in the intensity of the light source used between tests (the in-house method used the more intense source). As it is known that intensity is not directly related to photoactivity (Fujishima *et al.*, 2000), the higher intensity could have caused inactivation of bacteria by irradiative processes, independent of the photocatalytic process.

This could cause the reported value to incorrectly include UV facilitated inactivation in addition to photocatalytic inactivation.

There are further publications reporting the photokilling efficacy of photocatalysts which also use different methods. Dunlop *et al.* (2010) reported an assay in which individual silicone 'culture chambers' were adhered to the same substrate, allowing duplicate treatment and control analysis on a single substrate, therefore removing any variability caused by using multiple substrates. While this is useful, the differences between this and other procedures used by other authors make comparison difficult. A study by Fisher *et al.* (2014) used a very similar procedure to the BS ISO, but several modifications such as those made to the light source intensity mean care must be taken when comparing to values reported via BS ISO or indeed other methods.

Despite these modifications, the methods previously mentioned follow the same basic procedure: inoculate the photocatalyst with known number of bacteria, apply radiation of known intensity and wavelength for a given time and recover viable cells, then culture and count the viable bacteria recovered. A pertinent issue with this procedure is the amount of time required; in addition to irradiation time (up to 24 hours) and culture time (18-48 hours), the number of worker hours required to prepare media, inoculate, recover, dilute, spread and count is rather inhibitory and could dissuade authors from exploring the antimicrobial properties of their films at all. A faster test, potentially with fewer steps, could encourage more authors to explore antimicrobial properties with greater adherence to a prescribed test, promoting standardisation.

1.4 – Dopant optimisation

As discussed, the main drawback of TiO_2 is that it is only activated by UV light. Adding impurities, or dopants, to the TiO_2 can improve activity in the visible light region and thus higher photocatalytic activities can be achieved (Yu *et al.*, 2005). The process of adding these elements is known as doping and is of considerable focus in the literature; many dopants have been explored in recent years. Some of the most common of these are shown in Figure 4.

Figure 4: Periodic table of elements showing commonly used dopants in the literature. Carbon: (Irie *et al.*, 2003); Nitrogen (Fujishima *et al.*, 2008); Iron: (Choi *et al.*, 2010); Copper: (Yoong *et al.*, 2009) Silver: (Seery *et al.*, 2007).

Dopants can incorporate into the existing titania crystal lattice via interstitial or substitutional doping. Small, strongly anionic or electronegative dopants like nitrogen and carbon incorporate interstitially, occupying gaps in the existing lattice and creating midgap states close to the valence band (Liu *et al.*, 2011; Breault and Bartlett, 2012). This is in contrast to cationic dopants; given similar radius and valence to the host titanium atom, the dopant incorporates substitutionally and tends to create impurity bands closer to the conduction band (Liu *et al.*, 2011). In substitutional doping, the dopant atom replaces a host atom, i.e., substitutes for a titanium atom. This can only

occur if the size of the dopant atom is similar to the host atom. Another important consideration with substitutional doping is the valence of the dopant compared to the host atom; as titanium exists as a Ti^{4+} ion in TiO_2, substitutional dopants should be of similar valence to minimise charge compensation mechanisms, which distort the titania lattice. Trivalent and pentavalent ions have been considered as dopants to substitute for the tetravalent titanium ion in the lattice. For example, trivalent iron and pentavalent vanadium have both been used to improve the visible light photoactivity of titania (Subasri *et al.*, 2010; Khan and Berk, 2014). Trivalent dopants create electron acceptor level within the band gap, creating a p-type semiconductor where the primary charge carrier is the hole. Conversely, pentavalent dopants create electron donor levels, creating an n-type semiconductor where the primary charge carrier is the electron (Carp *et al.*, 2004).

One of the most useful properties of titania is the ability to not only suppress growth, but to actively kill a wide range of microorganisms (Foster *et al.*, 2011). While increasing the activity of a photocatalyst is the main aim of doping the titania, increasing the photocatalytic inactivation of microorganisms is more complex than increasing photoactivity. As discussed in *section 1.2*, many factors such as crystallinity (phase, size and structure), substrate type (glass, stainless steel), surface area (of the both the photocatalyst and the microorganism), preparation method (magnetron sputtered, sol-gel derived, nanoparticle synthesis) and microorganism species affect experimental outcomes (Kühn *et al.*, 2003; Caballero *et al.*, 2014). Additionally, some dopants may increase bacterial kill rate, but not increase photoactivity. In some cases, the dopant increases photoactivity in addition to being inherently antimicrobial.

Previous work (Ratova, 2013; Fisher *et al.*, 2014; Kelly *et al.*, 2014; Priha *et al.*, 2015; Ratova *et al.*, 2015) has indicated promising dopants from both of these categories, two of which are niobium and molybdenum; the effects of these dopants as reported in the literature are explored in this section.

1.4.1 – Improving visible light activity: niobium doping

Dopants may increase the visible light activity of titania photocatalysts via several mechanisms, one of which is by introducing intermediate energy levels within TiO_2 crystals, effectively lowering the band gap energy. This means that light of longer wavelengths (containing less energy) can activate the film, in the manner described in *section 1.1.2*. Another mechanism is by acting as charge trapping centres; usually, the e-h pair recombines very quickly, around 10 picoseconds (Pelaez *et al.*, 2012) to 200 nanoseconds (Ozawa *et al.*, 2014) after separation. Depending on the orientation of the dopant element within the titania matrix, it can 'hold' the electron away from the hole for a longer period of time. This increases the chance of O_2 and H_2O molecules encountering the e-h pair and forming the radical oxygen species required for photocatalytic reactions (Zaleska, 2008).

Niobium doping is a not uncommon in the literature, with most authors finding increases in photoactivity at low dopant levels. The majority of production methods were via a chemical sol-gel process and no microbiological data were found for films where this dopant was used. Nevertheless, it is explored here for potential application to antimicrobial thin films, as dopants of similar ionic radius such as tungsten (the ionic radius of W^{5+} is 76 pm, Nb^{5+} is 78 pm) have shown to be effective in improving photocatalytic inactivation of microorganisms (Venkatasubramanian *et al.*, 2008; Joya *et al.*, 2011).

A study by Hirano and Matsushima (2006) produced Nb-doped TiO_2 via various chemical sol-gel methods. They found that a dopant concentration of 10%mol. niobium greatly improved the rate of methylene blue dye degradation compared to pure TiO_2; indeed, the activity was around a degree of magnitude greater. However, this trial was conducted using UV irradiation, so this should be considered when comparing to other authors' work. The authors suggest that the increase in photoactivity is attributed to three factors: a slight reduction in band gap energy, an increase in the surface absorptivity and an increase in the surface acidity. This is similar to

findings using tungsten as a dopant, where the increased in activity was heavily attributed to increase in surface acidity (Pan and Lee, 2006); the rate of a reaction tends to increase the further from neutral pH a system is (Atkins and de Paula, 2014).

At a niobium concentration of 20 %mol., the film was found to absorb 40% more light (assessed via UV-Vis spectroscopy) than pure TiO_2 controls and stronger surface interactions with the reactant (acetone) were found. Both of these properties were expected to improve photoactivity (Mattsson *et al.*, 2006). The photoactivity was assessed using a solar-irradiated acetone degradation method, measured via Fourier-transform infrared spectroscopy (FTIR). It was found that, despite the improved light absorption and reactant adsorption kinetics, the pure TiO_2 films had a much higher efficacy than the doped films. This was attributed to the relatively high niobium concentration used – the niobium formed NbO_x clusters, which then acted as charge recombination centres. These are areas that promote e-h recombination, reducing the likelihood of O_2 or H_2O encountering them. This results in the formation of fewer reactive oxygen species and so fewer target reactions (Carp *et al.*, 2004). This phenomenon was also noted by Kaleji *et al.* (2012), who assessed the structure and activity of varying concentrations of niobium. They found that 1 %mol. niobium doped onto TiO_2 thin films resulted in increased activity (measured by methylene blue degradation) compared to undoped controls. However, doping above this concentration reduced activity. This was attributed to the niobium distorting the anatase lattice (and so suppressing crystal growth) and the introduction of charge recombination centres, as was found in the study by Mattsson *et al.* (2006). It must be highlighted that the irradiation source was an 8 W UV lamp, which would have increased the activity of pure TiO_2 films and so makes comparison difficult.

Doping with several elements in the same sample, known as co-doping, has also been employed. A similar study by the same group (Kaleji *et al.*, 2013) produced TiO_2 films, TiO_2 films doped with 1% mol. Nb and TiO_2 films with 15%mol. Sn. Additionally, they produced a co-doped film containing both 1%mol Nb and 15%mol. Sn. The crystal structure was found of be mixed-

phase (anatase and rutile) for the Sn-doped and co-doped film, but not for the Nb-doped film, indicating that for similar annealing temperatures, tin acts as a rutile promoter. Crystallinity for both anatase and rutile phases reduced linearly with addition of dopants – undoped titania had the highest crystallinity, followed by mono-doped, with co-doped having the greatest reduction. Again, this suggests substitutional integration into the titania matrix and thus inhibition of crystal growth. The photoactivity was assessed by methylene blue degradation under both UV and solar light. The co-doped film showed much higher activity than the other samples and the undoped controls. The authors attributed this increase in activity to three main factors: decrease in the size of the band gap, reduction in particle size (thus yielding a higher surface area) and an increase in electron trapping sites, preventing charge recombination and thus increasing the likelihood of further reactions. A similar increase in activity was noted by Breault and Bartlett (2012), who co-doped TiO_2 with niobium and nitrogen. They found a large reduction in band gap energy (measured via UV-Vis spectroscopy) and much higher activity (via methylene blue degradation), compared to the undoped control. They also found that the dopants caused the film to have smaller particles compared to the control, similar to Kaleji's group.

While various testing methods make quantitative comparison challenging, some general conclusions can be made. Firstly, high dopant concentrations reduce photoactivity, due to suppression of crystal grain growth (caused by lattice distortion), formation of two-phase materials and introduction of charge recombination centres. This could be because the pentavalent niobium forms Nb_2O_5, which may substitute with oxygen in the titania lattice, disrupting crystal growth. Conversely, low dopant concentrations were shown to improve photoactivity in both UV and solar light. Authors frequently attributed this to a reduction in band gap energy and a concurrent reduction in particle size (and so increased surface area); it is therefore challenging to deconvolute these two mechanisms. While no specific microbiological studies or trials were found, niobium exhibits properties that highlight it for further research.

1.4.2 – Inherent antimicrobial properties and improving visible light activity: molybdenum doping

The ionic radius of molybdenum is similar to tungsten and niobium (Mo^{5+} has a radius of 75 pm) and so is expected to have similar effects on the visible light activity. Doping titania with molybdenum to improve visible light photocatalytic response has been demonstrated by several authors. Similar to other transition metal dopants, most of the photocatalysts were produced via sol-gel synthesis. Molybdenum is unusual among common dopants, in that it acts as a dual-function dopant; it influences photoactivity while simultaneously and independently acting as an antimicrobial, a property it retains even when not irradiated (Fisher *et al.*, 2014).

Khan and Berk (2014) produced molybdenum-, iron- and vanadium-doped titania coatings via a sol-gel method and compared their activity to one another, a pure TiO_2 control and a commercial TiO_2 powder. They found that all of the doped films had higher activities than pure TiO_2 and the commercial powder, assessed by measuring the degradation of methylene blue under a simulated solar lamp. When the dopant concentration was fixed at 0.125 %mol., molybdenum-doped titania was shown to have the highest activity. However, at concentrations of 0.25 %mol., iron-doped titania had the highest activity, followed by vanadium-doped, with molybdenum-doped having the lowest. This behaviour suggests that Mo-doping affects the titania in more ways than merely lowering the band-gap, as for a given concentration, Mo-doped titania consistently had the smallest band-gap. Factors such as crystal size and structure, as well as electronic properties such as formation of trapping or recombination sites, are influenced by the addition of molybdenum. This is further shown when the concentration of molybdenum was increased to 2 %mol.; a sharp decrease in photoactivity is seen, indicating that the 'hindering properties' outweigh the 'beneficial properties'.

A study was conducted by Devi and Murthy (2008), wherein the photocatalytic efficacy of sol-gel derived Mo-doped TiO_2 was estimated using the breakdown of tebuconazole (a common pesticide), measured via UV-Vis spectroscopy (in a similar manner to the methylene blue degradation test).

The optimum concentration was found to be 5.66 %at. measured by EDX; this concentration was also found to have the smallest band-gap (2.58 eV), compared to the other concentrations tested (5.12 %at. 2.81 eV. 11.02 %at., 2.7 eV). In addition, under solar light irradiation this concentration showed a 33 % increase in overall degradation of tebuconazole and a 2.4 times faster reaction rate compared to undoped TiO_2. However, doping with molybdenum actually reduced photoactivity under UV compared to undoped TiO_2; this was ascribed to an increase in number of recombination centres.

A band-gap energy reduction was noted and correlated to an increase in activity compared to pure TiO_2 controls by Wang *et al.* (2013), using TiO_2-Mo nanoparticles. Despite not being thin films, the relationships between doping and activity, crystallinity and band-gap are still relevant. The authors found that the doped nanoparticles had better activity under solar illumination, measured by methyl orange degradation. The optimum concentration of doped molybdenum was 2 %at. The increase in activity was attributed to the lowered band-gap of 3.05 eV and the Mo particles on the surface acting as e-h trapping sites. In agreement with other authors, they found that increasing the molybdenum content decreased the size and 'quality' of the crystals. Increasing concentration above 2 %at. decreases the activity. This is ascribed to the loss of crystallinity and the molybdenum surface particles transitioning from e-h trapping sites to recombination centres. In contrast to the study by Devi and Murthy (2008), the authors found improved activity under both UV and solar irradiation.

Sol-derived Mo-doped titanium dioxide powders were compared with both Ti-doped molybdenum trioxide (MoO_3) powders and TiO_2-MoO_3 in equal measure in a study by Gutbrod and Zollfrank (2013). They found that, when illuminated with fluorescent light, all test samples had a higher activity against methylene blue than pure TiO_2 controls. Interestingly, it was found that TiO_2-MoO_3 had the highest activity; this is contrary to the work of other authors, equal concentrations of molybdenum species would likely affect the crystallinity of the titania. However, the authors propose that it is a more chemical mechanism that is responsible for this higher activity, as opposed to a photocatalytic mechanism. Mo-doped titania had the second highest

activity, followed by the Ti-doped MoO_3. No chemical mechanisms were ascribed to the other compositions trialled, so it can be said that this study agrees with the literature; Mo-doped titania has improved response in visible light compared to undoped controls.

In a study by Liu *et al.* (2010), pure TiO_2 and Mo-doped TiO_2 films were produced using a sol-gel method. In addition, a multi-layered TiO_2-Mo/TiO_2 film was produced. In agreement with Devi and Murthy (2008), they found that TiO_2-Mo had a lower activity (measured via methyl orange degradation) than pure titania under UV; they did not test the sample using solar light, however. Although no concentration information is given, they state that the TiO_2-Mo/TiO_2 had higher activity than pure titania. It could be that the blend of these materials reduces the relative concentration of molybdenum, lessening the hindering effects on crystallinity associated with high concentrations. Layering materials is also explored in the work of Natori and Kobayashi (2009), where a Langmuir-Blodgett production technique was used to create a Mo-doped TiO_2 film. It was found that the film had higher activity compared to undoped controls, estimated by measuring stearic acid breakdown under simulated solar light. The true effect of these multilayering studies in questionable however, as the generation of ROS and therefore capacity for further reactions is primarily a surface reaction.

A study by Di Paola *et al.* (2002) loaded polycrystalline TiO_2 particles with a variety of transition metal dopants, including molybdenum and tungsten, using a wet impregnation method. Activity was assessed by measuring breakdown of the compound 4-nitrophenol. They found that all dopants lowered the band-gap energy of the TiO_2 nanoparticles, but only tungsten increased the activity. This is in contrast to the other dopants, that despite lowering the band gap, actually resulted in a decrease in photoactivity. Two mechanisms for this reduction were proposed. Firstly, a reduction in active sites on the surface of the particles; however, it should be noted that this hypothesis is not found in the work of other authors. It may be that the concentration of the dopant used was high enough to create a surface layer, or surface barrier effect and so seemingly reduced active sites. The second mechanism proposed is an increase in recombination centres – this is in

accord with the literature. The authors also explored the effect of molybdenum on the surface acidity. They found that with increasing molybdenum concentration, the pH of any surface liquid reduced. They ascribed this to an increase in Mo^{6+} ions. This surface acidity property has the potential to increase photoactivity in other systems, as the further away from neutral pH a reaction takes place, the faster it occurs (Atkins and de Paula, 2014).

It is interesting to note that papers relating to the effect of molybdenum doping on microbial viability are scarce. However, the effect of molybdenum oxides on microorganisms, with no focus on photocatalysis, is established. Zollfrank *et al.* (2012) conducted a trial, wherein sol-derived MoO_3 was loaded onto both polyurethane (PU) and titanium rods and incubated with a suspension of *Staphylococcus aureus*. They found that both the PU and Ti surfaces coated with MoO_3 had no viable bacterial load after 6 hours, while no antimicrobial effect was seen on the uncoated controls. The optimum concentration of molybdenum was found to be 5 %at. It is unlikely that the antimicrobial effect observed was due to ion leaching mechanisms; Inductively coupled plasma atomic emission spectroscopy (ICP-AES) has been used elsewhere (Fisher *et al.*, 2014) to determine the extent of leaching of the molybdenum ions from the film. After an initial burst of 0.73 ppm in two hours, it was found that the molybdenum ions had leached fewer than 0.04 ppm after 48 hours. This low level of release implies that the molybdenum ions are not readily leachable. This supports the mechanism proposed by Zollfrank. The antimicrobial effect was not ascribed to a leaching ion diffusion, but to an equilibrium ion diffusion (11), (12)

$$MoO_3 + H_2O \leftrightarrow H_2MoO_4 \qquad (11)$$

$$H_2MoO_4 + 2H_2O \leftrightarrow 2H_3O^+ + \qquad (12)$$
$$MoO_4{}^{2+}$$
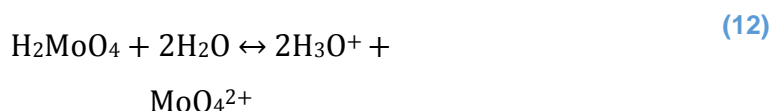
The authors propose that it is the H_3O^+ molecules, known as hydronium ions, which drive a pH change that killed the *S. aureus*. In effect, this is similar to

the mechanism suggested by Di Paola *et al.* (2002), strengthening the argument for pH driven inactivation of microorganisms.

In a similar study by the same group (Lorenz *et al.*, 2011), it was found that using TiO_2 as a substrate material instead of PU or titanium improved the antimicrobial effect compared to that seen in the study by Zollfrank *et al.* (2012). Interestingly, these tests were done without illumination, so the proposed mechanism cannot be photocatalytic; the proposed mechanism is the same as that described above, but the increase in activity comes from the greater surface area of the porous TiO_2, compared to the relatively non-porous PU and titanium.

In a study by Fisher *et al.* (2014), TiO_2 thin films with varying concentrations of molybdenum were produced via magnetron sputtering and the activity assessed using the methylene blue degradation technique. A dopant molybdenum concentration of 7 %at. was found to produce the highest photocatalytic activity. Analysis of crystallinity showed that all samples above 3 %at. concentration of molybdenum had mixed-phased anatase/rutile crystals, suggesting that molybdenum acts as a rutile promoter. Molybdenum-doped TiO_2 was found to be highly effective against *Escherichia coli* – a 99.999 % reduction in viable bacteria within 4 hours was observed using a modified BS ISO 27447:2009 procedure (the main procedure of which was described in *section 1.3.2*) under visible light. Interestingly, the same reduction was observed in both solar-illuminated and dark conditions. This could be due to the antimicrobial effects of molybdenum discussed in the studies of Zollfrank *et al.* (2012) and Lorenz *et al.* (2011). While this dual effect is ultimately beneficial for antimicrobial applications, the presence of this effect leads to difficulty in differentiating between photocatalytic and pH-driven inactivation of microorganisms.

Comparison between different authors' work is challenging for several reasons. The different methods used to grow photocatalysts (sol-derived, magnetron sputtered etc.) are difficult to compare due to topographical, crystallographic and surface chemical differences. In terms of assessing activity, authors may use one of the several commonly used tests described in *section 1.3*, usually measuring the breakdown of an organic compound.

The variety of tests leads to a lack of consistency across the literature, as the activity given by the breakdown of one compound may not be directly transferable to another compound. Also, because there is no universally-adopted standardised test for determining antimicrobial properties, laboratory-specific variations or modifications to the current most common test (BS ISO 27447:2009) may hinder comparison of activity values reported by different authors. In addition, the aforementioned British standard used is very time-consuming, prone to user error and requires a high level of microbiological expertise – these factors may discourage authors from investigating the photokilling efficacy of photocatalysts at all, ultimately inhibiting development and progression of the field.

1.5 - Aims

As can be seen, niobium and molybdenum are promising dopants that improve the activity of titania photocatalysts under visible light irradiation conditions. The effect of these dopants on the antimicrobial effects of the photocatalyst however are not well established. This could be in part due to prohibitive or unattractive existing test methods. It therefore follows that the primary aims of this project are to:

1. *Establish the antimicrobial effects of niobium-doped and molybdenum-doped titanium dioxide thin film photocatalysts.*
2. *Develop a test to evaluate antimicrobial effects of photocatalysts that is faster, simpler and requires less microbiological expertise than the BS ISO 27447:2009.*

Chapter 2

TITANIA SURFACE COATINGS

Surface coatings can be employed whenever the desired surface property of a material is different to that of the bulk material and are used both decoratively and functionally. One type of surface coatings are thin films, where the coating thickness ranges from nanometres to micrometres. Photocatalytic titania coatings are often produced in a thin film and in this Chapter, the processes involved will be explored.

2.1 – Surface coatings

In the broadest terms, a surface coating is a distinct layer of material that separates a substrate from its environment. Coatings are ubiquitous in the modern world and can be found in almost every industry. Surface coatings can be decorative, changing the appearance of a substrate – for example, in printing applications (Jehn, 1992; Garcia *et al.*, 2006) or in the production of graphics for wares and products (Sawatsky, 2004). Coatings are also employed functionally, modifying the interface properties of the substrate material. Properties such as friction coefficient and wear resistance (Cosemans *et al.*, 2003; Berman *et al.*, 2013), electrical and thermal conductivity (Kelly and Zhou, 2006; Vassen *et al.*, 2009), adhesiveness (Ashokkumar and Adler-Nissen, 2011) and wettability (Genzer and Efimenko, 2006) have all been appropriately modified with the use of surface coatings and are well-established in industry. Of particular interest are coatings that can destroy or inhibit the growth of microorganisms, with both copper- and silver-based coatings being extensively researched (Yoon *et al.*, 2007; Fabrega *et al.*, 2009; Ren *et al.*, 2009).

Surface coatings based on titanium dioxide have also received great interest in recent years. The antimicrobial properties of these coatings are especially interesting, as many sectors would benefit from such a coating – medical applications, industrial food preparation areas and commercial kitchens, along with hygienic domains such as bathroom fixtures and fittings (Fernández-Ibáñez *et al.*, 2009; Page *et al.*, 2009; Foster *et al.*, 2011).

2.1.1 – Thin film coatings

One specific category of functional coatings are thin films. Thin films are usually less than 1 µm in thickness, are uniform and structured and are highly versatile. Several techniques have been used to produce thin films, such as atomic layer deposition (Iancu *et al.*, 2015), molecular beam epitaxy (Chow, 1991), chemical vapour deposition (Ditta *et al.*, 2008; Foster *et al.*, 2010; Gardecka *et al.*, 2015) and various etching processes (Lahmar *et al.*, 2016). One of the most common fabrication techniques involves the use of

sol-gels, where nanoparticles are suspended in a gel matrix (Fu *et al.*, 2005; Gelover *et al.*, 2006; Joya *et al.*, 2011; Mills *et al.*, 2016; Kaleji *et al.*, 2017). The gel is then applied to the substrate uniformly, so that as the gel dries, a coating is deposited. While sol-gel fabrication has been extensively implemented, it can lead to porous coatings and while it is useful for batch-level production of thin films, can be prohibitively expensive for larger scale projects due to reliance on chemical precursors (Klein, 1991).

In addition to these techniques, fabrication via physical vapour deposition processes are also possible. In physical vapour deposition (PVD), the composition of the coating is much easier to control, as solid high purity target materials are used instead of chemical precursors. Additionally, titania films deposited via magnetron sputtering deposition (a type of PVD) have a lower porosity compared to films produced via a sol-gel method.

This reduction in porosity leads to a reduction in surface area, which has the potential to decrease activity for a given thickness. While this superficially seems counterproductive to the fabrication of active, functional films, the consequence of this is that films fabricated via magnetron sputter deposition have less variance in activity with thickness, as changing thickness does not significantly change the surface area (Carp *et al.*, 2004). The denser films obtained using magnetron sputtering are more structurally stable than sol-gel coatings and can lead to higher activity via higher quality crystal growth. The effects of densification of coatings is explored in *section 2.3.*

Finally, the technique is readily scalable to industrial applications. The ability to exert greater control over film properties, in addition to producing higher-quality films than other techniques and scalability factors, led to the magnetron sputter deposition technique being used for this work.

2.2 – Magnetron sputter deposition

In order to discuss aspects of magnetron sputter deposition, the underlying principles must first be explained and an appreciation for the various processes obtained.

2.2.1 – Vacuum processes

Like all PVD processes, evaporation and vacuum process are integral to magnetron sputtering. These processes involve creating a vapour of the desired coating material (also called the target material, or target) and allowing this vapour to adsorb and condense onto the substrate. Evaporation processes usually take place in high-vacuum conditions, typically between one micropascal to one millipascal (Deshpandey and Bunshah, 1991). A vacuum is employed in order to increase the mean free path (MFP) between the target and the substrate. In this context, the MFP is the average distance a particle of evaporated target material will travel before undergoing a random collision. When the MFP is less than the distance between the target and substrate, the probability of evaporated particles leaving the target and subsequently condensing on the substrate is low, as the target particles would likely collide with other species and be scattered. In an appropriately high vacuum, evaporated atoms can travel in a collision-free path from target to substrate. Not only does this increase the rate of deposition of the coating, it also enables fabrication of coatings with similar chemical composition to the target material, as the particles will not have undergone peripheral reactions.

In order to achieve appropriate vacuum, several pumps are usually required. Likewise, adequate control and monitoring of the chamber pressure requires different gauges. At relatively low vacuum (from atmospheric pressure to 0.1 Pa) a rotary pump may be employed, along with a Pirani gauge. Rotary pumps achieve vacuum via positive displacement of air from the chamber to the surroundings, relying on viscous flow. A Pirani gauge determines the chamber pressure via thermal conductivity. A voltage is applied to a filament within the chamber and a nearby thermometer detects the heat discharged

across a gas. The voltage is set so as to keep this heat discharge constant; as the chamber pressure drops, fewer gas molecules collide with the filament, reducing the thermal conductivity. Thus, an increasingly high voltage is required to maintain constant heat discharge. This voltage can be monitored and used to monitor the pressure (Shie *et al.*, 1995).

At around 0.1 Pa, a rotary pump becomes unable to achieve higher vacuum, because there are too few gas molecules to be affected by viscous flow. At this stage, more specialised pumps must be used, such as turbomolecular pumps and diffusion pumps. While turbomolecular pumps have excellent pumping ability, they contain moving parts, hindering reliability and increasing complexity. In contrast, a diffusion pump has no moving parts and is therefore very reliable and is capable of achieving high-vacuum conditions of around 0.1 μPa. Additional benefits include low cost and rapid pumping speed. A diffusion pump consists of a heater, column and jet assembly and relies on the evaporation of oil to impart momentum to gas molecules to remove them from the chamber. One notable feature of a diffusion pump is that it must be kept under vacuum itself – if the oil is exposed to atmospheric pressures while hot, it is likely to oxidise, preventing operation of the pump. Therefore, a backing pump is also employed, wherein a rotary pump is attached to the base of the diffusion pump system.

The pump achieves such a high vacuum by evaporating oil with a low vapour pressure using the heater and allowing the oil vapour to rise in the column, which terminates in a downwards-facing jet assembly. As the diffusion pump is mounted directly below the chamber, gas molecules in the chamber may descend into the column via diffusion. The gas molecules may then encounter the downwards jets of oil vapour, resulting in the gas molecules becoming trapped in droplets of oil. As the gas molecule-oil droplet complexes fall back toward the cooler oil in the heater, the oil condenses, freeing the gas molecules. The gas molecules have now been transported away from the chamber (thus lowering chamber pressure) but remain in the system. At this point, the backing pump transports the gas molecules to the exhaust, removing them from the system.

2.2.2 – Sputtering processes

Sputtering is a term to describe the physical process of ions impinging on a target of desired material, ejecting atoms and ions of the target material. These atoms and ions are then free to move within the deposition chamber, with the aim of adsorbing and reacting on a substrate. To accomplish this process, several steps must be taken. Firstly, the deposition chamber must be evacuated of air to create a vacuum, as described in *section 2.2.1*. A typical single-magnetron setup is shown in Figure 5.
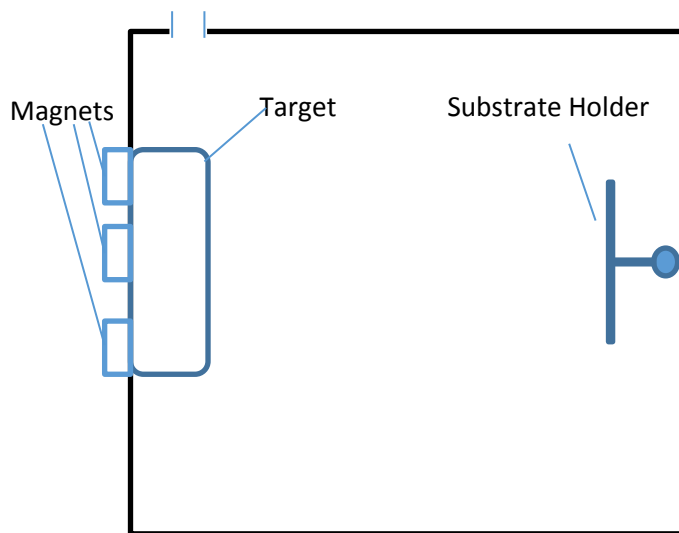
Figure 5: Deposition chamber with single-magnetron setup. Powerful magnets are located on the exterior of the camber behind the target, which is the desired deposition material. In this example, a planar substrate holder is used. The square chamber is evacuated of air using pumps via a vent.

Once the chamber is under vacuum, an inert gas such as argon must be introduced into the chamber (Figure 6). This is known as the process gas.
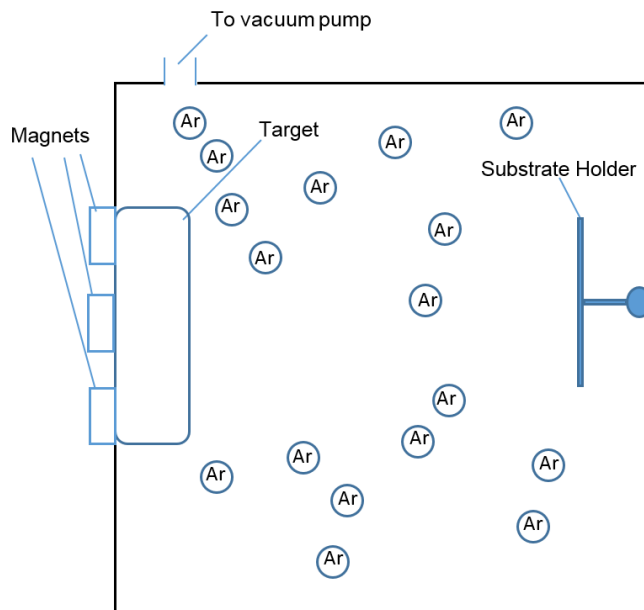
Figure 6: Deposition chamber with argon as a process gas. Argon has been added to the evacuated chamber at such a rate as to reach an equilibrium with the evacuation rate; in this manner, the amount of argon present is tunable to the specific parameters required.

A potential difference between the target (cathode) and chamber (anode) is introduced – this causes a build of charge to occur on the target. Seed electrons within the chamber, generated either by random ionising thermal collisions between argon atoms, or ionisation of argon caused by cosmic rays, are accelerated away from the cathode. Electrons that gain enough energy from this acceleration can then proceed to ionise more argon. The energy gained from this acceleration is impacted by the MFP within the chamber, which also highlights the importance of low and precisely controlled pressures in this system. The potential difference then causes the positively-charged ionised argon to accelerate towards the target. When the argon ion strikes the target, kinetic energy is transferred and electrons and target atoms are ejected. Argon ions, electrons from the argon and electrons from the target collide with the process gas, causing further ionisation (Figure 7).
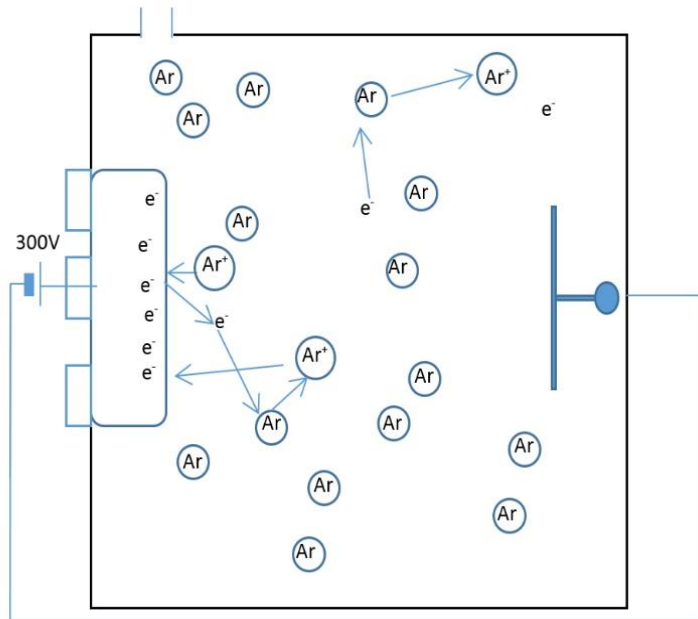
Figure 7: Schematic diagram of seed electron-argon ionisation mechanics, and subsequent electron ejection from target. Several concurrent mechanics occur here; cosmic waves and thermal collisions cause random ionisation of argon, and the applied potential difference between the target (cathode) and the chamber (anode) causes the ionised argon to accelerate towards the target and collide. This collision causes a cascade reaction which causes electrons to eject from the target, causing further ionisation of argon.

The resulting cascade generates a plasma. Argon atoms that received energy from the electrons, but fail to ionise, return to the ground state by emission of a photon. This causes the plasma to have a characteristic colour emitted from it, called a glow discharge. Another effect of the argon ions impinging on the target, is the subsequent ejection of target material. When the argon ion impinges upon the target, depending on the energy of the collision, it may 'burrow' into the target and cause a cascade reaction; the collisions cause target atoms, ions and electrons to be ejected from the target (Figure 8). The ejected material may deposit and condense on the chamber walls, fixtures and substrate (Westwood, 2003). It is therefore the aim of sputter processes to eject target material into the chamber towards the substrate, with the goal of uniformly coating the substrate material to produce a homogenous, dense film.

The rate at which deposition occurs is of great importance in these processes, as it can influence coating properties as well as influencing

commercial viability. The deposition rate is influenced by many factors, such as plasma locality and density, in addition to target species; heavier species require more kinetic energy to be imparted in order to cause a cascade and subsequent ejection of target material.
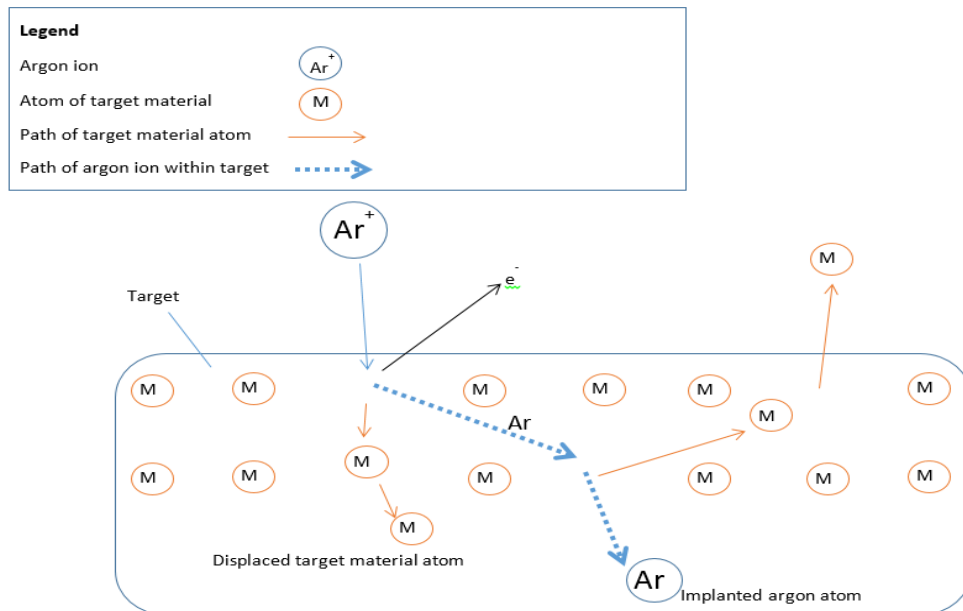
Figure 8: Burrowing argon ions lead to ejection of electrons and target atoms. The accelerated argon ions collide with (ejecting an electron from the target) and burrow into the target, causing the atoms of the target material to displace. A cascade reaction occurs, wherein the argon becomes more burrowed into the target and the atoms of the target displace further towards the boundary, eventually ejecting into the chamber.

The processes described so far concerns PVD sputtering techniques in general. What separates magnetron sputtering from other kinds of sputtering is the use of powerful magnets to manipulate the plasma; as the plasma contains most of the electrons and ions, manipulation of such can result in a more efficient and controlled process, with greater deposition rates. Magnets are mounted behind the target and so a magnetic field is applied parallel to the target. When an electron is ejected from the target, it is subject to the Lorentz force; this force changes the direction of the ejected electron, so that it forms a semi-circular orbit close to the target. If the electron does not make any collisions during its first orbit, it returns to the target. However, if the electron loses energy due to a collision with an argon atom, it cannot return to the target and so makes a series of semi-circular 'hops' around the target,

dictated by the arrangement of the magnets (Figure 9) (Rossnagel, 1991; Westwood, 2003).
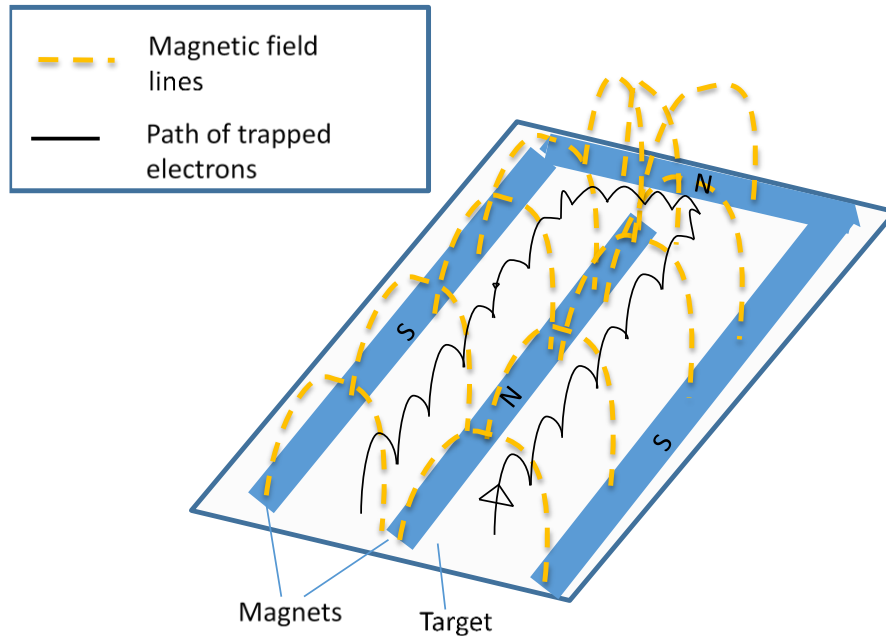
Figure 9: Path of ejected electron around a target, dictated by an arrangement of the magnets in the magnetron. The solid line indicates the path of trapped electrons, while the dashed lines indicate magnetic field lines. Adapted from Westwood (2003).

Ejected electrons therefore become trapped in a spiral tunnel path close to the surface of the target, as opposed to escaping like the atoms and ions. Magnetically trapping these electrons increases the probability of ion bombardment and so promotes further ionisation, vastly improving the sputter rate (Kelly and Arnell, 2000).

As mentioned, ejected target atoms and ions can deposit anywhere within the chamber. In order to increase the probability of deposition on the substrate, an unbalanced magnetron system can be used. In conventional or balanced systems, the outer and inner regions of each magnetron have equivalent magnetic strengths. Contrastingly, in an unbalanced system the outer and inner regions of each magnetron have different magnetic strength (Parsons, 1991). There are two types of unbalanced system; inner regions stronger than outer regions, known as type-1 and outer regions stronger than inner regions, known as type-2. This leads to changes in the magnetic field

lines – escaped electrons are guided by these field lines, either converging back towards the target (type-1), or out towards the substrate (type-2). Maintaining plasma neutrality, ions are dragged along with these electrons (Kelly and Arnell, 2000). Thus, in type-1, the plasma is confined to the vicinity of the target, but in type-2, the plasma is extended into the chamber and to the substrate (Figure 10). Extending the plasma to the substrate has the direct effect of increasing ion density at the substrate surface, resulting in an increased ion bombardment of the growing film. This ion bombardment can be thought of as an atomic peening mechanism, imparting energy into the growing film, promoting diffusion of coating species and increasing density. These effects are further explored in *section 2.3*.

Substrate Holder
Plasma

| N | S | N |

Conventional (balanced) magnetron

| N | S | N |

Type-1 unbalanced magnetron

| N | S | N |

Type-2 unbalanced magnetron
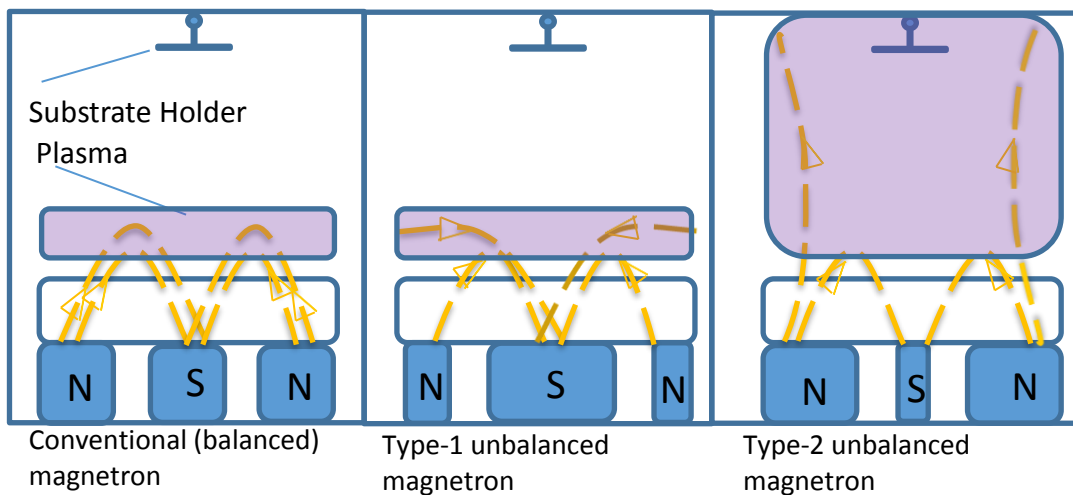
Figure 10: Effect of balanced, type-1 and type-2 unbalanced magnetron configurations on plasma density. The size of the solid blue quadrangles correlates to the amount of magnetic material in each region. By adjusting the polarity and amount of magnetic material, at each magnet, the magnetic field lines can be manipulated. As plasma density follows magnetic field lines, this property can be used to manipulate the position and density of the plasma.

While the use of type-2 unbalanced magnetrons represents improvements in the quality of sputtered films over balanced magnetrons, the processes described so far have only discussed the use of a single magnetron. The plasma can be manipulated further by using multiple-magnetron systems. In these systems, the magnetic field lines of adjacent magnetrons can interact and so the orientation (and thus polarity) of secondary magnetrons must be considered.

It follows that the secondary magnetron can have identical ('mirrored') polarity, or opposite polarity (termed 'closed field'). If a mirrored polarity is used, the magnetic field lines interact in such a way as to direct secondary electrons towards the chamber walls; this is sub-optimal, as electrons directed in this manner do not contribute to the plasma density at the substrate, reducing ion bombardment of the growing film, creating sub-optimal structures.

In the more effective polarity orientation, closed field, the field lines interact in order to direct electrons towards the substrate; this effectively extends the plasma into the chamber towards the substrate, increasing plasma density at the substrate, resulting in more efficient deposition (Figure 11) (Kelly and Arnell, 2000).

Mirrored configuration   Closed-field configuration
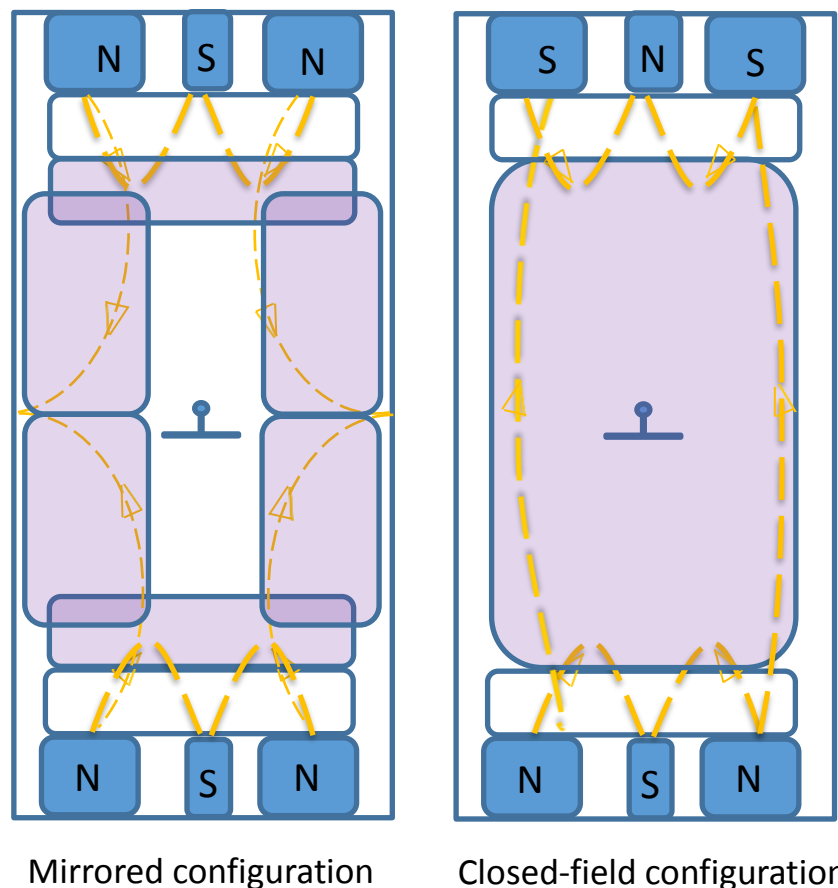
Figure 11: Effects of mirrored configuration (left) and closed-field configuration (right) on plasma (purple) around rotating substrate holder (centre). By manipulating the orientation to a closed-filed configuration, plasma density can be increased at the substrate holder. Adapted from Kelly and Arnell (2000).

2.2.3 – Reactive sputtering processes

The processes discussed so far have focussed on the deposition of purely metallic coatings; the sputtered target material deposits onto the substrate, without reacting with other species. This is ideal when the intended coating is the same composition as the target material. However, if the desired coating has a different composition to the target, additional processes are required.

One such process is reactive sputter deposition, also known as reactive mode – in this mode, reactive gas species are introduced into the deposition chamber. During deposition, the evaporated target material undergoes reactions with present reactive gas species, to produce a compound coating. Common reactive gasses include oxygen and nitrogen, to produce metal oxide coatings and metal nitride coatings, respectively. While the reactive mode enables deposition of compound coatings, it is not without additional complex processes to consider. Introduction of reactive gasses can have profound effects on the structure of the coating; equally, the stoichiometry of compound coatings must be considered. Additionally, attention must be given to the rate of deposition.

The chief factor in these considerations is the partial pressure of reactive gas in the chamber. At low partial pressures, reactive gas species may react with deposition material (from the target) at the substrate; this is known as the metallic mode. In the metallic mode, deposition rates can be relatively high and are similar to non-reactive modes. However, there are usually too few reactive gas species present to create a stoichiometric coating. This leads to the production of a sub-stoichiometric coating, which is not desirable.

In order to produce coatings of stoichiometric composition, the partial pressure of the reactive species must be increased. This is usually achieved by increasing the flow rate of the species into the chamber. However, the relationship between coating properties and flow rate of the gas is non-linear (Musil *et al.*, 2006). As the reactive gas flow is increased, only small changes in the partial pressure of the gas are observed. This is because there is sufficient deposition material within the chamber to react with the gas, preventing increases in pressure. However, if the flow rate is increased

further and exceeds the absorption/reaction capacity of the deposition material, the reactive gas will begin to react with the target surface. This creates a more resistive oxide layer, which reduces the target voltage. The lower target voltage reduces the acceleration of argon ions towards the target, lowering the amount of kinetic energy transferred on impingement. This makes sputtering less efficient and drastically reduces deposition rate; this mode of action is the 'oxide mode' and the target is said to be 'poisoned'. When in oxide mode, any further increase of the flow rate of reactive gas will result in linear increase in partial pressure of that gas. Thus, despite lower deposition rates, stoichiometric coatings may be produced.

Once the oxide layer has been formed, it may only be removed by reverting to the metallic mode. This is achieved by reducing the partial pressure of the reactive gas species within the chamber past a secondary critical value and allowing the targets to 'sputter off' the oxide layer – this is known as 'sputter cleaning'. Interestingly, this secondary critical value is lower than the first critical value, where the target enters the poisoned mode. This behaviour is called hysteresis and is represented graphically in Figure 12.
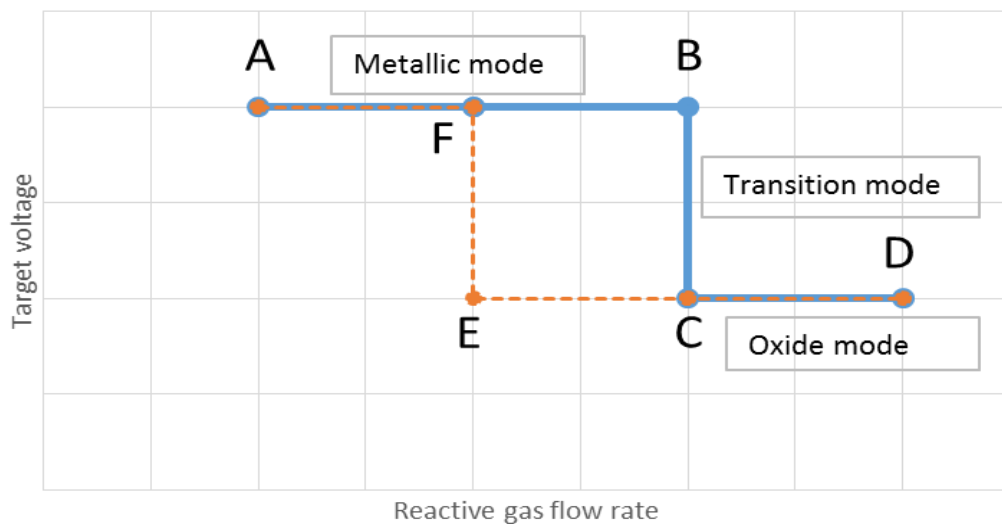
Figure 12: Hysteresis characteristics with target voltage as a function of reactive gas flow. The critical value for the change from metallic mode (A-B) to poisoned mode (C-D) is higher than the critical value (E) for reverting back to metallic mode. Adapted from Banyamin (2014).

The lower critical value for reverting back to metallic mode is caused by the reduction in target voltage. The oxide sputters off at a much lower rate than the metal and takes a long time to be removed.

In reactive mode systems, it is desirable to increase the partial pressure to produce stoichiometric coatings, but the partial pressure must not become too high, or coating structure may be negatively affected (discussed in *section 2.3*). Additionally, exceedingly high pressures may reduce deposition rates further. Therefore, control of the partial pressure of reactive gas within the chamber is vital. The flow rate and thus partial pressure, of the reactive gas can be controlled automatically using an optical emission monitoring (OEM) system. Such systems consist of a fibre optic cable adjacent to a window of the chamber connected to a monochromator and detector, which can then control the flow rate of the reactive gas into the chamber. When the plasma is ignited, a glow discharge effect occurs; it emits a spectrum of photons characteristic to its constituent particles, i.e. the target material. A prominent, characteristic wavelength within this spectrum can be selected using the monochromator and measured using the detector; as deposition rate remains constant, intensity of the wavelength remains constant. When in metallic mode, the maximum is known as the 'full metal signal'.

When the reactive gas is added to the chamber, the resulting reactions cause the colour of the plasma to change and the intensity of the characteristic wavelength to decrease. In this way, the intensity of the characteristic wavelength can act as an analogue for the partial pressure of the reactive species. Therefore, a specified percentage of the full metal signal can be set, such that the OEM system increases the flow rate of the reactive gas until the detected emission is at the set percentage of the full metal signal. The flow rate is then tightly throttled by a rapid response valve to ensure constant emission percentage is maintained.

As discussed, the formation of an oxide layer on the target drastically reduces target voltage and sputtering rate. However, being a semiconducting material (and so more resistive than the pure metal target), charging effects must also be considered. When a potential difference is applied across an

anode and cathode separated by an insulating material, the material will charge until a dielectric barrier discharge occurs, also known as an arc. These arcs can result in droplets of material being ejected from the target and condensing on the substrate, causing damage and stress to the growing coating and negatively impacting the structure. In addition, the arc may provide a nucleation point on the target for further arcs to form, resulting in a feedback loop that ultimately reduces the effectiveness of the coatings and damages the magnetron. Finally, the arc can cause rapid and unpredictable fluctuations in voltage and plasma density, which may affect the stoichiometry of the growing coating. It is clear that control of arcing behaviour is critical.

One such manner of control is the use of a pulsing DC power supply – the use of a pulsing magnetron system is termed pulsed magnetron sputtering process. When the target voltage is pulsed, the build-up of charge is reduced, minimising the probability of an arc forming. The effect of pulsing is on coating structure illustrated in Figure 13. In Figure 13a, no pulsing was used during the deposition process; it can be seen that the coating is heterogeneous, porous and has a rough surface. This contrasts with Figure 13b, where pulsing was used – the coating is dense, homogenous, with a smoother surface.
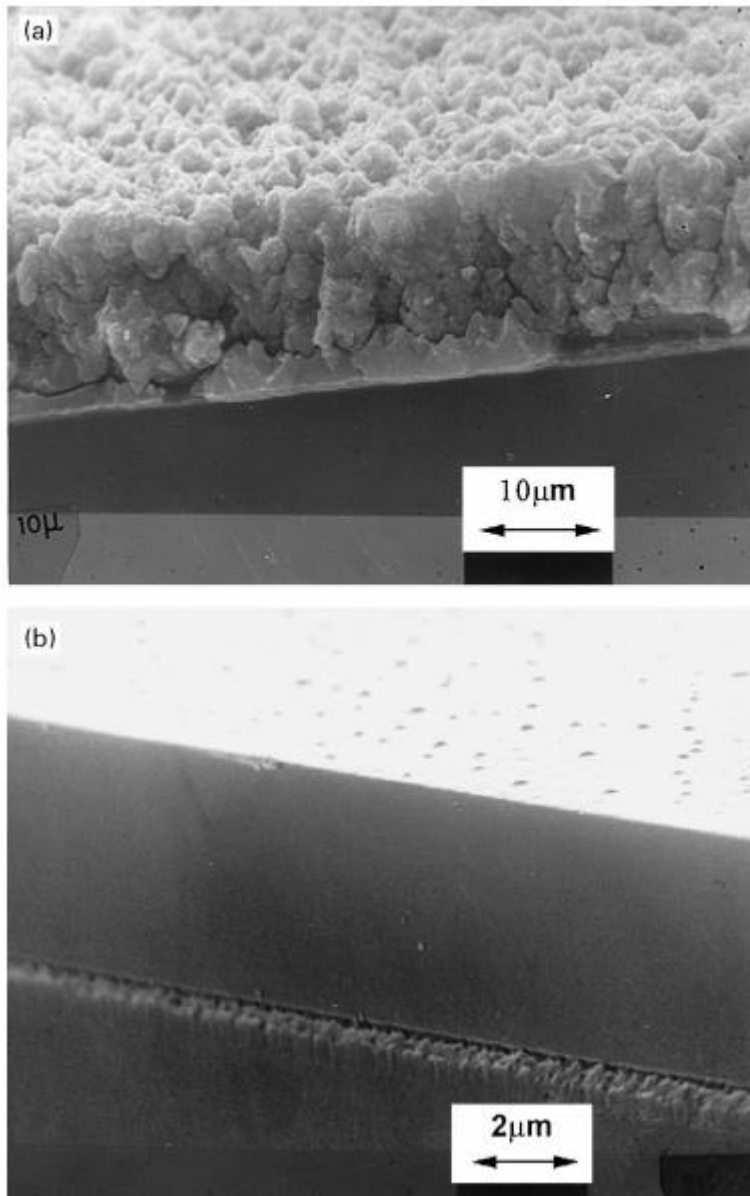
Figure 13: SEM micrograph of fracture sections of alumina deposited by a) DC reactive sputtering processes, without pulsing and b) pulsed DC reactive sputtering coatings (Kelly and Arnell, 2000). The coating deposited via a pulsed system is much more homogenous with fewer stress features than the coating deposited in the DC mode.

Pulsed DC deposition is a combination of the frequency of the cycle and the ratio between voltage on and off times, i.e. negative and positive voltages phases. Pulsing was only found to be effective at reducing arcing when the frequency was above 20 kHz. Above this, suppression of arcing was most prominent when the voltage off-time was approaching the same as the voltage on-time (Kelly and Arnell, 2000).

2.3 – Structure of coatings

The above section describes the processes of magnetron sputter deposition and how these processes can be used to produce a stoichiometric compound coating on a substrate. There are various factors that can influence the structure of the coating during deposition.

2.3.1 – Structure zone model

The classification of coating structure into characteristic 'zones' and subsequent correlation with various deposition parameters has been previously done by several authors (Thornton, 1974; Craig and Harding, 1981; Kelly and Arnell, 2000) and are known as structure zone models

- Zone 1 coating structures are characterised by a heterogeneous repeating columnar structure, separated by void spaces. The resulting coating is highly porous and is best described by the term 'porous columnar'.
- Zone 'T', a transition zone between 1 and 2. Structures in this zone are characterised by dense columnar, poorly defined structures with no void spaces.
- Zone 2 coating structures are characterised by dense columnar structures similar to zone T, but have better defined boundaries, appearing highly faceted. They are therefore less porous than zone 1 coatings, but retain a degree of heterogeneity and can be described as 'dense columnar'.
- Zone 3 coating structures can be columnar or equiaxed grains, with flat, smooth surfaces. They are characterised by a fully dense, homogenous coating.

While there are many factors that influence the structure of the growing coating, such as deposition atom incidence angle, target-substrate distance and substrate roughness, some parameters are considered key to the structure of the coating. The production of a coating in one of these zones over another is governed by these key parameters, identified in the model.

The first key parameter is the homologous temperature, given by the temperature of the substrate divided by the melting temperature of the target material. This parameter essentially describes the thermal energy of atoms of target material once deposited (where they are known as adatoms). This thermal energy is directly related to the ability of the adatoms to diffuse and thus their mobility. This is critical, because if the adatoms are free to diffuse on the substrate, they are more likely to form dense, uniform, homogenous structures, as observed in zone 3. Contrastingly, if adatoms have limited mobility post-deposition, then the coating is more likely to be influenced by geometry when growing. That is to say, when an atom condenses onto the substrate, it will adsorb and form a nucleation point for other atoms. Further atoms deposited are more likely to adsorb to the nucleation site, forming a tower or column. This in turn leads to 'shadowing' effects, where the peaks created by previously deposited material occlude other areas on the substrate. As the adatoms lack the energy to diffuse along the substrate and fill the gap, a columnar structure with void spaces is therefore formed. This leads to heterogeneous, porous coatings, as seen in zone 1 (Kelly and Arnell, 2000). This problem is compounded when rougher substrates are used, as the deposited material will likely condense on the peaks of the substrate before the valleys, resulting in an even more columnar coating structure. The angle of incidence of target ions is also critical when the homologous temperature is low, as columns would grow in the direction of incidence. If this is not perpendicular to the substrate, shadowing effects can be more pronounced. Therefore, higher homologous temperatures are vital for high-quality zone 3 coating structures.

The second key parameter is the influence of energetic particle bombardment, which can be considered as ion energy. This parameter describes the influence of the argon ions within the plasma on the deposited growing film. The reasons for the importance of this parameter are similar to that of homologous temperature; when argon ions of high energy bombard the deposited atoms, kinetic energy is transferred, increasing the energy of the adatom and increasing the ability to diffuse. Incident ion energy is intrinsically difficult to determine and so a number of analogues, or

'parameters that may affect ion energy', can be used, depending on specific system apparatus. One way to represent ion energy is using the partial pressure of argon within the chamber. This is because, with increasing partial pressure, the mean free path of argon ions reduces, increasing the likelihood of argon ion collision with neutral argon species, decreasing ion energy. Therefore, with low argon partial pressure, the probability of collision remains low and the mean free path and ion energy remain high. Another way to represent ion energy would be the magnitude of the bias voltage applied to the substrate. A bias voltage is a negative voltage is applied to the substrate holder, accelerating the positively-charged argon ions towards the substrate, thus increasing the kinetic energy. The magnitude of acceleration experienced by the ion is proportional to the magnitude of the negative voltage applied to the substrate and is therefore related to the amount of kinetic energy imparted and so this value can be used as an analogue of ion energy. Using bias voltage as an analogue of ion energy can only be used in systems where a bias voltage is employed, which may not be suitable for all coating applications; while this has been used successfully, it can introduce intrinsic stresses into the coating and so was not used in this project (Windischmann, 1992).

The third key parameter identified in the model is the ion flux, or the ion-to-atom ratio at the substrate. This parameter describes the number of argon ions relative to the number of deposited target atoms. The importance of this parameter is again similar to the previous two key parameters and is related to energy transfer. A higher ion flux results in more argon ions per deposited atom, resulting in more kinetic energy transferred per atom; each atom has more energy transferred to it, improving the ability of the atom to diffuse and form zone 3 coatings (Zhou *et al.*, 2008).

The combination of these three parameters significantly contribute to the structure of the coating. The identification of these parameters in the model led to the development of structure zone diagrams. Initially, Thornton (1974) developed a structure zone diagram (Figure 14) that incorporated homologous temperature and the pressure of argon (relating to the ion energy).
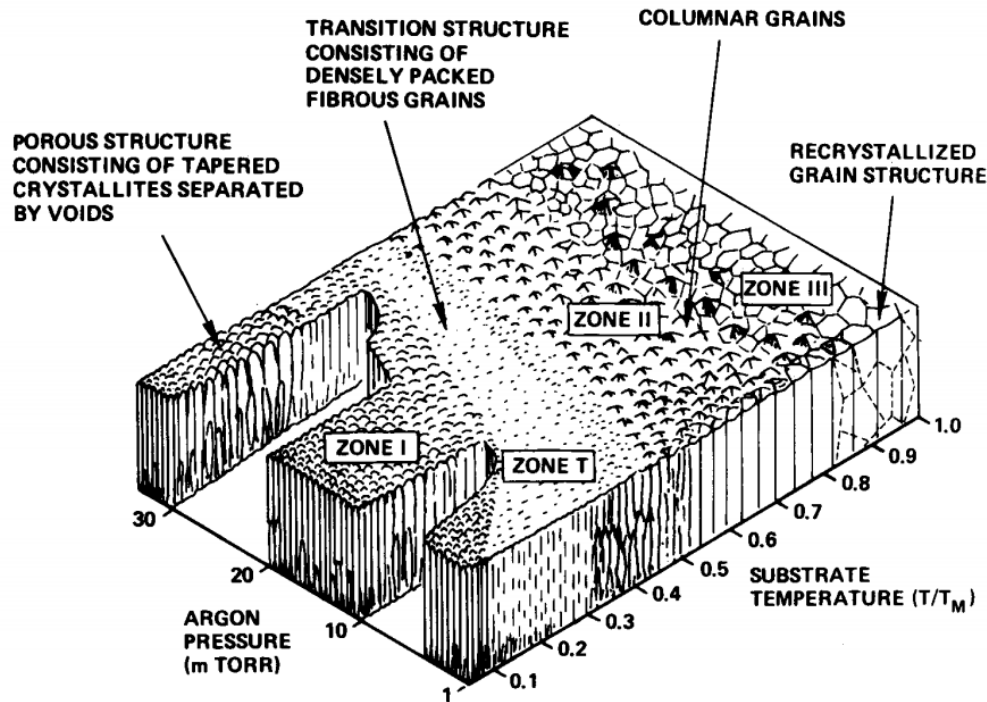
Figure 14: Structure zone diagram describing the influence of homologous substrate temperature and argon pressure on the structure of the coating. This model demonstrates the relationship between the deposition variables of homologous temperature (substrate temperature) and ion energy (argon pressure) and structure characteristics of the coating. Zone one structures exhibit a porous and columnar structure, which is prone to stress fractures and failure. Zone T structures, also described as transition zone structures, exhibit a fibrous and heterogenous structure similar to zone 1, but are more closely packed, reducing porosity. Zone two structures, while not particularly porous, still exhibit a columnar structure, incorporating areas there are prone to stress failure. Zone three structures exhibit a dense recrystallised structure, wherein the coating evenly distributes the stress, minimising failure. Original diagram proposed by Thornton (1974), adapted by Craig and Harding (1981).

In this diagram, the transition between different structure zones can be seen to vary as a function of both the argon pressure and homologous temperature; for a given structure zone, the temperature required for transition increases with argon pressure. This model, while useful, does not incorporate the ion flux parameter, which was identified by Kelly and Arnell (2000) as a key parameter independent of the ion energy. This led to the development of a novel structure zone diagram, incorporating the influence of the three key parameters (Figure 15).
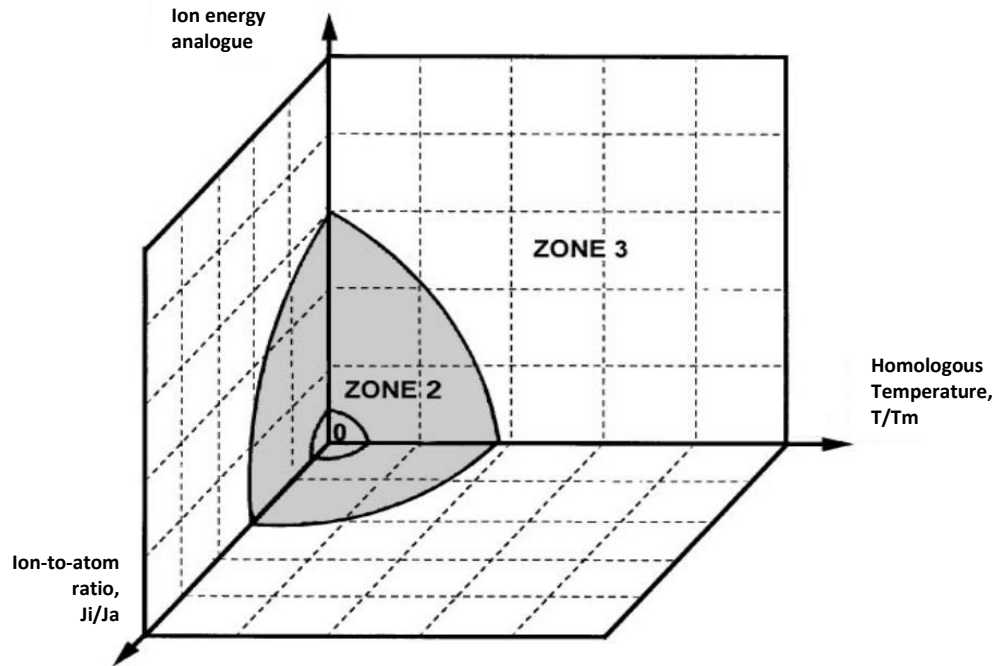
Figure 15: Structure zone diagram incorporating ion energy, ion-to-atom ratio and homologous temperature. This diagram, while omitting a graphical representation of the structure of the coatings, includes the third key parameter in coating structure. Adapted from Kelly and Arnell (2000).

While this diagram does not illustrate the structure of each zone, it is more suited to closed-field unbalanced magnetron sputtering systems. This is because, in these types of systems, ion flux is inherently high and so the incorporation of this parameter is vital. Using this diagram, it can be seen that an ideal point exists where the three parameters can remain as low as possible, while maintaining zone three structures. This is important for several reasons. Firstly, maintaining high homologous temperatures is costly, requiring the heating of the substrate holder. This can also be said for increasing the ion energy, either by increasing bias voltage or reducing argon pressure; increasing the bias voltage can incur costs in additional components and units of electricity and reducing the argon pressure can increase the pump-down time, increasing time between coating cycles and therefore reducing deposition efficiency. Secondly, excessive magnitude in any of the three key parameters can lead to excessive intrinsic stresses being introduced into the growing coating.

2.3.2 – Coating stress

The term stress has been previously mentioned, but the importance of it has not yet been described. Stress can be considered intrinsic, from within the coating itself, or extrinsic, due to the relation with the substrate. Furthermore, intrinsic stress can be considered as either tensile stress or compressive stress; each type of stress arises from different processes and is more common in different structural zones.

Tensile stress can be considered as the expansion of area of the coating relative to its volume. It occurs mainly in zone one structures and is thought to be caused due to the porous columnar growth. As the deposition atoms condense onto existing peaks, the atoms at a boundary with a void space may experience an unbalanced bonding force. This effectively causes the distance between a boundary atom and a neighbouring atom to decrease, reducing the area of the column. However, as the lattice volume must be maintained, the columnar structure expands in order to maintain constant volume. This expansion causes the coating to experience tensile stress (Westwood, 2003). Excessive tensile stress causes a convex curvature of the substrate and thus coating, when viewed from the substrate side. This stretching may cause the coating to crack or fracture along the columns, leading to a reduced adhesion of the coating to the substrate and potential delamination. In addition to hindering coating performance, these areas of breakage cause difficulty in analysis, for example, by causing breaks in the conductive surface leading to charging effects when performing SEM analysis.

Compressive stress can be considered as the inverse of tensile stress and is a reduction in the area of the coating relative to its volume. This is caused during the densification processes that promote zone 3 coating structures and so is more commonly observed in these structures. Compressive stress is thought to be related to atomic peening, which is the striking of the deposited atoms by the argon ions, transferring kinetic energy – this can be compared with the striking of a hammer on a metal surface. Such a process induces compressive stress evenly and relives tensile point stresses. The

result is a reduction in areas of extreme stress, leading to fewer point failures. However, compressive stress may still be observed in excess; excess compressive stress can cause concave curvature of the coating and substrate when viewed from the substrate side, which can contribute to poor adhesion and buckling or delamination of the coating (Westwood, 2003).

Due to the nature of tensile stress, it is usually only observed in zone 1 structures and contributes to point failures and fractures. Therefore, induction of tensile stress should be avoided in the production of well-adhering dense coatings. Induction of compressive stress is a product of the processes that produce zone 3 coatings. This induction relieves tensile stress, redistributes the stress through the coating and may improve mechanical properties. However, extremes of either type of stress can lead to deformation of the substrate, jeopardising adhesion of the coating and potentially making the substrate unsuitable for intended use. The coating stress must be significantly less than adhesion strength in order to make useful coatings (Campbell, 1970). Therefore, despite the beneficial properties of compressive stress, care must be taken with the key parameters during deposition to avoid introduction of unnecessary stress.

A final note on stresses would be the consideration of extrinsic stresses – that is, stress that is not intrinsic to the film. These tend to be thermal stresses, induced via thermal treatment either intra- or post-depositionally. Thermal stresses are usually caused by a mismatch in the coefficient of thermal expansion between the film and the substrate. This might especially arise at higher temperatures, where significant expansion might occur, although has been observed at temperatures around 500 ^{0}C for significantly mismatched materials (Lopez *et al.*, 2013). The effect of thermal stress is the propagation of cracks and fractures throughout the film, leading to poor adherence and delamination. Therefore, care should be taken when selecting appropriate substrates and consideration to appropriate thermal treatment temperatures should be given.

2.4 – Summary

In this chapter, an overview of the fabrication methods for titania thin films was given, with magnetron sputter deposition focussed on. The processes and various key parameters were described. Particular attention was drawn to the effect of deposition pressure on the mean free path and its implications for ion energy; consideration was also given to temperature and ion flux and how these parameters relate to produce coatings of different structures.

The closed-field unbalanced magnetron sputtering (CFUMS) deposition techniques facilitate the production of high-quality titania films, which then need to be characterised. The instruments and processes for thin film characterisation are discussed in the next Chapter, Chapter Three.

SURFACE CHARACTERISATION TECHNIQUES

As described in the previous Chapter, coatings and films can be considered in distinct zones: the substrate-coating interface, the coating bulk and the coating-air interface. Of specific interest to this work are the coating-air interface and the bulk; in order to create and develop functional films, accurate and appropriate measurements of various properties of the film must be measured. Of chief interest to this work are the topographical, structural, compositional and photocatalytic properties. In this Chapter, the instruments, techniques and methods used to characterise the films will be described.

3.1 – Investigating the surface interface

There are a variety of techniques available to investigate the surface interface properties of samples. One specific interface property of interest to this study is the topography. Topographic characterisation can provide information on the uniformity and roughness of a sample, indicating quality of deposition, roughness and surface area, which can influence photocatalytic activity – as described in *section 1.2*. Topography can be broken down into quantitative and qualitative measurements – for example, micrographs generated via electron microscopy can yield important and informative images, indicating interesting structures and features, but provide no quantitative data. Conversely, profilometric techniques can provide 3-dimensional surface maps in addition to quantitative analyses of roughness and surface area.

3.1.1 – Surface imaging techniques

High-resolution, magnified images of the surface interface are a useful tool in determining the general structure of the surface and can provide a first-stage screen for filtering poor-quality samples. Large defects in the surface such as gouges, scratches and debris are easily detected using imaging techniques. While these kinds of analyses do not provide quantitative topographical data, imaging can usually evaluate a much larger area than quantitative techniques, which is ideal for screening and first-stage investigations.

Scanning electron microscopy (SEM) is one of the most common analytical tools used across many disciplines of science and engineering. The technique is able to generate high-resolution images at magnifications of up to 500,000x, but also has a large depth of field, allowing larger areas to be quickly viewed at a range of appropriate magnifications. Additionally, SEM's typically have a rotating stage and sample holder, facilitating rapid sample-switching and improving efficiency by reducing time-per-sample. Thus, SEM analysis was chosen as first-stage screening process for this work.

Scanning electron microscopes rely on the detection of electrons that have impinged on a sample and have undergone elastic or inelastic collisions. During operation, the SEM chamber and column are evacuated of air. High-energy electrons (around 20kV) fired from an electron gun impact on the sample, undergoing both elastic and inelastic collisions. Inelastic collisions are those that do not conserve momentum; kinetic energy is imparted from the colliding electron into the sample. In this case, transfer of kinetic energy from the colliding electrons to the inner electrons of the sample species causes these electrons to be ejected from their related atom. These ejected electrons, known as secondary electrons, are guided towards a detector using a positive voltage bias (Goldstein *et al.*, 2018).

Once the secondary electrons have been guided to the detector, they are accelerated using a high-voltage positive bias towards a scintillator (a device or material that emits flashes of light when struck by energetic particles). The acceleration gives the electrons enough energy to cause the scintillator to flash. These flashes are then detected by a photomultiplier located outside of the SEM chamber, which converts them into an electrical signal. This electrical signal is then decoded by computer software. As the electron gun scans in a raster fashion across the surface of the sample, a 2-dimensional intensity map, or image, can be generated using these data.

Importantly, samples analysed via SEM must be electrically conductive, otherwise the incident electrons will collect on the sample and exhibit a charging behaviour. The effect of this is areas that glow brightly, obfuscating any useful information from the analysis. This must be kept in mind when selecting an appropriate acceleration voltage.

3.1.2 – Surface profiling techniques

Profiling is the act of measuring the dimensional characteristics of a surface and has been facilitated by several techniques. One of the more basic techniques is known as stylus profilometry, where a stylus attached to a cantilever is physically moved across the surface of interest. The cantilever moves sympathetically with the physical features of the surface; signal transducers then translate this movement into a trace, or profile, of the surface, which can then be displayed using appropriate software (Euan, 1996). A significant downside of this technique is the two-dimensional nature of the profile, which limits the usability of the technique. Additionally, as the stylus must be physically moved across the surface, fragile coatings may be damaged or otherwise changed, affecting the physicochemistry and rendering samples potentially unusable for further analysis or use.

A technique known as atomic force microscopy is commonly used to assess physical features of surfaces. AFM uses a similar configuration as stylus profilometry, wherein a probe is attached to a cantilever. However, whereas stylus profilometry relies on the physical resistance against the movement of the stylus to obtain sympathetic movements in the cantilever, AFM is able to detect resistance provided by the atomic force. The advantage of this is twofold. Firstly, the AFM is able to obtain information about the surface without affecting the physicochemistry, enabling the same surface to be used in subsequent analyses. Secondly, AFM is many times more sensitive than stylus profilometry, able to resolve surface features on the nanometre scale. However, this leads to the technique taking a long time to analyse samples, making it less suitable for high-throughput work, or samples with a larger area (Binnig *et al.*, 1986; Xia and Whitesides, 1998; Diebold, 2002; Lee *et al.*, 2008).

Another such technique is optical profilometry, which is a non-contact, non-destructive profiling technique for surfaces based on the principles of superimposition and interference. When two beams of light with similar wavelengths are combined, or superimposed, they cause constructive and

destructive interference. This manifests as an interference pattern consisting of intermittent 'fringes' (Figure 16).
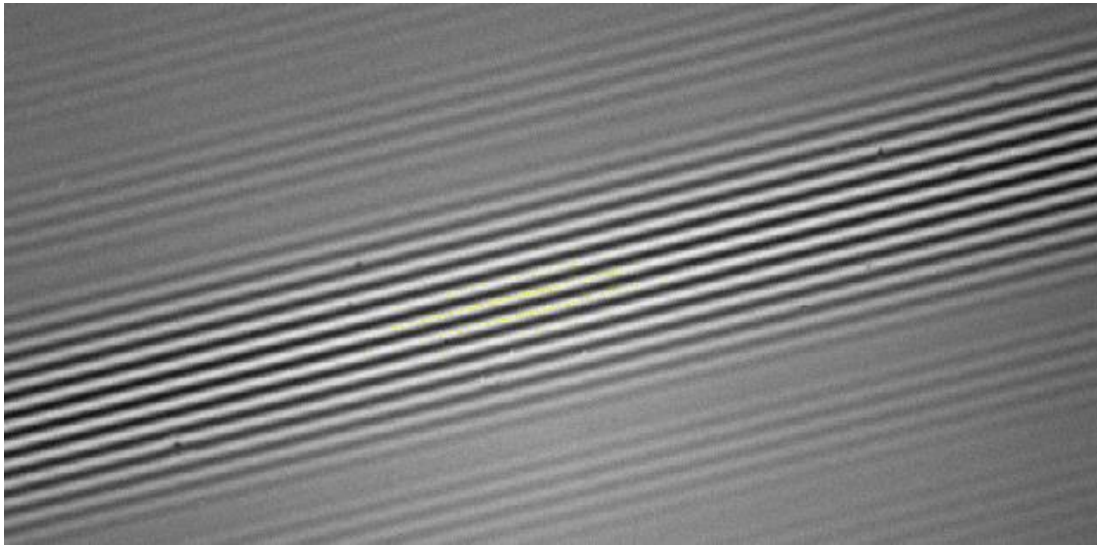
Figure 16: Classical interference pattern visualised via optical profilometry. The principles of this technique require the detection of superimposed light waves, combine when exactly in phase. This is realised as intermittent fringes as the maxima and minima of the waves combine.

Maximum interference is caused when two waves of identical wavelength in the same phase are superimposed. Optical profilometry exploits this property to compile a three dimensional map of the surface. Typical configurations are comprised of a light source, beam splitter, digital camera, objective, stage and reference mirror (Figure 17).
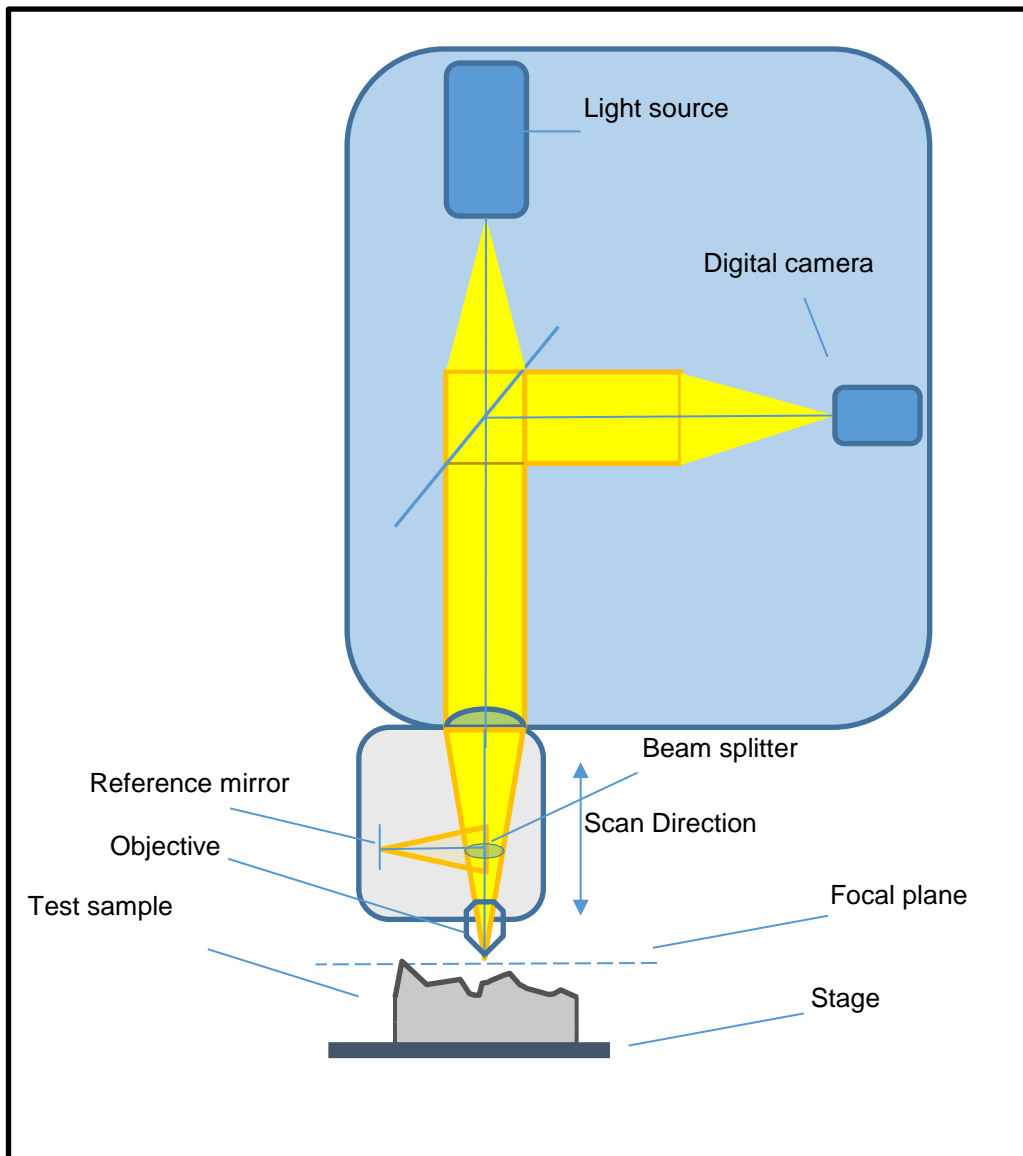
Figure 17: Schematic diagram of white-light profilometer. A digital camera, light source, and unidirectional reflector are encased in a housing. The light beam travels from the source towards the beam splitter, where it splits towards a reference mirror and the stage. The beam has a fixed focal plane, which is at the same distance as the reference mirror. In this way, the two superimposed light beams are in phase when a sample is in the focal plane; the sample is scanned through the vertical of this focal plane, so that the interference maxima are detected for the whole sample by a digital camera. Computer software then consolidates this information into a 3D map of the sample.

From the beam splitter, the focal plane and reference mirror are equidistant. When a sample is in the focal plane (i.e. in focus), light is reflected both from the sample and reference mirror in the same phase and since they come from the same source, the same wavelength. Therefore, an interference pattern is created. As the sample is moved through a 'scan length' in the vertical axis, the interference pattern changes depending on the part of the

sample in the focal plane. Each pixel in the digital camera corresponds to a specific set of x, y coordinates. Computer software then detects and records the z coordinate at which maximum interference is detected by each pixel and this then composited into a surface map of the sample (Fischer *et al.*, 1999; Whitehouse, 2000). The surface map can be adjusted using post-processing effects, which are typically used to 'fill-in' void pixels (areas that have received no data) and to remove 'tilt' from a surface. Removing tilt is analogous to levelling the map, so that the curvature of a sample is ignored, and the surface topography stands out.

In addition to a visual map of the sample area, various quantitative data are obtained describing the deviations from an ideally flat surface. A summary of the values used in this work is shown in Table 1.

Table 1: Parameters measured by optical profilometry relevant to this work. The parameters detailed here were used in this work to measure appropriate features of the coatings, namely the roughness and thickness.

Abbreviation	Description	Explanation
Sa	Area average roughness	Indicates the arithmetic mean of the deviations in the texture from a hypothetical ideal flat surface, while rejecting extreme outliers. It is an indication of roughness across the area of the surface.
Ra	Profile average roughness	As Sa, but for a line profile laid across the surface.
Sz	Area peak-to-valley distance	Indicates the largest peak-to-valley distance found over the area of the surface. Is the arithmetic mean of the five largest peak and valley deviations from the hypothetical ideal flat surface – represents the extremes of the surface. Can be used to identify the size of shelves or steps.
Rz/Rdz	Profile peak-to-valley distance	As Sz, but for a line profile laid across the surface.

3.2 – Investigating the bulk

The bulk comprises the majority of the film and as such can heavily influence the overall performance. Information such as film composition and crystallinity are two factors that affect photocatalysis that are highly relevant to this work and investigations into them can help to explain and predict for film efficacy.

3.2.1 – Energy dispersive X-ray spectroscopy

As one of the key investigations of this work was the addition of dopants to films, accurate measurement of dopant concentrations was imperative. Information about the elemental composition of a sample can be obtained using SEM equipment discussed in *section 3.1.1*, using a technique called energy-dispersive X-ray spectroscopy (EDX). In contrast to SEM, which collects purely topographical data about the interface, EDX collects atomic compositional information about the interface – this can be extended into the bulk material by increasing the electron acceleration voltage to better penetrate the sample.

In EDX, an electron gun is used to accelerate electrons into the atoms of the sample, knocking low-energy electrons out of their shells. As electrons in higher energy states fall into the lower energy states vacated by the ejected electrons, characteristic X-rays of specific energy and wavelength may be emitted (Figure 18). The magnitude of this energy can be detected and compared to a reference database and the atomic species from which it originated thus determined. If the sample contains multiple elements, the frequency of detection of a specific X-rays can be correlated to its atomic mass and so the relative percentages of each element determined (Bindell, 1992). In doing so, dopant concentrations can be determined, and the stoichiometry of the coating ascertained.
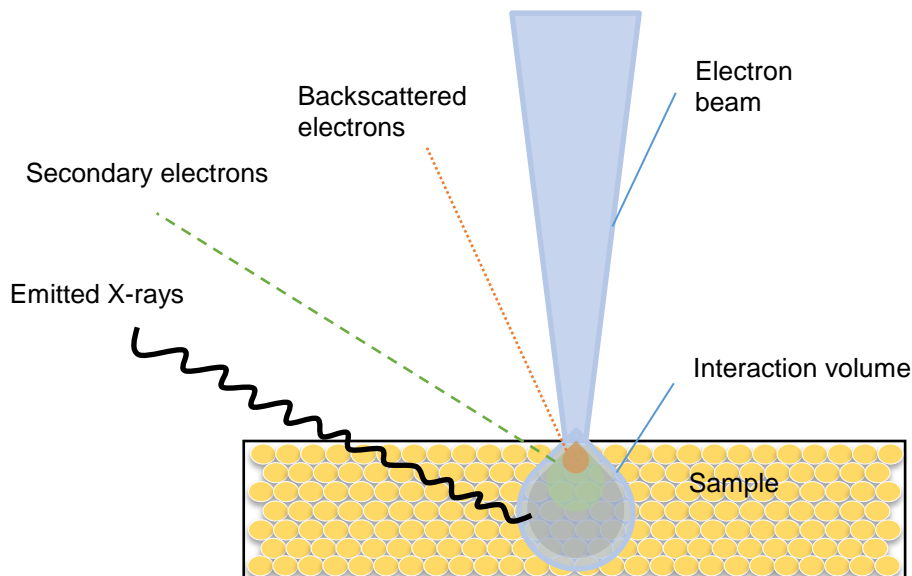
Figure 18: Interaction volume of the electron beam with information gathered at different depths. Initially, the incident electrons interact only with the interface of the sample, causing the incident electrons to be 'backscattered' (orange). With increasing interaction volume, more energetic electrons can penetrate deeper into the sample, interacting with atoms of the sample material. These electrons may ionise the sample atoms, generating secondary electrons. These secondary electrons can be detected similarly to backscattered electrons and can be equally used to image the sample (green). Finally, the greatest interaction volume with the most energetic electrons can be used for energy-dispersive X-ray spectroscopy (black); energetic incidence electrons collide with electrons in sample atoms, displacing them, and generating X-rays. These X-rays can be detected and compared to reference databases to identify the source element.

However, a key consideration when using EDX systems is the possibility of peak overlapping and light-element detection issues. That is to say, while EDX is used throughout the literature, it is commonly acknowledged to be an interpretable technique. Peak overlapping is the phenomenon of the EDX software being unable to detect the distinct emitted X-rays from different elements. Essentially, the obtained X-rays are compared to a reference database; these reference spectra were obtained using specific electron gun voltages. If a different electron gun voltage is used, the emitted X-ray may not match the reference, making interpretation difficult. Furthermore, even if the electron gun voltages are similar, the emitted electrons can interact with different subshells of electrons; when considering mixed-element samples, this can lead to emitted X-rays of similar energies and/or wavelengths which, upon being detected, are difficult to deconvolute into their true source (Statham, 2002).

This problem is especially evident when attempting to quantify 'light elements'; these elements have fewer than 11 protons and are classed as 'low-Z' elements. This is because the 'windows' used in the collections of X-rays in EDX systems can interfere with X-rays emitted from these elements. Of specific note here is that oxygen has eight protons, making it a light element. As oxygen is a significant component of the semiconductor titanium dioxide, the focus of this work, care must be taken when interpreting the quantification of this element (Ro *et al.*, 1999; Osan *et al.*, 2000; Ro *et al.*, 2004).

3.2.2 – X-ray diffraction crystallography

As discussed in *section 1.2*, the typical ideal crystallinity for a titania photocatalyst has few grain boundaries, large crystals and is in the anatase phase. To this end, X-ray diffraction (XRD) was used to investigate the crystallinity of the samples. This instrument measures the diffraction of X-rays through a crystal to determine crystalline phase, orientation and structure. The instrument can be used to generate large amounts of data pertaining to the crystalline structure, which can be refined to elucidate the atomic and molecular structure of a sample. However, in this work, the instrument was only used for crystallographic fingerprinting

The most appropriate mode for investigating the crystal phase of thin films is the grazing incidence technique (Bouroushian and Kosanovic, 2012), which involves the following: in an X-ray diffractometer, monochromatic X-rays are directed towards the sample at angle θ. When an X-ray interacts with the electron cloud of an atom in the crystal lattice, it is diffracted at identical angle θ. When a second, simultaneous X-ray from the same source is diffracted by an electron cloud of an atom in a different plane to the first, the diffraction angle is also θ. The difference between these two diffracted waves is the extra path length that the second wave travels (Figure 19).
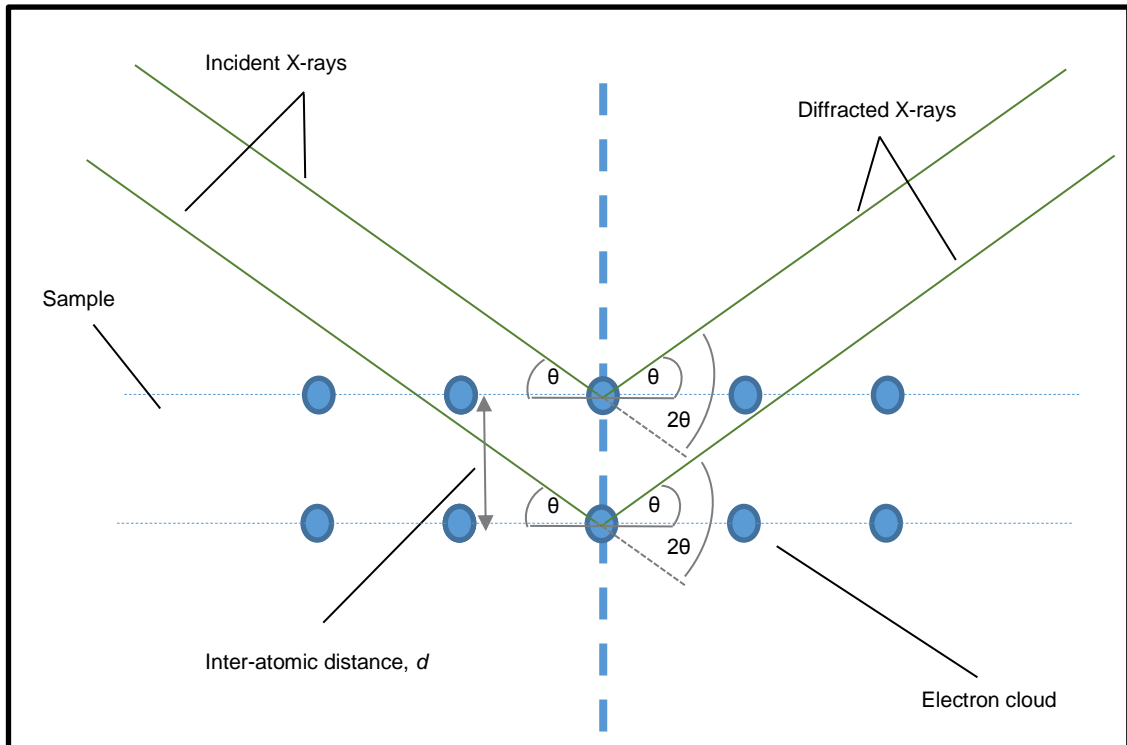
Figure 19: Incident X-rays interact with electron clouds (blue circles) in different planes and diffract at identical angles to the incidence angles (θ). From this, the inter-atomic distance can be calculated. Adapted from Toney (1992).

Geometry yields that the extra path length is equal to dSinθ, where d is the spacing between atoms in different planes, in the same orientation and θ is the angle the incident beam makes with the plane. As previously mentioned, when two waves of very similar wavelength are in phase, they undergo constructive interference. Therefore, if the diffracted waves are in phase, the resulting superimposed wave forms a maximum, or peak. This is called the Bragg condition and is described by the Bragg equation (13).

$$n\lambda = dSin\theta \qquad \text{(13)}$$

Where λ is the wavelength of the incident beam and n is an integer, conveying the condition that the diffracted waves must be in phase.

Using a detector mounted on a goniometer (a device that measures angles), the angle at which the maxima occur can be determined and so, the inter-atomic spacing for that phase orientation calculated. The goniometer can be rotated around the sample; in this manner, other maxima at different angles can be detected. These correlate to the inter-atomic spacing d for different

phase orientations. The maxima can be plotted as a function of the angle at which they are found (known as 2θ) and thus an XRD pattern can be generated. This pattern or trace acts as a 'crystallographic fingerprint' and so can be compared to a reference database to determine crystal phase (Bindell, 1992; Banyamin, 2014).

In addition to this mode, known as ambient mode, a non-ambient mode can be used. Non-ambient mode, also known as hot stage XRD, can vary the temperature while scans are operating. In hot stage XRD, the sample is mounted inside a small oven, permeable to X-rays, while scanned. In this manner, it is possible to heat the sample and scan at different temperatures, to investigate how the crystalline structure changes with annealing parameters.

3.3 – Assessing the activity

As previously discussed (*section 1.2*), the activity of a film is not an independent variable, rather, it is dependent on the other properties of the film. For example, should two films be identical except for roughness, it is expected that the rougher film will have a higher activity due to its higher surface area. Similarly, if two films of identical composition and roughness but different crystallinities were tested, the film with the more optimal anatase: rutile ratio would have higher photoactivity (Mathews *et al.*, 2009). The relationship between activity and crystallinity is more complex than the relationship between activity and topography, for several reasons. Chiefly, it is because that optimum crystallinity has few grain boundaries and large TiO_2 crystals; however, these properties lead to a lower surface area than smaller crystals with more grain boundaries. As many properties of the film affect the activity in some way, predicting the activity from other measures can be highly complex. Therefore, it is best practice to measure activity directly.

3.3.1 – Methylene blue degradation

There are a number of established methods of testing photocatalytic activity, which all involve measuring the breakdown or degradation of organic materials. Examples include the degradation of stearic acid (Klaysri *et al.*, 2017), acetone (Ratova *et al.*, 2017) and rhodamine B dye (Ratova *et al.*, 2018). However, the most widely used test is likely the methylene blue test. It has a relatively low toxicity, is easily handled and is inexpensive. Whilst the limitations of the method due to photosensitisation and other effects have been reported by several authors (Yan *et al.*, 2006; Mills, 2012), the use of the dye for evaluation of photoactivity of new photocatalytic materials is recommended by ISO10678 (British Standards Institution, 2010) and was therefore chosen for the evaluation of photocatalytic films in this work.

Methylene blue is a blue organic dye with a molecular formula of $C_{16}H_{18}N_3SCl$, that strongly absorbs light at λ=665 nm. When the dye comes

into contact with ROS produced via a photocatalyst, it undergoes a photo-mineralisation process (14) (Mills *et al.*, 2012).

$$C_{16}H_{18}ClN_3S + 25.5O_2 \xrightarrow{TiO_2+hv\geq3.2eV} HCl + H_2SO_4 + 3HNO_3 + 16CO_2 + 6H_2O \quad \textbf{(14)}$$
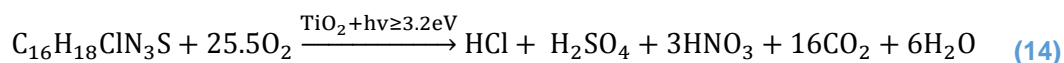
As the dye undergoes photo-mineralisation, it changes from blue to colourless. A spectrophotometer system can be used to monitor this colour change – as it becomes colourless the intensity/amplitude of the absorbance peak at λ=665 nm reduces. This reduction can be plotted against time to determine the first-order rate equation constant, *k*. This value is interpreted as the measure of activity of the sample (Inagaki *et al.*, 2006). A schematic for a typical methylene blue degradation test rig is shown below (Figure 20).
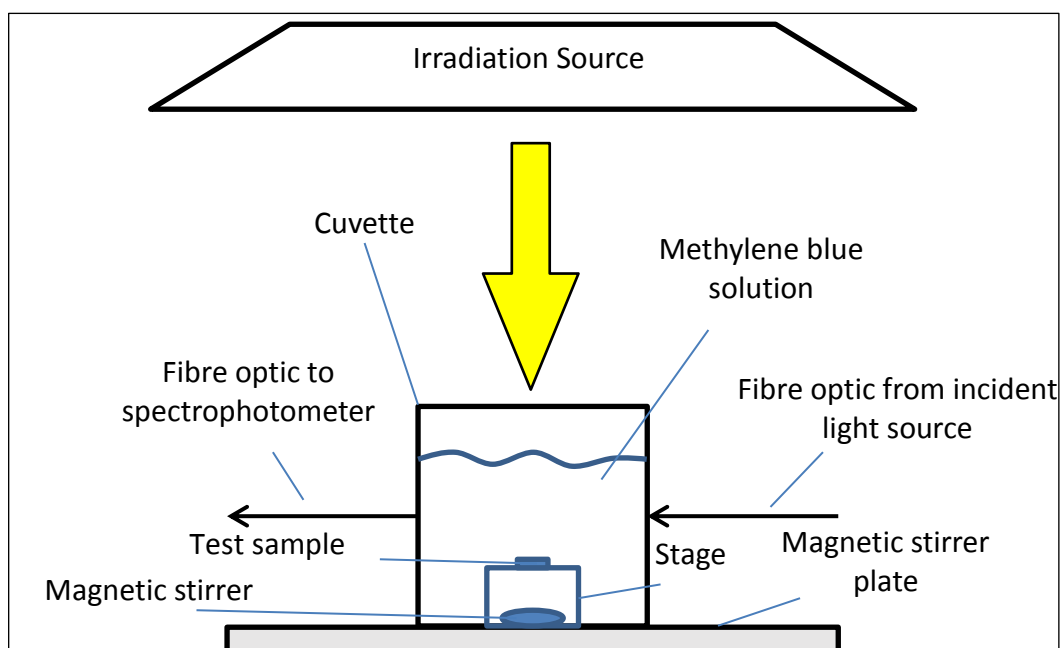
Figure 20: Schematic diagram of methylene blue degradation test. A cuvette is placed upon a magnetic stirrer plate in a cuvette holder. A magnetic stirrer and small stage are placed inside the cuvette and the test sample placed on the stage. The cuvette is filled with methylene blue. Fibre optic cables are used to carry light from an incident source to the cuvette and then from the cuvette to the spectrophotometer. The irradiation source activates the sample, causing decolourisation of the methylene blue, which is detected by the spectrophotometer.

3.4 – Summary

In this Chapter, the various techniques used to investigate the properties of interest in the films were described. The techniques of SEM and optical profilometry can give data on the topography of the surface interface in a high-throughput, large-area manner, while the composition and crystallinity of the surface interface and bulk can be investigated using EDX and XRD. Finally, the methylene blue degradation test can be used to directly assess the photocatalytic activity of samples. These techniques will be used to characterise titania surface coatings produced in the next Chapter, Chapter Four.

FABRICATION and CHARACTERISATION of COATINGS

Photocatalytic coatings can be produced by the use of physical vapour deposition unbalanced magnetron sputtering techniques, as outlined in Chapter Two. This Chapter will describe the production parameters and settings that were used to fabricate a range of coatings. In addition, the characterisation techniques explored in Chapter Three will be applied to the coatings produced in this Chapter, so the development of the coatings can be seen. This will elucidate the effect of varying production parameters on film properties.

4.0 – Method

This section will describe in detail the methods used to produce titania films on substrates.

4.0.1 – Substrate preparation

Two kinds of substrate were used: glass and stainless steel. The stainless steel substrates were 20 mm x 10 mm stainless steel coupons cut from a 1 m x 2 m sheet (Type 304, Finish 2B, Metal Sheets Ltd, Liverpool) via a steel cutting guillotine tool. The coupons were then sterilised via autoclave at 121 ^{0}C for 20 minutes. The protective plastic backing was removed from these coupons, after which they were dipped in 95 % ethanol (Ethyl alcohol, Sigma-Aldrich Company Ltd, Dorset) and flamed, to remove any adhesive residue from the backing. They were then submerged in isopropanol (2-Propanol ≥99.5 %, Sigma-Aldrich Company Ltd, Dorset) and ultrasonically cleaned at 50-60 kHz (Sonicor SC121TH, Sonicor Inc, West Babylon) for 10 minutes. The coupons were cleaned in groups of five; it was observed that more than this increased the chance of scratching the surface of the coupon. The substrates were then stored in clean dry petri dishes (35 mm x 10 mm petri dish, Scientific Laboratory Supplies, Nottingham) at room temperature until they were coated.

The glass substrates were fabricated from glass microscope slides (Starfrost 3 ″ x 1 ″ ground, Knittel Glass, Waldemar Knittel, Braunschweig), cut to 20 mm x 10 mm coupons with a diamond-tip glass cutter. The coupons were sterilised as described above, then submerged in isopropanol and ultrasonically cleaned, as with the stainless steel coupons described above.

4.0.2 – Deposition of coatings

Two rigs of the same model (Teer Coatings Rig UDP450, MIBA, Teer Coatings Ltd, Droitwich Spa) were used to deposit the coatings. Rig A was situated at Manchester Metropolitan University, Manchester, England. Rig B was situated at Teer Coatings Ltd., Droitwich Spa, England.

Each rig had three 300 mm x 100 mm type-2 unbalanced planar magnetrons vertically installed through the chamber walls, allowing for three separate target materials, as well as several gas inlets to allow for reactive sputtering (described in *section 2.*2). The targets selected to coat the substrates were two titanium targets in the closed-field configuration, with the dopant target as either niobium or molybdenum, depending on the desired the composition. All targets had a purity greater 99.8 %.

4.0.2.1 – Deposition on stainless steel; Rig A

All coatings were deposited onto stainless steel coupons using rig A and were doped with molybdenum. These coatings were designated as 'set 1'. For a batch of samples, 25 coupons were affixed onto a flat sample holder using rolled tabs of Kapton tape (51408 Orange Masking Tape 12 mm x 33 m, Tesa, Milton Keynes). One coupon from each batch was partially occluded with Kapton tape, so that a step height could later be measured and the film thickness inferred. The sample holder, mounted on a rotating arm, was then loaded into the rig chamber, with the coupons at a distance of 110 mm from the target. The sample holder was then occluded by a retractable shield and the chamber sealed. The vacuum switch was closed and the chamber was lowered to a base pressure of 2 mPa, measured via Pirani gauge (Edwards PRM-10, Edwards, Burgess Hill) in the low-vacuum region and Penning gauge (Edwards CP25K Penning Gauge Head, Edwards, Burgess Hill) in the high-vacuum region. Argon was added to the chamber at a rate controlled via a mass flow meter (MFM GM50A, MKS andover) connected to a mass flow controller (247D, MKS andover) that allowed the equilibrium pressure to be 0.1 Pa. This was the deposition pressure.

The magnetrons were then sputter cleaned for 20 minutes; the two titanium targets were driven at a power of 1 kW in pulsed DC mode, with pulse settings of 4 µs off-time and a frequency of 100 kHz. This gives a total off-duty of 40 % and therefore a duty of 60 % according to the duty cycle equation (15):

$$D = \frac{T}{P}$$

Where D is duty, T is signal on-time and P is time period (100 kHz has a period of 1×10^{-5} seconds). When the dopant was used, the power to the dopant target was set to 180 W and kept in direct current mode. Power was supplied by a Pinnacle Plus+ power supply (Pinnacle Plus+ Pulsed-DC Power Supply, Advanced Energy, Fort Collins). Once the targets had been cleaned, oxygen was introduced to the chamber. This process was controlled by OEM. The percentage of the full-metal signal selected for this work was 15 %, which has previously been found to produce stoichiometric titanium dioxide coatings (Ratova, 2013).

The shield was retracted and the substrate holder set to rotate at four revolutions per minute. The coating was deposited over two hours, with readings of pressure, voltage and current and OEM signal taken every 20 minutes for process control. After 2 hours, the power to the magnetrons was turned off and the chamber was left under vacuum for a further 30 minutes. After 30 minutes, the chamber was vented and the samples removed.

4.0.2.2 – Deposition on glass; Rig A

These coatings were designated 'set 2'. Coatings were deposited onto glass in an identical way to those deposited onto the stainless steel substrates described in *section 4.0.2.1*, except that three types of coatings were produced; in addition to the molybdenum-doped titanium dioxide coatings deposited onto stainless steel, niobium-doped titanium dioxide coatings were also produced. When the niobium target was used, the power driving the dopant magnetron was kept at 100 W.

When the molybdenum target was used, the power driving the dopant magnetron was varied. While the power driving the magnetron during sputter cleaning was kept at 180 W, the power during deposition was either 100 W, 150 W, or 180 W.

These powers were chosen to drive the magnetrons, as previous work had shown these to be conducive to crystalline titania structures, have detectable levels of dopant without forming distinct phases of the dopant and could therefore have the potential to enhance visible-light activated photocatalytic properties (Ratova *et al.*, 2013; Fisher *et al.*, 2014; Kelly *et al.*, 2014; Ratova *et al.*, 2015). The power driving the molybdenum-target magnetron was varied due to interest in the effect of molybdenum on the anatase-to-rutile shift – progressive molybdenum concentrations in the titania lattice promote the rutile shift (Li *et al.*, 2011). This effect does not occur for niobium-doped titania (Hanaor and Sorrell, 2011) and so the power driving the niobium-target magnetron was not varied.

4.0.2.3 – Deposition on glass; Rig B

Rig B was very similar to Rig A, with the only differences being the sample holder (cylindrical/drum type as opposed to an arm) and omission of a sample shield.

As the rig did not contain a sample shield, sputter cleaning runs were alternated with deposition runs. In order to sputter clean the targets, the chamber was closed and lowered to a base pressure of 2 mPa. Argon was added to the chamber at a rate that allowed the equilibrium pressure to be 0.1 Pa. This was the deposition pressure. The magnetrons were driven at the power and duty described in *section 4.0.2.1*.

After cleaning, the chamber was vented. For every deposition run, fifty coupons were affixed to the cylindrical sample holder using rolled tabs of Kapton tape and the sample holder was loaded into the chamber. The chamber was then lowered to the base pressure of 2 mPa. Argon was added to the chamber at a rate that allowed the equilibrium pressure to be 0.1 Pa. This was the deposition pressure. The magnetrons driving the two titanium targets were driven at the powers and duties described in *section 4.0.2.1*.

The dopant target used was either niobium or molybdenum. When used, the power to the magnetron driving the molybdenum target was 180 W, with a duty of 100 %. When niobium was used as a dopant, the power to the magnetron driving the target was 100 W, with a duty of 100 %. In addition to the doped samples, pure (undoped) titanium dioxide coatings were also produced. These samples were designated 'set 3'.

4.0.3 – Annealing of coatings

After deposition, the samples were annealed to induce crystallinity. The effect of annealing time and temperature was investigated for the samples with glass substrates.

4.0.3.1 – Annealing samples with stainless steel substrate; Rig A

The samples with a stainless steel substrate coated using Rig A were annealed using a Carbolite furnace oven (Carbolite LHT6/30, Carbolite, Hope Valley). The temperature was increased by 15 °C per minute up to 600 °C, which was then held for 30 minutes. After 30 minutes, the oven was turned off and the samples were allowed to cool to room temperature within the oven.

4.0.3.2 – Annealing samples with glass substrate; Rig A

The glass substrate samples coated using Rig A were annealed using the same furnace described in *section 4.3.1*. However, these samples were annealed at 500 °C, for either 30 or 60 minutes, to investigate the effect of different annealing times at a lower temperature than the samples deposited onto stainless steel substrates. After the allotted time, the oven was turned off and the samples were allowed to cool to room temperature within the oven.

4.0.3.3 – Annealing samples with glass substrate; Rig B

The temperature of annealing for the samples with a glass substrate coated using Rig B was informed by hot stage XRD measurements (*section 4.0.4.4*). One sample from each batch was analysed using the hot stage and subject to the programme described in *section 4.0.4.4.*

After hot stage analysis, the annealing temperature that yielded the highest weight fraction ratio of anatase to rutile was chosen as the temperature used to anneal the remaining samples for that composition. The weight fraction ratio was determined by (16)

$$f = \frac{1}{1 + 1.26(\frac{IR}{IA})}$$

<div align="right">**(16)**</div>

Where f is the weight fraction ratio, IR is the XRD peak intensity of the rutile 110 peak and IA is the XRD peak intensity of the anatase 101 peak (Spurr and Myers, 1957).

After analysis, the samples were annealed at the temperatures described in Table 2. This temperature was informed by the weight fraction analysis, along with other considerations. Samples were placed into the oven and the temperature was increased by 15 °C per minute up to the temperature described, which was then held for 30 minutes. After 30 minutes, the oven was turned off and the samples were allowed to cool to room temperature within the oven.

Table 2: Annealing temperatures used for different sample batches and compositions.

Sample type	Annealing temperature, ^0C
TiO_2 batch one	590
TiO_2 batch two	590
Nb-doped TiO_2 batch one	520
Nb-doped TiO_2 batch two	520
Mo-doped TiO_2 batch one	Did not anneal *
Mo-doped TiO_2 batch two	520

The first batch of molybdenum-doped titania coatings were not further annealed due to unaccountable differences in crystal growth behaviour observed during the hot stage analysis – this is further explored in *section 4.1.3.3.*

4.0.4 – Characterisation of coatings

The coatings were characterised using the techniques described in Chapter Three. Details of settings and parameters are described below.

4.0.4.1 – Energy dispersive X-ray spectroscopy

Data regarding the composition of the coatings were gathered using EDX. An EDAX Apollo 40SDD detector (EDAX Inc., Mahwah NJ, USA) was used to collect EDX data. The EDX instrument was integrated into a ZEISS Supra 40VP (Carl Zeiss AG, Oberkochen, Germany) SEM instrument. An acceleration voltage of 20 kV and a scan time of one minute were used. Data were compiled and interpreted by EDAX Genesis software (EDAX Inc., Mahwah NJ, USA).

4.0.4.2 – Scanning electron microscopy

Two instruments were used during this project: the JEOL JSM5600LV (JEOL USA, Inc., Peabody USA) and the Zeiss Supra 40VP. Two instruments were used because it was found that the JEOL JSM5600LV could not obtain images of films with poorly conducting substrates/breaks in the films (due to high acceleration voltage of the electron gun causing charging effects at the surface). These images were therefore taken using the ZEISS Supra 40VP, as this instrument was able to obtain images with a lower electron gun acceleration voltage. Both instruments were used in secondary electron detection mode. A range of acceleration voltages from 3 kV to 20 kV were used depending on required resolution and charging effects of the sample. The working distance was informed by the acceleration voltage and ranged from 14 mm to 20 mm from the sample.

4.0.4.3 – Optical profilometry

For this work, a ZeGage system (ZeGage 3D Optical Surface Profiler, Zemetrics, Zygo, Middlefield) was used to gather profiling data. The sample to be analysed was placed on an anti-vibrational stage approximately 5mm from the objective of the profilometer. Objectives of 10x and 50x magnification were used. Scans were collected with a signal threshold of 0.5 % and saturation level of 10 %. They were conducted from the centre

position with a scan length of 50 µm. Three scans per sample were collected. The post-processing effects consisted of removing the polynomial fit from the map, with a tilt order of fit – essentially, this mathematically removed curvature from the scan of the sample, allowing more precise and reliable roughness and thickness data to be obtained. The roughness (Ra) and thickness (Rdz) were recorded from each scan.

4.0.4.4 – X-ray diffraction crystallography

The instrument used to gather XRD traces was a PANalytical X'pert[3] Powder X-ray diffraction system fitted with a PIXcel[1d] detector in point detector mode (PANalytical LTD, Cambridge). The X-rays were generated by applying a voltage of 40 kV and current of 40 mA to a copper target, resulting in Cu K_α ejection wavelength of $\lambda=0.154$ nm. The hot stage used was an HTK 1200N (Anton Parr, Graz, Austria).

Crystallographic fingerprinting was achieved using the flat sample stage, which simply mounts the sample on a stable surface enabling scanning at ambient temperature. For this scan, the starting angle of the detector was 20° 2θ, moving in incremental steps of 0.05° 2θ to a final angle of 70° 2θ, resulting in one thousand discreet intensity measurements. The collection time was 5 seconds per step, leading to overall collection time of 83.4 minutes.

Hot stage XRD was used to investigate optimum annealing conditions for the samples as described in *section 4.0.3.3*. The hot stage XRD programme is described below. The first and final scans were longer scans conducted at ambient temperature used before and after temperature change, as described above. The other scans focussed on a smaller range of angles to quickly identify the characteristic primary peaks of anatase and rutile, during hot stage measurements. The starting angle of the detector was 24° 2θ, moving in incremental steps of 0.04° 2θ to a final angle of 28° 2θ, resulting in one thousand discreet intensity measurements. The collection time was 5 seconds per step, leading to overall collection time of 8.4 minutes. A schematic representation of this is shown in Figure 21.
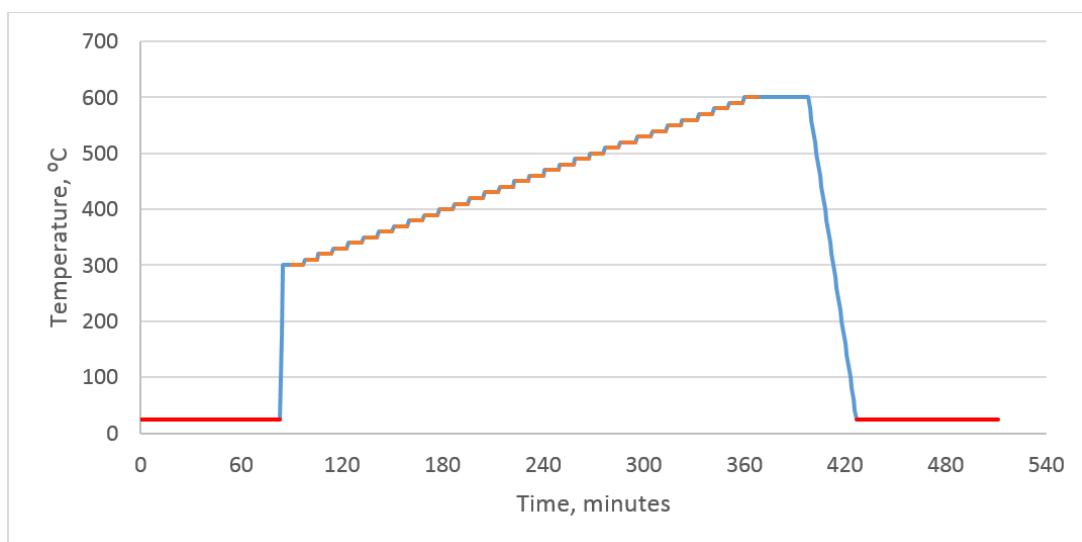
Figure 21: Schematic illustrating variable time and temperature parameters for scanning thin films from amorphous phase. Longer scans (red) at ambient temperature. Shorter scans (orange) after changes in temperature (blue). Longer scans at the beginning and end of the process provided greater resolution over a greater range of 2θ angles (20^0 – 70^0 2θ), while the shorter scans (~24^0 – 28^0 2θ) at non-ambient temperature were used to identify changes in the main characteristic anatase 101 (25.3^0) and rutile 110 (27.5^0) peaks.

The data gathered were interpreted by HighScore Plus software (PANalytical LTD, Cambridge) and displayed using Data Viewer software (PANalytical LTD, Cambridge).

4.0.4.5 – Methylene blue degradation

The methylene blue degradation test was used to measure the activity of the samples. To measure this degradation and thus activity, the photocatalytic sample was first immersed in 1.5 µM methylene blue solution (M9140, Sigma-Aldrich Company Ltd, Dorset) at a pH of 6.7 for one hour in the dark. This step was performed to promote equilibrium of adsorption-desorption effects prior to monitoring the absorbance. Then, the sample was mounted on a perforated stage above a magnetic stirrer in a 45mm x 45mm x 42.5mm cuvette (704.002-OG, Hellma Analytics, Müllheim, Germany).

The cuvette was fitted in a bespoke cuvette holder, placed on a magnetic stirrer plate (Big Squid white, IKA, Staufen, Germany) and filled with 35 mL of methylene blue solution. An irradiation source (Blak-Ray XX-15BLB Bench Lamp, UVP, Upland) was fitted with two bulbs (Philips Master TL-D 15 W/840, Philips, Amsterdam) and set 300 mm above the sample.

Fibre optic patch cables (QP400-1-VIS-NIR, Ocean Optics, Dunedin, Florida, US) were run from a tungsten-halogen incident light source (HL-2000, Ocean Optics, Dunedin, Florida, US) to the cuvette holder and then to a spectrophotometer (USB2000+VIS-NIR, Ocean Optics, Dunedin, Florida, US). The spectrophotometer was connected to a computer and data were collected and interpreted by Spectrasuite software (Spectrasuite, Ocean Optics, Dunedin, Florida, US). The irradiation source was activated and magnetic stirrer plate was switched on at 400 rpm. The spectrophotometer was previously calibrated against distilled water and these files were loaded into the software. The intensity of the absorbance peak at $\lambda=665$ nm was then monitored for one hour, with a reading taken once per second. The data were exported from Spectrasuite into Excel (Microsoft Excel 2010, Microsoft, Reading). The absorbance intensity at a given time was compared to the absorbance at the start time and the natural logarithm of this value taken and plotted against time. From this, a curve was generated and the gradient of degradation able to be calculated – the first-order rate constant *k*. As this was generally an extremely small value, the constant was multiplied by a factor of 100,000 before plotting.

4.0.4.6 – Statistical analysis

Data were analysed for statistically significant differences and relationships as appropriate using IBM SPSS Statistics version 23. Data were analysed for normality using a Shapiro-Wilk test. Data that were not normally distributed were log-transformed to approximate a normal distribution. Normally distributed data were analysed for differences between groups using a one-way ANOVA with post-hoc Tukey tests for pairwise comparison. Data that were not able to be transformed to a normal distribution were analysed using non-parametric tests instead; a Kruskal-Wallis test with post-hoc Mann-Whitney U-tests for pairwise comparison was used to identify differences between groups. Relationships were investigated using linear regression models. The alpha level for these tests was set to 0.05; differences/relationships were considered significant if $p < 0.05$.

4.1 – Results and discussion

The data gathered through the characterisation processes above are described and illustrated here. In this section, each set is sequentially characterised in full and then comparisons between sets are made.

4.1.1 – Characterisation of set 1

4.1.1.1 – Composition

Analysis of the elemental composition of the molybdenum-doped titanium dioxide films showed that titanium and oxygen were approximately stoichiometric for individual films, despite small inter-film variation. Greater variation was noticed in the amount of oxygen present, but this was not surprising; as a light element (a 'low-Z' element, with fewer than 11 protons), oxygen has difficulty being accurately and precisely quantified by EDX systems (Ro *et al.*, 1999; Osan *et al.*, 2000; Ro *et al.*, 2004). In addition, as EDX detects elements within a few microns of the surface, it may also include any molecular oxygen from the air that had adsorbed onto the of the sample surface; similarly, the EDX beam likely penetrated to the substrate, which would have then have caused the detector to receive information about the substrate. The average molybdenum concentration in the films was 7±2 %at. (Figure 22), therefore when stainless steel is used as a substrate, driving the dopant magnetron at power of 180 W yields a film of 7 % molybdenum.
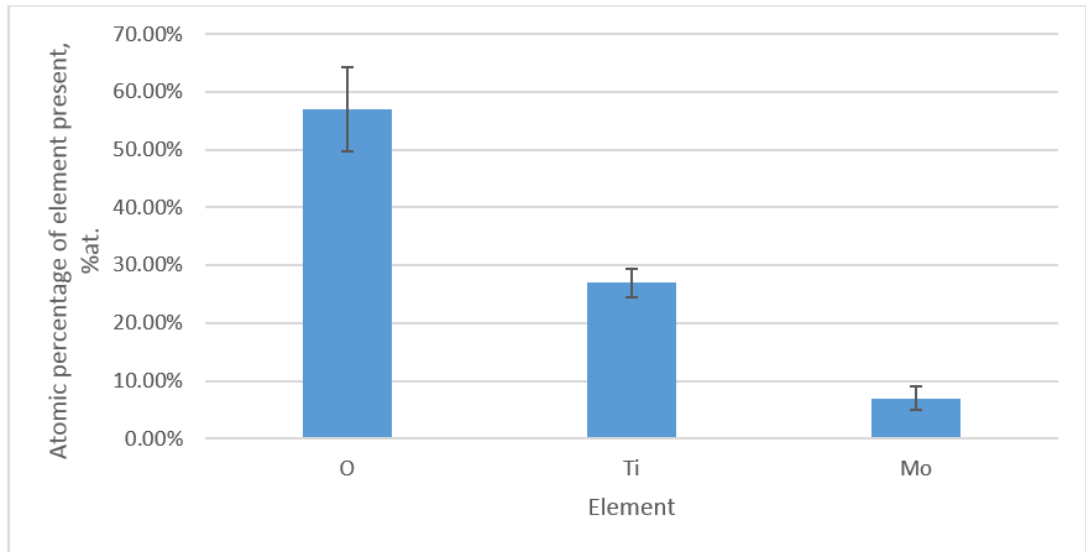
Figure 22: Atomic percentage concentrations of the elements in the films. O= oxygen. Ti = Titanium. Mo = molybdenum. The concentrations of titanium and oxygen were approximately stoichiometric, with a mean doped molybdenum concentration of 7 %at. N=17

4.1.1.2 – Topography

The films deposited onto stainless steel substrates were imaged using SEM. SEM inspection showed that the deposited films were non-uniform and non-homogenous, with a fragmented structure. The coatings were likely conformal to the stainless steel, as evidenced by the native isle-and-channel structure visible in both uncoated stainless steel (Figure 23A) and the coated samples (Figure 23B and C).
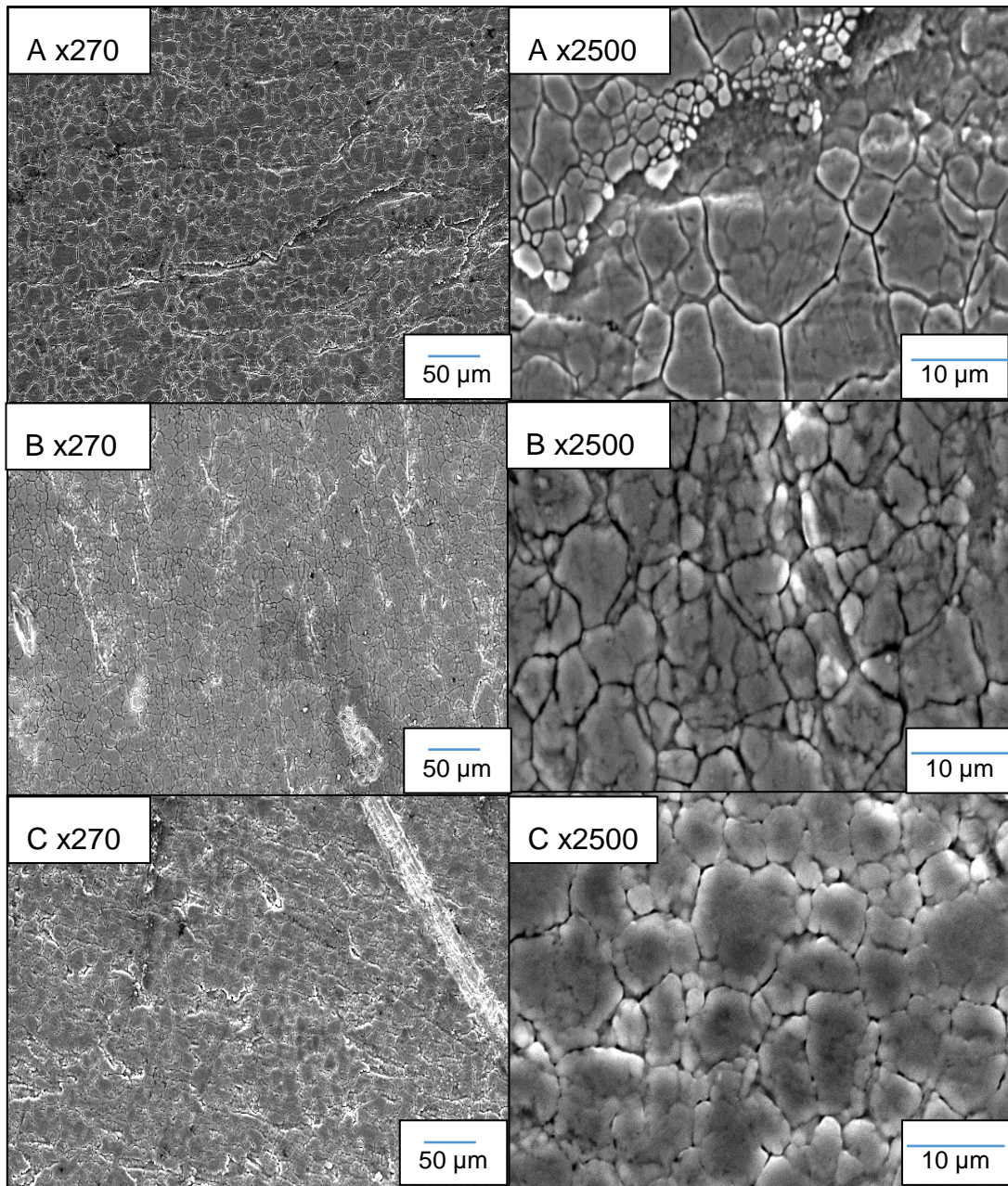
Figure 23: Representative SEM images (x270 and x2500) of films deposited onto stainless steel substrates. The uncoated stainless steel coupons (A) appear similar to the Mo-doped titania samples (B and C), indicating conformal deposition along the stainless steel isle-and-channel structure.

4.1.1.3 – Profilometry

The similarities observed in SEM were not seen using profilometry. Coated samples had an average roughness of 376±108 nm, so were significantly rougher than uncoated samples, with an average difference of 190 nm (Figure 24, p<0.001).
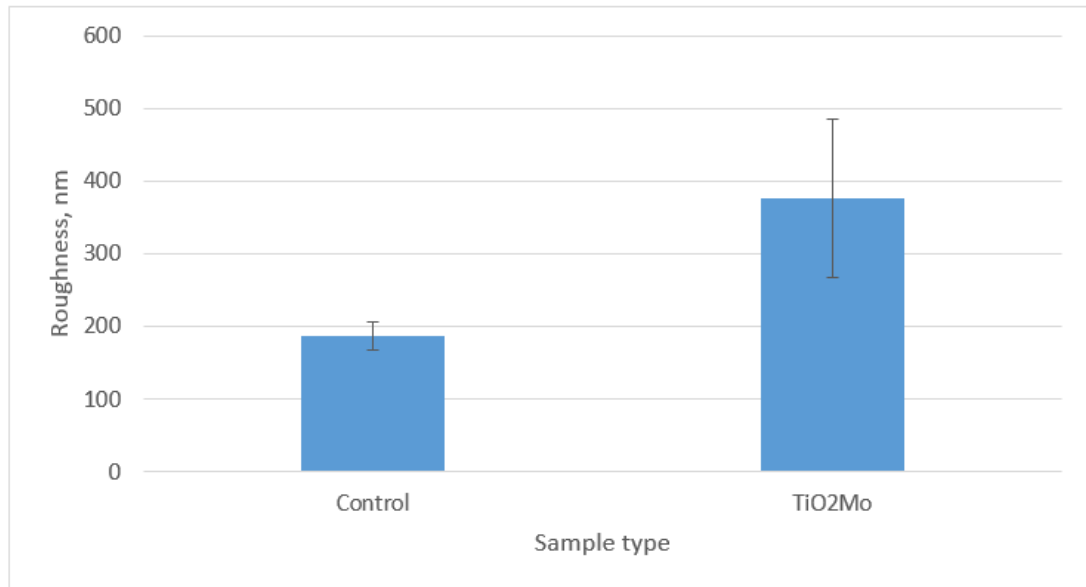
Figure 24: Differences in roughness between uncoated control and molybdenum-doped titanium dioxide coatings on stainless steel substrates. There was a significant difference in the mean roughness between the coated substrate and control (190 nm, p<0.001).

This is not surprising, as although the magnetron sputter technique produces conformal coatings, the roughness is reliant on several factors, such as the condensation mechanism of coating material onto the substrate. This condensation can occur around nucleation points, where atoms of deposited material first adsorbed onto the substrate – these are known as adatoms. When additional adatoms are present, given sufficient energy, they will diffuse freely along the substrate and produce a homogenous, dense, smooth coating. However, if they adatoms have insufficient energy to diffuse, then the nucleation points will become the primary site for target material to condense, leading to a granular, columnar structure. This structure is porous and has an increased roughness compared to the substrate. In addition, fine cracks or damage in the film caused by deposition stresses or thermal treatment can be observed to increase roughness, as can structures with a small grain size, polycrystalline texture, or many grain boundaries. The

thickness of the coating could not be measured using the step-height method via optical profilometer, as the roughness obfuscated the step – a representative sample is shown in Figure 25.
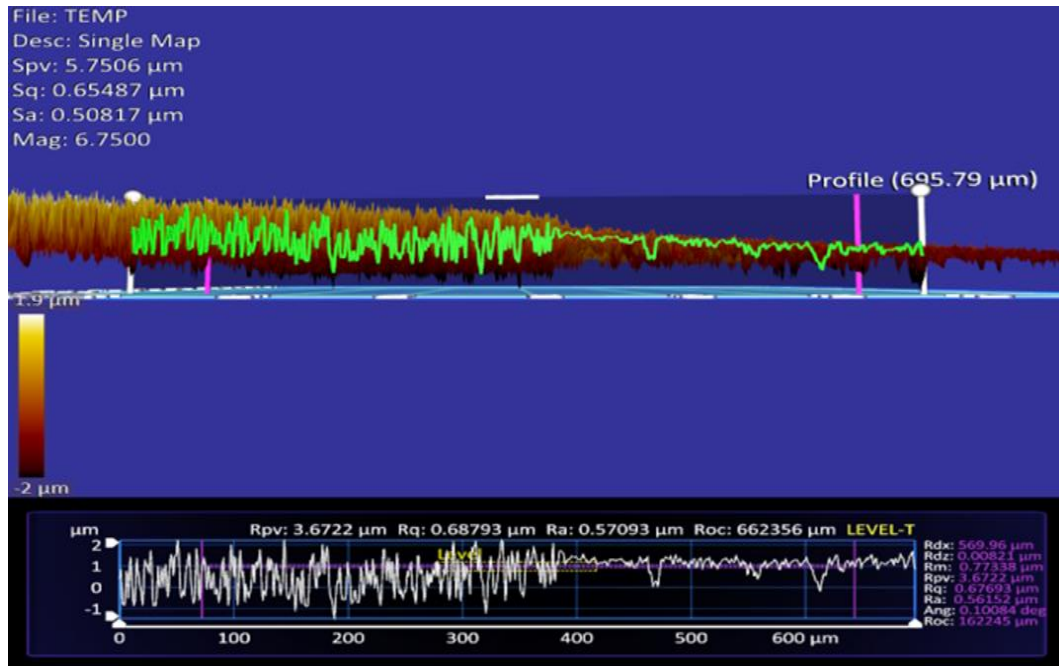
Figure 25: Side profile of a TiO$_2$Mo coated stainless steel sample. Profile illustrates increase in roughness from the uncoated region (right) to the coated region (left), obfuscating the step-height and reducing the ability to determine thickness.

The profile shows that the coated area (0 µm-390 µm on the x-axis of the lower plot) is much rougher than the uncoated area (390 µm- 695 µm on the x-axis of the lower plot). An alternative technique to measure coating thickness that has been used successfully in the literature is cross-sectional SEM – a cross-section of the coating and substrate is imaged and the coating thickness calculated from the total thicnkess minus the substrate thickness (Chun *et al.*, 2001). This could have been used to determine the thickness of these coatings when the step-height method was unable to produce data.

4.1.1.4 – Crystallinity

Annealing the sample at 600 ^{0}C for 30 minutes induced crystallinity in the molybdenum-doped titanium dioxide coatings (Figure 26).
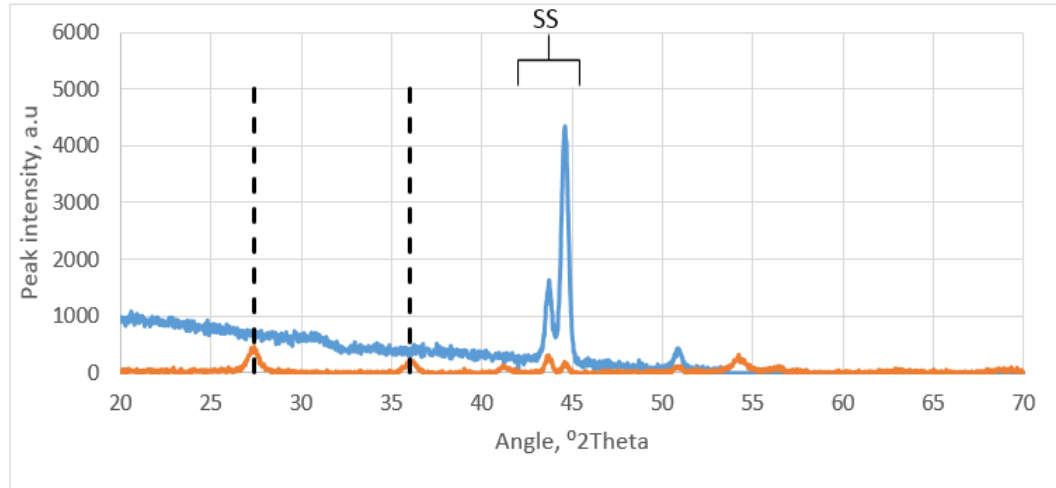
Figure 26: Representative XRD pattern for uncoated stainless steel (blue) and Mo-doped titania coatings annealed at 600 ^{0}C (orange). Characteristic rutile 110 (27.5^0) and 101 (36.01^0) peaks are displayed as dashed lines, while the typical peaks from stainless steel are displayed using brackets and denoted SS. The Mo-doped titania samples exhibited no anatase crystallinity, but did develop rutile crystallinity. The presence of the stainless steel peaks in the representative coating trace is likely due to X-rays penetrating the coating and interacting with the underlying substrate.

Characteristic peaks at 27.5^0 (110) and 36.01^0 (101) confirm the presence of the rutile phase. The peaks at around 47^0 are characteristic of the underlying stainless steel substrate – this can be seen prominently in the uncoated control sample, but also in the TiO_2Mo-coated sample. This is because the incident X-rays can pass through thin films, interacting with and reflecting from the structures in the underlying substrate; it is not indicative of stainless steel crystalline structures within the film. Interestingly, no anatase crystallinity was detected. This implies that, at 600 ^{0}C, the TiO_2 crystals had completely progressed through the anatase phase and into rutile. While this is the typical transition (Kim *et al.*, 2002), the absence is unusual, as several authors have found that titania exhibits high levels of anatase crystallinity after annealing at temperatures close 600 ^{0}C and that rutile in isolation is found after annealing at higher temperatures, around 900 – 1100 ^{0}C (Kim *et al.*, 2002; Hou *et al.*, 2003). However, more recent work by Hanaor and Sorrell (2011) considers the consensus to be that the non-reversible transformation occurs at around 600 ^{0}C, but can be encouraged to occur at

temperatures around 400 ^{0}C by the addition of rutile-promoting dopants, or suppressed up to around 1200 ^{0}C by the addition of rutile-supressing dopants. This is in agreement with Yang *et al.* (2018), who identified a range of temperatures from 400 ^{0}C to 1000 ^{0}C for the anatase to rutile transformation. Therefore, the absence of an anatase phase after annealing at 600 ^{0}C could be considered due to the addition of the molybdenum, which here acts as a rutile-promoting dopant.

4.1.1.5 – Activity

The activity of the samples was inferred by the breakdown of methylene blue. The rate constant at which breakdown occurred was used as an analogue for activity.

The average activity of the molybdenum-doped titanium samples was 3.0×10^{-5} s^{-1} $\pm 1.6 \times 10^{-5}$ s^{-1}, which was significantly greater than the undoped control samples (U=0, p=0.017), which had negligible degradation for the same conditions (2.33×10^{-7} s^{-1}). This degradation shows that the molybdenum-doped titania exhibited activity under fluorescent light (Figure 27).
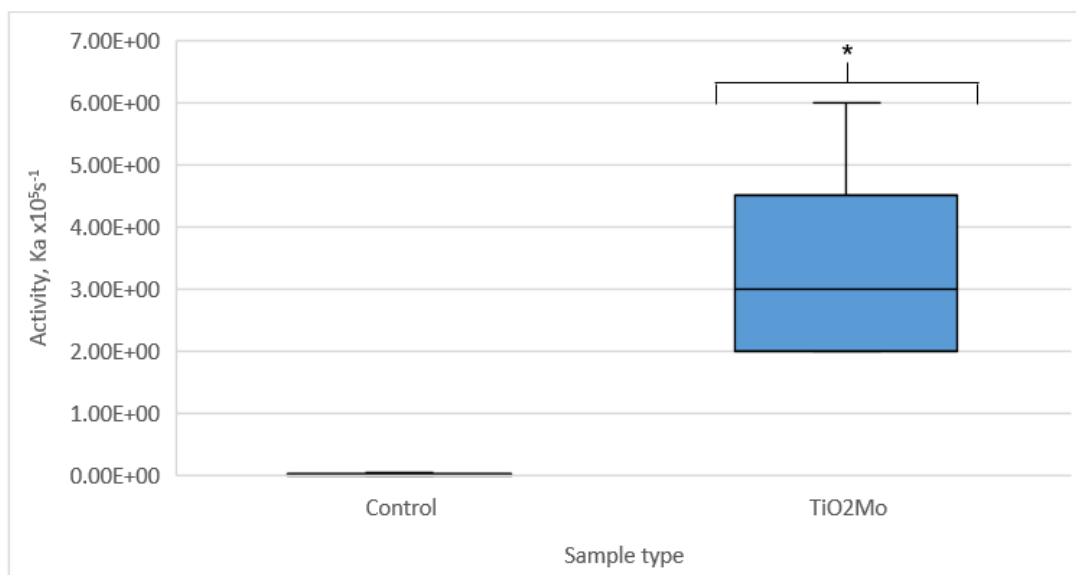
Figure 27: Activity of molybdenum-doped titania coatings compared to uncoated stainless steel controls. Brackets and * indicate significant differences to control. The coated samples exhibited an average activity of 3.4×10^{-5} s^{-1}, which was significantly different to the uncoated control samples (p=0.017). N=7.

The activity observed is encouraging, indicating that molybdenum-doped titania may degrade methylene blue.

4.1.2 – Characterisation of set 2

4.1.2.1 - Composition

Analysis of the atomic concentration of the film components showed that the titanium and oxygen had an approximately stoichiometric relationship. However, earlier discussions about the difficulty in detecting light elements such as oxygen should be considered; hence, the stoichiometric appearance does not preclude the presence of oxygen vacancies in the coating, nor the possibility of adsorbed molecular oxygen from the environment. The dopants, being heavy *d*-block elements, were detected with high precision. Low variation was observed for each of the dopant treatments, indicating low variability in dopant concentrations between batches of coatings. When niobium was used as the dopant target, an average of 4 %at. was found in the film. The amount of molybdenum in the film increased with increased power driving the dopant magnetron (R^2=0.954, p<0.001). When 100 W of power was used, an average of 3 %at. molybdenum was found; this increased to 7 %at. when 150 W of power were used and 9 %at. when 180 W of power were used (Figure 28).
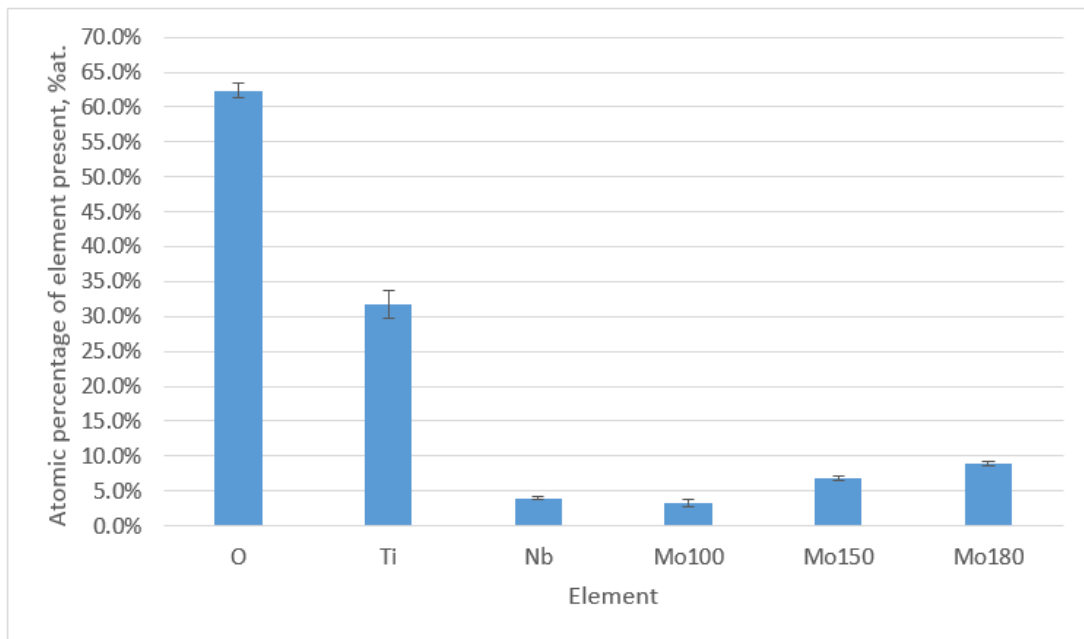
Figure 28: Atomic percentage concentrations of the elements in the films. O = oxygen. Ti = Titanium. Nb = niobium. Mo100, 150, 180 = molybdenum when 100 W, 150 W, or 180 W of power was supplied to the molybdenum target on the dopant magnetron respectively. The concentrations of titanium and oxygen were approximately stoichiometric. The average niobium concentration in the Nb-doped coatings was 4 %at., while the Mo100, Mo 150 and Mo180 samples had a mean molybdenum concentration of 3 %at., 7 %at. and 9 %at. respectively. N=12.

The amount of dopant in the coating was consistent across batches, so the samples were designated accordingly in Table 3.

Table 3: Sample designations by dopant type and concentration.

Dopant	Power to dopant magnetron, W	Concentration of dopant in coating, %at.	Sample designation
Niobium	100	4	Nb
Molybdenum	100	3	Mo1
Molybdenum	150	7	Mo2
Molybdenum	180	9	Mo3

Interestingly, 180 W provided a molybdenum concentration of 7±2 %at.in set 1, compared to the 9 %at. found here. However, this could be an effect of the difference in substrate; stainless steel contains several elements in its composition, so the EDX software may have had difficulty in deconvoluting

any overlapping peaks from the combination of characteristic X-rays emitted, potentially assigning them to incorrect elements. When these elements were manually removed from the scan, the software recalculates the atomic concentration for the remaining elements, which may introduce further artefacts or errors, obfuscating the real mean. This could also help to explain the large variance seen in this dopant compared to in set 2 – all variations in dopants in set 2 are within 14 % of the mean, whereas in set 1, the molybdenum has a variance of 29 % of the mean, which is high.

Nevertheless, because the 9 %at. molybdenum samples in set 2 are within one standard deviation of the 7 %at. in set 1 they could be considered relatively similar, given the reasons described above.

4.1.2.2 – Topography

The doped films were imaged using SEM, at magnifications of 270x and 2500x. Inspection of the SEM images of the niobium-doped titania coatings showed that the deposited films were mostly smooth, featureless and conformal to the glass substrate (Figure 29), compared with the set 1 coatings deposited onto stainless steel (Figure 23). Inspection also revealed a 'brush stroke' pattern on the coatings at magnifications of 270x, along with dark 'gaps' in the coating. These features are presumably where the coating has been abraded or damaged post-deposition. At higher magnification (2500x), pits, holes and debris can be observed.
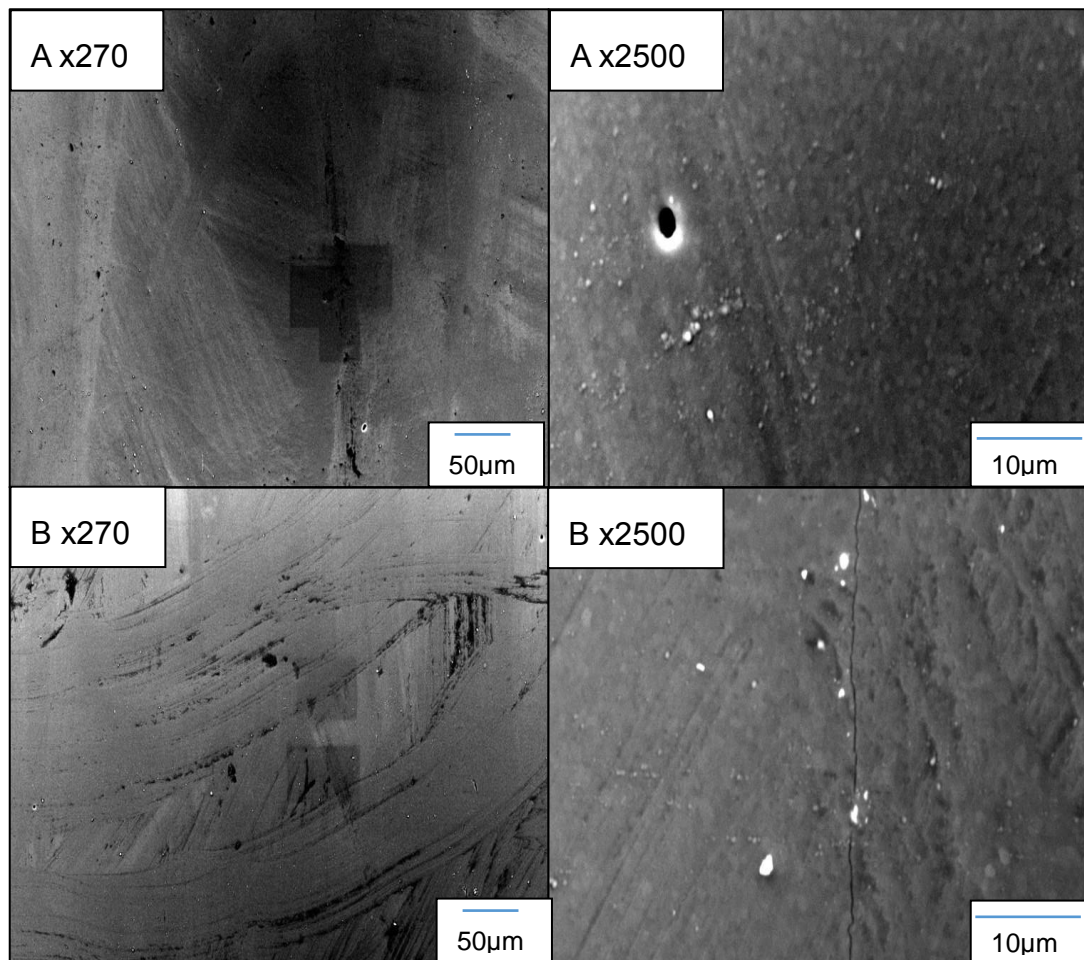
Figure 29: Representative SEM images (x270 and x2500) of the niobium-doped titania coatings on glass substrates. A and B correspond to different samples from different deposition runs. The samples show a mainly smooth surface similar to uncoated glass (not shown due to charging effects), interspersed with brush-stroke abrasions, debris, and pits.

Inspection of the SEM images of the molybdenum-doped titania coatings showed that the deposited films were mainly smooth, featureless and

conformal to the glass substrate, although some debris was observed (Figure 30).
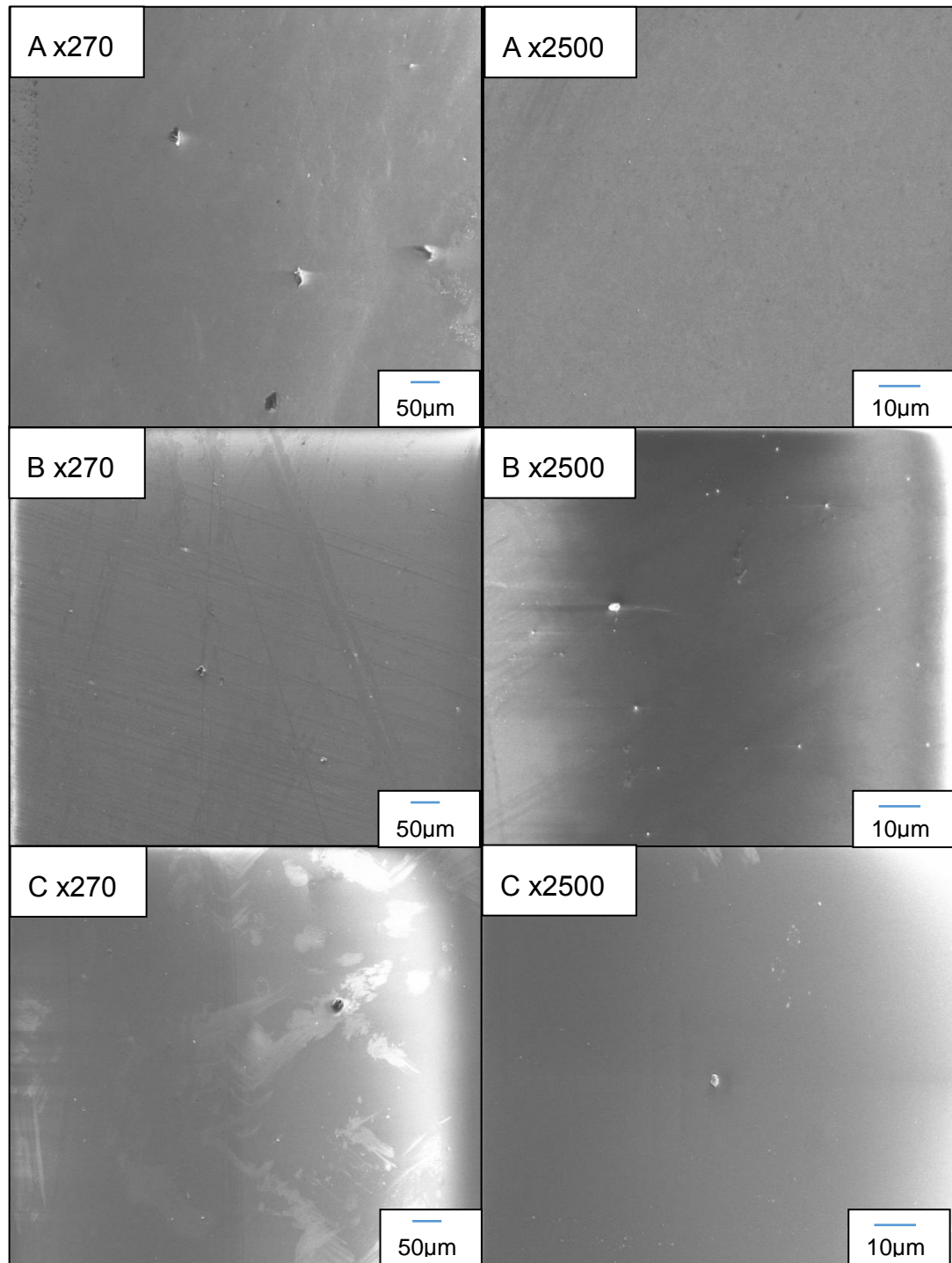
Figure 30: Representative SEM images of the molybdenum-doped titania coatings on glass substrates, at magnifications of x270 and x2500. A, B, and C correspond to Mo1, 2 and 3 respectively. Bright areas in the images indicate localised charging/ artefacts from the instrument. Brush-stroke abrasions, debris, and pits can be observed across all samples.

Small debris can be observed on the surface of the coatings in Figure 30A, B

and C. In addition, the 'brush-strokes' observed on the niobium-doped films (Figure 29) can also be seen on these samples; this is especially apparent in Figure 30B and C. These features may have been caused by post-depositional stress, abrasion, or damage – collectively known as post-depositional events. Bright areas in the images correspond to areas affected by electron charging – this occurs when the electrons fired at the sample by the electron gun cannot dissipate due to breaks or fractures in the underlying coating. The electrons begin to accumulate, increasing the local negative charge; the detector interprets this charging as an increase in signal and therefore these areas appear brighter. In the upper-left of Figure 30A at the lower magnification, pitting can be observed, indicating an absence of coating at this location.

While no striking or significant differences were observed between the various molybdenum samples, more intense 'brush-strokes' and more debris were observed on the niobium-doped coatings than the molybdenum-doped coatings. This could be due to the difference in hardness between the dopant elements – niobium has a Vickers hardness of 870–1320 MPa, while molybdenum as a hardness of 1400–2740 MPa (Samsonov, 1968). The niobium-doped coatings could be considered softer than the molybdenum-doped coatings and therefore more prone to damage. However, as the concentration of dopants present in the films was relatively small, the contribution of the dopant to the hardness of the overall material is debatable. While secondary or dopant materials can clearly influence the overall hardness of a material, especially in alloy-type materials such as steel (Filho *et al.*, 2017), it is difficult to generalise here, especially as Vickers hardness is considered an indentation hardness – the damage shown in niobium-doped samples could be considered more of a scratch or abrasion than indentation. To that end, the Mohs scale indicates that niobium has a hardness of 6, while molybdenum has a hardness of 5.5. Therefore, the niobium would be expected to have fewer scratches and abrasions than the molybdenum-doped samples, given the same exposure.

Alternatively, the damage observed could be an indicator of excessive intrinsic tensile stress – as mentioned in *section 2.3.2*, intrinsic tensile stress

can cause cracks and breaks along the deposited columns in zone 1/T structures. However, a counter to this argument is that zone 1/T structures are rarely seen using CFUMS techniques – the tensile stress is reduced by the atomic peening mechanism that occurs due to argon ion bombardment of the growing film, causing a shift to a coating of overall compressive stress. The effect of this is the formation of generally dense, zone 2/3 coatings. Therefore, the origin of these breaks remains unknown, but can likely be ascribed to the post-depositional events already mentioned for the molybdenum-doped coatings.

4.1.2.3 – Profilometry

Uncoated glass coupons had a mean roughness of 8±2 nm. The niobium-doped titania coupons had a roughness of 14±9 nm, which was significantly larger than the uncoated coupons (U=87.0, p=0.001). The roughness of the molybdenum samples (Mo1: 12±5 nm; Mo2: 11±5 nm; Mo3: 6±3 nm) was not significantly different than uncoated control and did not vary with respect to power to the dopant target (x^2=5.91, p=0.052).

Therefore, the only coating that had a significantly higher roughness than the uncoated glass slide controls was the niobium-doped titania (Figure 31).
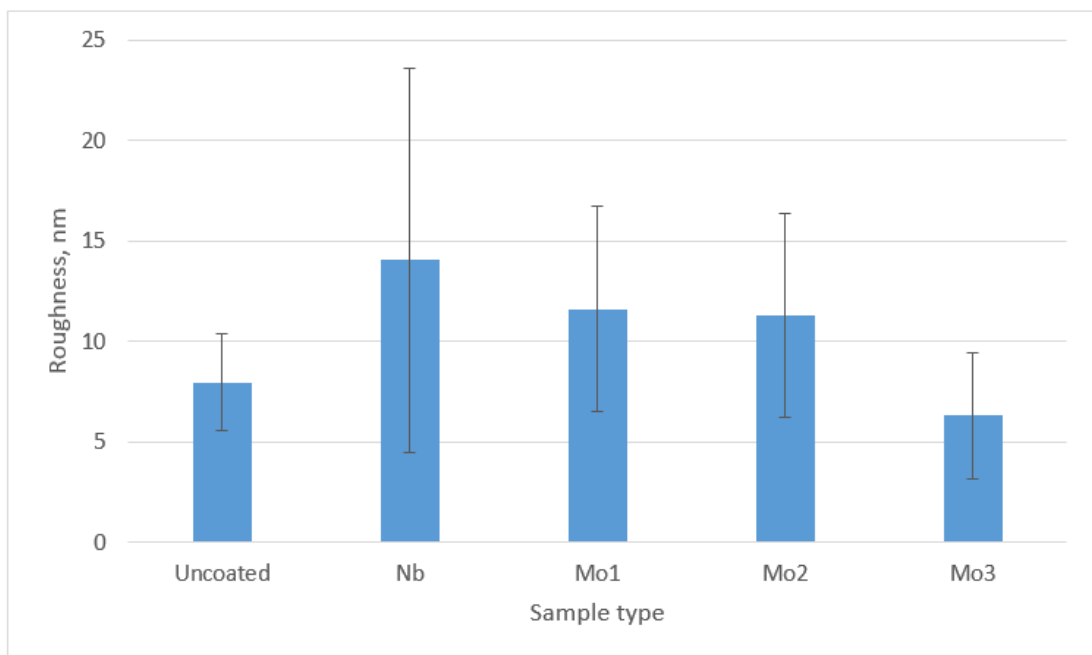
Figure 31: Mean roughness of the coating compositions. Uncoated = uncoated glass coupons. Nb = niobium. Mo1, 2, 3 = 3, 7, 9 %at. molybdenum. There were no significant differences in mean roughness between coating types or control, indicating that the coatings retained the low roughness properties of the glass substrata. N=30 uncoated, 15 Nb, 10 Mo1, 9 Mo2, and 8 Mo3, with the roughness of individual samples calculated as the mean of five positions on the sample.

The 'brush-strokes', marks and pits seen on the niobium-doped samples in *section 4.1.2.2* were also investigated using the optical profilometer. The patterns appear to be gaps in the coating that have been abraded or removed by friction (Figure 32). Between these areas, the coating seemed smooth and featureless, so the features are likely indicative of post-deposition events as opposed to pre-deposition or intra-deposition effects.
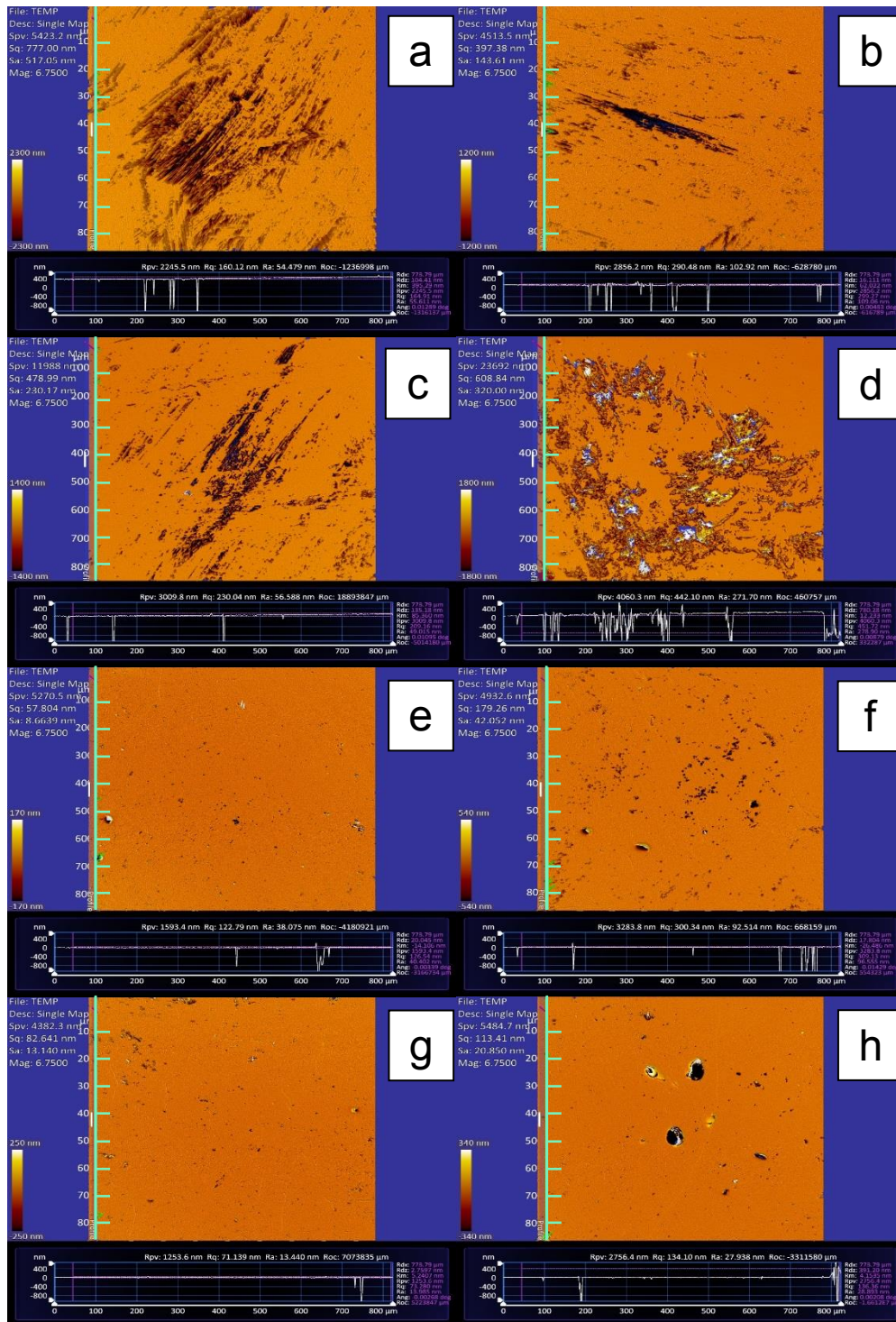
Figure 32: Representative optical profilometer scans showing the abraded/brushed areas of the coating (a-d) and the smoother areas of the coating (e-h). Although e-h have smoother areas, gaps and pits are still visible across the sample surface. Profile transect taken from left-hand side of each scan. Scale indicators on the transect line represent 100 μm intervals.

In agreement with the SEM analysis, fewer of these features were observed on the molybdenum-doped samples (Figure 33), although several gaps and features can be observed in Figure 33d.
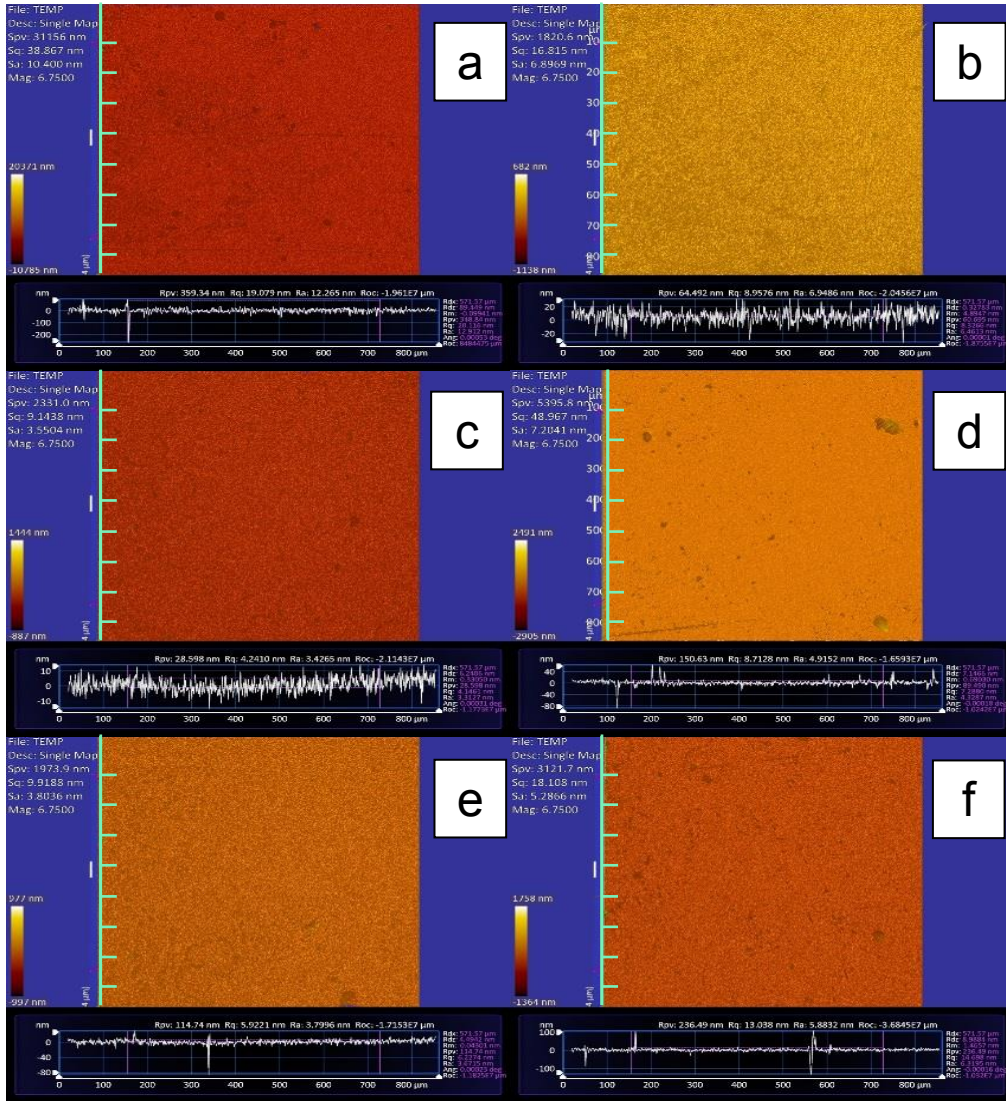
Figure 33: Optical profilometer scans showing smooth, homogenous areas of the molybdenum-doped coatings, with few inclusions or features. Some pitting or scratches can be observed in Figure 33d. Profile transect taken from left-hand side of each scan. Scale indicators on the transect line represent 100 μm intervals.

The thickness of the coatings was determined by measuring the step-height using profilometer scans, such as in Figure 34. The step-heights for these coatings (deposited onto glass substrates) were distinct, compared to the step-heights of the Set 1 coatings (deposited onto stainless steel substrates).
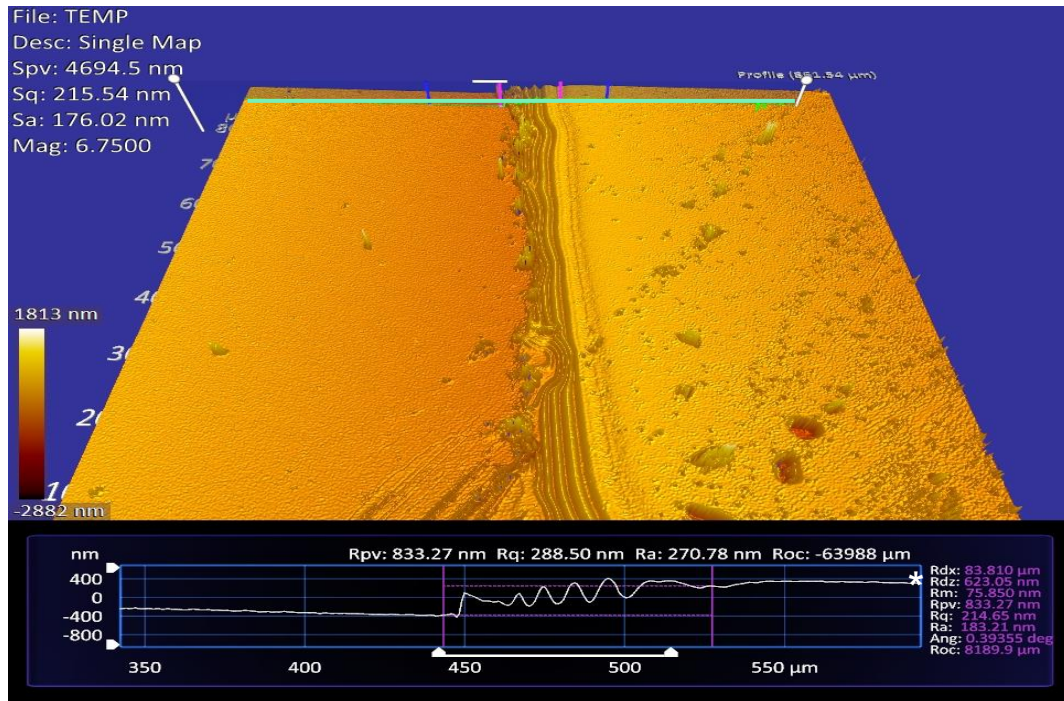
Figure 34: Profilometer scan illustrating the step-height method used. Profile transect taken from the top of the scan. The Rdz value (indicated here with * in the bottom-right of the figure) indicates the difference in height between the coated (right-hand side) and uncoated (left-hand side) sections of the coupon, and thus the coating thickness.

The thickness of the coatings varied depending on the dopant and power to the dopant target (Figure 35).
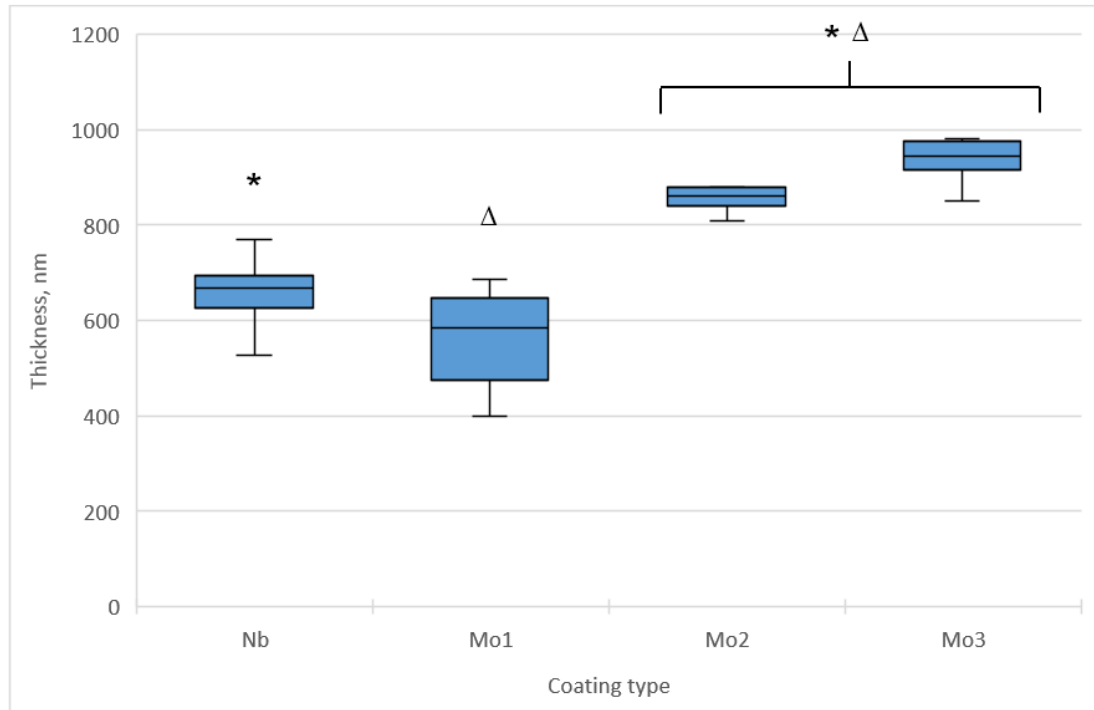
Figure 35: Median thickness of the coating compositions. Nb = niobium. Mo1, 2, 3 = 3, 7, 9 %at. molybdenum. Paired Δ and * symbols indicate significant differences from each other (p<0.003). The thickness of the coatings increased with increasing power to the dopant magnetron.

The coating type had a significant effect on thickness of the coating (x^2=24.89, p<0.001). After applying a Bonferroni correction for pairwise comparison, it was found that there were significant differences in median thickness between the niobium-doped coatings and the 7 % and 9 % molybdenum-doped coatings (U<0.001, p=0.001; U<0.001, p<0.001). Furthermore, the 3 % molybdenum-doped coatings were found to have a significantly different median thickness to the 7 % and 9 % molybdenum doped coatings (U<0.001, p=0.003; U<0.001, p=0.002). When molybdenum was used as the dopant, a significant relationship was found between power to the dopant magnetron and coating thickness (R^2=0.841, p<0.001).

Essentially, thickness of the coating increased with increasing dopant content in the coating, as there was simply more material present in the coating. Indeed, the least thick film (Mo1) had a dopant content of 3 %at., increasing through the niobium-doped film (Nb) at 4 %at., then through the 7 %at. (Mo2) and 9 %at. (Mo3) molybdenum-doped films.

4.1.2.4 – Crystallinity

Niobium- and molybdenum-doped titania coatings were investigated for crystallinity. The as-deposited samples exhibited no crystallinity (Figure 36).
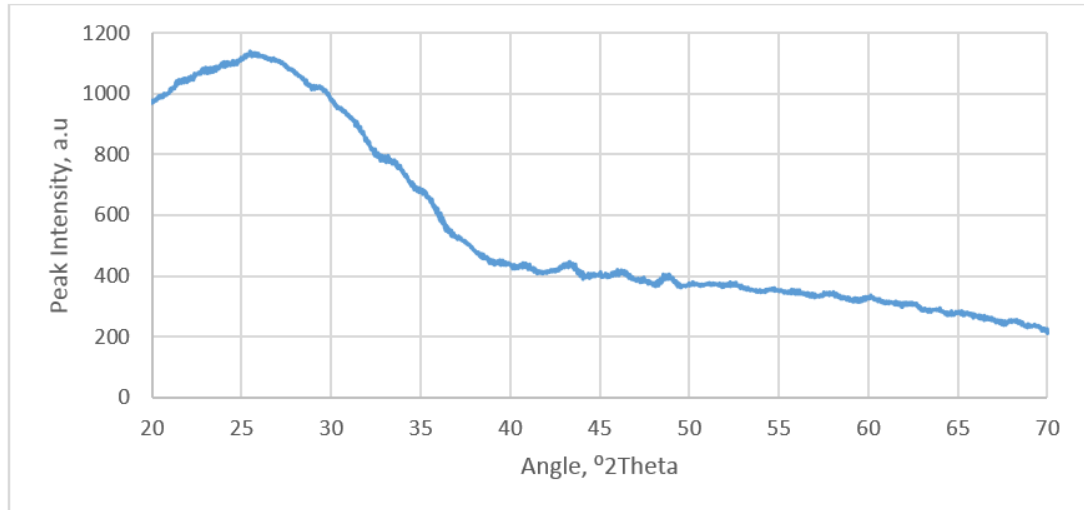
Figure 36: Representative XRD pattern of as-deposited niobium- and molybdenum-doped coatings on glass coupons. The amorphous structure of the coating can be observed by the lack of characteristic peaks.

Annealing the samples at 500 ^{0}C for either 30 or 60 minutes induced crystallinity in all coating compositions compared to as-deposited samples. Both annealing times yielded anatase crystallinity in the niobium-doped coatings. The characteristic anatase 101 (25.3^0), 004 (38^0) and 200 (48^0) peaks can be seen in Figure 37. Annealing for 60 minutes yielded narrower, more intense anatase peaks, indicating larger grain sizes (Scherrer, 1918; He *et al.*, 2018).
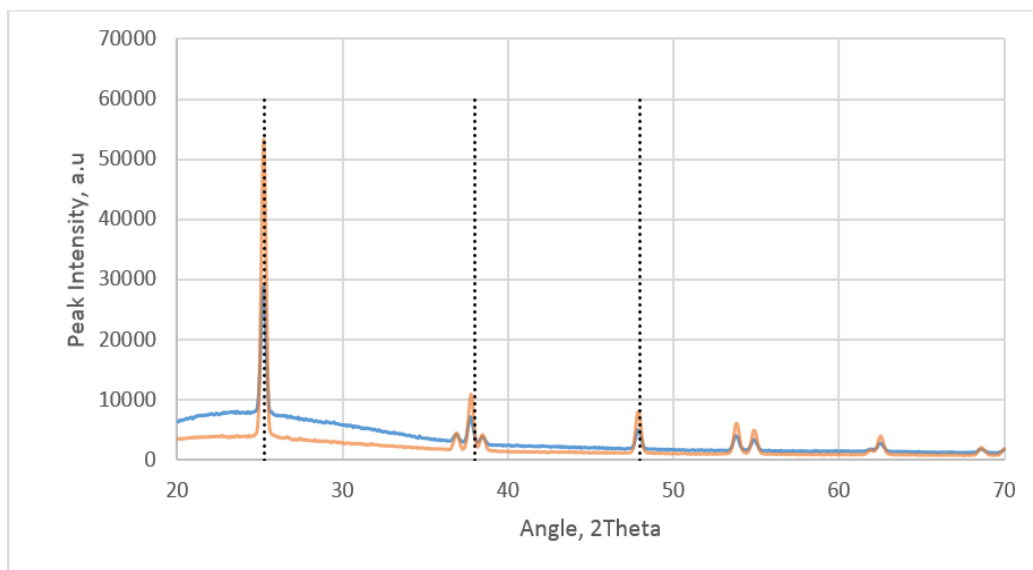
Figure 37: Representative XRD pattern for Nb-doped titania coatings annealed at 500 ^{0}C for either 30 minutes (blue) or 60 minutes (orange). Characteristic anatase 101 (25.3^0), 004 (38^0) and 200 (48^0) peaks are displayed as dotted lines.

Annealing the titania coatings containing 3 %at. molybdenum for either time period also yielded anatase crystallinity (Figure 38), although a small rutile 111 peak was detected at 42^0 when annealed for 60 minutes.
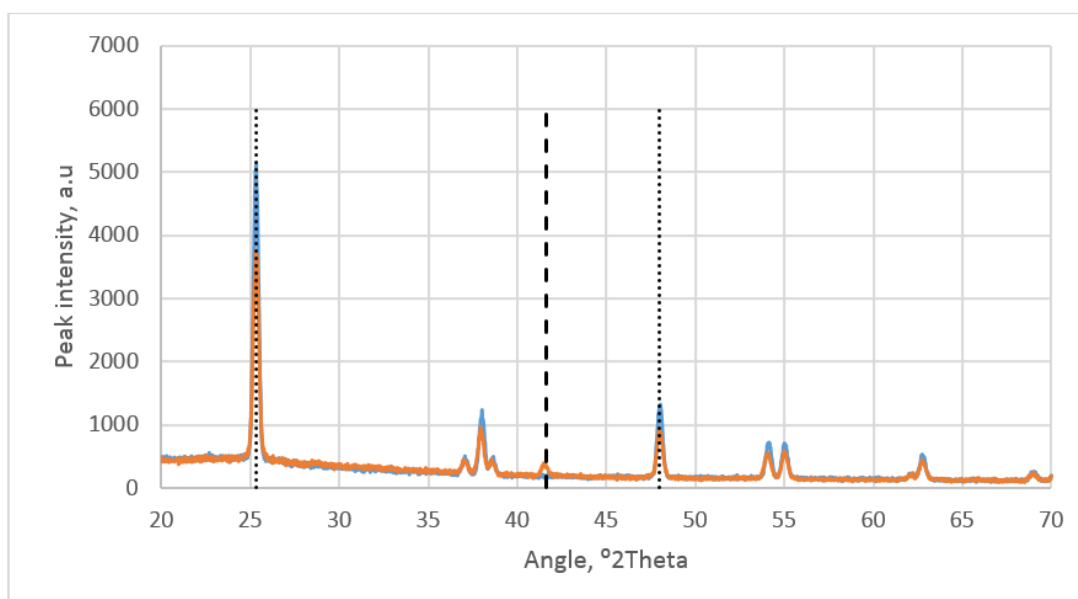
Figure 38: Representative XRD pattern for 3 % Mo-doped titania coatings annealed at 500 ^{0}C for either 30 minutes (blue) or 60 minutes (orange). Anatase 101 (25.3^0) and 200 (48^0) peaks are displayed as dotted lines, while rutile 111 (42^0) is displayed as a dashed line.

Annealing the sample for 30 minutes yielded more intense anatase peaks compared to annealing for 60 minutes, although only the one rutile peak was

observed. A similar effect was seen in the 7 %at. Mo-doped coatings. While annealing for both times yielded anatase crystallinity, the number and intensity of rutile peaks increased when the samples were annealed for 60 minutes compared to 30 (Figure 39). In addition, the anatase peaks appeared lower in the 60-minute samples, suggesting that suppression of the anatase phase is concurrent to the onset of the rutile phase. This mixed-phase is further evidenced by the peak cluster around 38^0, which are a mix of anatase 004 and rutile 200 peaks.
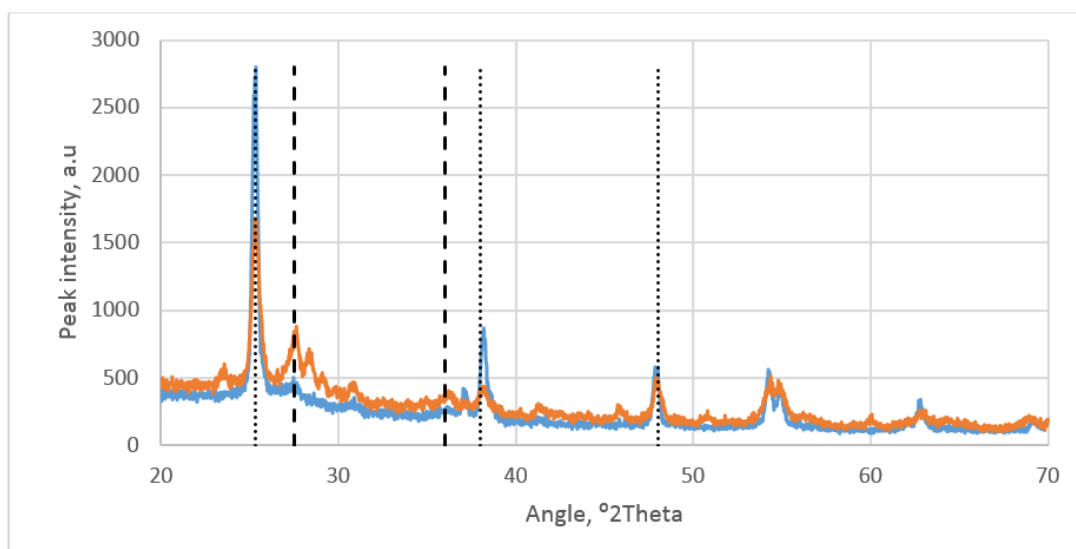
Figure 39: Representative XRD pattern for 7 %at. Mo-doped titania coatings annealed at 500 ^{0}C for either 30 minutes (blue) or 60 minutes (orange). Anatase 101 (25.3^0), 004 (38^0) and 200 (48^0) peaks are displayed as dotted lines, while rutile 110 (27.5) and 111 (42^0) are displayed as dashed lines.

Annealing the 9 %at. Mo-doped samples for either 30 or 60 minutes yielded primarily rutile crystallinity, with no distinct characteristic anatase peaks (Figure 40).
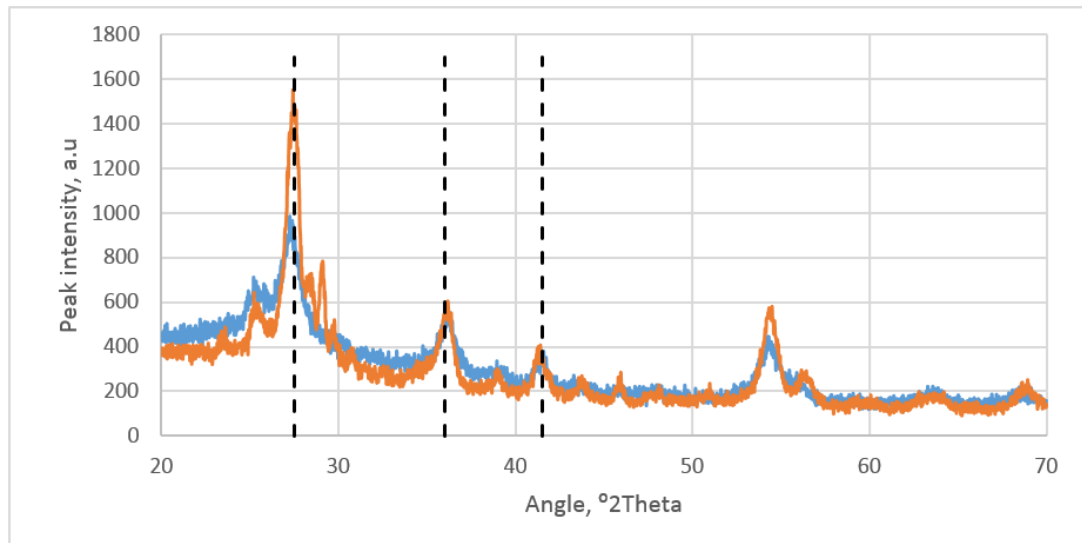
Figure 40: Representative XRD pattern for 9 %at. Mo-doped titania coatings annealed at 500 ^{0}C for either 30 minutes (blue) or 60 minutes (orange). Rutile 110 (27.5), 101 (36.01^0) and 111 (42^0) are displayed as dashed lines.

The number and intensity of characteristic anatase peaks appear reduced, while characteristic rutile peaks are abundant and intense, compared to lower concentrations of molybdenum in the film. This implies that increasing molybdenum concentration in the film reduces the number and intensity of anatase crystals and the increases the amount of rutile crystals within the film. This agrees with the results found in set 1, where the titania film was doped with 9 %at. molybdenum – no anatase crystals were found in those films. This progressive change in crystal phase with increasing molybdenum concentration can be seen when the films were annealed for 30 minutes in Figure 41.
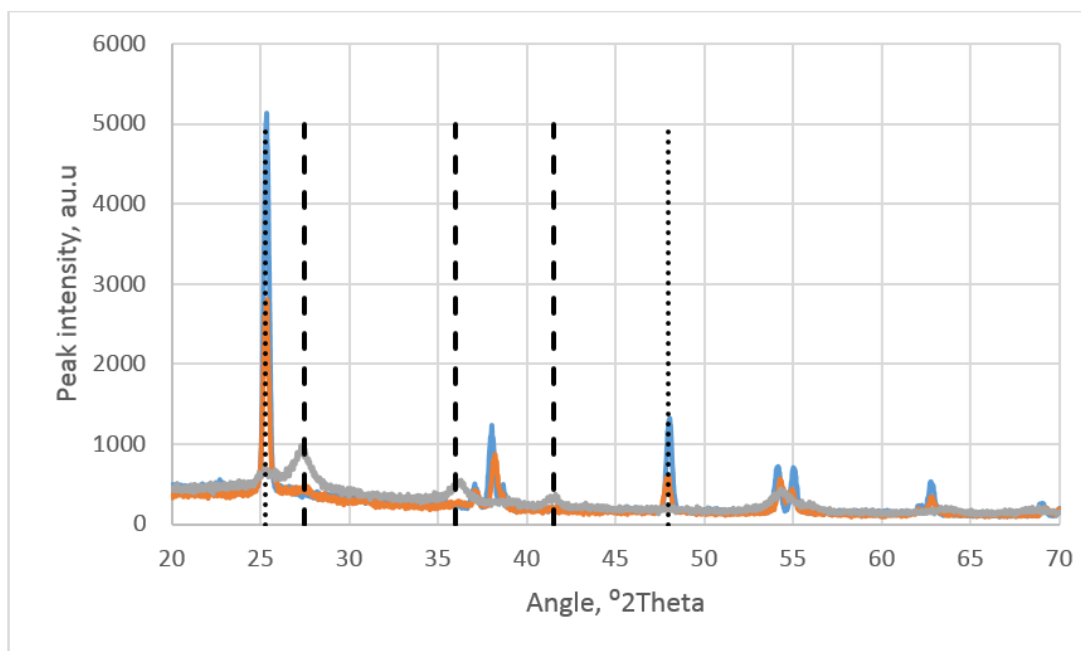
Figure 41: Representative XRD pattern for each concentration of molybdenum within the film, annealed at 500 ^{0}C for 30 minutes. As the concentration of molybdenum within the film increases (3%, blue; 7%, orange; 9% grey), the intensity of the anatase peaks decrease, films begin to exhibit rutile crystallinity. Anatase 101 (25.3^0) and 200 (48^0) peaks are shown as dotted lines, while rutile 110 (27.5^0), 101 (36.01^0) and 111 (42^0) are shown as dashed lines.

This effect could also be seen when the films were annealed for 60 minutes (Figure 42).
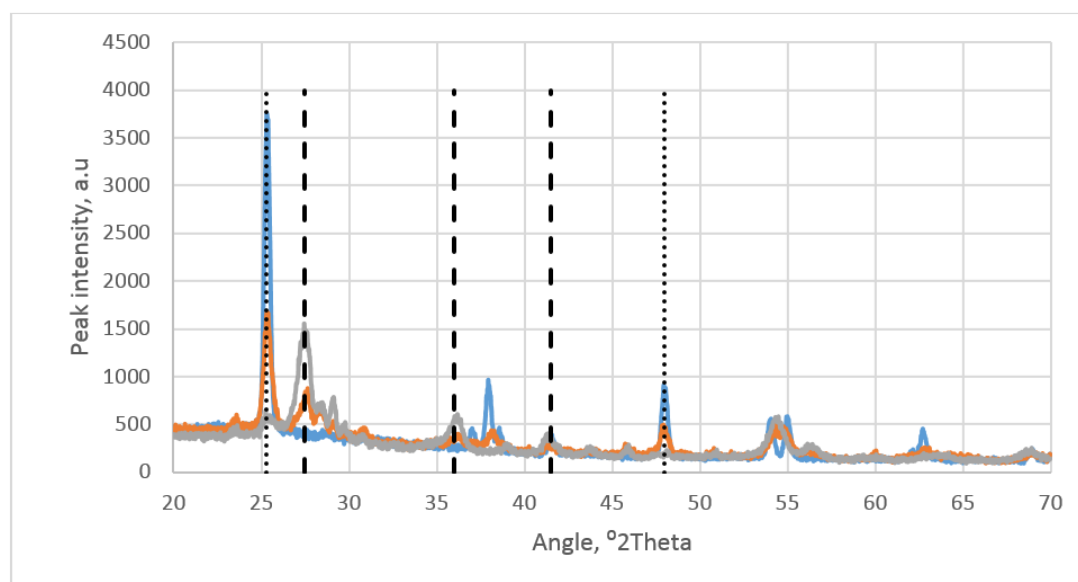
Figure 42: Representative XRD pattern for each concentration of molybdenum within the film, annealed at 500 ^{0}C for 60 minutes. As the concentration of molybdenum within the film increases (3%, blue; 7%, orange; 9% grey), the intensity of the anatase peaks decrease, films begin to exhibit rutile crystallinity. Anatase 101 (25.3^0) and 200

The effect of molybdenum as a rutile promotor is especially evident when observing the dynamics of the 101 anatase peak at 25.3^0 compared to the rutile 110 peak at 27.5^0 (Figure 43).
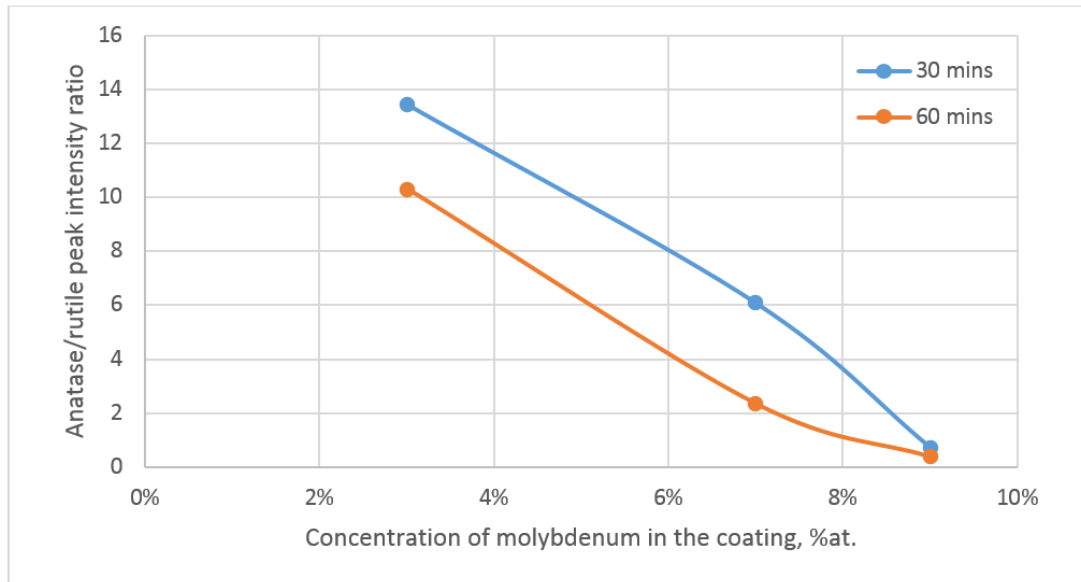
Figure 43: Ratio of anatase 101 peak (25.3^0) and rutile 110 peak (27.5^0) by molybdenum concentration. At 3 %at. and 7 %at. molybdenum concentration, the samples annealed for 30 minutes (blue) exhibited a higher ratio of anatase/rutile peaks at than the samples annealed for 60 minutes (orange). However, when the molybdenum concentration was 9 %at., the ratios were similar.

When the 3 %at. molybdenum coatings were annealed for 30 minutes, the ratio between the 101 anatase peak and the rutile 110 peak was 13.4, indicating a minimal rutile content. This decreased to around 10.3 when annealing was increased to 60 minutes, still implying negligible rutile content. There was a considerable reduction in the anatase: rutile ratio in the 7 %at. molybdenum coatings, from 13.4 to 6 for 30 minutes annealing and from 10.3 to 2.3 for 60 minutes annealing.

The implications of this are that the molybdenum content has much more influence over the anatase to rutile transition than an additional 30 minutes annealing time. This is further evidenced by the 9 %at. molybdenum coatings – there was minimal difference in anatase to rutile ratio between annealing times, but there was considerably less anatase present in the coating than the 7 %at., despite an increase of only 2 %at. Although the suppression of the anatase phase and promotion of the rutile phase was mainly influenced

by the dopant concentration in this work in agreement with Li *et al.* (2011), the annealing time clearly did have an effect for lower concentrations of dopant.

It is therefore apparent that the anatase to rutile transition is an effect of both the dopant concentration and the annealing time. This is thought to be related to underlying anatase requirements – compared to the stable rutile phase, anatase is metastable. For example, anatase crystals require a critical level of lattice strain to prevent rutile transition. As annealing temperatures increase, crystallite size is increased, relieving lattice strain – after a critical point, the crystals transition to rutile, reducing crystallite size (Inagaki *et al.*, 2006). Similarly, depending on the dopant, a critical level exists where the effect on the lattice cannot be tolerated and the anatase transitions into rutile (Hanaor and Sorrell, 2011; Kaleji *et al.*, 2017).

4.1.2.5 - Activity

As with set 1, the activity was inferred from the first-order rate constant of the breakdown of methylene blue. The activities of the sample types are shown in Figure 44.
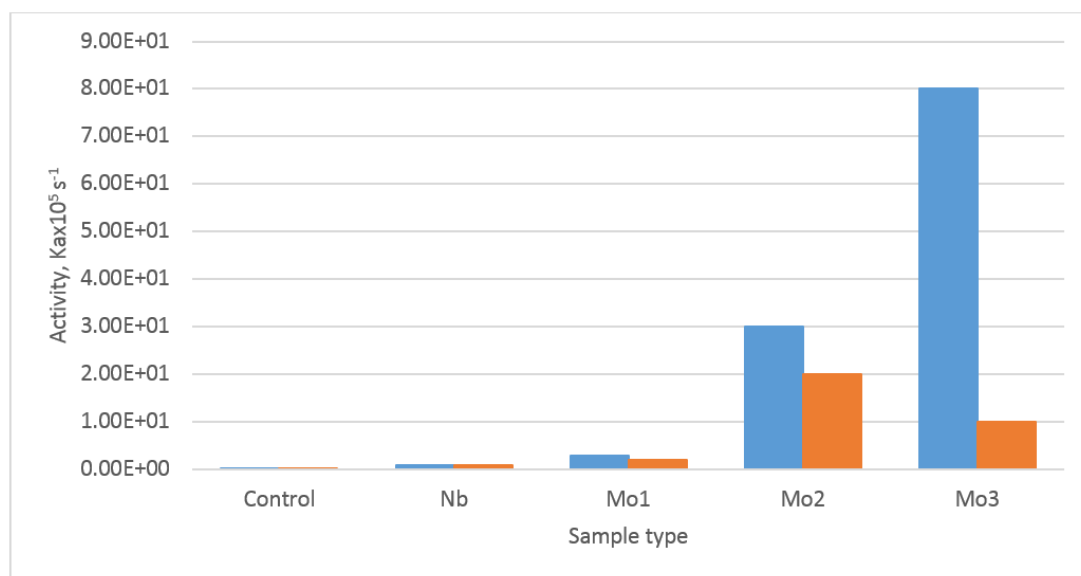
Figure 44: Activity of the set 2 samples as determined by degradation of methylene blue. Blue: Samples annealed for thirty minutes. Orange: Samples annealed for sixty minutes. Control: uncoated glass samples as a control. Nb = niobium-doped samples. Mo1, 2, 3 = 3, 7, 9 %at. molybdenum. Higher concentrations of molybdenum, and shorter annealing times, yielded samples with higher activity. N=1.

Doping the sample with molybdenum improved the activity of the coatings more than niobium. The samples that most rapidly degraded the methylene blue were the molybdenum-doped samples; furthermore, increasing the amount of molybdenum present increased the activity accordingly. This is likely due to molybdenum substitution into the titania lattice, redshifting the bandgap and improving activity (Lu *et al.*, 2018a). This is interesting to note, as the highest activity was found in the samples with the least anatase and most rutile crystallinity. The niobium-doped samples showed very little activity; annealing for thirty minutes yielded a higher activity (9.5×10^{-6} s^{-1}) than annealing for sixty minutes (8.25×10^{-6} s^{-1}), although this difference is likely negligible. Annealing the samples for 30 minutes generally yielded higher activity than annealing for 60 minutes, implying that shorter annealing time can contribute to better crystallinity and higher activity. However, due to the lack of repeat readings, this observation should be considered carefully.

Especially interesting is the low activity of the niobium-doped samples when considering the crystallographic properties observed using XRD. The niobium-doped samples generally had much larger grains and much more anatase content than the 7 %at. and 9 %at. molybdenum-doped samples, so it could be expected that the niobium-doped samples exhibit higher activity. However, this is not the case; furthermore, the 3 %at. molybdenum samples had comparable grain size and anatase content yet had an improved response. This could imply that the niobium does not improve visible light activity, whereas molybdenum does. A key consideration in these results however, is the low sample numbers for the activity testing results. As each sample type had only one sample tested, no statistical tests could be performed, so the data should be interpreted with caution.

4.1.3 – Characterisation of set 3

4.1.3.1 – Composition

Three compositions were investigated for set 3. Pure titanium dioxide coatings with no dopant were found to be stoichiometric, given the considerations to light elements already discussed.

The niobium-doped titania coatings had a stoichiometric ratio of titanium and oxygen and contained a mean of 4 %at. niobium. This was consistent with the niobium-doped films produced in set 2.

The molybdenum-doped titania coatings had a mean concentration of 8 %at. Molybdenum. Interestingly, this was different to the 180 W molybdenum-doped samples in set 1 (7±2 %at.) and set 2 (9 %at.), although is within one standard deviation of the set 1 samples. In addition, the ratio of oxygen to titanium was found to be 65:23, which was not stoichiometric. The large standard deviations for the samples however suggests that there may be an approximate 2:1 ratio, especially given the EDX considerations discussed, such as peak overlapping and deconvolution issues and light element detection problems. In addition, the quantification of light elements such as oxygen are sometimes poorly measured using EDX systems and so the amount of oxygen measured in these coatings may be over-reported (Ro *et al.*, 1999; Osan *et al.*, 2000; Ro *et al.*, 2004).

Another key consideration is that the samples of the second batch from this set and composition were much darker and less transparent than the first batch. This may be due to a different OEM system used during fabrication which may have suffered from calibration issues.

This could have led the system to throttle the oxygen flow too much, creating an oxygen-lean atmosphere. This would create a sub-stoichiometric metal-rich film, creating large voids within the film and increasing the refractive index (Poelman *et al.*, 2004; Haque *et al.*, 2014; Li *et al.*, 2015). The coating would be unlikely to be able to support a metastable crystalline structure such as anatase and might collapse to the more stable rutile phase, with smaller crystals, very easily.

On the contrary, calibration issues could have also led the system to throttle the oxygen flow too little, creating an oxygen-rich atmosphere. This would impact the mean free path of the sputtered titanium, reducing the amount of titanium that reached the substrate and reducing the angle of incidence of the titanium to the substrate – this would lead to oblique growth of columnar structures in the film. Oblique growth would promote a porous columnar zone 2 structure due to shadowing effects, hindering densification and therefore crystalline growth (Kelly and Arnell, 2000). In addition, above a certain point, the amount of oxygen in the chamber can cause defects and voids similar to those observed in metal-rich films, which in turn cause a high refractive index (Haque *et al.*, 2014). The EDX from batch two indicated a high oxygen content and low titanium content and lowered molybdenum content, implying this may have been the case.

4.1.3.2 – Profilometry

As with set 2, the uncoated glass coupons had a mean roughness of 8±2 nm.

The roughness of the coatings varied depending on batch and composition and ranged from 5 nm to 19 nm (Figure 45). No significant differences were found between the sample compositions, except for the second batch of the titanium dioxide samples. These samples had a mean roughness of 5.8±0.8 nm, which was significantly different (p=0.01) to the first batch, which had mean roughness of 7.1±0.7 nm. The mean difference was 1.32 nm. While this difference is very small, it may indicate differences in the deposition process between batches of the same composition.

The mean roughness for the niobium-doped samples was 8.5±2.7 nm, which was significantly different to the second batch of titanium dioxide samples (mean difference of 2.7 nm, p=0.005). There were no significant differences in the mean roughness for the other coating compositions.
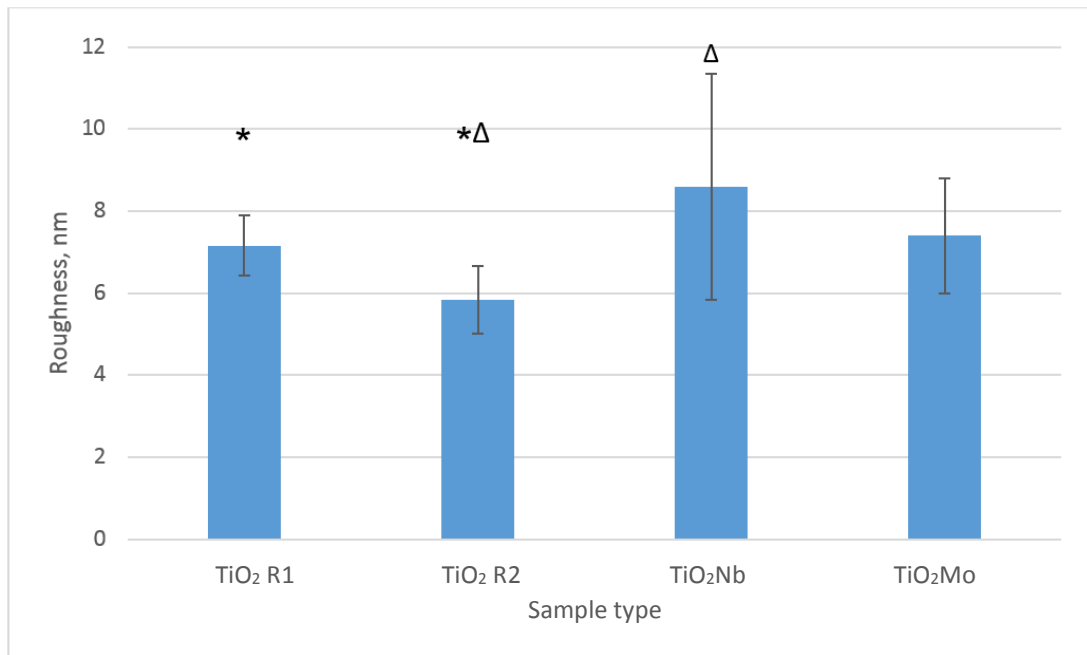
Figure 45: Mean roughness of the coating compositions in set 3. Paired Δ or * symbols indicate a pair significantly different to each other ($p < 0.05$). The roughness of the first and second batch of titanium dioxide (TiO_2 R1 and TiO_2 R2 respectively) were significantly different to each other, so are shown separately. The only other significant difference in roughness was between the second batch of undoped titania and the niobium-doped coatings (TiO_2Nb). There were no significant differences between the molybdenum-doped titania (TiO_2Mo) and any other coating type, nor between the other batches of the coating types. N=10, with the roughness of individual samples calculated as the mean of five positions on the sample.

In contrast to set 2, the features observed using SEM techniques were not seen using profilometry. Despite exhibiting a higher mean roughness, samples from the first batch of titanium dioxide coating showed no striking or significant differences by inspection of profile scan to the second batch (Figure 46).
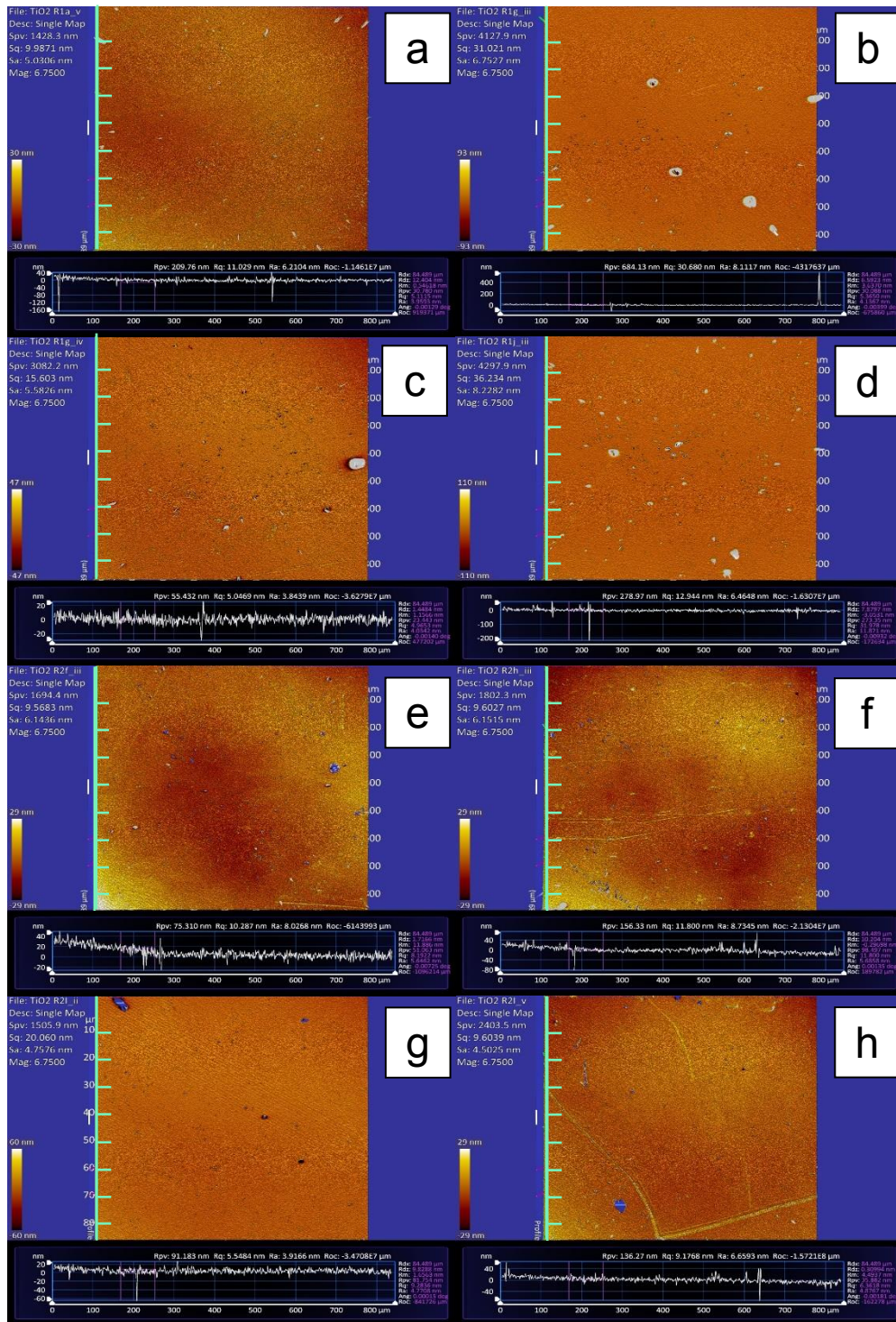
Figure 46: Representative optical profilometer scans showing the smooth and homogenous undoped titania coatings. No striking differences were observed between batch one (a-d) and batch two (e-h). Profile transect taken from left-hand side of each scan. Scale indicators on the transect line represent 100 μm intervals.

This is especially apparent when comparing Figure 46a-d (batch one) with Figure 46e-h (batch two). Both batches seem to contain a little debris, but

are smooth and homogenous. Similarly, the niobium-doped samples appeared to be mainly smooth and homogenous. Some features and patterns were seen, specifically in Figure 47c and Figure 47d. These patterns appear as small 'steps' and may indicate post-depositional damage.
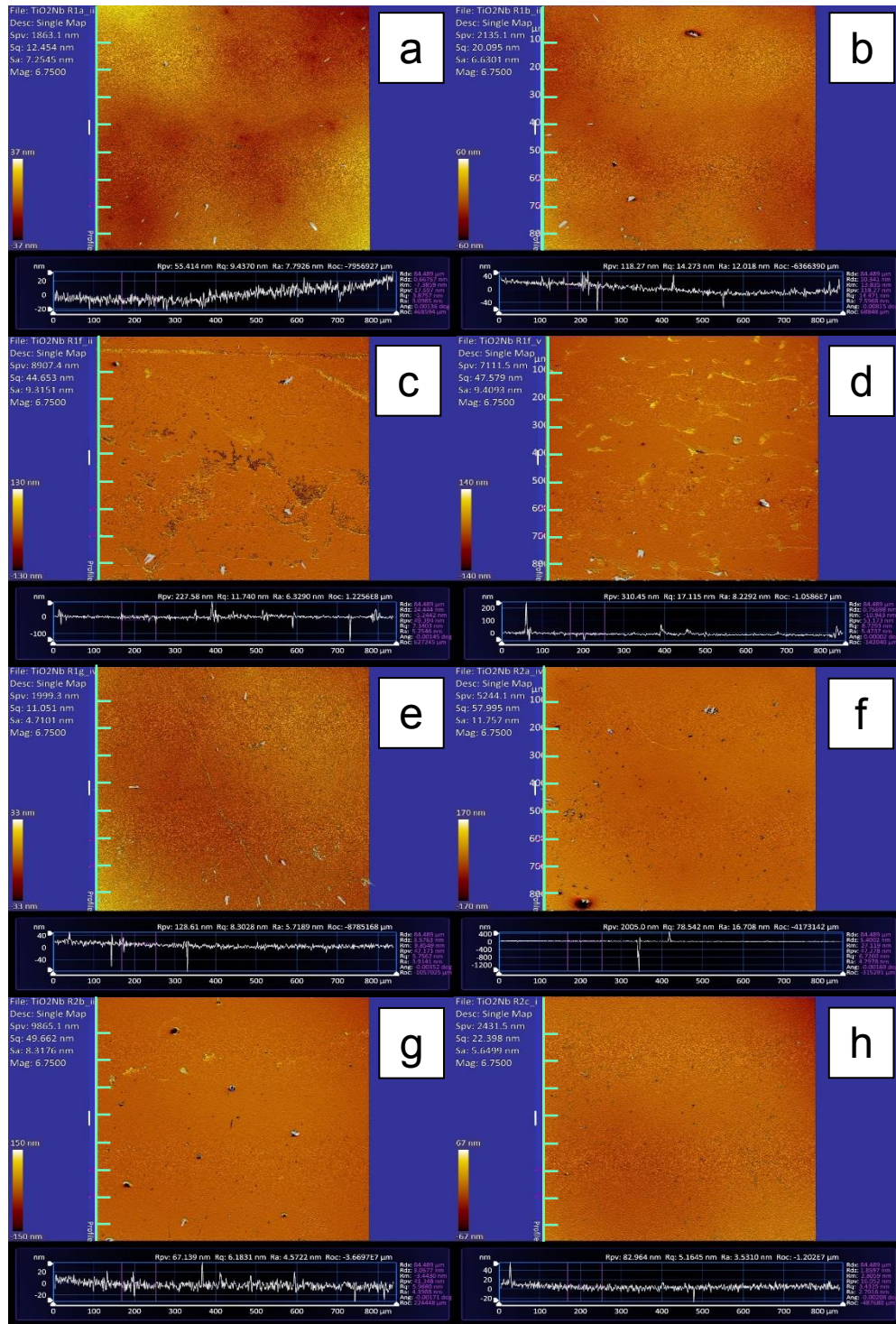
Figure 47: Representative optical profilometer scans showing the smooth and homogenous niobium-doped titania coatings, with the exception of C and D; patterns

The molybdenum-doped samples showed a variability in topography (Figure 48). There were large areas on several samples that were smooth, homogenous and featureless (Figure 48b, Figure 48d-g).
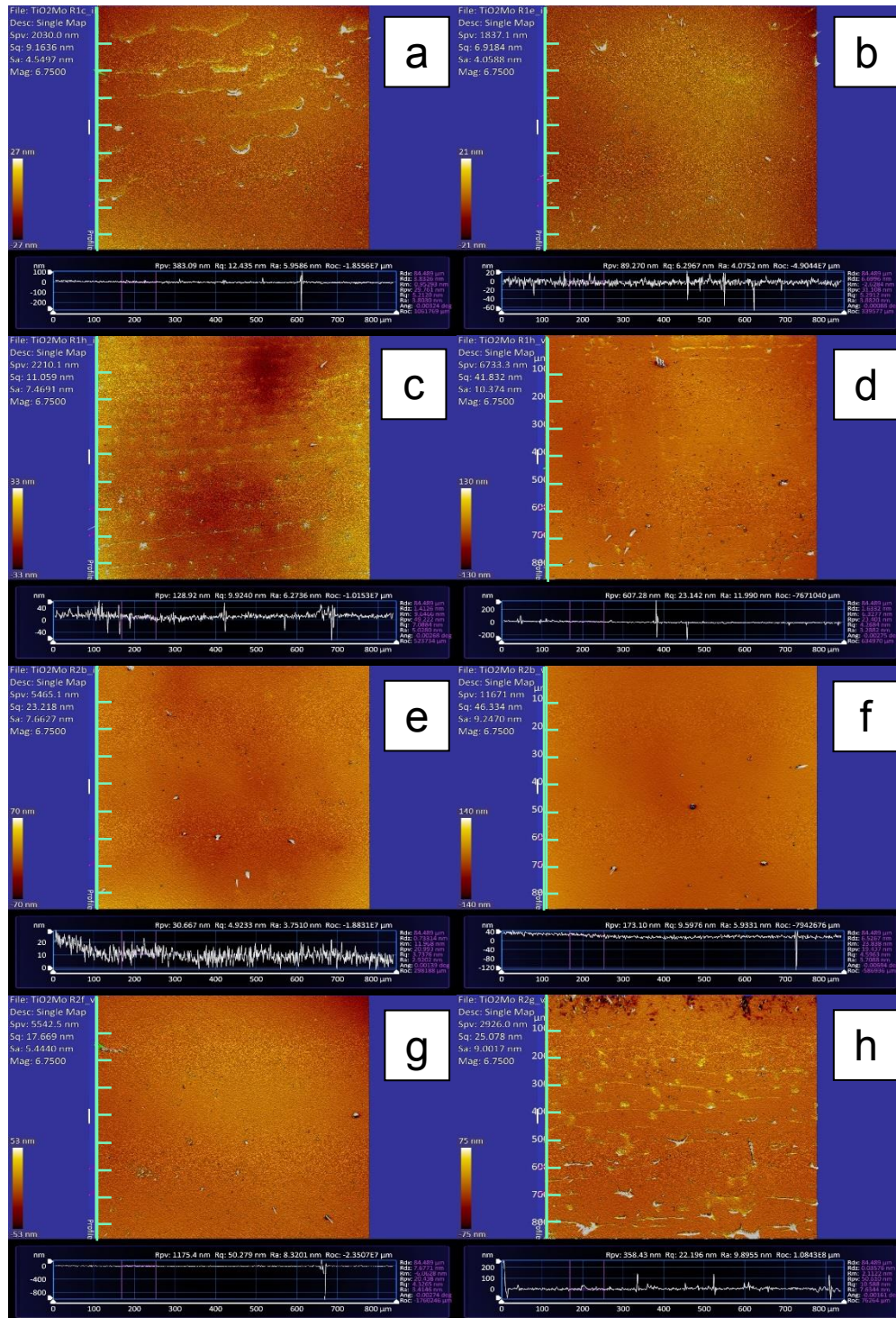
Figure 48: Representative optical profilometer scans showing the variation in sample topography in the molybdenum-doped titania samples. Samples b and d-g show

However, there were also numerous samples (Figure 48a, Figure 48c, Figure 48h) that had patterns and inclusions, similar to those observed in the niobium-doped titania coatings from set 3 (Figure 47c-d). While the source of these patterns and brush-strokes is unknown, it is speculated that they occur primarily from post-depositional damage; this may occur during handling and analysis. Alternatively, the damage may occur immediately after deposition; as the deposition chamber is vented, air rapidly re-enters. This rapidly changing air pressure could creature sheer stress and as the inside of the chamber may still be hot, the films may still be prone to rearrangement. The rapid ingress of air could therefore damage the fragile new coating, creating the interesting patterns seen, particularly in Figure 47c-d and Figure 48a, c and h. Reducing the rate of venting may ameliorate this in future experiments.

4.1.3.3 – Crystallinity; hot stage investigation

As described in *sections 4.0.3.3* and *4.0.4.4*, the hot stage XRD was used to investigate the crystallinity at different temperatures. The samples were first scanned to ascertain their crystallinity before annealing. The weight fraction ratio of anatase to rutile was determined for each temperature investigated. This ratio was then used in conjunction with other observed parameters, to inform the annealing temperature of the remaining samples. Here, the hot stage investigation is presented first, followed by ascertaining the crystallinity of each sample composition once annealed in *section 4.1.3.4*. In this section, the as-deposited sample is shown, followed by a baseline-corrected hotstage investigation with background counts removed, then the amount of anatase to rutile is displayed and finally the weight ratio for each temperature is tabulated.

For the pure titanium dioxide samples, batch one was crystalline as-deposited, before any increase in temperature using the hot stage (Figure 49).
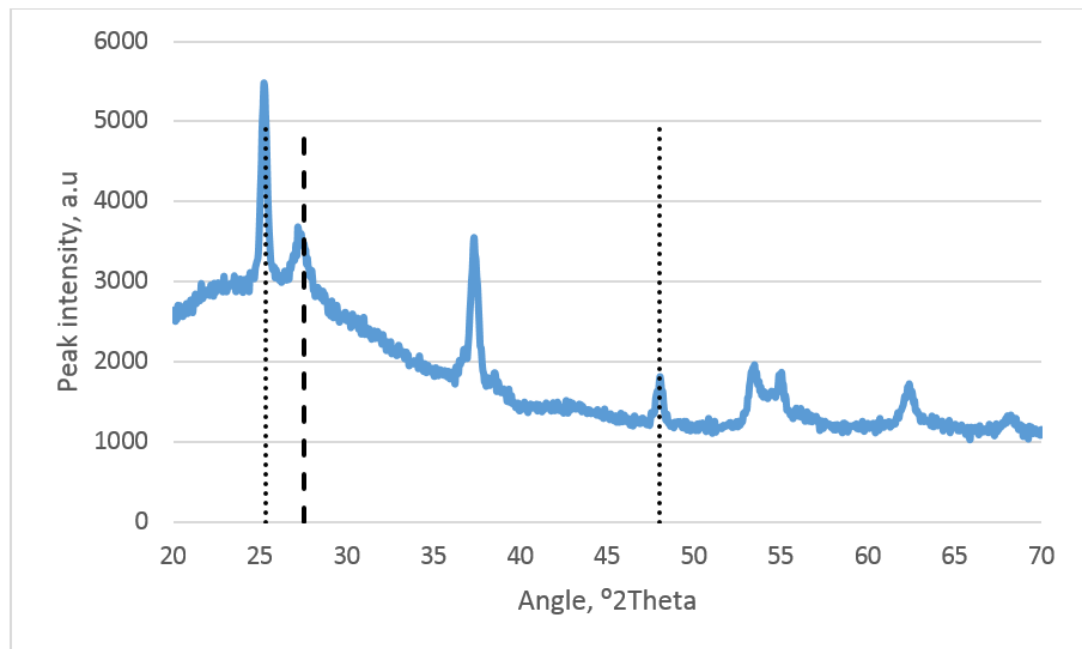
Figure 49: Representative XRD pattern of batch one as-deposited titanium dioxide coatings on glass coupons. Characteristic anatase 101 (25.3⁰) and 200 (48⁰) peaks are shown with a dotted line and the rutile 110 (27.4⁰) peak with a dashed line. Peaks can be observed at these angles, suggesting a crystalline as-deposited mixed-phase material.

The presence of anatase and rutile peaks indicates that the deposition process was more energetic than anticipated; using the model developed by Kelly and Arnell (2000), this can be attributed to an excessively high homologous temperature of the substrate during deposition, an overly high argon ion to deposition atom ratio, or an extreme average ion energy. An excess in these parameters can cause recrystallization during deposition. While this effect has applications in industrial-scale productions (as crystallinity developed during deposition reduces the need for a distinct annealing process, reducing associated costs), it can also introduce excessive intrinsic (and thermal, if the excessive parameter is the homologous temperature) stresses into the film. These stresses may contribute to film failure and delamination, poor adhesion, small grain size, or excess growth of crystals in a non-preferential orientation (Gautier *et al.*, 2001) .

Due to the pre-existing crystallinity, there was only a small change in the intensity of the anatase peak with annealing, but development of a rutile peak can be seen with increasing annealing temperature (Figure 50).
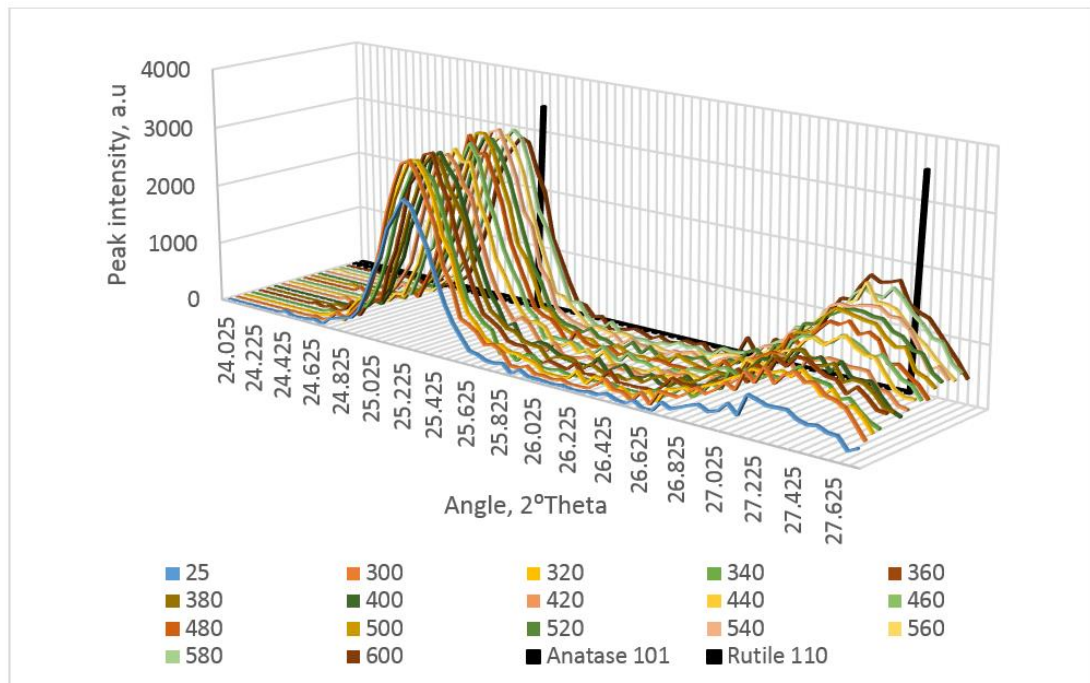
Figure 50: Hot stage XRD pattern of batch one titanium dioxide coatings. The anatase 101 (25.3⁰) and rutile 110 (27.5⁰) peaks are indicated by vertical black lines. There is little change in peak intensity for the anatase peak between annealing temperatures, but a development of a small rutile peak, indicating a crystalline as-deposited material.

Although little change was observed in Figure 51, increasing the annealing temperature resulted in a weak increase in the intensity of the anatase peak (R^2=0.44, p<0.0001) and a stronger increase in the intensity of the rutile peak (R^2=0.84, p<0.0001). Interesting to note is that while increasing the temperature tended to increase the intensity of the anatase peak, the highest temperatures clearly do not produce the most intense peaks – this could imply that these structures are converting to the rutile phase, suggesting that even with pre-existing crystallinity, annealing will still induce crystal change from anatase to rutile.
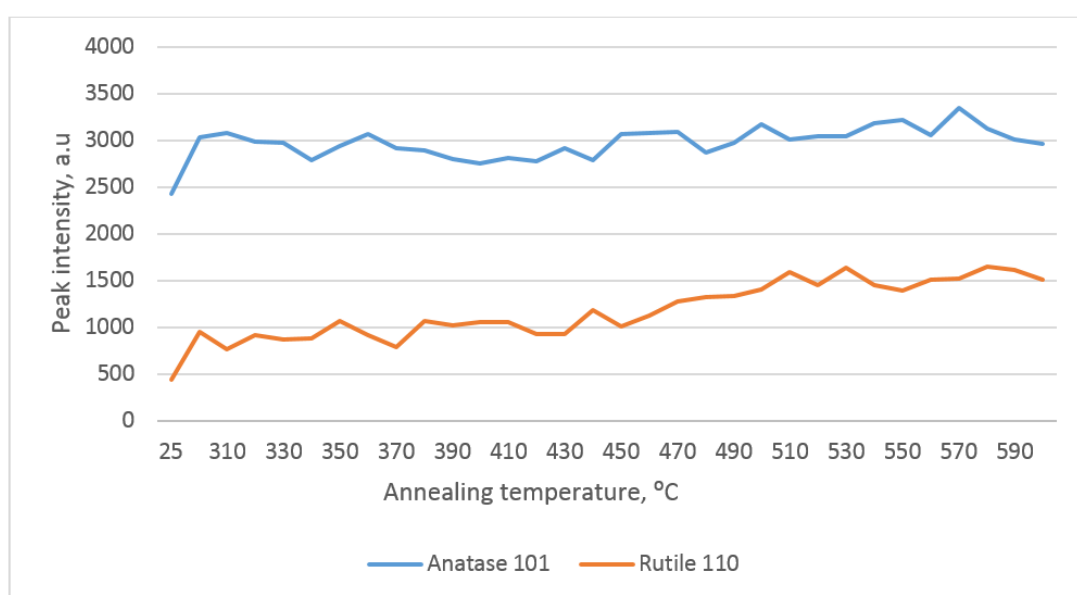
Figure 51: Change in the anatase 101 peak intensity (blue) and rutile 110 peak intensity (orange) of batch one titanium dioxide coatings with temperature. There was relatively little change in peak intensity with temperature due to the pre-existing crystallinity.

As the film was already crystalline, thermal treatment via annealing did not did not improve the anatase: rutile weight fraction ratio. Indeed, the highest anatase fraction was obtained without annealing, at 25 ^{0}C. This information, along with similar for each composition investigated, is provided in tabulated form in *Appendix B*.

When the second batch of pure titanium dioxide coatings were investigated, no crystallinity was observed before the hot stage process (Figure 52).
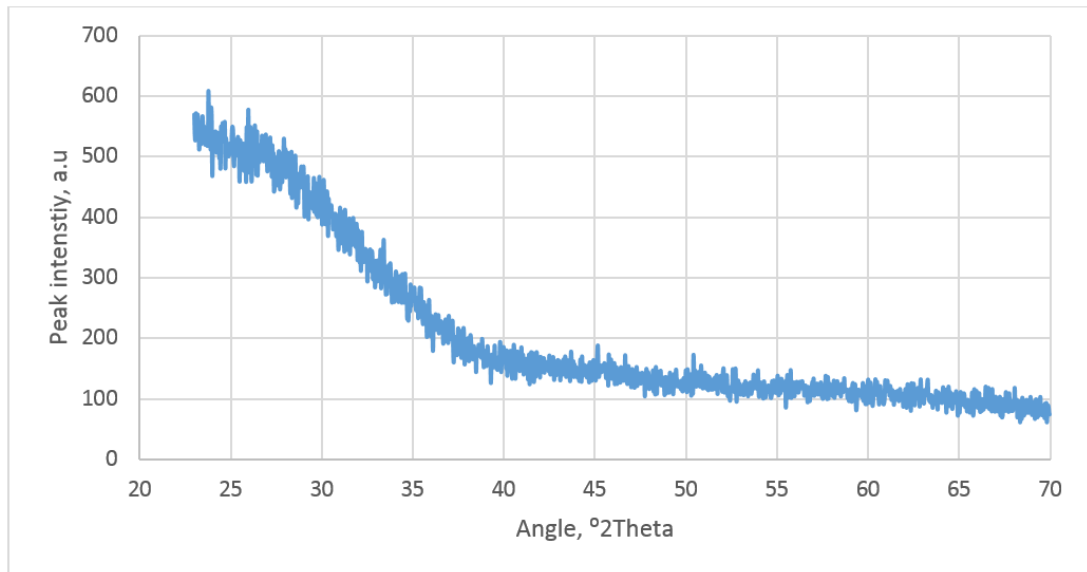
Figure 52: Representative XRD pattern of as-deposited batch two titanium dioxide coatings on glass coupons. No crystallinity was observed.

The absence of crystallinity is not unexpected, as previous batches coated using rig A were not crystalline as-deposited either. This implies that the deposition process was not overly energetic or stressful to the film.

The hot stage XRD scan shows the development of the anatase 101 peak; no rutile development was observed (Figure 53).
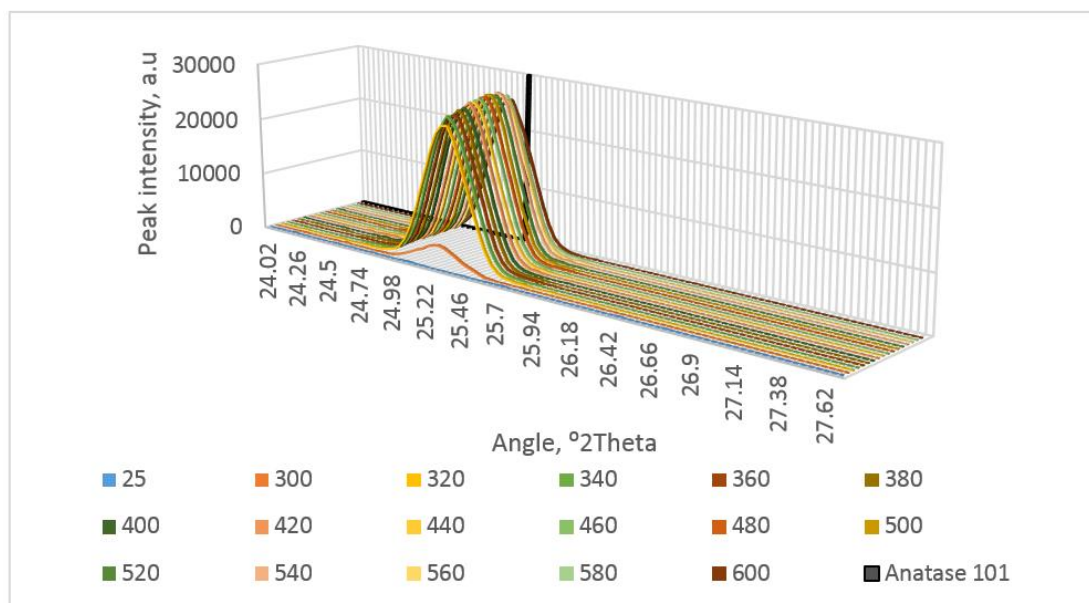
Figure 53: Hot stage XRD pattern of batch two titanium dioxide coatings. The anatase 101 (25.3^0) peak is indicated by a vertical black line. Annealing the sample induced anatase crystallinity, but did not induce rutile crystallinity.

Anatase crystallinity was rapidly induced between 300 ^{0}C and 320 ^{0}C. After this initial rapid increase in intensity, a temperature zone of slower increase

was noted between 320 ^{0}C and 460 ^{0}C, after which the intensity of the peak plateaued and began to decrease slightly (Figure 54).
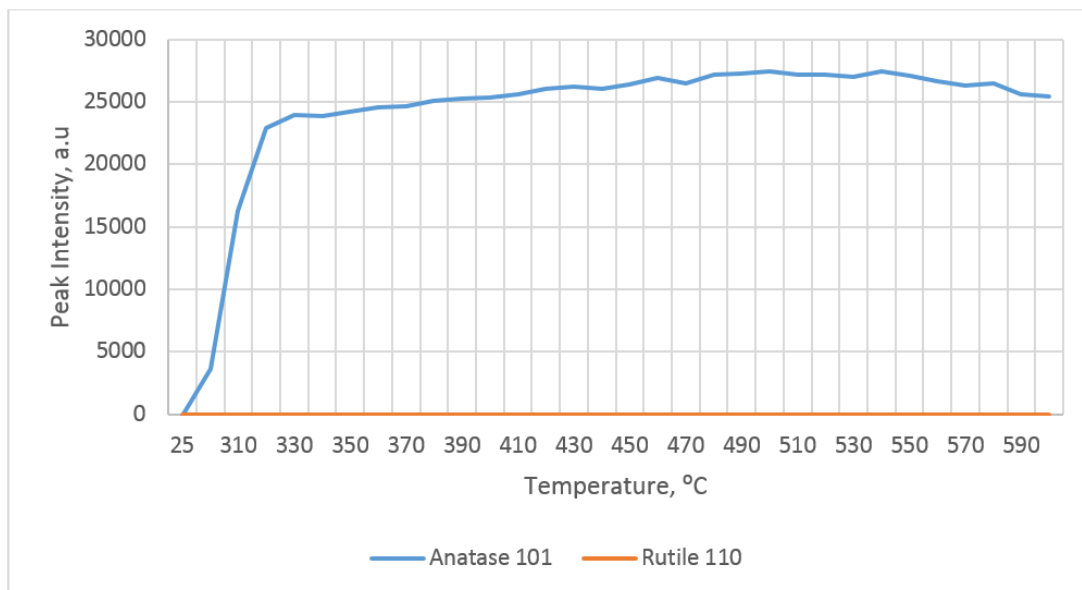
Figure 54: Change in anatase 101 peak intensity (blue) and rutile 110 peak intensity (orange) of batch two titanium dioxide coatings with temperature. The anatase peak rapidly developed from 25 ^{0}C to 320 ^{0}C, after which it plateaued. No changes were observed in the intensity of the rutile peak.

After the initial increase in crystallinity (after 340 ^{0}C), a small significant correlation between the peak intensity and annealing temperature was observed, despite the slight reduction above 550 ^{0}C (R^2=0.55, p<0.0001).

At all annealing temperatures, the weight fraction ratio was 1, indicating a negligible amount of rutile present. Therefore, there is no single optimum temperature, rather several appropriate annealing temperatures could be considered.

When the niobium-doped titanium dioxide samples were investigated, no crystallinity was observed before the hot stage processes for either batch (Figure 55).
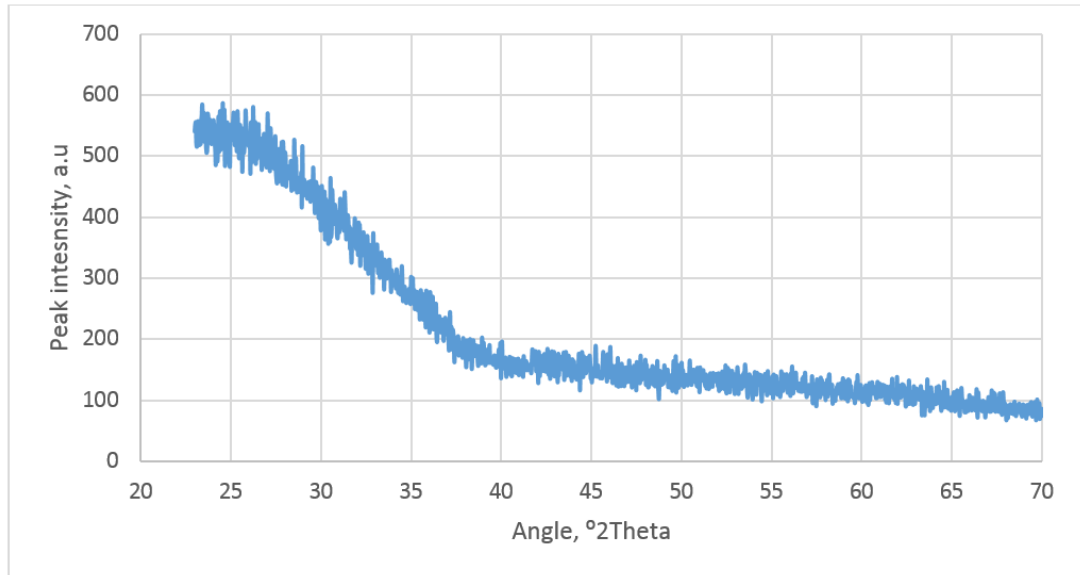
Figure 55: Representative XRD pattern of as-deposited niobium-doped titanium dioxide coatings on glass coupons. No crystallinity was observed.

Similar to the second batch of titanium dioxide samples, hot stage scanning of the niobium-doped titania coatings showed the development of the anatase 101 peak (Figure 56).
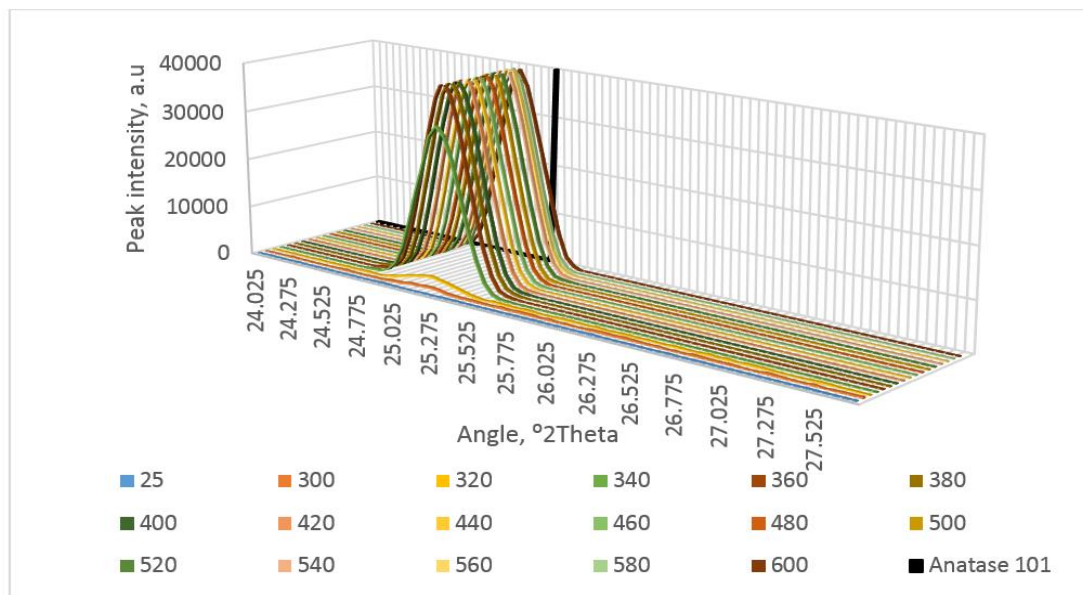
Figure 56: Representative hot stage XRD pattern of the niobium-doped titanium dioxide coatings. The anatase 101 (25.3^0) peak is indicated by a vertical black line. Annealing the sample induced anatase crystallinity but did not induce rutile crystallinity.

The first batch of niobium-doped coatings behaved in a similar manner to the second batch of titanium dioxide samples, developing strong anatase crystallinity between 300 ^{0}C and 350 ^{0}C (R^2=0.89, p=0.005), after which it plateaued with a slight decrease with increasing annealing temperature (R^2=0.61, p<0.0001) (Figure 57). No rutile peak developed during annealing.
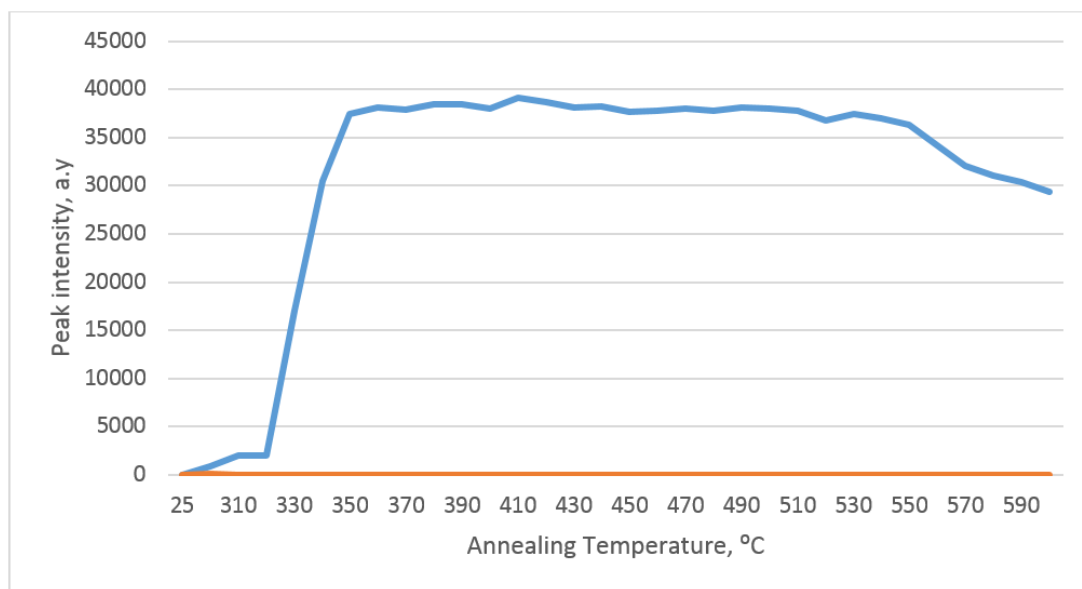
Figure 57: Change in anatase 101 peak intensity (blue) and rutile 110 peak intensity (orange) of batch one niobium-doped titanium dioxide coatings with temperature. Development of the anatase peak was delayed until 320 ^{0}C, where it then developed rapidly until 350 ^{0}C, after which it plateaued. No changes were observed in the rutile peak intensity.

However, for these samples, there was a slight delay in the development of the anatase peak – in pure titania, the peak began to rapidly develop at 320 ^{0}C, whereas in this batch of niobium-doped titania, rapid anatase development occurred between 320 ^{0}C and 350 ^{0}C. Additionally, there was a decrease in peak intensity above 530 ^{0}C, which suggests that, while no rutile phase was formed, the anatase crystals may have decreased in size. This adds to the argument that higher annealing temperatures negatively affect anatase crystallinity (Nakaruk *et al.*, 2010).

Despite the higher temperature required to induce the anatase peak compared to pure titania, this batch of niobium-doped titania exhibited strong anatase crystallinity and when annealed above 310 ^{0}C, had weight ratio of 1, indicating the absence of rutile phase. Therefore, as with mentioned for pure titania, several annealing temperatures could be considered.

The second batch of niobium-doped titania samples responded similarly to annealing; anatase peak intensity rapidly developed between 310 ^{0}C and 330 ^{0}C (R^2=0.9991, p=0.019) before plateauing, preceding a slight decrease with increasing annealing temperature (R^2=0.81, p<0.001) (Figure 58).
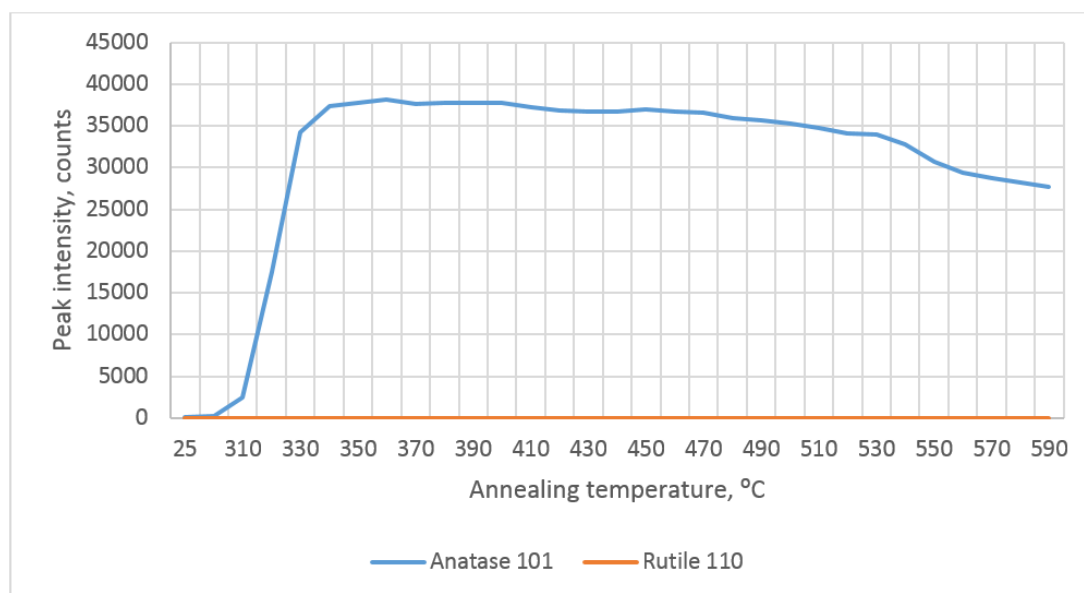
Figure 58: Change in anatase 101 peak intensity (blue) and rutile 110 peak intensity (orange) of batch two niobium-doped titanium dioxide coatings with temperature. Development of the anatase peak was delayed until 310 ^{0}C, where it then developed rapidly until 340 ^{0}C, after which it plateaued. No changes were observed in the rutile peak intensity.

No rutile peak was observed over the range of annealing temperatures and so similar to the first batch of niobium-doped titania coatings and the pure titania coatings, several temperatures could be considered at which to anneal the coating. Despite this, it was again noticed that the increasing temperature led to a reduction in peak intensity; while the reduction with temperature began at around 460 ^{0}C, a more pronounced reduction was seen at around 530 ^{0}C, in agreement with the first batch of niobium-doped titania samples and the second batch of pure titania samples from this set.

It is interesting that anatase crystallinity is strong at such low annealing temperatures for the second batch of TiO_2 coatings and the niobium-doped coatings, with strong crystallinity achieved between 320 ^0C – 350 ^0C; anatase crystallinity is usually observed at around 400 ^0C – 600 ^0C (Hanaor and Sorrell, 2011; Lin *et al.*, 2013). Coatings such of these have immense potential for industrial applications, as the reduction in cost associated with annealing at high temperatures (especially for large-scale operations) is valuable.

When the first batch of molybdenum-doped coatings were investigated, no crystallinity was observed before the hot stage process (Figure 59).
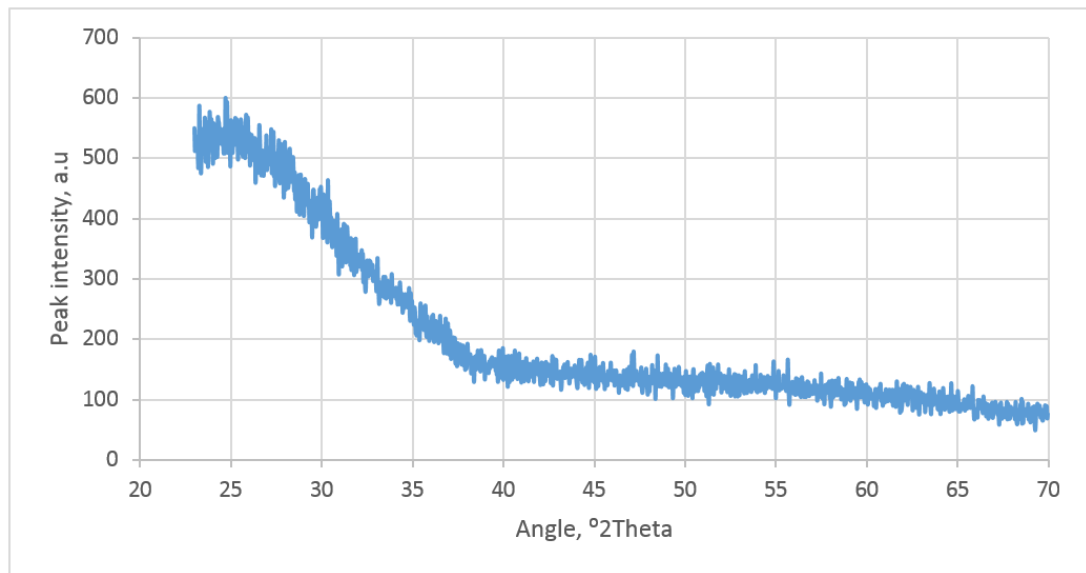
Figure 59: Representative XRD pattern of as-deposited batch one molybdenum-doped titanium dioxide coatings on glass coupons. No crystallinity was observed.

Once hot stage investigation commenced, the development of the anatase 101 peak at 24.7^0 and the rutile 110 peak at 27^0 can be clearly seen (Figure 60).
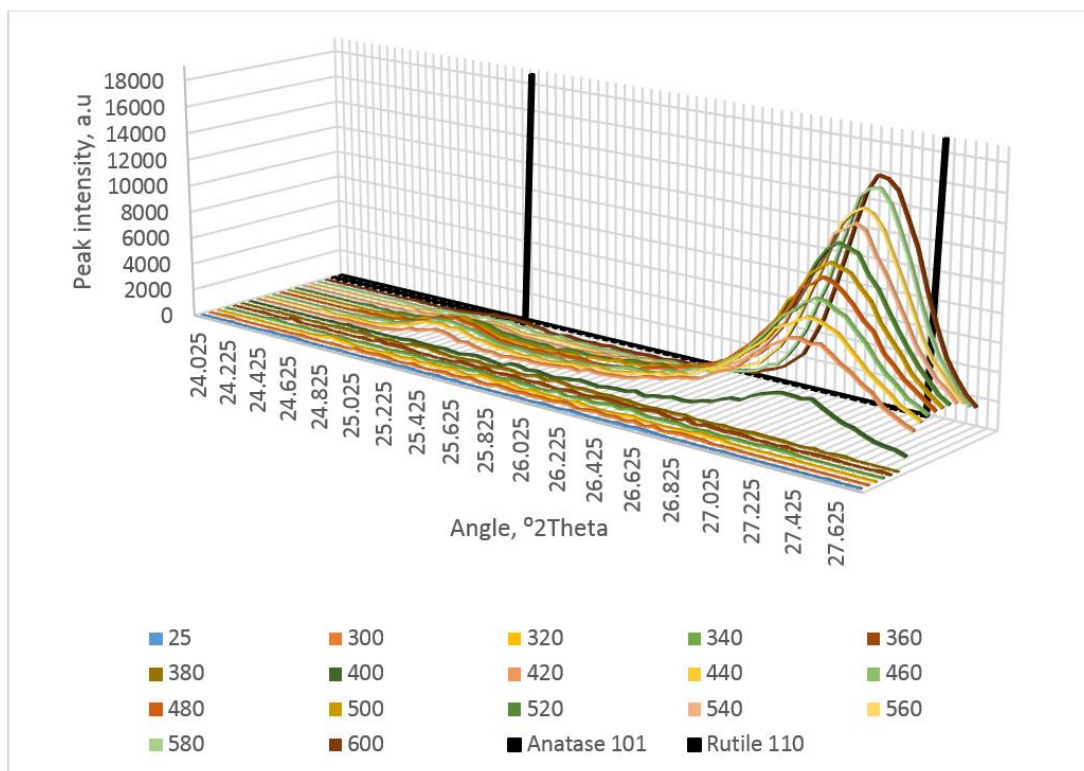
Figure 60: Hot stage XRD pattern of batch one molybdenum-doped titanium dioxide coatings. The anatase 101 (25.3⁰) and rutile 110 (27.5⁰) are indicated by vertical black lines. Annealing the sample induced little anatase crystallinity, but induced rutile crystallinity to a greater extent.

No crystallinity was observed before 380 ^{0}C, as opposed to the previous coating compositions which exhibited crystallinity at much lower temperatures, i.e., with less thermal energy input. Interestingly, the sample did not seem to progress through amorphous, then anatase, then rutile with increasing annealing temperature, as is typical (Mathews *et al.*, 2009; Nakaruk *et al.*, 2010); the crystallinity seemed to skip the anatase phase and transition directly into rutile (Figure 61).
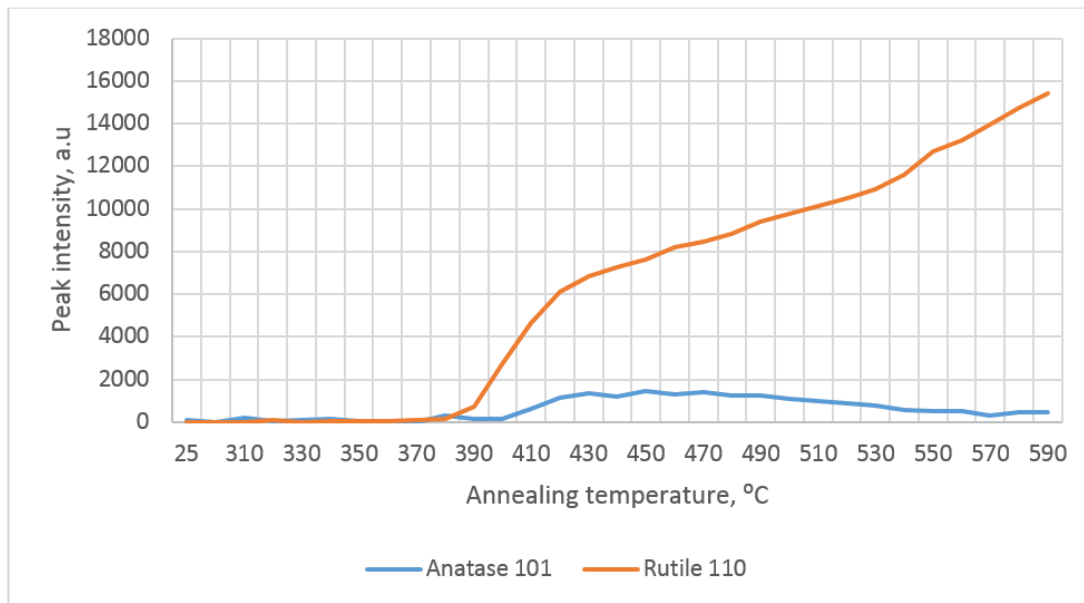
Figure 61: Change in anatase 101 peak intensity (blue) and rutile 110 peak intensity (orange) of batch one molybdenum-doped titanium dioxide coatings with temperature. The development of anatase and rutile crystallinity was delayed in these samples, with a rutile peak forming at around 380 ^{0}C and an anatase peak forming at 400 ^{0}C. The rutile peak proceeded to increase, whereas the anatase peak was suppressed.

A rutile phase developed at around 380 ^{0}C, before a small anatase peak developed at 400 ^{0}C. Between 390 ^{0}C and 430 ^{0}C, the rutile 110 peak increased in intensity rapidly (R^2=0.94, p=0.001), while the anatase peak increased marginally (R^2=0.86, p=0.007). After this rapid increase, the rutile peak increased more slowly in intensity (R^2=0.98, p<0.0001). This is in contrast to the anatase peak intensity, which then decreased in intensity with increasing annealing temperature after 450 ^{0}C (R^2=0.3, p<0.043).

Due to the delayed onset of the crystallinity, no weight ratio data were obtained before 380 ^{0}C. After crystallinity began to develop around 390 ^{0}C, the rutile peaks developed much more rapidly than the anatase – the highest weight ratio after development of crystallinity was 0.137, indicating very low levels of anatase compared to rutile – this was found at an annealing temperature of 430 ^{0}C. As there was never more anatase than rutile present in the sample, these samples are difficult to compare with other samples in the set.

Similarly, when the second batch of molybdenum-doped titanium dioxide coatings were investigated, no crystallinity was observed prior to annealing (Figure 62).
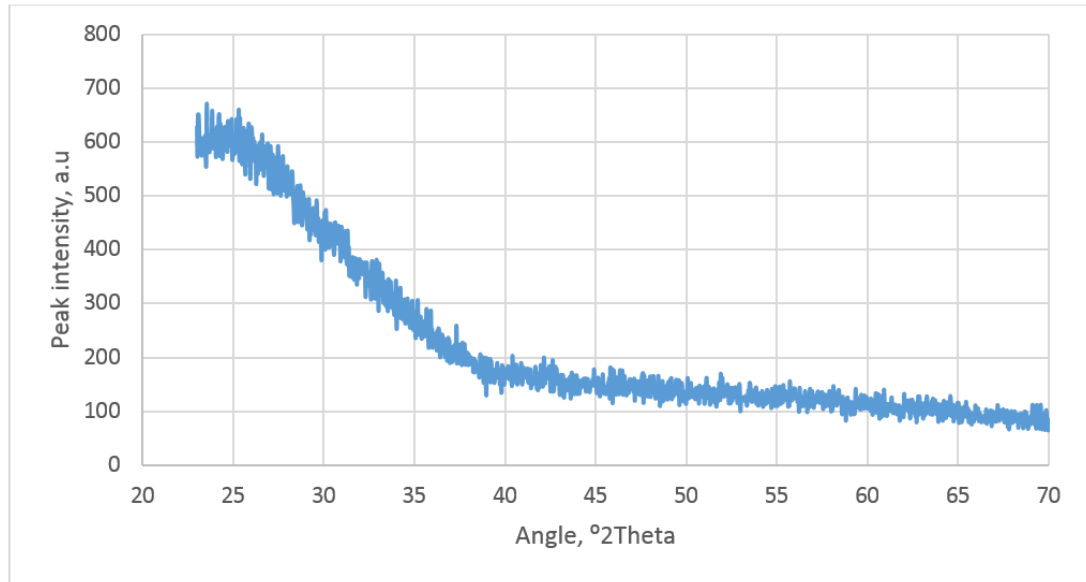
Figure 62: Representative XRD pattern of as-deposited batch two molybdenum-doped titanium dioxide coatings on glass coupons. No crystallinity was observed.

Upon hot stage investigation, development of both anatase 101 and rutile 110 peaks were observed (Figure 63).
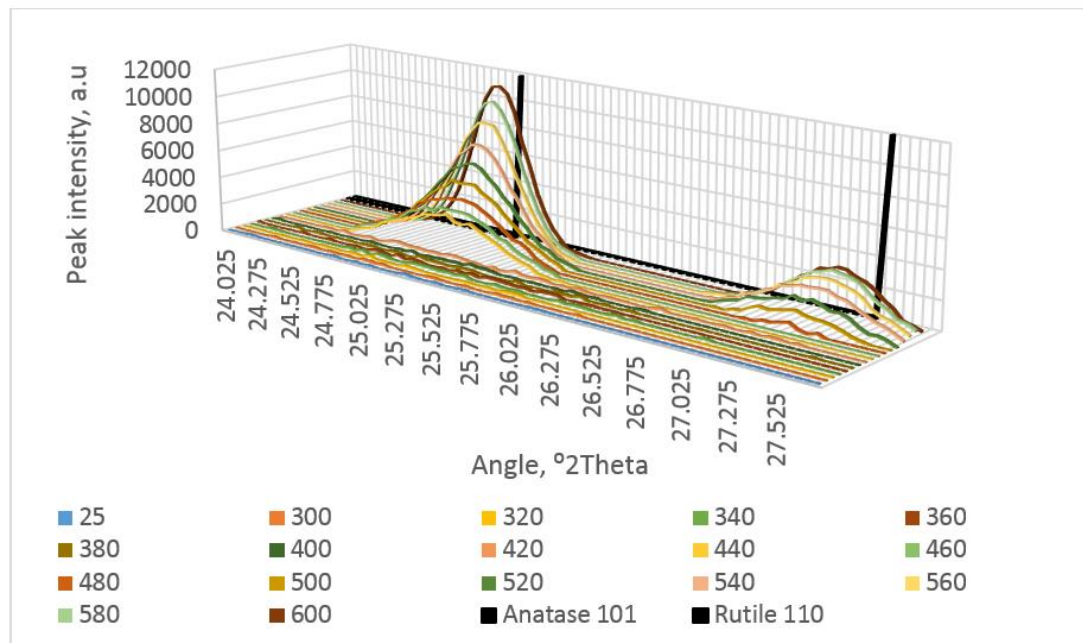
Figure 63: Hot stage XRD pattern of batch two of the molybdenum-doped titanium dioxide coatings. The anatase 101 (25.3^0) and rutile 110 (27.5^0) are indicated by vertical black lines. Annealing the sample induced anatase crystallinity and rutile crystallinity.

Similar to the first batch of molybdenum-doped samples, the second batch of molybdenum-doped titania required a considerably higher annealing temperature to develop crystallinity, only exhibiting an anatase peak after 420 ^{0}C and a rutile peak after 480 ^{0}C. Indeed, it was observed that from 300 ^{0}C to 420 ^{0}C, the intensity of either peak did not increase with annealing temperature (anatase: R^2=0.153, p=0.18; rutile: R^2=0.002, p=0.89) (Figure 64). After this temperature, the intensity of the anatase 101 peak rapidly increased, plateaued and then increased approximately linearly from 460 ^{0}C onwards (R^2=0.98, p<0.001). The intensity of the rutile peak increased from 470 ^{0}C to 580 ^{0}C (R^2=0.97, p<0.001), after which it plateaued.
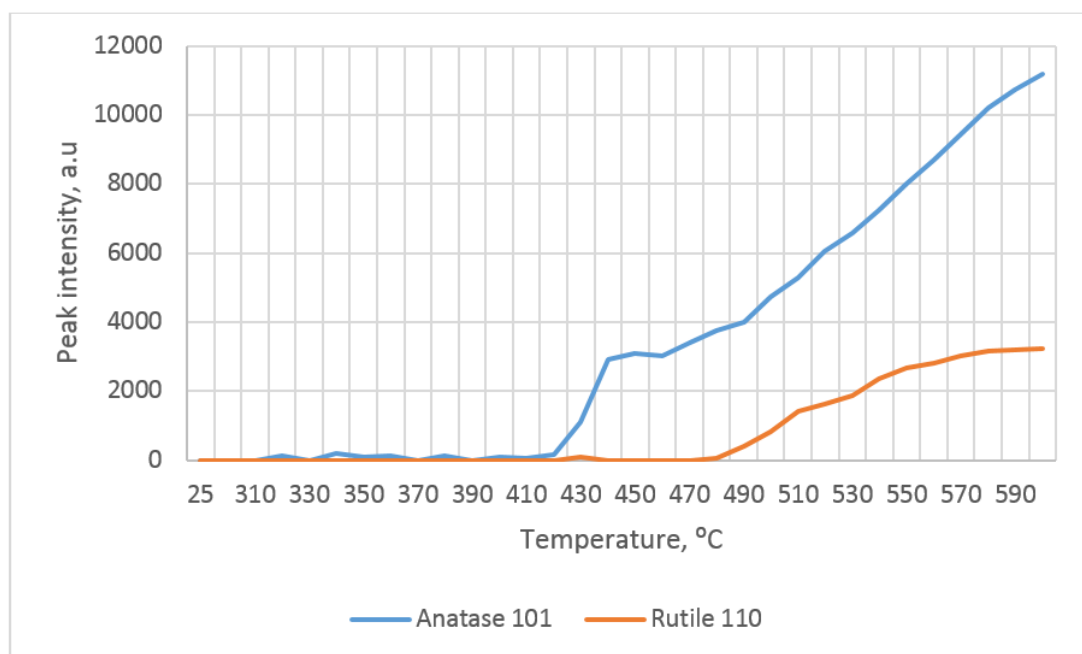
Figure 64: Change in anatase 101 peak intensity (blue) and rutile 110 peak intensity (orange) of batch two of the molybdenum-doped titania coatings with temperature. The development of anatase and rutile crystallinity was delayed in these samples, with an anatase peak forming at around 420 ^{0}C and a rutile peak forming at 480 ^{0}C. The anatase peak increased rapidly at first, then plateaued and then increased again. The rutile peak had a slower, more gradual increase and so was overall less intense than the anatase peak.

Due to the delayed onset of the crystallinity, no weight ratio data were obtained before 420 ^{0}C. In contrast to the first batch of molybdenum-doped coatings, this batch exhibited the typical phase transitions with annealing temperature – amorphous, through anatase, then rutile. There were therefore annealing temperatures that led to developments of different crystal phases and crystal phase mixtures. Within these temperatures, there was a range of

optimum annealing temperatures, 440 ^{0}C – 500 ^{0}C, that yielded a weight ratio of 1, implying negligible rutile content.

4.1.3.4 – Crystallinity; XRD confirmation

After the temperature(s) that yielded the highest weight ratios of anatase to rutile was ascertained, the final annealing temperatures for the remaining samples was selected. The selection was informed by the hot stage XRD investigation and other observations from previous coating sets.

The pure titania coatings were annealed at 590 ^{0}C. Despite the first batch of pure titania coatings being crystalline as-deposited and hot stage investigation indicating that further thermal treatment did not increase the weight fraction of anatase: rutile, this batch was annealed at the same temperature as the second batch of pure titania coatings. This temperature was chosen for batch two as it yielded a weight ratio of 1, indicating a negligible rutile content. In addition, annealing at 590 ^{0}C allowed a fairer comparison with Set 1 stainless steel samples, which were annealed at 600 ^{0}C. In this way, other observations between the coatings could be made more easily, such as ease of delamination. Upon annealing both sets of coatings at 590 ^{0}C, representative samples were analysed.

When batch one was analysed, the peak intensity for both anatase 101 and rutile 110 was found to be relatively small, indicating poor quality crystals, with small grain size (Figure 65). In addition, the peaks appear to be on top of a shoulder. This may due to the glass substrate used – the incident X-ray may have penetrated through the entire coating and the detector received reflected X-rays from the amorphous substrate below. However, it is more likely that due to the low intensity of peaks, there was a low signal-to-noise ratio, and so the background noise is visible as a 'shoulder'.

Alternatively, the shoulder could be due to peak broadening effects, which indicate small, poor quality crystals (Hanaor and Sorrell, 2011; He *et al.*, 2018; Niu *et al.*, 2018). The poor crystallinity observed was not unexpected, as the crystalline as-deposited coatings were likely to contain high levels of intrinsic stress, as the parameters that are conducive to forming crystalline as-deposited coatings are the same parameters than commonly lead to stresses. For this batch, the anatase – rutile weight ratio was 0.48, indicating a weight content of 48 % anatase and 52 % rutile.
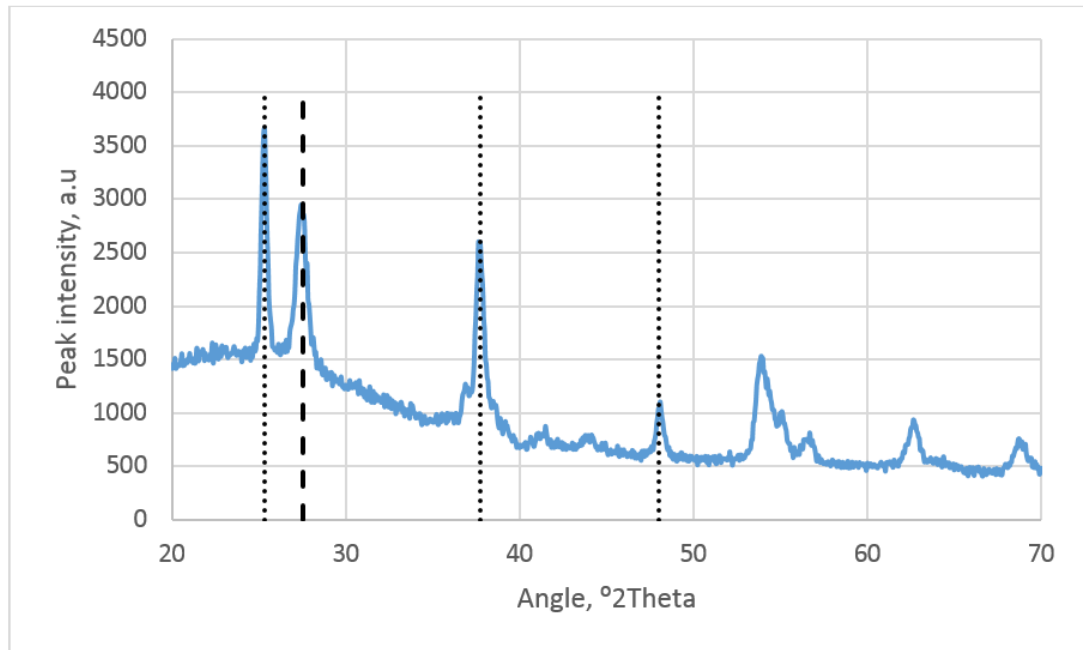
Figure 65: Representative XRD pattern of batch one pure titania coatings, annealed at 590 ⁰C. The anatase 101 (25.3⁰), 004 (38⁰) and 200 (48⁰) peaks are indicated by a dotted line, while the rutile 110 (27.5⁰) peak is indicated with a dashed line. Crystallinity was observed to be both anatase and rutile, indicating a mixed-phase material.

When batch two was analysed, the peak intensity for the anatase 101 peak was found to be much higher, indicating large crystals in the preferred orientation, with few grain boundaries. No distinctive rutile peaks were observed (Figure 66).
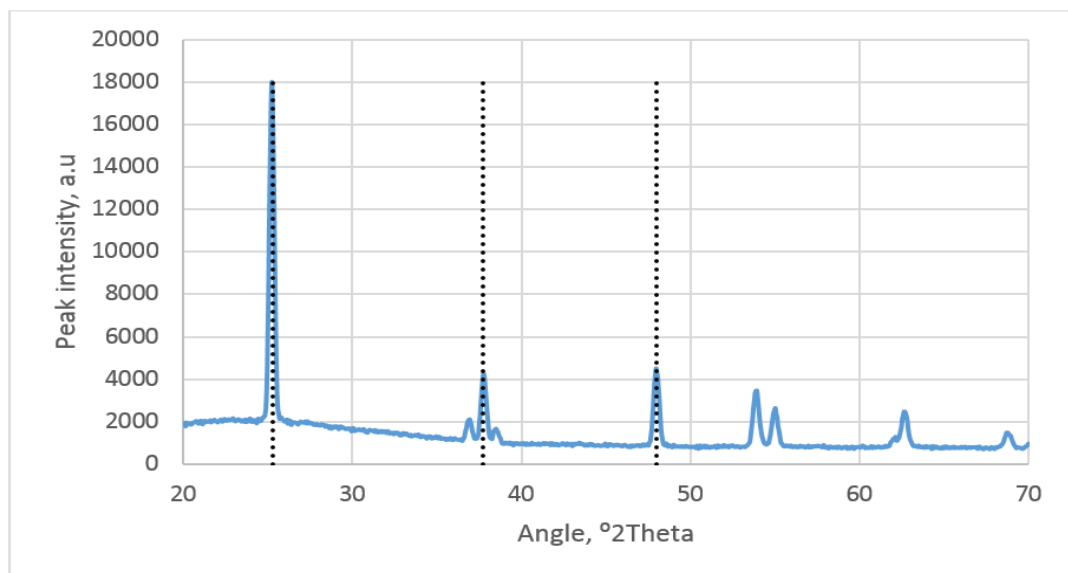
Figure 66: Representative XRD pattern of batch two pure titania coatings, annealed at 590 ⁰C. The anatase 101 (25.3⁰), 004 (38⁰) and 200 (48⁰) peaks are indicated by a dotted line. Crystallinity was observed at these angles, indicating an anatase material.

The niobium-doped coatings had a range of optimum temperatures, where the anatase – rutile weight ratio implied negligible rutile content. Of these temperatures, 520 ^{0}C was used to anneal the samples. This was chosen as the XRD peak for this temperature was sharp, indicating large, high-quality crystals.

After annealing the batches, the crystallinity was found to be highly anatase, with few grain boundaries and large crystals. No rutile peaks were observed (Figure 67). This is similar to the response seen from the second batch of pure titania coatings, suggesting that TiO_2 batch one had a distinct process to batch two and the niobium-doped coatings.
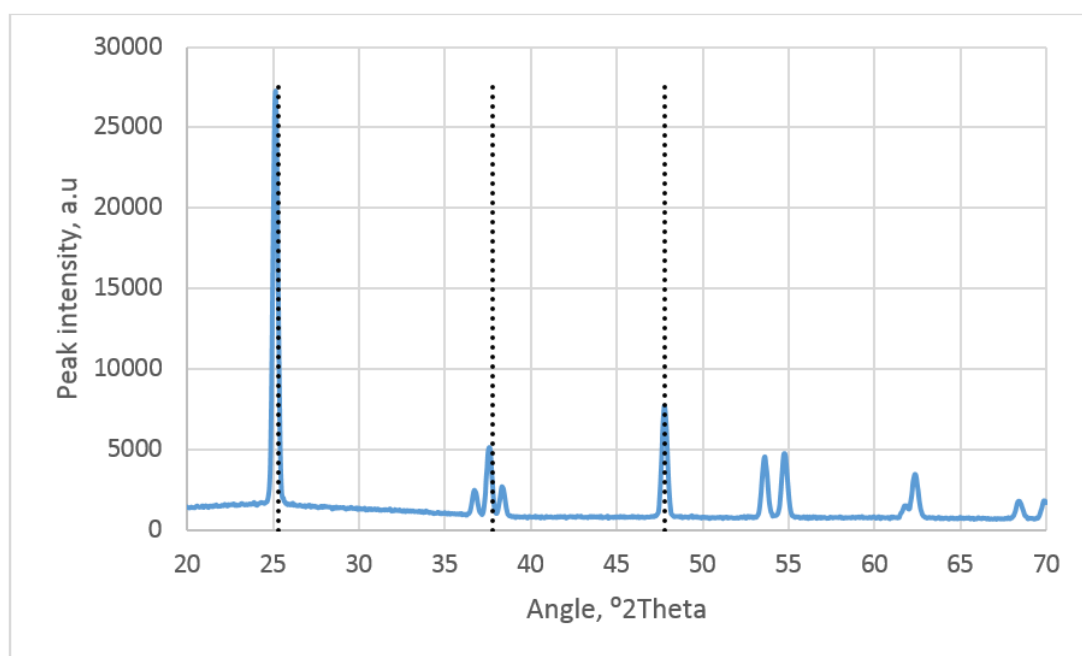
Figure 67: Representative XRD pattern of the niobium-doped titania coatings, annealed at 520 ^{0}C. The anatase 101 (25.3^0), 004 (38^0) and 200 (48^0) peaks are indicated by a dotted line. Crystallinity was observed at these angles, indicating an anatase material.

The first batch of molybdenum-doped titania samples had unusual properties, in that they seemingly bypassed the anatase phase and progressed directly to rutile. As shown in Figure 60 and Figure 61, there was no annealing temperature that yielded more anatase than rutile. Due to this, it was difficult to ascertain whether they were comparable to the other sets and batches produced; they were therefore not annealed or investigated further in this work.

The second batch of molybdenum-doped samples had a range of annealing temperatures that yielded an anatase – rutile weight ratio of 1, indicating negligible rutile content, as shown in Figure 61. Despite this, the samples were annealed at 520 ^{0}C; at this annealing temperature, there was an anatase – rutile weight ratio of 0.75, indicating 75 % anatase and 25 % rutile content by weight. The reason for annealing at this temperature and not the temperature that yielded a higher anatase content, was to provide easier comparison of thermal stress effects with the niobium-doped titania samples; for example, the optical properties and effects on the adhesion.

After annealing at 520 ^{0}C, the crystallinity was found to be mostly anatase, with some rutile present (Figure 68). The weight fraction calculation showed this to be around 70 % anatase and 30 % rutile by weight.
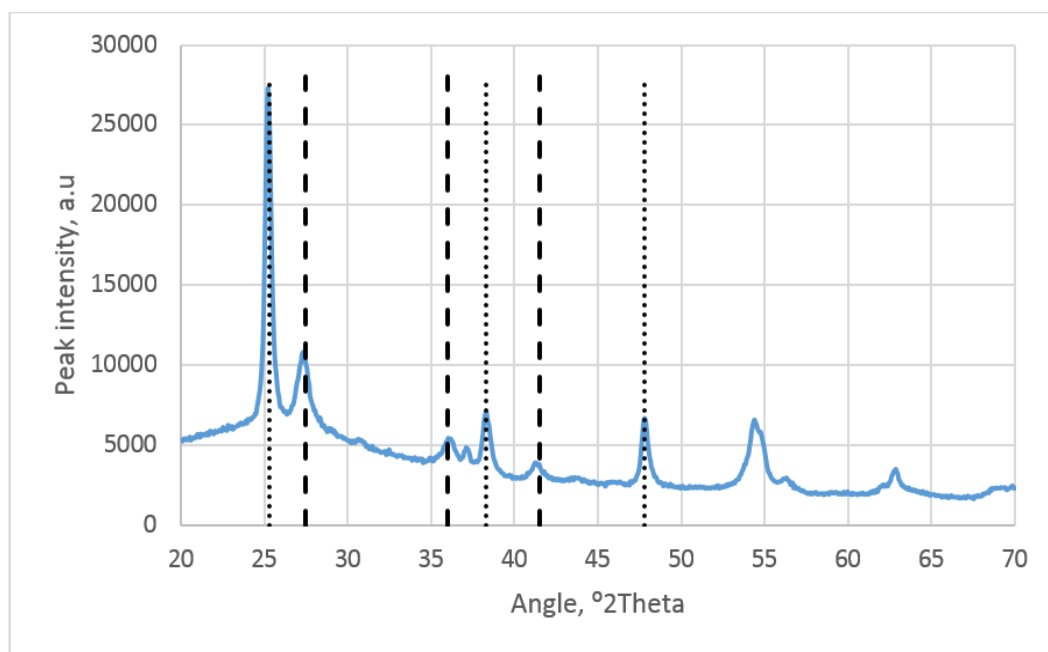
Figure 68: Representative XRD pattern of the molybdenum-doped titania coatings, annealed at 520 ^{0}C. The anatase 101 (25.3^0), 004 (38^0) and 200 (48^0) peaks are indicated by a dotted line, while the rutile 110 (27.5^0), 101 (36.01^0) and 111 (41.5^0) peaks are indicated with a dashed line. Crystallinity was observed to be both anatase and rutile, indicating a mixed-phase material.

From the analysis of these samples, it is clear that annealing temperature can be a critical factor in the development of crystalline films. This development occurs as a nucleation-recrystallisation process and so the dynamics are not immediately obvious (Hanaor and Sorrell, 2011). It is interesting to note that, for the second batch of titania coatings and the

niobium-doped coatings, crystallinity did not significantly change at temperatures above 320 ^{0}C – 350 ^{0}C.

Despite a reduction in anatase peak intensity in the niobium samples above 530 ^{0}C, peak broadening was not observed, so crystallinity was not deemed to be negatively impacted. This, combined with the strong anatase crystallinity observed for the annealing conditions investigated in set 2, led to the conclusion that niobium has a rutile-inhibiting effect on titania. Several authors have noticed the effects of niobium on titania crystallinity, generally agreeing that doping titania with niobium inhibits the transition from anatase crystals to rutile (Arbiol *et al.*, 2002; Kamisaka *et al.*, 2009; Uyanga *et al.*, 2014; Gardecka *et al.*, 2015), corroborating the results found here.

This is in contrast to the molybdenum-doped samples. Across each of the sets, the molybdenum-doped samples have consistently had smaller crystals when compared to the other samples. In addition, doping the titania with molybdenum typically promotes the formation of rutile crystals, sometimes to the complete transition from anatase to rutile. The anatase to rutile transition was also related to the concentration of molybdenum in the coating; higher concentrations promote coatings of more rutile character, implying a progressive distortion of the lattice. This has also been noticed by several authors (Matteucci *et al.*, 2006; Li *et al.*, 2011).

4.1.3.5 – Activity

The samples that showed the highest activity under visible light were the molybdenum-doped samples, with an average activity of 5×10^5 s^{-1}, which was different to control (U=0.0, p=0.037). The second-highest activity was found in niobium-doped coatings, although these showed very low activity; an average activity of 0.8×10^{-5} s^{-1} and 1×10^{-5} s^{-1} for batch one and two respectively. While these were statistically significantly different to the control (U=0.0, p=0.034), they did not have a different average activity to the undoped titania samples (U=10.0, p=0.186), which in turn did not show different activity to control (U=3.0, p=0.48). The differences implied via statistical analysis should be treated with caution, given the similarities in observable performance (Figure 69).
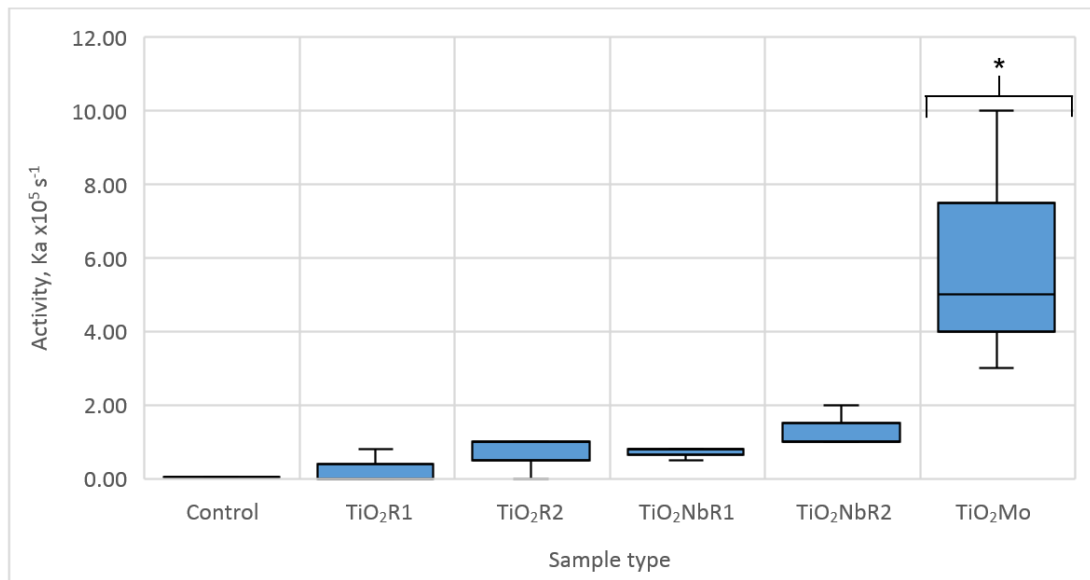
Figure 69: Activity of the set 3 samples as determined by degradation of methylene blue. Brackets and * indicate significant real differences to control (p<0.05) Control: uncoated glass samples as a control. TiO$_2$R1: batch one of the pure titanium dioxide samples. TiO$_2$R2: batch two of the pure titanium dioxide samples. TiO$_2$NbR1: batch one of the niobium-doped titanium dioxide samples. TiO$_2$NbR2: batch two of the niobium-doped titanium dioxide samples. TiO$_2$Mo: molybdenum-doped titanium dioxide samples. The molybdenum-doped titania samples exhibited significantly different activity to control and were the most active samples (p=0.036), followed by the niobium-doped samples. However, despite the niobium-doped samples exhibiting greater activity than control, they did not have significantly different activity to the undoped titania coatings and therefore any differences implied via statistical analysis should be interpreted cautiously. N=3.

It should be noted that delamination and flaking effects were observed with the molybdenum-doped coatings. One possible effect of this delamination

was that the surface area of the active photocatalyst was increased, increasing the number of binding sites for the methylene blue and therefore degrading the dye at a higher rate. This would lead to an artificially high reported photoactivity. Furthermore, the post-depositional damage noticed in the samples in *section 4.1.3.2* may have affected the samples in complex ways; it may have increased the activity of the molybdenum-doped samples by causing low-level delamination and increasing the surface area, but decreased the activity of the niobium-doped samples via the introduction of stresses and recombination centres.

The low activity observed for the pure titanium samples is not surprising, as titanium dioxide photocatalysts are only activated by ultraviolet light (Dalrymple *et al.*, 2010) and this test investigated the response under fluorescent light. However, the niobium-doped samples did not have a significantly different activity to the titania samples, suggesting that doping the titania with niobium did not improve visible light response. Similar results were seen for the niobium-doped samples from set 2, strengthening this conclusion. While this is in contrast to some work (Kaleji *et al.*, 2012; Joshi *et al.*, 2013; Wu *et al.*, 2017), it has been noted by several research groups throughout the literature (Mattsson *et al.*, 2006; Kaleji *et al.*, 2013; Yin *et al.*, 2016) and warrants further investigation.

This is especially interesting when considering the crystallographic properties of the niobium-doped coatings compared to the molybdenum-doped coatings. As in set two, the niobium-doped titanium dioxide coatings exhibited a higher anatase – rutile ratio and larger crystals, than the molybdenum-doped coatings, yet had consistently much lower activity. Indeed, the activity was rarely much better than the control for these samples. This suggests that the quality and size of the crystals or the amount of anatase present in the sample compared to rutile is not the ultimately governing factor in determining visible-light photoactivity. Furthermore, the 9 %at. molybdenum-doped samples in set 2 had the highest activity of all samples tested, despite having the worst crystallinity – almost 100 % small-crystallite rutile. Similar results were found by (Sreedhar *et al.*, 2017), who determined that above 1.5 %at. molybdenum, anatase crystallinity is

significantly impacted – yet activity improved with increasing concentration despite this. This has several implications.

Firstly, there is currently debate in the literature regarding the optimum anatase – rutile ratios. Some authors (Allen *et al.*, 2005; Batzill, 2011; Xu *et al.*, 2011; Luttrell *et al.*, 2014) have found that pure anatase photocatalysts yield higher photoactivity, while others (McEvoy *et al.*, 2013; Kaleji *et al.*, 2017) indicate that some optimum anatase-rutile mix yields higher activity. The results obtained in this study suggest that, provided the titania is crystalline, then several other factors can contribute to the photoactivity with complex dynamics. This is further evidenced when comparing the 9 %at. molybdenum coatings from set two with the equivalent coatings from set 3; there was only a 1 %at. difference in molybdenum content but an order of magnitude difference in activity (8×10^{-4} s^{-1} for set 2, 5×10^{-5} s^{-1} for set 3). This is interesting, as the set 2 coating in question had very small crystals, primarily in the rutile phase. What is clear is that activity is not a function of crystallinity alone; indeed, once there exists a crystal structure, other factors (discussed in *section 1.2*) seem to play greater roles in the overall activity of titania photocatalysts.

Secondly, the dynamics of the dopants could be considered. Both molybdenum and niobium have been thought to substitute for titanium in the titanium dioxide lattice, as their radii and valence are similar to titanium – a comparison is shown in Table 4.

Table 4: Comparison of the size and valence of titanium, niobium and molybdenum. The atomic radii are similar in size and increase in size with increasing valence.

Atom	Atomic radii, pm	Valence
Titanium	136	4
Niobium	137	5
Molybdenum	145	6

Indeed, there is considerable literature supporting the substitution of both molybdenum (Guo *et al.*, 2013; Wang *et al.*, 2013; Khan and Berk, 2014) and niobium (Michalow *et al.*, 2012; Uyanga *et al.*, 2014; Gardecka *et al.*, 2015).

Molybdenum has been found to improve activity by red-shifting the bandgap of titania. As the radius of molybdenum is similar to titanium, there is generally a minimum lattice distortion (at low dopant concentrations) when the dopant's *d* orbitals hybridise with the base structure's oxygen *p* orbitals. The effect of this is that the distance between the titanium atoms and oxygen atoms decreases after doping with molybdenum, implying that the covalent character of the bond was reduced, making it more ionic. Covalent bonds are then formed between molybdenum and oxygen, permitting the molybdenum to exist in multiple oxidation states (Lu *et al.*, 2018b). Further studies indicate that the molybdenum exists in several oxidation states [4+, 5+, 6+] within the titania crystal, which is thought to permit extensive hole scavenging and electron donation, with a 'cyclic' pattern (Nguyen *et al.*, 2015; Yoon *et al.*, 2018).

Additionally, surface-level molybdenum can act as charge trapping centres, preventing carrier recombination. This charge trapping can occur by either 'shuttling' electrons away from the hole or creating 'wells'. The work of Dargahi *et al.* (2018) suggests that the redshifting effects of molybdenum are beneficial, but more attention must be paid to the recombination sites. They propose that carbonaceous compounds have the potential to 'hold' electrons, so reduced graphene oxide was used as a substrate for the molybdenum-doped titanium dioxide. In this way, the titanium dioxide crystals produce the e-h pair, the doped molybdenum provides the above-mentioned cyclical hole-scavenging electron-donating process, which is complemented by the shuttling and holding of the electron by the reduced graphene oxide substrate.

These complementary processes were also investigated by Khan *et al.* (2018), who found similar results. However, they found that increasing the molybdenum dopant concentration above 1% blue-shifted the bandgap, reducing activity. Several authors have found this – above a critical coating concentration, molybdenum leads to a reduction in photoactivity (Devi and

Murthy, 2008; Wang *et al.*, 2013; Khan and Berk, 2014). This is in contrast to the results of (Sreedhar *et al.*, 2017) and this study, where the coatings with the highest molybdenum content consistently had the highest photoactivity. One explanation might be that the majority of research groups use sol-gel or CVD fabrication techniques to produce their coatings. These methods, while useful, can lead to porous, zone 1/T/2 coatings. Additionally, with these methods, dopants added above a soluble concentration can actually precipitate inside the crystals instead of substituting into the lattice, as was noticed by Khan *et al.* (2018). This contrasts with the magnetron sputtering method used here and by Sreedhar *et al.* (2017), which typically only produces zone 2/3 coatings. Additionally, as limits of solubility are not applicable to physical vapour deposition processes, due to their non-equilibrium nature, much higher dopant concentrations can be realised without corresponding precipitation effects. Therefore, the negative results observed with high molybdenum concentrations may be an effect of secondary processes, which are reduced with magnetron sputtering techniques.

In contrast to the consensus that molybdenum doping improves visible light response, the literature is conflicted on the role of niobium. While some authors dispute the substitution of titanium by niobium in the lattice (Kamisaka *et al.*, 2009; Gardecka *et al.*, 2015), finding the clusters of Nb_2O_5 instead, most authors have found that niobium will substitute with titanium (Mu *et al.*, 1989; Arbiol *et al.*, 2002; Lee *et al.*, 2014; Yin *et al.*, 2016; Kaleji *et al.*, 2017). This is likely true, corroborated by several research groups and by the fact that niobium and molybdenum share similar electron configurations, only differing by one electron in the *d* shell. Indeed, niobium is actually closer in size and valence than molybdenum, so should substitute more than molybdenum. Thus, it is unlikely that the niobium will have not substituted into the lattice due to size or valence mismatch, as molybdenum seems to have achieved this with greater difference in parameters.

In addition, although niobium doping has been found to blueshift the bandgap and reduce photoactivity (Yin *et al.*, 2016), most authors have found that doping with niobium redshifts the bandgap (Lee *et al.*, 2014;

Uyanga *et al.*, 2014; Kaleji *et al.*, 2017; Niu *et al.*, 2018; Zarrin and Heshmatpour, 2018). This is thought to be achieved by the aforementioned substitution creating donor electron level near the conduction band. In contrast to the multiple oxidation states found with molybdenum, niobium tends to exist as in the $5+$ state only; Nb^{5+} is able to substitute into gaps in the lattice vacated by Ti^{4+}, creating a donor electron level near the conduction band, red shifting the bandgap. This can be ascribed to Ti^{4+} reducing to Ti^{3+} for every Nb^{5+} introduced, or one Ti vacancy for four Nb^{5+} introduced; essentially, this is a charge compensation mechanism. As Nb^{5+} has one fewer electrons than Ti^{4+}, the $Ti^{4}+$ must exist in a reduced state as Ti^{3+}. Alternatively, $4Nb^{5+}$ can be substituted for four $Ti^{4+,}$ giving a net charge of $4+$. A Ti^{4+} vacancy is then induced, leading to no net charge (Arbiol *et al.*, 2002; Lee *et al.*, 2014).

While this substitution occurs readily, it has been shown to cause vacancies, which then act as recombination centres. The doped niobium can form double bonds with neighbouring oxygen atoms, forming niobyl clusters concomitantly to the creation of vacancies and recombination centres (Mattsson *et al.*, 2006). The work of Mu *et al.* (1989) describes issues with trivalent and pentavalent dopant ions generally, finding that the formation of the electron donor level also acts a recombination centre. This implies that despite the improved bandgap parameters, the recombination centres play a greater role in the photoactivity. This was expanded by Niu *et al.* (2018) and Zarrin and Heshmatpour (2018), finding that using the doped titania in conjunction with reduced graphene oxide resulted in far greater photoactivity-this was ascribed to shuttling of the electrons away from the holes, preventing recombination. These works corroborate the molybdenum-doped titania-reduced graphene oxide findings of Dargahi *et al.* (2018) and Khan *et al.* (2018) discussed above. The lack of niobium-doped titania activity found in this study can now likely be explained by an excessive charge carrier recombination rate, caused by the formation of vacancies and the electron donor level inherent in pentavalent dopants such as niobium. Evidently, charge carrier recombination considerations are of key importance.

In addition to the mechanism discussed above, molybdenum also has a potential second mode of action that would help to explain its superior activity compared to niobium. Doped molybdenum, especially in higher concentrations, has the potential to form MoO_3 clusters at the coating interface. This molybdenum trioxide can undergo surface reactions with adsorbed water, forming an equilibrium with molybdic acid. Molybdic acid will also react with nearby water, dissociating to equilibrium with molybdate ions and hydronium ions. The hydronium ions create an acidic environment, functionally changing the pH of the environment close to the surface (Zollfrank *et al.*, 2012). This acidic environment is favourable to the conversion of methylene blue to the colourless leucomethylene blue, both independently and synergistically with the photocatalytic mechanisms discussed (Mowry and Ogren, 1999; Kozlov *et al.*, 2003), leading to a high activity rate. It is important to distinguish between photocatalytic activity and other mechanisms, so the high activity obtained in the present study must be taken with caution.

This leads to another point to note – the use of the methylene blue test as an estimator of photoactivity. There are several problems associated with the use of this dye as a probe reactant that are reported in the literature. While its use is described in a BS ISO standard (British Standards Institution, 2010), slight deviations from the protocol can lead to difficulty in comparing results, between projects. Several key points of deviation were noted by Mills *et al.* (2012).

One such point was the purity of the dye. The ISO standard calls for the methylene blue dye suspension to have a high purity, defined by molar absorptivity of $7.4 \times 10^4 \, M^{-1} \, cm^{-1}$ at $\lambda = 665$ nm. However, this value has a high range reported in the literature, as noticed by Mowry and Ogren (1999). This could be due to differences in dye manufacture or laboratory preparation method. Related to the purity of the dye is the concentration. Using a dye of lower concentration than the BS ISO would result in higher reported photoactivity values for a given sample. There are two reasons for this: because there would be greater transmission of light through the dye and therefore higher irradiance at the photocatalytic surface and because there

would be fewer methylene blue molecules to compete for adsorption sites on the photocatalytic surface.

Another such point is pH of the suspension. The pH of the methylene blue suspension is critical. In basic conditions, coulombic attraction causes methylene blue molecules to move towards the photocatalytic surface and adsorb, increasing the efficiency of the reaction. While this may be desired in end-user reactions, it is not ideal when determining photocatalytic activity alone. Mills and O'Rourke (2011) found that below the point of zero charge in the methylene blue solution (about pH 6.6), this coulombic attraction dropped significantly. They recommend a testing pH of around 5.5 to minimise the coulombic attraction and therefore higher-than-real photoactivity measurement. However, pH 5.5 is acidic – an environment suggested by Ratova (2013) to promote the transition from the blue-coloured methylene blue (MB) to the colourless leucomethylene blue (LMB) and corroborated by the pH change driven by molybdenum dioxide – molybdic acid discussed above. The ideal pH for accurate estimation of photoactivity is therefore unclear.

The stirring/agitation of the dye was also noted. The ISO recommends stirring every 20 minutes of the reaction. However, as photo-mineralisation of methylene blue only occurs when the MB molecule is adsorbed to the photocatalytic surface, constant stirring is recommended to maintain a constant reaction rate. While this is a deviation from the ISO standard, it is adopted across the literature (Toyoda *et al.*, 2004; Inagaki *et al.*, 2006; Mathews *et al.*, 2009; Mills *et al.*, 2012). One problem of the need for constant stirring is the inability to use the primary testing setup recommended by the ISO: it is recommended that a glass column is affixed to the photocatalytic material, the column is filled with methylene blue and irradiated whilst monitoring $\lambda=665$ nm. However, with the need for continuous stirring, it is inappropriate to have a stirring device occluding the photocatalytic material from the irradiation source. The ISO recommends a secondary setup for use in this case; this is often further modified, with many laboratories using custom-made, non-standardised setups. While the variability in systems used can create difficulties when comparing results, the

secondary/adapted systems enable continuous stirring, which is advantageous in obtaining accurate measurements.

It is also important to highlight the photosensitising effect of light on methylene blue dye. As the dye absorbs light strongly at λ=665nm, photons can excite electrons within the dye molecule. In the electronically excited state, dye molecules (D*) can 'inject' or 'dispose' of this electron into the conduction band of the photocatalyst, becoming a dye free radical (D•+). These dye radicals then go on to decompose, becoming bleached or colourless (17).

$$D^* + photocatalyst \rightarrow D^{\bullet+} + photocatalyst \; (e^-)$$

$$D^{\bullet+} \rightarrow bleached \; products \qquad \text{(17)}$$
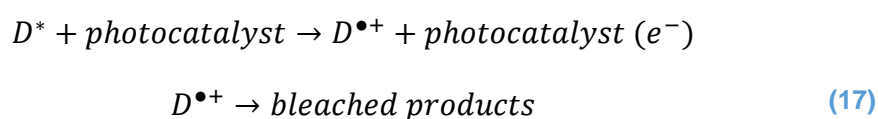
This process changes the colour of the dye from blue to colourless, which is difficult to distinguish from the photocatalyst-mediated reaction – this could lead to inappropriately high photoactivites being reported. Additionally, the donated electron in the conduction band of the photocatalyst can go on to react with oxygen, forming products such as hydrogen peroxide. These secondary oxidising products can again contribute to the breakdown of MB, obscuring the activity of the photocatalyst (Mills *et al.*, 2012).

For these reasons, using methylene blue testing for the determination of photocatalytic activity of visible-light activated photocatalysts could be considered inappropriate (Yan *et al.*, 2006; Mills, 2012; Rochkind *et al.*, 2015) and perhaps authors investigating visible-light photocatalysts should use alternative probe reactants such as acetone, formaldehyde and stearic acid, among others (Mattsson *et al.*, 2006; Kafizas *et al.*, 2009; Akbarzadeh *et al.*, 2010; Klaysri *et al.*, 2017; Ratova *et al.*, 2017; Ratova *et al.*, 2018).

However, despite these problems, methylene blue continues to be used across the literature to investigate the photocatalytic activity of both UV- and visible-light activated photocatalysts, as many of the arguments against the use of the methylene blue test can be countered by measuring the degradation caused by the irradiation source alone and subtracting this from the value obtained from the photocatalytic test. The use of this probe

reactant remains very useful in comparing work between groups (Rao *et al.*, 2016; Kaleji *et al.*, 2017; Khan *et al.*, 2018; Niu *et al.*, 2018; Yoon *et al.*, 2018; Zarrin and Heshmatpour, 2018).

4.2 – Summary

In this chapter, the effects of two dopants – niobium and molybdenum – were investigated in relation to the fluorescent-light activity of titania photocatalysts. In addition, the effect of the substrate and annealing time and temperature were explored.

It was found that the molybdenum-doped samples consistently had higher photoactivity despite poorer crystallinity, which may be due to limitations of the method; literature exists that supports the notion that molybdenum forces a pH change in the local environment, artificially increasing methylene blue breakdown and so seeming to improve photoactivity. Conversely, the superior photoactivity may be due to intrinsic charge carrier separation effects. This is in contrast to niobium-doped samples, that had consistently lower photoactivity, but superior crystallinity. Several sources throughout the literature note the reduction to the bandgap of titania with niobium doping, but hypothesize that the charge carriers recombine more quickly, due to the pentavalent niobium ions creating vacancies in the titania lattice, which act as recombination centres. One trend noticed in this study and by several authors is the effect of the dopants on the anatase to rutile transformation. Doping the titania with molybdenum consistently promoted the phase transition, whereas doping with niobium consistently inhibited it.

Promising studies exist that combine doped titania and a separate material for charge carrier separation functionality – further investigations could combine the materials studied here with a material such as reduced graphene oxide, to create more optimised functional coatings. Future studies could use an alternative photoactivity test, as the limitations of the methylene blue test could have resulted in non-representative values of photoactivity of these samples – the high visible light activity of the molybdenum doped samples may have been due to the protonating effect of surface-level molybdenum trioxide. It could be the case that the dopants have similar effects on the actual activity of the photocatalyst, in addition to affecting microorganisms via different pathways. For this reason, selected

molybdenum- and niobium-doped titania samples were investigated for their antimicrobial effects. This is explored in the next Chapter, Chapter Five.

DETERMINING ANTIMICROBIAL PROPERTIES

While photoactive surfaces have many uses and applications across sectors, an under-exploited aspect is the ability to inhibit the growth of and kill microorganisms. This Chapter will describe the methods used to determine the photocatalytic-antimicrobial properties of the surface coatings created in the previous Chapter and aspects associated with these processes.

5.0 – Method

5.0.1 – Preparation of diluents, media and reagents

In most cases, materials were sterilised prior to use. Sterilisation of media and equipment was achieved by autoclaving at 121 °C for 20 minutes. The photocatalytic surfaces prepared in *section 4.0* were considered disinfected after the annealing stage and were handled aseptically afterwards to avoid contamination. All contaminated materials were sterilised via autoclave at 121 ^{0}C for 20 minutes before disposal.

5.0.1.1 – Preparation of diluents

Two diluents were used throughout this work – distilled water and saline.

Distilled water was obtained using the RiOs system (RiOs Essential Water Purification System, Merck, Gillingham), dispensed into 0.5 L Duran bottles (Duran laboratory glass bottles, DWK Life Sciences, Wertheim am Main) and sterilised. Sterile distilled water was stored for a maximum of four weeks at ambient temperature. Saline was prepared to a concentration of 0.85 % *w/v* by dissolving one saline table (OXOID, Basingstoke) in 0.5 L distilled water, dispensing into a 0.5 L Duran bottle and sterilised. Sterile saline was stored for a maximum of four weeks at ambient temperature.

5.0.1.2 – Preparation of culture media

Nutrient media (broth and agar), prescribed by BS ISO 27447, was used throughout this work (Nutrient broth, CM0001, OXOID, Basingstoke; Nutrient agar, CM0003, OXOID, Basingstoke). Both nutrient agar and nutrient broth contain the same nutrients (Table 5).

Table 5: Composition of the nutrients in nutrient broth and agar. Lab-Lemco powder is a proprietary meat extract powder.

Component	Concentration, % (*w/v*)
Meat extract (Lab-Lemco powder)	1.0
Yeast extract	2.0
Peptone	5.0
Sodium chloride	5.0

Fresh sterile nutrient broth was prepared by adding 6.5 g of nutrient broth powder to 0.5 L of distilled water in a 0.5 L Duran bottle, mixing thoroughly and sterilising as per *section 5.0.1*. Sterile nutrient broth was stored for a maximum of four weeks at ambient temperature.

Nutrient agar was prepared by adding 14 g of nutrient agar powder to 0.5 L of distilled water and mixing thoroughly in a 0.5 L Duran bottle. Sterilisation was achieved by autoclaving at 121 °C for 20 minutes. The agar was then poured into sterile plastic petri dishes (Select Petri Dish, SLS2002, SLS, Nottingham) and allowed to set. Sterile nutrient agar plates were refrigerated and stored for a maximum of four weeks at 4-6°C.

5.0.1.3 – Preparation of neutralising broth

At several points during this work, neutralising broth was used to act as a preferential reactant for ROS produced by the photocatalyst, preventing the ROS from reacting with bacteria. This is used by several authors (Luppens *et al.*, 2002; Kelly *et al.*, 2014; Vazquez-Sanchez *et al.*, 2015) and is recommended by BS ISO 27447.

Neutralising broth was prepared by adding 15 g of soya lecithin (Optima Healthcare Lecithin, Holland and Barrett, Warwickshire) and 7.5 g TWEEN 80 (TWEEN 80, Sigma-Aldrich Company Ltd, Dorset) to 0.5 L distilled water in a 1 L conical flask (1000 mL Borosilicate Glass Narrow Neck Erlenmeyer Flask, Fisher Scientific, Hampton). This was then dissolved by boiling, dispensed into a 0.5 L Duran flask and sterilised via autoclaving as per *section 5.0.1*. Neutralising broth was stored for a maximum of four weeks at ambient temperature.

5.0.2 – Maintenance and handling of microbial cultures

One of the most important techniques in microbiology is aseptic technique. This is the practice of actively avoiding the introduction of microorganisms into an experiment. This is important, as results are likely to be invalidated by the presence of a second microorganism species. The microorganism chosen for this work was *Escherichia coli* 8739, purchased from the American Type Culture Collection (ATCC® 8739™, American Type Culture Collection, Manassas). This organism is indicated by BS ISO 27447.

5.0.2.1 – Freezer storage of culture

The organism was revived according to manufacturer's instructions, inoculated into 10 mL of sterile nutrient broth and incubated for 18 hours at 37 °C in an orbital incubator at 180 rpm. In order to preserve the culture for the length of the project, freezer stock cultures were used. This prevents 'aging' of the culture, i.e. slows the rate of mutation within the DNA of the culture. This is important as single mutation may cause a variety of expressive differences, casing the culture to behave differently than expected. To prepare the organism for long-term storage and reduce viability loss over time, a 'freezer mix' was employed (Hubálek, 2003; De Paoli, 2005). This was prepared by combining 300 g of glycerol (Glycerol [Molecular Biology], BP229-4, Fisher BioReagents, Fisher Scientific, Hampton) with 1 L of sterile deionised water. A volume of 10 mL of freezer mix was added to the broth culture and incubated at 37 °C for a further thirty minutes. Afterwards, 1.5 mL aliquots of the suspension were dispensed into cryogenic vials (Cryogenic Vial Classic, 2.0 mL, LW3334, Alpha Laboratories, Hampshire) and kept in the freezer at -80 °C. The culture, or 'freezer stock', was kept in the freezer and only removed to subculture the organism onto nutrient agar plates (monthly), which were used on a day-to-day basis for experiments.

5.0.2.2 – Subculturing and fridge storage of culture

To maintain purity of the freezer culture, subcultures were used for day-to-day experiments. The microorganism was subcultured by taking a small amount of frozen material from the cryotube using a flame-sterilised nichrome loop and performing a streak plate onto nutrient agar, to obtain isolated colonies. The plate was then incubated at 37 °C overnight, checked for purity and stored in a refrigerator at 4 °C. This agar plate containing the subculture was used as the stock plate and stored for a maximum of four weeks.

5.0.2.3 – Standardised washed cell suspension

Most experiments required the microorganism to be in known concentrations and in a specific growth phase. To facilitate this, fresh overnight broth cultures were grown immediately prior to any experiment. One colony of *E. coli* 8739 was aseptically removed from a stock plate and inoculated into 10 mL of fresh sterile nutrient broth in a sterile disposable universal bottle (Sterilin 128A Universal Container, CON2700, SLS, Nottingham). This was incubated at 37 °C for 18 hours with shaking at 180 rpm. Cells were harvested by centrifugation (Sigma 4-5L Centrifuge, Sigma Laborzentrifugen GmbH, Osterode am Harz) at 2300G for 10 minutes, resuspended in 10 mL of sterile saline and mixed using a vortex mixer (Rotamixer Vortex-Mixer, HTZ Limited, Croydon) for 10 seconds. The suspension was then centrifuged again (2300G, 10 minutes), then resuspended sterile saline to an optical density of 0.9-1.1 at 540 nm (Jenway 6305 UV/Visible Spectrophotometer, Chelmsford). This was then diluted 1:10 in sterile saline to make a "standardised washed cell suspension". The standardised washed cell suspension was prepared to remove any nutrient material, which might cause growth and affect cell number.

Work in this laboratory has demonstrated this to be of $1.26 \pm 0.38 \times 10^8$ cfu mL^{-1}, confirmed via ten-fold serial dilution and colony counting; the washed cell suspension was serially diluted by aseptically aliquoting one millilitre of suspension into 9 mL of sterile saline and mixed for 60 seconds using a vortex-mixer, diluting the suspension 1:10. This was repeated eight times to

a final dilution of 1×10^{-8}. A 100 µL aliquot of each dilution was spread-plated onto sterile nutrient agar plates in duplicate and allowed to dry. Plates were inverted and incubated at 37 ^{0}C for 18 hours, prior to colony counting.

The number of colonies counted was inferred to be the same as the number of colony forming units inoculated onto the plate, i.e., one colony comes from one colony forming unit. Therefore, this number represents the number of cells that remained viable after exposure to the photocatalyst. The concentration of remaining viable cells was determined by transforming the number of colonies counted into a cfu mL^{-1} value, to allow comparison across work.

5.0.3 – Determining photocatalytic antimicrobial potential of surfaces

In order to develop useful surface coatings, accurate measurements must be made. Of primary importance to this work are the photocatalytic antimicrobial capabilities. As discussed in *section 1.3.2,* currently the most widely used test is the British standard 27447:2009 (British Standards Institution, 2009), based on the earlier Japanese standard Z 2801:2000 (Japanese Standards Association, 2000). An adaptation of the BS ISO 27447 was used to determine the visible light activated photocatalytically induced antimicrobial properties of the coatings produced in *section 4.0.2*. Coatings on both stainless steel and glass substrates were investigated; as the protocol was the same for both substrate types, the method is presented here as the substrate type followed by the method.

5.0.3.1 - Standard antimicrobial test – stainless steel samples

The antimicrobial activity of the coatings produced in *section 4.0.2.1* were investigated at four time points: t=0 hours, t=1 hour, t=3 hours and t=24 hours and under two light conditions – irradiated and dark. Two molybdenum-doped titania samples, in addition to two uncoated controls were used per time point per light condition. The experiment was conducted twice.

5.0.3.2 - Standard antimicrobial test – glass samples

The antimicrobial activity of the coatings produced in *section 4.0.2.3* were investigated at four time points: t=0 hours, t=1 hour, t=3 hours and t=24 hours and under two light conditions – irradiated and dark. Two each of niobium-doped titania and molybdenum-doped titania samples, four undoped titanium dioxide samples and three uncoated controls were used per time point per light condition. The experiment was conducted twice.

5.0.3.3 - Standard antimicrobial test – method

The base of two sterile 23 cm x 23 cm plastic trays (Corning square bioassay dish, CLS431272, Merck, Gillingham) were covered sterile paper towels (sterilised by wrapping in aluminium foil (Aluchef premier foil, Terinex.

Bedford) and autoclaving at 121 ^{0}C for 20 minutes) and saturated with sterile water. Fifty microliters of the standardised washed cell suspension were aliquoted on to the surface of each sample. A 1 cm x 2 cm piece of polyethylene film (Select Petri Dish bag, SLS2002, SLS, Nottingham), disinfected by immersion in 70 % ethanol (Ethanol Solution 70%, BP82011, Fisher BioReagents, Fisher Scientific, Hampton) for 24 hours and air-dried for 18 hours in a Class 2 biosafety cabinet (Bio 2+ Class 2 Microbiological Safety Cabinet, Envair Ltd, Haslingden), was placed on top of each sample and smoothed over to evenly distribute the liquid suspension on the sample without spilling and to prevent drying. Specifically, this entailed placing the polyethylene film on top of the coupon using forceps (sterilised by immersion in ethanol and flaming), and then using the forceps to 'press' the film along the coupon. As the films were cut to the exact size of the coupon, pressing down and smoothing the film along the coupon evenly distributes the bacterial suspension on the coupon along the entire area, without causing spillage. Afterwards, the samples were then placed into sterile petri dishes.

Petri dishes containing the dark control samples were wrapped in aluminium foil to prevent light ingress. The petri dishes containing the samples were placed into the plastic trays and the tray lid was replaced. Both trays were then put into a large cooled illuminated incubator (Gallenkamp, Loughborough, UK) at 20 °C for 24 hours, containing six fluorescent tube lamps (Sylvania, Ontario, Canada) to activate the coatings, positioned in pairs 30 cm, 60 cm and 90 cm from the samples. Previous work in this laboratory (Caballero *et al.*, 2014) has shown that the samples within the petri dishes are exposed to a large portion of visible light (λ=400-700 nm of intensity 2.70-3.99 W m^{-2}) and a small portion of UV (λ=290-400 nm of intensity 0.05-0.12 W m^{-2}).

At the corresponding time point, a sample was removed from the incubator. The stainless steel coupons were immersed in a sterile universal bottle containing 10 mL sterile neutralising broth, while the glass coupons were immersed in 5 mL sterile saline. This difference was because the neutralising broth was found to interfere with subsequent absorbance measurements that are detailed in *section 6.2.1.5*. Ancillary experiments in this laboratory have

demonstrated that there was no difference in cell viability between recovery in neutralising broth and recovery in saline when using the glass coupons.

The universal bottles were mixed vigorously using a vortex mixer for 60 seconds, then the resultant suspension was 10-fold serially diluted three times and plated out as described in *section 5.0.2.3*.

5.0.3.4 – Statistical analysis

Data were analysed for statistically significant differences and relationships as appropriate using IBM SPSS Statistics version 23. Data were analysed for normality using a Shapiro-Wilk test. Data that were not normally distributed were log-transformed to approximate a normal distribution. Normally distributed data were assessed for differences using an ANCOVA to assess the effects of the variables in isolation, a three-way general linear model to identify any interaction effects between the variables and a one-way ANOVA with post-hoc Tukey tests for pairwise comparison to identify differences between each sample set. The alpha level for these tests was set to 0.05; differences/relationships were considered significant if $p < 0.05$.

5.1 – Results and discussion

5.1.1 – Photocatalytic-antimicrobial properties of coatings on stainless steel coupons

In agreement with the photoactivity results obtained in *section 4.1* for these samples, the molybdenum-doped titania coupons showed strong antimicrobial properties after one hour of irradiation (Figure 70).
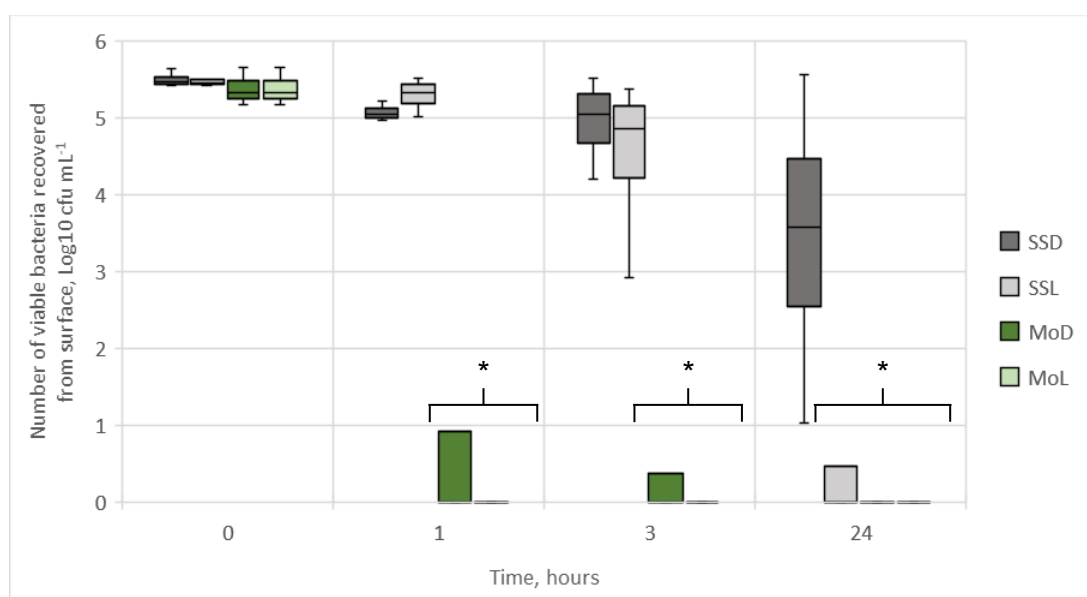
Figure 70: Viability of bacteria over time on test surfaces. SS = stainless steel, Mo = molybdenum-doped titania. D = non-irradiated, L = irradiated. Brackets and * indicate significant differences to t=0 (p<0.001). The irradiated molybdenum rapidly reduced viable microorganisms to below the level of detection after one hour. The non-irradiated molybdenum samples did not reduce the viable cells below the level of detection until after 24 hours, although an approximate 4-log and 4.5-log drop in viable cell number was found after one hour and three hours respectively. A 4.5-log drop in viable cells was observed on the irradiated stainless steel surface after twenty-four hours. N=2.

The number of viable bacteria recovered from the surfaces at t=0 h was similar across all sample types, about 5.5 Log_{10} cfu mL^{-1}. After one hour, the irradiated molybdenum-doped samples had caused significant inactivation of the microorganisms below the level of detection – approximately a 5.5-log drop (p<0.001), whereas an approximate 4.5-log decrease was observed on the non-irradiated molybdenum-doped samples (p<0.001). After three hours, a further half-log drop was observed on the non-irradiated molybdenum-doped samples. This contrasts with the uncoated steel samples; on the irradiated samples, a significant reduction in the number of viable bacteria

recovered was only observed after twenty-four hours ($p<0.001$), whereas no significant reduction was observed on the non-irradiated samples ($p>0.5$).

This indicates that the molybdenum-doped titania coatings have strong antimicrobial properties with and without irradiation. Although inactivation appeared more rapid with irradiation (recovery below the level of detection did not occur on the non-irradiated coatings until 3 hours, whereas this occurred at 1 hour for the irradiated coatings), no significant interaction effects were found between irradiation status and coating ($F=1.3$, $p=0.261$).

This implies that the coatings were equally effective in both light and dark conditions (or rather, the coatings were not empirically potentiated by irradiation). While it was interesting that no beneficial effects were found for the irradiation, given that the photoactivity was measured and confirmed via the degradation of methylene blue obtained in *section 4.1*, it is not surprising; the antimicrobial efficacy of molybdenum-doped titania coatings in both the light and dark has been reported. Although photocatalysts require irradiation by photons with enough energy to cause activation, the observations in this work confirm previous studies which suggest molybdenum-doped titania coatings on stainless steel substrates can have a dual-function effect (Fisher *et al.*, 2014; Kelly *et al.*, 2014). Indeed, the reduction observed indicates that the inactivation of microorganisms on molybdenum-doped titania was not entirely photocatalytically mediated; controlling for the effects irradiation status (heating effects and effect of the small UV portion emitted by the lamps) and time (natural kill/decay rates of the microorganisms), fewer viable organisms were still recovered from the molybdenum-doped samples ($F=70.96$, $p<0.001$).

The potential antimicrobial mechanisms of these were discussed in *section 4.1* and are thought to be related to molybdenum clusters on the coating surfaces propagating a pH change via molybdic acid formation and dissociation. Indeed, the pH change driven by molybdenum and molybdenum trioxide clusters may be the primary antimicrobial mechanism observed in this study, explaining why no potentiation was observed when irradiated (Lorenz *et al.*, 2011; Zollfrank *et al.*, 2012); the irradiation status did not seem to affect the dissociation effects. While this may be the case,

the photocatalytic and pH mediated effects are clearly synergistic; this is evidenced by the more rapid reduction in viable recovered bacteria when irradiated compared to non-irradiated.

After twenty-four hours, fewer bacteria were recovered from all samples except the non-irradiated stainless steel samples. This could be due to natural cell death, lack of growth medium, or disruption to other growth conditions such as moisture. This would then shift the stationary phase replication-death equilibrium to death phase after a certain amount of time, regardless of other factors. Another more likely cause of the reduction in viability is damage caused to the microorganisms by exposure to small UV-portion of the spectra emitted from the lamps. This is suggested by the reduction seen on irradiated stainless steel compared to non-irradiated stainless steel – after 24 hours, there was a significant 5-log drop in viable cells recovered compared to t=0 h (p<0.001), whereas there was no significant reduction seen on the non-irradiated samples (p=0.055).

On the other hand, the temperature of the individual plastic trays (that the coupons were kept in during the experiment) was not monitored – it could be that the tray exposed to the lamps increased in temperature compared to the non-irradiated tray, which may have affected viability. Additionally, despite attempts to avoid desiccation, the microorganisms exposed to the lamps may have dried out over time, further obfuscating the real effects of the photocatalytic coatings. However, although these suggestions may help to explain the reduction observed on the irradiated samples compared to the non-irradiated, there was no significant effect found for irradiation status when controlling for the effects of coating and time (F=2.9, p=0.093) and no significant interaction effect between irradiation and time (F=2.71, p=0.105).

5.1.2 – Photocatalytic-antimicrobial properties of coatings on glass coupons

The modified antimicrobial test was performed on uncoated glass controls, pure titania, niobium-doped titania and molybdenum-doped titania, in both irradiated and non-irradiated conditions (Figure 71).

Similar numbers of bacteria were recovered from the different samples at t=0 h, as expected. This trend was also observed on the stainless steel samples as discussed above. In contrast however, no reduction in bacteria recovered was observed after one hour. While only molybdenum-doped titania was investigated on stainless steel, the equivalent coating on glass did not significantly reduce the number of viable organisms recovered after one hour compared to t=0 h with either irradiation state (p=1.0). Indeed, the only significant reduction in number of cells recovered across all sample types, times and irradiation status was on the molybdenum-doped titania samples, irradiated for 24 hours – an average reduction of ~2 Log10 cfu mL^{-1} compared to t=0 h was observed on these samples (p<0.001). Recovery below the level of detection did not occur at all for any coating type, after any length of time, or for either irradiation type. This indicates that strong photocatalytically mediated antimicrobial properties were not present in these coatings.
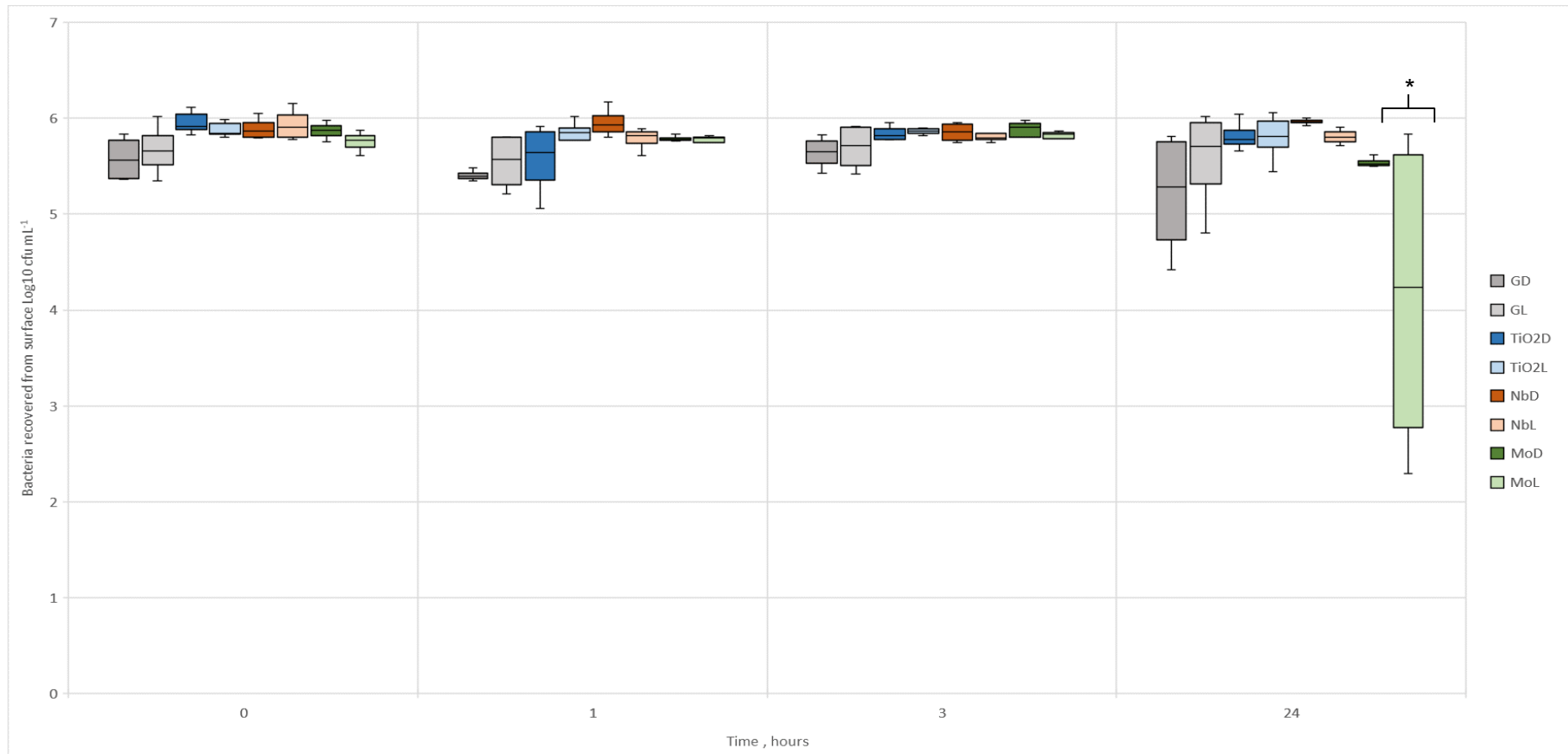
Figure 71: Viability of bacteria over time on test surfaces. G = glass; TiO$_2$ = titania; Nb = niobium-doped titania; Mo = molybdenum-doped titania. D = non-irradiated, L = irradiated. Brackets and * indicate significant differences from t=0 h (p<0.001). The irradiated molybdenum samples were the only samples to reduce the number of viable organisms compared to t=0 h. N=4 for all samples, except uncoated glass controls and TiO$_2$ samples, where N=8.

These results are unsurprising for the non-doped titania coatings as these coatings are activated solely by UV irradiation (Dalrymple *et al.*, 2010). The poor antimicrobial properties observed for the niobium-doped coatings are concordant with the low activity results observed in *section 4.1.3.5*, indicating at 4 %at., niobium does not improve the visible-light response, in agreement with Mattsson *et al.* (2006) and Yin *et al.* (2016).

Indeed, the studies that have found improved visible light activity using niobium tend to include or identify additional features that enhance activity. For example, an increased surface area is often noticed when doping with niobium, which can increase the number of active sites available for reactions to occur (Breault and Bartlett, 2012; Michalow *et al.*, 2012). Additionally, secondary dopants or codopants, have also been employed to facilitate improvements in visible light response. Secondary or codopants may transition the niobium-introduced electron donor recombination centre into a trapping site (Ma *et al.*, 2011), introduce additional mid-band states via the creation of heterojunctions (Pelaez *et al.*, 2012), or improve absorption of light leading to higher photon efficiency (Cottineau *et al.*, 2013). Other strategies include the use of carbonaceous compounds such as reduced graphene oxide, which can be incorporated into the photocatalyst to enhance charge carrier separation, shuttling electrons away from the holes and improving efficiency (Niu *et al.*, 2018; Zarrin and Heshmatpour, 2018). None of these additional features were present in this work and no significant increase in surface area was noticed for the niobium-doped compounds, indicating that additional strategies or features are key to improving visible-light response when doping with niobium. Future systems could therefore include the use of synergistic materials and codopants, in combination with dopants such as niobium, so to effect a multi-strategy response; the doped niobium reduces the bandgap allowing photons of lower energy to excite electrons from the valence band to the conduction band and the codopant or synergistic material (such as carbonaceous compounds) shuttles the electron away from the hole, improving separation and reducing the rate of recombination. These findings should be considered when designing photocatalytic systems.

While these strategies support the use of niobium in titania photocatalysts, work to date has not investigated the antimicrobial efficacy when employing these strategies, so it is difficult to make generalisations and comparisons to the present work. What is clear is that at 4 %at. concentration in titanium dioxide coatings, niobium does not improve antimicrobial properties compared to undoped titania. This signifies that, regardless of photoactivity, it does not have secondary or complementary antimicrobial mechanisms that can enhance or support photocatalytically-mediated antimicrobial mechanisms, such as pH-mediated or ion-diffusion effects.

The molybdenum-doped samples were the only ones to demonstrate significantly different effects to control, exhibiting a ~2 Log_{10} cfu mL^{-1} reduction in viable bacteria from control ($p<0.001$); this concurs with the photoactivity results obtained in *section 4.1.3.5*. However, the coatings were less effective when glass was used as a substrate than when stainless steel was used, as can be seen by the lack of inactivation after one hour and three hours; instead the reduction is only observed after 24 hours. Interestingly, the photoactivity was comparable for the molybdenum-doped titania coatings on both stainless steel (Set 1, $3.4 \times 10^{-5}\,s^{-1}$) and glass (Set 3, $6.0 \times 10^{-5}\,s^{-1}$), with comparable concentrations of molybdenum.

However, as discussed previously, photoactivity is not an analogue for photocatalytic-antimicrobial effects; the various factors discussed in *section 1.2* are critical. The key difference between the substrates used here is likely the surface area. Coatings deposited via CFUMS are conformal, so the coating approximates the surface area and topography of the substrate. In *section 4.1*, the roughness of the coatings was assessed; although roughness is not the same as surface area, they tend to have a positive correlation (Terada *et al.*, 2005; Donoso *et al.*, 2007).

As can be seen in *section 4.1*, the average roughness of the molybdenum-doped titania coatings on stainless steel is 376 nm, while on glass, the equivalent coatings had an average roughness of 7.1 nm. These differences in roughness (and surface area) may explain the disparity between comparable MB degradation results and different photoinactivation results.

The inactivation of *E. coli* is much more sensitive to changes in surface area than the degradation of methylene blue molecules, primarily due to size difference – the cells are in the order of a few micrometres, whereas methylene blue is a simple molecule (a few nanometres in size). Therefore, the smoother coatings deposited onto the glass substrates were less active against *E. coli*, as they had fewer available active sites and sites for adsorption of the cell compared to the coatings on stainless steel (van Grieken *et al.*, 2009a). This was also found by Rtimi *et al.* (2017), who demonstrated that for photocatalysts of identical composition, roughness is correlated with bacterial inactivation, but not with the breakdown of pollutants. It was ascribed to numbers of 'catalytic points' in contact with the bacterium and the resulting ease of transfer of ROS; smoother surfaces have fewer points of contact with cells and so can be said to have a reduced adsorption capacity.

It is the reduction in adsorption capacity that occurs concurrently with reduced surface area that is critical. Bacteria have been shown to be inactivated with greater efficiency when they adsorb to the surface of the photocatalyst; here, there may be several reactive species present, such as hydroxyl radicals, hydrogen peroxide and superoxide, in addition to the primary reactive species (the electron and the hole) from the photocatalyst (Fujishima *et al.*, 2008). When a bacterium is adsorbed to the surface, all these reactive species may interact with the cell, causing more efficient inactivation through a combination of increased volume of attack (more reactive species available, so can attack multiple sites at once) and different modes of attack. However, when the bacterium is not adsorbed to the surface, the reactive species must travel to the cell from the surface to be effective. During this travel, the species are likely to react with non-target reactants, being scavenged by other molecules – this is especially important when considering real-world applications for this technology, such as wastewater remediation. This results in a reduction in efficiency, as fewer reactive species are available for attack; furthermore, it has been shown that at distances more than around one micrometre, only hydrogen peroxide is available for attack (Foster *et al.*, 2011). This clearly indicates the importance

of adsorption of the cell to the surface, as when not adsorbed, fewer reactive species of fewer types can react with the cell, reducing efficiency. Indeed, several authors have noted this as a critical parameter when designing systems for photocatalytic inactivation of bacteria (Gogniat *et al.*, 2006; Verdier *et al.*, 2014) and the results of this work concur.

Despite these explanations for the lack of photocatalytically mediated antimicrobial effects observed in these samples, the pH-mediated antimicrobial effects of molybdenum that were observed on the stainless steel coatings would still be expected. However, in contrast to previous work, no antimicrobial effects were detected for molybdenum-doped coatings when no irradiation was provided. The pH mediated effects are caused by molybdenum trioxide clusters that are exposed to water and form an equilibrium with molybdic acid, which goes on to dissociate adsorbed water molecules to hydroxonium ions. Because of this necessity for the water molecules to be adsorbed, the pH change can be very local (Lorenz *et al.*, 2011), occurring close to the surface. The pH change could then actually be considered as a change in surface acidity, as opposed to a genuine modification to the pH of the environment (Di Paola *et al.*, 2002). Therefore, the reduction in surface area and adsorption capacity for microorganisms discussed would directly reduce the antimicrobial potential of the pH effect; this concurs with Lorenz *et al.* (2011), who suggest that the antimicrobial properties observed are a contact effect, in agreement with the catalytic-point contact-associated findings of Rtimi *et al.* (2017). This surface-proximity phenomenon may explain the comparable MB results and disparate antimicrobial results in both the light and dark, between the coatings on glass substrates and steel substrates. The interesting proposed pH-driven effects remain unexplored in this study, however, could be investigated; the localised pH change could be discerned via use of pH-sensitive dye probes and the fluorescence lifetime spectroscopy and imaging technique (Vroom *et al.*, 1999; Kuwana *et al.*, 2004). In this way, differences in pH between neighbouring molybdenum-doped titania and undoped titania could be elucidated. Additional further investigations, especially into the surface-related pH changes and effects and specifically how these relate to available

surface area and adsorption sites, are necessary to gain a full picture of the complex interconnected mechanisms related to photocatalytic inactivation of microorganisms.

It is difficult to make conclusions based on this data, as although several studies may help to explain the complex results obtained, ultimately there is disparity between the results obtained in the present work and the general findings in the literature. Consideration should be given to the variability of the coatings, as described in *section 4.1.3*. There was a high coefficient of variation of roughness noted for the doped titania coatings, which could have contributed to the variability in photocatalytic-antimicrobial properties of molybdenum-doped titania observed in this study. However, the roughness only varied in the order of a few nanometres; the real-world effects on adsorption sites is likely to be negligible. It is more likely that the delamination and flaking effects that were observed contributed to the variability – delaminated/flaked coatings have much higher surface area, in addition to dispersing throughout the liquid medium. This could increase ROS generation and homogeneity, as opposed to having a small 'envelope' of activity very close to the surface. This would also help to explain the large range of values found for activity for this sample type. To clarify this variability, additional repeats should be performed in future work. This would not only help to elucidate the true photoactivity and photocatalytic-antimicrobial efficacy of the coatings, but also improve the power of the statistical analysis, addressing robustness issues.

Furthermore, brief mention should again be given to the shortcomings and difficulties encountered during the use of the standard test. While more comprehensive arguments are given in *section 1.3.2,* it is salient to highlight here some key factors. The key shortcomings of the test are the number of variables to consider such as temperature, humidity and irradiation parameters; the inoculation size and vehicle and recovery medium should also be considered, along with the choice of control samples and number of test samples. Small differences in these reaction variables can affect the overall photocatalytic-antimicrobial efficacy reported, as shown by Foster *et al.* (2010). As with many microbiological testing methods, the validity of the

tests in comparing work between authors is suspect, without extensive transparency and reporting of laboratory techniques (Parker *et al.*, 2018). Other issues include the high level of technical expertise required, the prohibitive volume of replicates and reagents required to detect and statistically affirm antimicrobial properties and amount of time required to perform the test, all of which make the test unsuitable as a first-stage screen. Despite this, it remains a valuable test for the confirmation and determination of efficacy for photocatalytic-antimicrobial coatings, as obvious effects are easily detected, in addition to reductions in viability that do not include total eradication.

5.2 – Summary

In this chapter, the visible-light photocatalytic-antimicrobial properties of the coatings deposited in Chapter Four were investigated. The coatings investigated were molybdenum-doped titania coatings on stainless steel substrates, along with pure titania, niobium-doped titania and molybdenum-doped titania on glass substrates.

It was found that while the molybdenum-doped titania on steel substrates exhibited significant antimicrobial properties in both the light and dark after one hour, the coatings on glass did not. The niobium-doped and pure titania coatings showed no improved photocatalytic effects compared to uncoated glass controls over 24 hours. The only coating on the glass substrates to exhibit any antimicrobial activity was the molybdenum-doped titania, after 24 hours of irradiation, indicating a poor visible-light photocatalytic-antimicrobial response. In addition, the significant antimicrobial effect observed in the dark on the Mo-doped titania on steel was not observed on the Mo-doped titania coating on glass, despite similar coating composition and similar methylene blue degradation activities. The antimicrobial mechanism in the dark was proposed to be a pH-mediated surface effect, which may occur due to clusters of molybdenum trioxide at the surface of the coating; this trend has been noticed by several authors investigating the antimicrobial properties of MoO_3. The effect of the substrate on the formation of MoO_3 clusters was not explored, but would be beneficial to establish in future work.

The differences were then explored in the context of surface area and roughness; the coatings on glass had a much lower roughness and surface area than the equivalent stainless steel coatings. It is proposed that the concurrent reduction in available adsorption sites for the bacterial cells prevented both the photocatalytically-mediated antimicrobial properties and pH-mediated surface properties from being effective, while having no detrimental effect on the breakdown on methylene blue. Therefore, the critical parameter found in the present study for the inactivation of microorganisms was the surface area, which directly influenced the number of available adsorption sites. The surface area and roughness of real-world

photocatalytic systems for antibacterial applications must consider the sensitivity of bacterial cells to the surface area and the relative size of cells and surfaces features.

A key concern during this study was the suitability of the test as a first-stage screen for antimicrobial properties. Several promising rapid alternatives methods could exist, that would facilitate more authors exploring the antimicrobial properties of their coatings, without costly investment. These methods will be explored in the next Chapter, Chapter Six.

DEVELOPMENT of RAPID MICROBIOLOGICAL TESTING METHODS

While simple and rapid tests exist for the determination of photocatalytic activity, tests to determine the photocatalytic antimicrobial effects are limited. In this Chapter, a range of potential alternatives will be suggested. Furthermore, two of these suggestions will be explored in detail using a dynamic and iterative experimental protocol.

6.0 – Rationale

There currently is a need for a more practical, less complex and faster method to determine the photocatalytic-based antimicrobial activity of thin film coatings. The current method, based on the BS ISO 27447:2009 (British Standards Institution, 2009) has many steps where lack of standardisation may occur, reducing the validity of test and hindering comparison between researchers – in addition to requiring a high level of user expertise and being highly time consuming. It is clear that many research groups would benefit from a less labour-intensive, faster and more user-friendly test to determine this important property of the coating. It is therefore the overarching aim of this project to investigate and develop such a method. Several existing methods used to rapidly enumerate bacterial load could be employed or adapted to achieve this goal.

6.0.1 – Overview of potential methods

There are several existing techniques for the rapid enumeration of bacterial load and both total count methods and viable count methods can be found in the literature (Davis, 2014). However, as the overall aim of the method is to determine how many cells remain viable after treatment with a photocatalytic material, viable count methods are chiefly of interest. In addition to classifying methods by total count and viable count, they can be loosely classified as 'direct' methods or 'indirect' methods. Direct methods do not infer the number of viable cells by culturing and/or monitoring them; instead, the individual cells are counted directly. Several of the most promising techniques reported in the literature are briefly described here.

6.0.1.1 – Direct methods

Direct rapid methods include viability staining, wherein two dyes are applied to the cells to be enumerated; the viable cells stain preferentially with one dye and non-viable cells with the other. The effect is that viable cells appear one colour and non-viable another, enabling identification and enumeration by image analysis. Stains like this include LIVE/DEAD stain (Boulos *et al.*, 1999).

A modified version of a direct viability count method involves incubating cells to be enumerated with a low concentration of a division-inhibiting antibiotic, such as nalidixic acid or ciprofloxacin. When the cells attempt to divide, the action of the antibiotic prevents this, instead causing the cells to elongate and enlarge. A non-selective dye such as acridine orange or methylene blue can then be used to stain all cells. The elongated cells (those that attempted to divide, i.e. those that were viable before staining) can be counted by automatic image analysis (Singh *et al.*, 1989; Buchrieser and Kaspar, 1993; McFeters *et al.*, 1999).

Another example of a direct technique is FISH (fluorescent *in situ* hybridisation). This is a fluorometric technique where DNA of the target cell is hybridised with a fluorochrome and counted under microscope using image analysis (Kepner and Pratt, 1994). While this technique does not differentiate between viable and dead cells, a modified version in which the fluorochrome is hybridised with rRNA of the target cell has been shown to differentiate between viable and non-viable cells. This is because rRNA has a vital role in protein synthesis and is therefore expressed by metabolically active (and thus viable) cells (Baudart *et al.*, 2015). Therefore, upon microscopic image analysis, only viable cells would fluoresce and be counted and enumerated. However, a caveat of this method is that viable non-dividing or dormant cells (such as those in the stationary phase) downregulate protein synthesis, and thus have reduced ribosomal activity (Luidalepp *et al.*, 2016). These cells would be unlikely to have much rRNA to hybridise with the fluorochrome, and as such may not be detect during analysis.

6.0.1.2 – Indirect methods

In contrast to direct techniques, indirect techniques infer the bacterial load by measurement of a characteristic related to growth. Several 'indirect' rapid techniques have been reported. One such technique is impedance monitoring. In this technique, the electrical conductance (the inverse of impedance) of a liquid medium is monitored as bacteria divide within it. Initially, the conductance of the medium is low. As bacteria divide, they metabolise the electrically inert medium into compounds with a greater charge-carrying capacity. The effect is an increase in conductance with

increasing bacterial growth. Due to the doubling-time nature of bacterial growth dynamics, it follows that the time to detect a change in conductance is proportional to the initial inoculum concentration. Therefore, the time taken to register a change in conductance can be correlated with initial inoculum size, enumerating the cells in the inoculum (Cady *et al.*, 1978; Eden and Eden, 1984; Silley and Forsythe, 1996; Dastider *et al.*, 2015).

Another indirect technique involves the use of resazurin dye. Resazurin reduction assays have been used by the dairy industry to assess contamination and ascertain microbial loads of milk products (Nixon and Lamb, 1945; Jack, 1977; Alivehmas *et al.*, 1991; Garciaarmesto *et al.*, 1994; Zhou *et al.*, 2005) . In this assay, bacteria are incubated with the resazurin - unlike staining techniques, the dye does not affect or damage the cells. Instead, metabolism-associated cofactor molecules such as reduced nicotinamide adenine dinucleotide phosphate (NADPH), reduced nicotinamide adenine dinucleotide (NADH) and reduced flavin adenine nucleotide ($FADH_2$) reduce the dye. These molecules cause resazurin to reduce to resorufin, becoming highly fluorescent and resulting in a colour change from blue to pink (Candeias *et al.*, 1998; González-Pinzón *et al.*, 2012). The intensity of the change in colour is proportional to the amount of actively respiring bacteria; this can be seen by visual inspection (Figure 72), or can be measured using a spectrophotometer (Cai *et al.*, 2013).
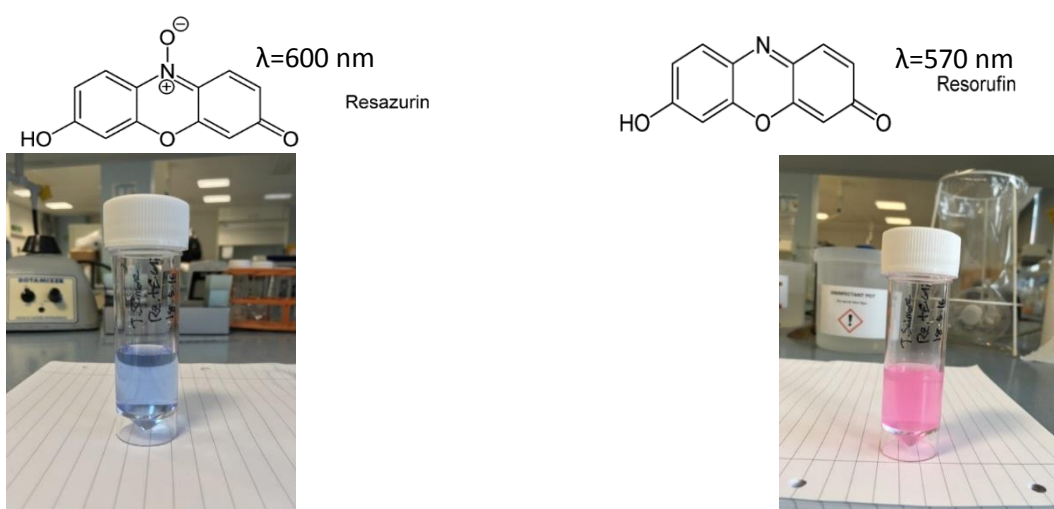
Figure 72: Appearance, molecular structure and absorbance wavelength of resazurin (left) and resorufin (right). The blue resazurin reduces to the pink resorufin with increasing bacterial concentration.

A final technique to mention, often used in estimating the concentration of cells in a suspension, is the optical density technique, also known as the turbidity measurement technique. In this technique, monochromatic light is transmitted through a suspension of cells into a detector; the amount of light that is not absorbed by the cells and instead reaches the detector is calculated and the 'absorbance' of the suspension therefore determined. Therefore the amount of light absorbed by the cells is proportional to the biomass of the suspension – from this, the total cell concentration may be inferred if the characteristics (size, dry cell weight) of the organism are known (Koch, 1981; González-Pinzón *et al.*, 2012). Despite being a total count method, with some modifications this technique can be used to obtain information about the growth characteristics of the organism, which in turn can be used to estimate viable cell numbers.

6.0.1.3 – Method proposals

The techniques mentioned above all have qualities that may make them suitable for development for use in photocatalytic assays. However, the techniques that appear to most strongly match the selection criteria (rapid, user-friendly, accessible to non-microbiologists) are the resazurin technique and the optical density technique.

In the resazurin method, the overall change in colour or fluorescence is usually used as an indicator for concentration of actively respiring cells. In this method, to improve speed, the time taken to detect a colour change is used. The photocatalytic test surface would be inoculated, irradiated and the microorganisms recovered. Once recovered, the suspension would be mixed with a volume of resazurin and incubated for a short time. The colour change/fluorescence would then be determined by eye, or by using a spectrophotometer or fluorimeter. The time-to-detection (TTD) value would be compared to a control sample to identify any differences in cell number due to an intervention, or compared with a previously obtained standard curve, to relate to bacterial concentration.

In the optical density technique, a key advantage would be that the dynamics of growth could be seen in real-time using a growth analyser. This would

allow a real-time determination of the antimicrobial photocatalytic effect of the sample, as opposed to the treatment – enumeration sequence in the other methods described.

The growth analyser would consist of a spectrophotometer and incident light source, magnetic stirrer, stage, cuvette and irradiation source, similar to the testing setup described in Figure 20. This equipment would be placed inside an incubator at appropriate temperature. The photocatalytic test sample would be placed on top of the stage and the cuvette filled with a growth medium, such as nutrient broth.

The amount of light absorbed by the broth (the 'absorbance') would be recorded by spectrophotometer software and set as zero. Then, the broth would be inoculated with a known number of bacteria and the irradiation source and magnetic stirrer switched on. As the bacteria divide, the broth will become more turbid and therefore the absorbance would increase. The test sample would be activated by the irradiation source, killing bacteria. By recording the changes in absorbance, the changes in bacterial concentration can be observed. This plot could then be compared to the controls; the activity of the photocatalytic test piece would be inferred by the difference in growth dynamics compared to control.

Both proposed methods described above would be beneficial in determining the antimicrobial photocatalytic effects of surface coatings, more rapidly and with more accessibility than the previously established BS ISO derivatives.

6.0.2 – Chapter structure

This chapter pertains to the development of rapid methods. Two methods were identified as having potential and so these will be presented separately. The first method presented was based on the optical density growth monitoring techniques and is shown below in an iterative methods-results-methods format. The second test developed was based on the resazurin test, with different sensitivities and applications forming separate 'tiers' of the test.

6.1 – Optical density monitoring assay

The aim of the optical density monitoring method was to identify changes in growth behaviour *in situ* and in real time. This would enable rapid identification of photocatalytic-antimicrobial properties, without the need for separate incubation or culture steps; it can be thought of as a modification of the methylene blue style test.

As optical density is effectively an analogue for biomass (and therefore total cell number), this method does not enumerate the number of viable cells. Rather, any changes to typical growth dynamics can be assessed in comparison to a control. These changes can include the length of the stationary phase, the rate of reproduction/doubling time in the exponential phase, or the total increase in absorbance. In the developed method, photocatalytic-antimicrobial properties could be inferred by comparing a putative photocatalytic-antimicrobial sample with an inactive control and assessing the differences in growth dynamic.

6.1.1 – Assessing normal growth conditions

The aim of the method was to detect real-time changes in the growth dynamics of a cell population due to the action of an intervention. Similar systems have been previously used to identify the effects of interventions such as antibiotics, bactericidal compounds and reactive oxygen species (Stubbings *et al.*, 2004; Maia *et al.*, 2016); in the context of this project, the inactivation of cells caused by photocatalytic intervention could be determined by changes in growth dynamics.

To determine deviations from typical growth dynamics, these first had to be established and the growth analyser instrument tested. To that end, the growth conditions were first established with no interventions in the following experiment.

6.1.1.1 - Method

A test rig similar to the methylene blue rig described in *section 4.0.4.5* was used. A cuvette (growth chamber) and spectrophotometer inside a large incubator (set at 37 ^{0}C) were used to monitor the absorbance over time. The 45 mm x 45 mm x 42.5 mm cuvette and magnetic stirrer bead were sterilised via washing and rinsing with 70 % ethanol solution, followed by rinsing with sterile water. The cuvette was then fitted in a bespoke cuvette holder, with fibre optical patch cables connected to a tungsten-halogen incident light source and a computer with Spectrasuite data-logging software. A standardised washed cell suspension was prepared as per *section 5.0.2.3*; the cuvette was then filled with 32.5 mL of sterile nutrient broth and 3.5 mL of 1x10^8 cfu mL-1 *E. coli* cell suspension, after which a clear, clean petri dish lid was placed on top of the cuvette. The incident light source was switched on, the incubator set to 37 ^{0}C and the magnetic stirrer plate switched on at 400 rpm. The spectrophotometer software was previously calibrated against the mixture described above and these files were loaded into the software. The absorbance of the λ=600 nm peak was monitored and recorded for 18 hours, with a reading taken once per second. After 18 hours, the data were exported from Spectrasuite into Excel; the change in absorbance intensity was determined according to equation (18).

$$\frac{Abs_t}{Abs_0}$$

(18)

Where Abs_t was the absorbance at a given time and Abs_0 was the absorbance at t=0 h. This ratio was plotted against time.

Concurrently, at t=0 h, 1 h, 2 h, 4 h, 6 h and 18 h, 0.5 mL aliquots were removed from the cuvette and mixed with 4.5 mL of sterile saline. This dilution was repeated 8 times to a final dilution of 10^{-8}. To enumerate the cells, a Miles-Misra method of plate inoculation was performed from the dilution series (Miles *et al.*, 1938; Hedges, 2002). This method utilises fewer

agar plates by reducing the inoculum volume enabling more than one dilution to be inoculated onto one agar plate (but is less accurate than methods that utilise a larger inoculum volume). Each agar plate was divided into eight sectors and labelled according to the dilution series. A volume of 20 µL of each dilution was inoculated onto the corresponding plate section and allowed to dry – this was done in duplicate. Plates were inverted and incubated at 37 ^{0}C for 18 hours, prior to enumerating the cells via colony counting.

Preliminary experiments showed that undiluted broth caused excessive growth outside the scope of the spectrophotometer. To this end, the experiment was repeated, but with a more dilute broth – all aspects remained the same, except that the sterile nutrient broth was diluted 1:8 with sterile saline (known as 1/8th broth).

6.1.1.2 – Results and discussion

The growth analyser adequately recorded and displayed the growth dynamics of the cells (Figure 73). The full-strength broth caused off-scale readings and stochastic variations in peak absorbance intensity after around 14 hours, which are likely due to the number of cells causing excessive light scattering for the instrument. This was not seen when the 1/8th broth was used, as this limited the cell number to within the range of the instrument, despite similar numbers of viable cells. As the growth analyser showed promise in modelling growth curves, it was taken forward for use with an intervention.
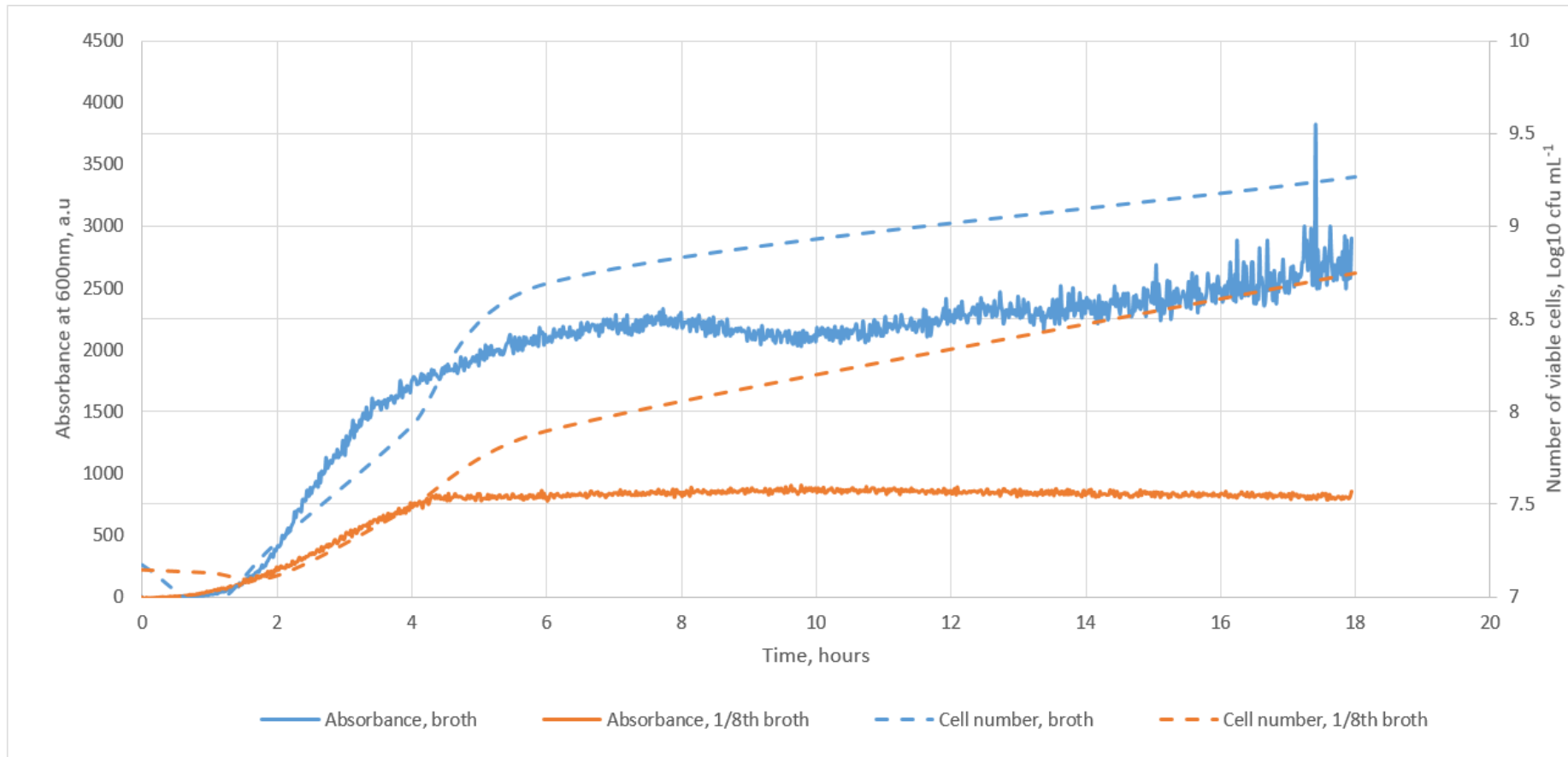
Figure 73: Growth dynamics of *E. coli* in full strength broth (blue) and broth diluted 1:8 with sterile saline (orange). The absorbance of the suspension is indicated on the left-hand axis, while the number of viable cells is indicated on the truncated right-hand axis. The full strength broth had greater absorbance and variability in absorbance, compared to the 1/8th broth. Despite the difference in broth concentration, there was only approximately a half-log difference in number of viable cells.

6.1.2 – Effect of UV irradiation on the viability of planktonic cells

To validate the growth analyser and ascertain its concordance to changes in growth dynamics, a suitable intervention first had to be selected. Titania-coated glass coupons were selected for use as a model intervention, therefore, UV irradiation was used throughout this section. To that end, a series of experiments were performed assessing the effects of UV irradiation on bacterial viability.

As the cells in the growth analyser would be planktonic, the effect of UV on planktonic cells was ascertained. Furthermore, the effect of the concentration of growth medium was investigated. To determine the effect of UV irradiation on planktonic cells (as would be the case in the growth analyser) and the effect of the liquid medium, the following experiment was performed.

6.1.2.1 – Method

Six sterile petri dishes were placed on six magnetic stirrer plates in a class 2 safety cabinet. A sterile magnetic stirrer bead was placed into each dish and a volume of 20 mL of sterile nutrient broth was aliquoted into two of the petri dishes; the same was done for 1/8th broth and sterile saline. A UV lamp with emission peak of λ=368 nm (Camag Dual Wavelength UV Lamp, Camag Scientific, Wilmington) was suspended 26 cm above the dishes. A screenshot of the spectrum for this lamp is shown in Figure 74.
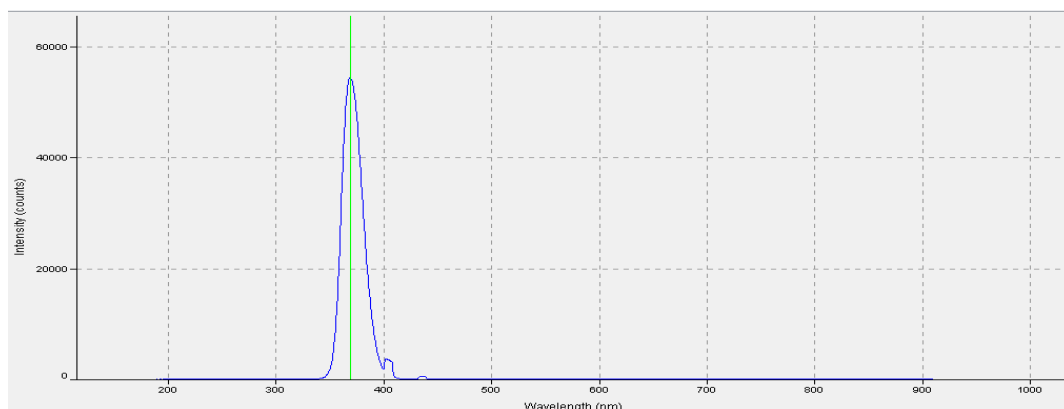
Figure 74: Spectrum of emission of the Camag lamp. The main emission peak at λ=368 nm is highlighted with the green line.

A standardised washed cell suspension was prepared as per *section 5.0.2.3* and 5 mL of a 1×10^8 cfu mL^{-1} *E. coli* suspension was aliquoted into each dish. One of each of the dishes containing the different media was occluded using aluminium foil, to act as a dark control. The magnetic sitter plates were switched on at 400 rpm and the UV lamp switched on.

At t=0 h, 2 h, 4 h, 6 h, 8 h and 24 h, 100 µL aliquots were removed from each dish and mixed with 900 µL of sterile saline in 1.5 mL Eppendorf Tubes (Eppendorf Tubes 3810X, Fisher Scientific, Hampton), previously sterilised via autoclave at 121 ^{0}C for 20 minutes. This ten-fold dilution was repeated eight times until a final dilution of 10^{-8}, plated out onto sterile nutrient agar according to the Miles-Misra method, incubated and counted as described in *section 6.1.1.1*.

6.1.2.2 – Results and discussion

Increases in cell number with time were noted for the broth-suspension and the 1/8th broth-suspension, regardless of irradiation status. No such increase was observed for the non-irradiated saline-suspension, but neither was a striking decrease in viability noted over 24 hours. However, the irradiated saline suspension showed a reduction in the number of viable cells, with a level below the limit of detection after 24 hours (signalling eradication). This can be ascribed to the action of the UV irradiation (Figure 75). It is interesting to note that the rate of inactivation was slow, with a 5-log reduction in viable cells observed after 8 hours.
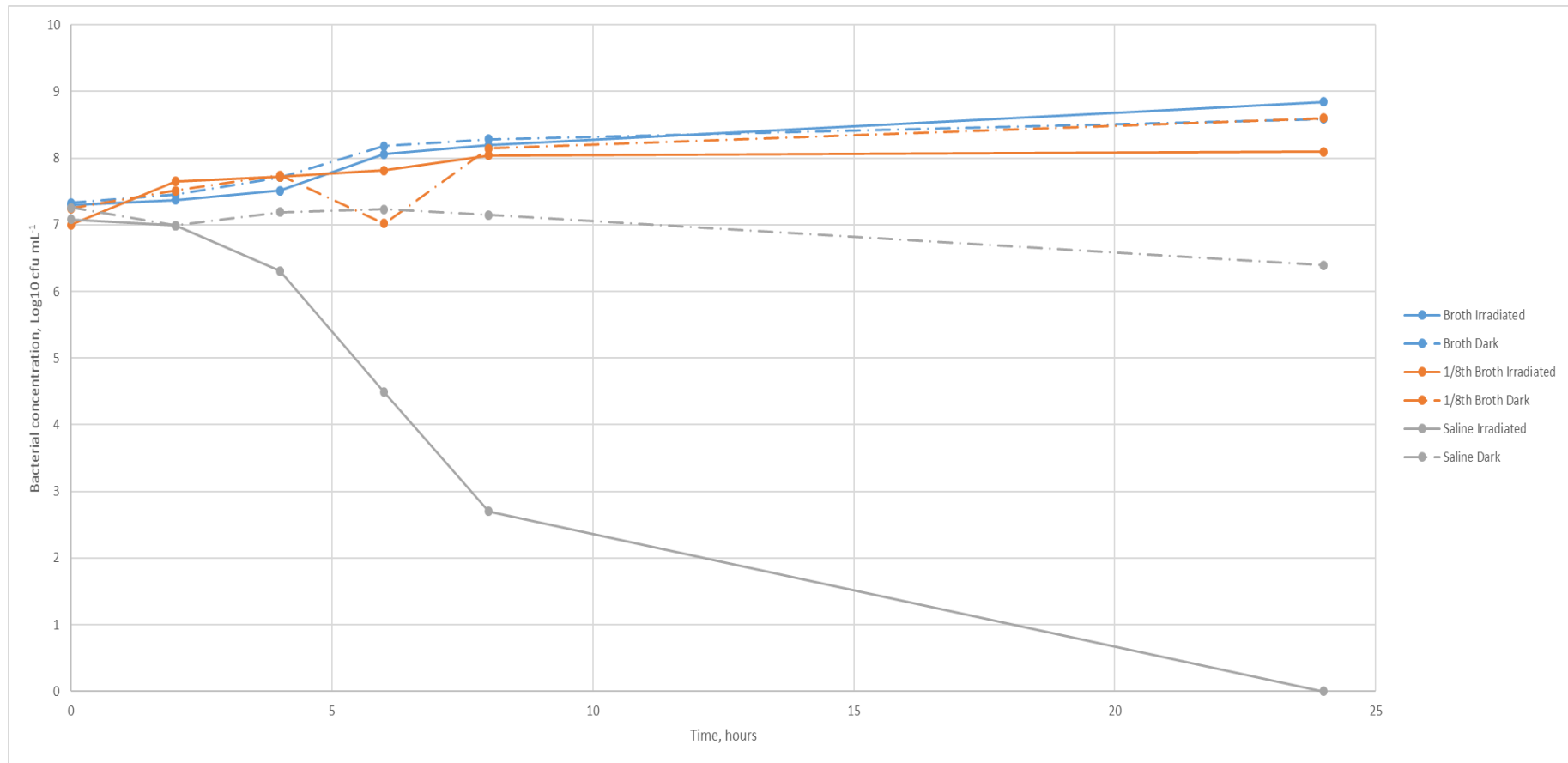
Figure 75: Changes in number of viable *E. coli* over 24 hours with and without UV irradiation, in nutrient broth, dilute nutrient broth, or saline. Irradiating the suspension did not appear to affect the number of viable cells, except for when saline was used as the medium; in this case, there was an approximate 4-log drop in number of viable cells after six hours and inactivation below the level of detection after twenty-four hours. N=1.

This could be related to the specific UV emission wavelength of the lamp used; UV sterilisation is usually achieved by using lamps with shorter wavelength, typically less than 280 nm. This UV subtype is termed UVC, which contrasts with medium-wavelength UVB (280-315 nm) and longer-wavelength UVA (315-400 nm). The greater inactivation effects of UVC occur due to the greater absorbance of this wavelength range by DNA; as UV inactivates cells via direct DNA damage, the greater absorbance causes more effective inactivation (Kim *et al.*, 2016; Murashita *et al.*, 2017). Therefore, the slow reduction in viability observed in the saline suspension could be due to the low absorption of the UVA by the DNA.

Nevertheless, these results show that broth, even when dilute, has a seemingly protective effect from the UV wavelength used. It could be that due to the wavelength used, the 'killing time' of the UV is longer than the doubling time of the *E. coli*, which would lead to an overall increase in the concentration of viable cells instead of a decrease. Alternatively, this may be because the addition of broth causes excessive scattering of the UV photons, potentially causing attenuation or redshifting effects, reducing their energy and reducing their bactericidal effect. However, due to a lack of experimental repeats, caution should be used when interpreting these results.

6.1.3 – Effect of medium concentration on intensity of UV

As mentioned in *section 6.1.2.2*, the medium could have attenuated the UV to the extent that it was no longer able cause inactivation of bacteria. The intensity of the UV through various media was explored in the following experiment.

6.1.3.1 – Method

The spectrophotometer patch cable was held in a clip and faced towards the Camag UV lamp, which was suspended 26 cm above a petri dish holder. The UV lamp was switched on and the intensity of the peak at $\lambda = 368$ nm

recorded. A clean, empty petri dish was placed onto the holder and the intensity recorded again. This was repeated for a petri dish filled with 20 mL of nutrient broth, 1/8th broth and saline. The data were inputted into Excel and the percentage reduction in intensity calculated for each condition compared to the first intensity measurement.

6.1.3.2 – Results and discussion

The intensity of the wavelength at λ=368 nm reduced with increasing concentration of medium. The maximum decrease in UV intensity was 21.87 %, observed when the full-strength, undiluted nutrient broth was used (Figure 76).
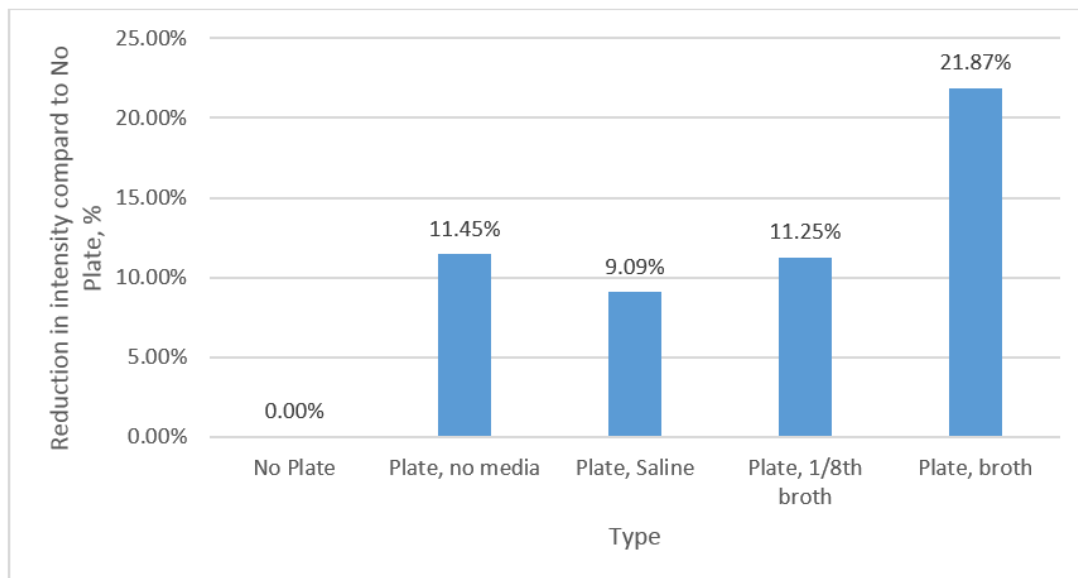
Figure 76: Percentage reduction in UV intensity with different media. The plate with no medium, plate with saline medium and plate with 1/8th broth medium exhibited similar reductions in the intensity of UV (11.45 %, 9.09 % and 11.25 % respectively). However, the plate with the full strength broth however exhibited a 21.87 % reduction in intensity, indicating potential dampening or scattering effects.

The saline and 1/8th broth reduced the intensity by 9.09 % and 11.25 % respectively, which was a similar to having a petri dish with no medium present (11.45 % reduction). These similarities indicate that the 1/8th broth is unlikely to attenuate the UV effects compared to saline, suggesting that when reductions in number of viable cells in 1/8th broth are not seen, it is not due to excessive scattering of the UV. Other factors, such as the specific UVA wavelength used in these experiments, must be considered for the lack of bactericidal effects observed.

While the reduction found to be caused by the broth is striking, it must be considered carefully; due to the direct/planar nature of the experimental setup and spectrophotometer, it is unknown whether the reductions observed are due to absorption, scattering, or other reflections away from the detector; reductions observed may not correspond to actual reductions of UV in the system (Mamane *et al.*, 2006). However, no additional peaks were observed with the addition of the media, indicating that no/minimal redshifting of the UV wavelength occurs. This implies that the photons retained their energy and therefore should be able to exhibit bactericidal properties.

This observation then suggests that the bacteria may be replicating faster than they are becoming inactivated; their doubling time is shorter than the UV killing time, which may be due to the ineffective bactericidal properties of UVA.

6.1.4 – Effect of titanium dioxide nanoparticles on the viability of planktonic cells

As the results from the previous viability experiments show, broth, even when dilute, nullifies the bactericidal effect of the UV (which was demonstrated in the saline suspension). This was then inferred to be because of a shorter doubling time compared to the UV kill-time. To investigate these possibilities, the effect of an additional stressor was studied. Titanium dioxide nanoparticles are well suited to the inactivation of planktonic cells (Verran *et al.*, 2007; Cai *et al.*, 2014); if the UV irradiation could activate titanium dioxide nanoparticles incorporated into the planktonic testing setup and demonstrate reductions in number of viable cells, then it could be inferred that the bacteria are not shielded in some way from the UV, nor that the UV does not reach/act upon the components of the testing setup.

The activation of the nanoparticles would cause ROS to be present throughout the suspension, reducing the number of viable cells in the suspension. The action of the nanoparticles could reduce the 'killing time' to below that of the doubling time, leading to observable reductions in viability. This has implications for the applications of the growth analyser. This experiment was performed to ascertain the presence of antimicrobial effects.

6.1.4.1 – Method

The method of Verran *et al.* (2007) was adapted for this experiment. A 0.2 % *w/v* concentration of titanium dioxide nanoparticles (Titanium (IV) oxide nanopowder [21 nm], Merck, Hampton) in sterile water was prepared. The petri dish-based setup described in *section 6.1.2.1* was used for this experiment, except that only sterile saline and 1/8th broth was used. A volume of 16.5 mL of either saline or 1/8th broth was added to sterile petri dishes. A standardised washed cell suspension was prepared as per *section 5.0.2.3*; 1 mL of a 1×10^6 cfu mL^{-1} *E. coli* suspension was mixed with 2.5 mL of 0.2 % titania nanoparticle suspension and then added to each dish. The lower inoculum load was used to limit the rate of increase in cell number, allowing more time for the nanoparticles to act. One of each of the dishes containing the different liquids was occluded using aluminium foil, to act as a dark control. The magnetic sitter plates were switched on at 400 rpm and the UV lamp switched on.

At t=0 minutes, 15 minutes, 45 minutes and 60 minutes, 100 µL aliquots were removed from each petri dish, diluted, plated, incubated and enumerated as described in *section 6.1.1.1*.

6.1.4.2 – Results and discussion

The number of cells recovered from the irradiated, saline-containing petri dish after 15 minutes was below the level of detection (Figure 77). Similar reductions in the number of viable cells recovered were observed on the irradiated 1/8th broth containing petri dish after 60 minutes, while no striking reductions were observed for the non-irradiated samples.
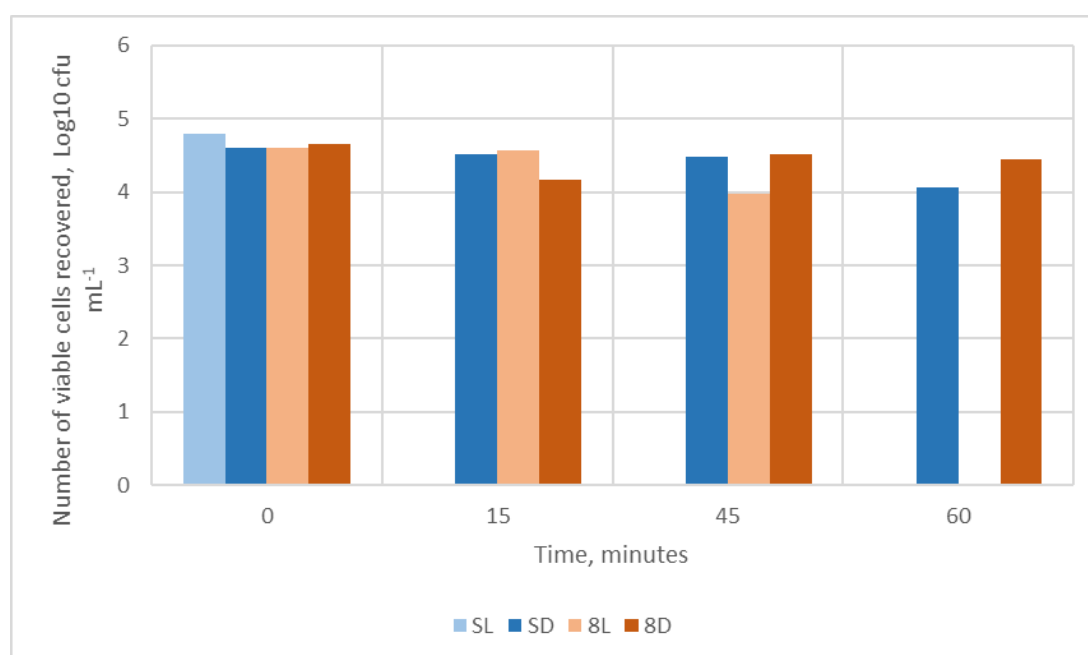
Figure 77: Changes in number of viable cells following treatment with 0.02 % titania nanoparticles over one hour. S = saline medium; 8 = 1/8th broth medium. L= irradiated with UV; D= not irradiated. After 15 minutes, the number of viable cells in the irradiated saline medium were reduced to below the level of detection. After 60 minutes, the number of viable cells in the 1/8th broth medium was reduced to below the level of detection; no striking changes were observed for the non-irradiated samples. N=1.

This indicates that the nanoparticles were able to cause inactivation of microorganisms, even in the presence of the 1/8th broth. This suggests that the UV is not attenuated by the 1/8th broth to an extent that it cannot activate the nanoparticles, although the data should be interpreted cautiously due to lack of repeat experiments.

However, visual inspection found that this concentration of nanoparticles was quite turbid; preliminary studies using the growth analyser showed stochastic changes in absorbance typical of excessive light scattering. The concentration of nanoparticles was reduced using 10-fold serial dilution until these stochastic changes subsided, which was at 0.0002 % *w/v*. The

antimicrobial potential of a suspension of nanoparticles at this concentration was investigated.

6.1.4.3 – Method

The above experiment was repeated, except that the concentration of nanoparticles in the petri dish was 0.0002 %. Furthermore, the experiment was monitored over a longer time, with 100 µL aliquots removed, diluted and plated at t=0 h, 0.5 h, 1 h, 2 h, 8 h and 24 h. As the bactericidal effects of the nanoparticles had been confirmed via the reduction of bacterial viability in saline, no saline trials were conducted using the lower nanoparticle concentration. Instead only 1/8th broth was used, to better simulate the growth analyser environment.

6.1.4.4 – Results and discussion

In contrast to the previous experiment using the higher concentration of nanoparticles, no reductions in viability were observed over one hour using the 0.0002 % nanoparticle suspension. Furthermore, the number of viable bacteria increased over the 24 hours, due to replication. This is despite the presence of the nanoparticles and irradiation by UV (Figure 78).
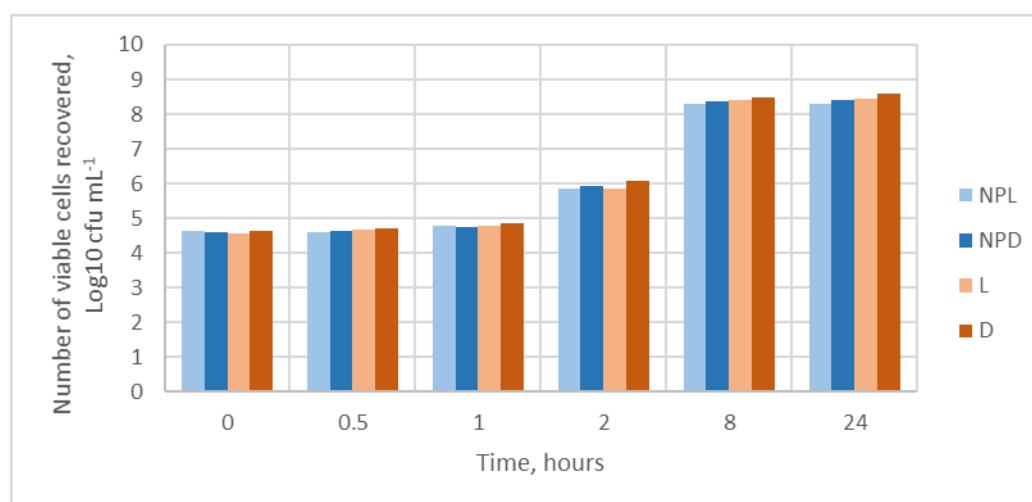
Figure 78: Changes in number of viable cells following treatment with 0.0002 % titania nanoparticles over 24 hours. NPL = irradiated nanoparticles; NPD = non-irradiated nanoparticles; L, D = UV-irradiated and dark controls. At this concentration of nanoparticles, no differences were observed between the irradiated suspensions and the non-irradiated suspensions. N=1.

At this concentration, titania nanoparticles did not cause inactivation of bacteria. Therefore, the antimicrobial effects of the titania nanoparticles are

unable to be used as a verification mode for the development of the growth analyser, nor can their effects be studied using the growth analyser. Bactericidal concentrations of nanoparticles cause stochastic variations in absorbance typical of excessive light scattering, whereas when the concentration of nanoparticles is reduced to accommodate this, any bactericidal properties are obfuscated by increases in bacterial cell concentration. However, due to the lack of experimental repeats for this experiment, this may not be entirely representative and so data should be interpreted cautiously.

6.1.5 – Determining the effectiveness of the growth analyser

Despite results from the previous experiments indicating that the bactericidal effects of UV irradiation were nullified when using nutrient broth-containing media, the growth analyser was employed to ascertain whether any differences could be established between treatment and control, elucidating the usefulness and sensitivity of such a method.

6.1.5.1 – Method

The experiment performed in *section 6.1.1.1* was repeated, with the following modifications; two cuvettes were employed in parallel, in order to record the effects of an intervention and control concurrently. The UV lamp described in *section 6.1.2.1* was suspended 26 cm above the cuvettes and petri dish lids were used to cover the tops of the cuvettes; one lid was occluded using aluminium foil top prevent UV light ingress, therefore acting as a control. A photograph of this setup is shown in Figure 79 and a schematic diagram shown in Figure 80. Furthermore, 1 mL aliquots were removed at t=0 h, 2 h, 4 h, 6 h, 8 h and 24 h for plating and enumeration. Finally, the intensity of the absorbance at λ=600 nm was monitored for 24 hours. This experiment was conducted twice.
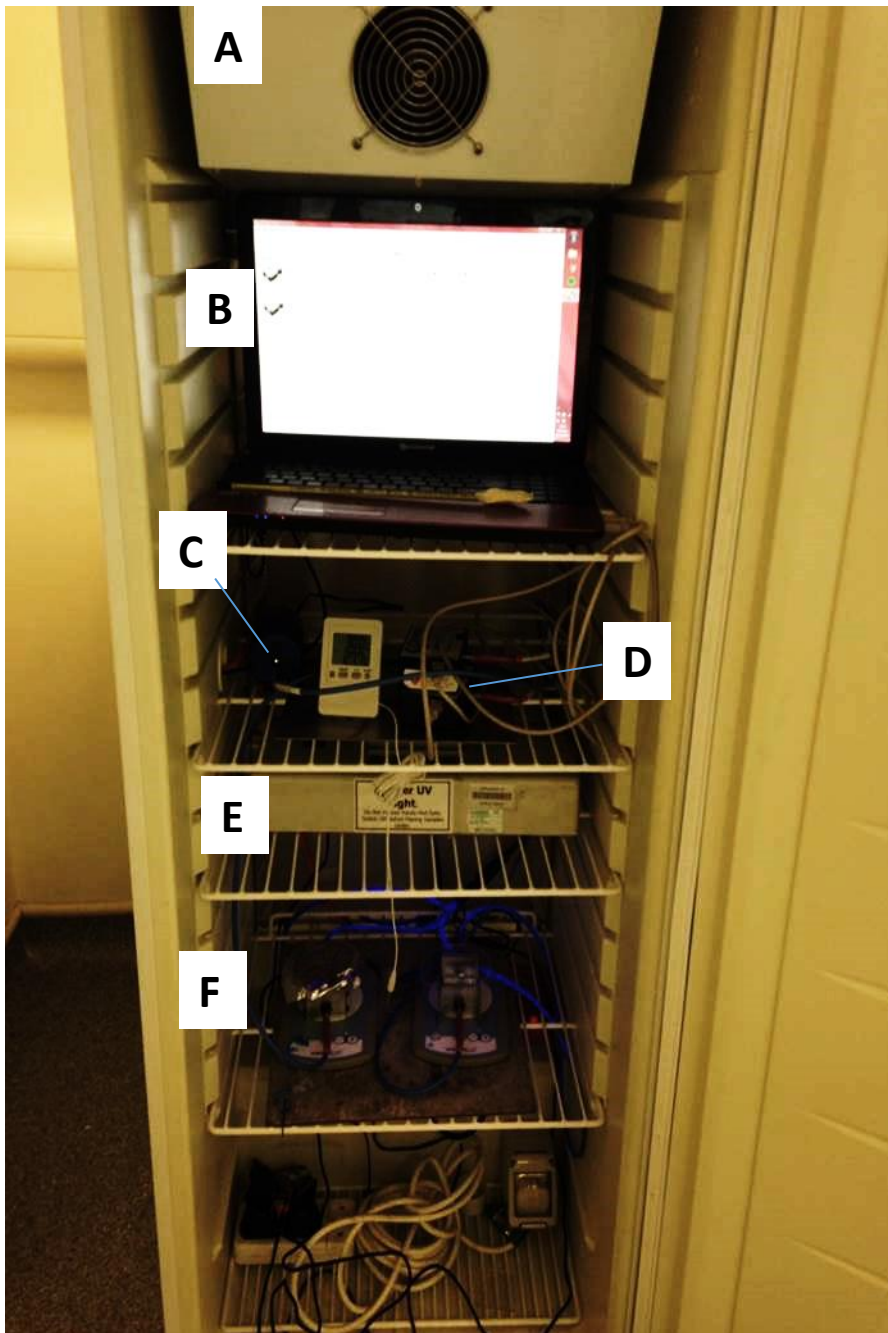
Figure 79: Experimental setup for the growth analyser. A: Incubator set at 37 ^{0}C. B: Laptop with data-logging software. C: Tungsten-Halogen incident light source. D: Spectrophotometers. E: Camag UV Lamp. F: Cuvette growth chambers on magnetic stirrer plates. The chamber on the left can be seen occluded by the foil-covered petri dish lid.
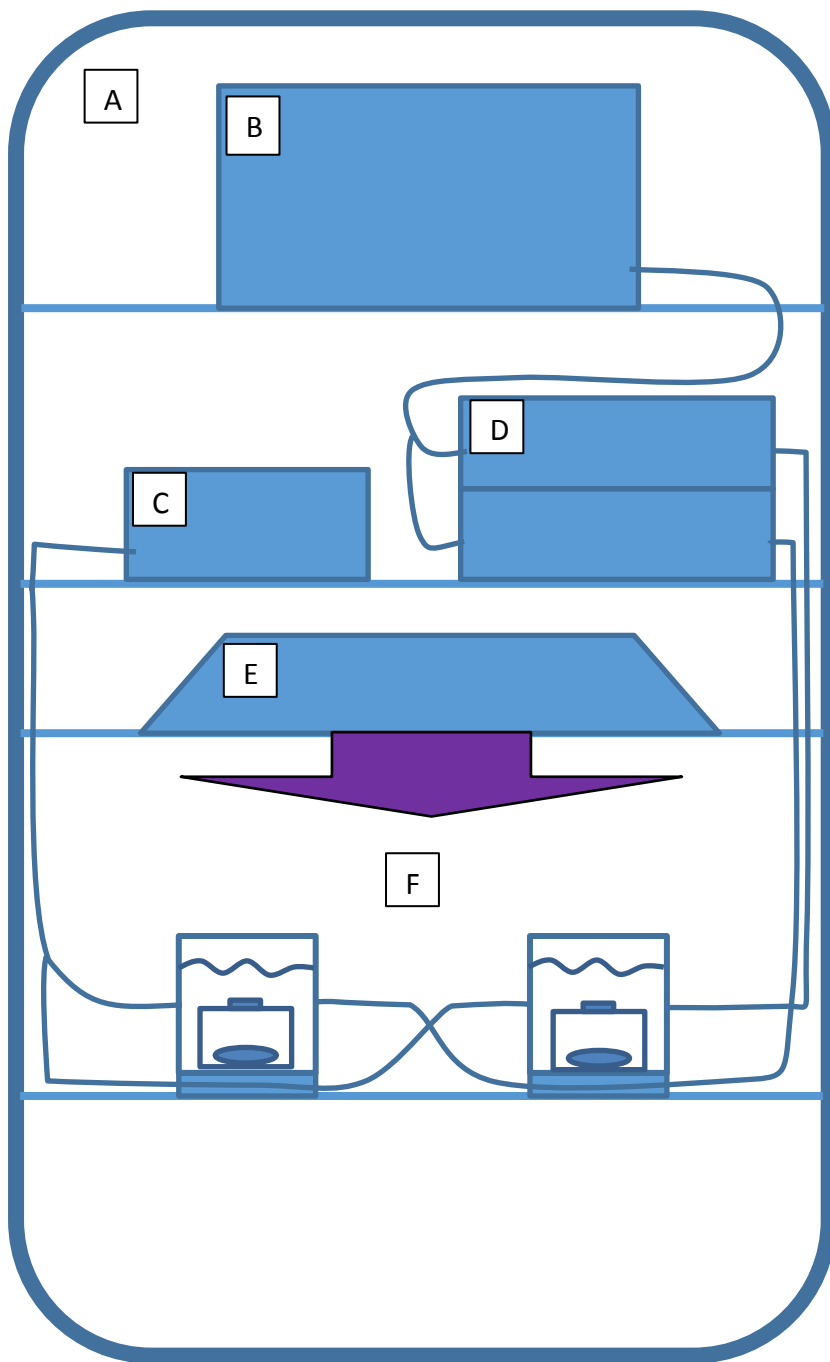
Figure 80: Schematic diagram of the setup for the growth analyser. A: Incubator set at 37 ^{0}C. B: Laptop with data-logging software. C: Tungsten-Halogen incident light source. D: Spectrophotometers. E: Camag UV Lamp. F: Cuvette growth chambers on magnetic stirrer plates. The chamber on the left can be seen occluded by the foil-covered petri dish lid.

6.1.5.2 – Results and discussion

The results from each repeat of this experiment are presented separately.

The first run of this experiment showed no striking differences in the number of viable cells at each time point between the UV-treated growth chamber and the control. However, the absorbance monitoring by the growth analyser was able to approximate these cell numbers (Figure 81), despite reporting some small differences in rate of division (gradient of curve) and overall cell number (overall maximum absorbance).

When the experiment was repeated, similar results were found. The UV did not reduce the overall viability of the organisms over 24 hours. Despite this lack of bactericidal action, the recorded absorbance did seem to correspond to the dynamics of the number of viable cells. However, after around 18 hours, the growth analyser began to report excessive stochastic variation in absorbance, so data after this time should be considered with caution. Nevertheless, before this point, both the UV and dark absorbance plots follow the dynamics of cell growth (Figure 82).
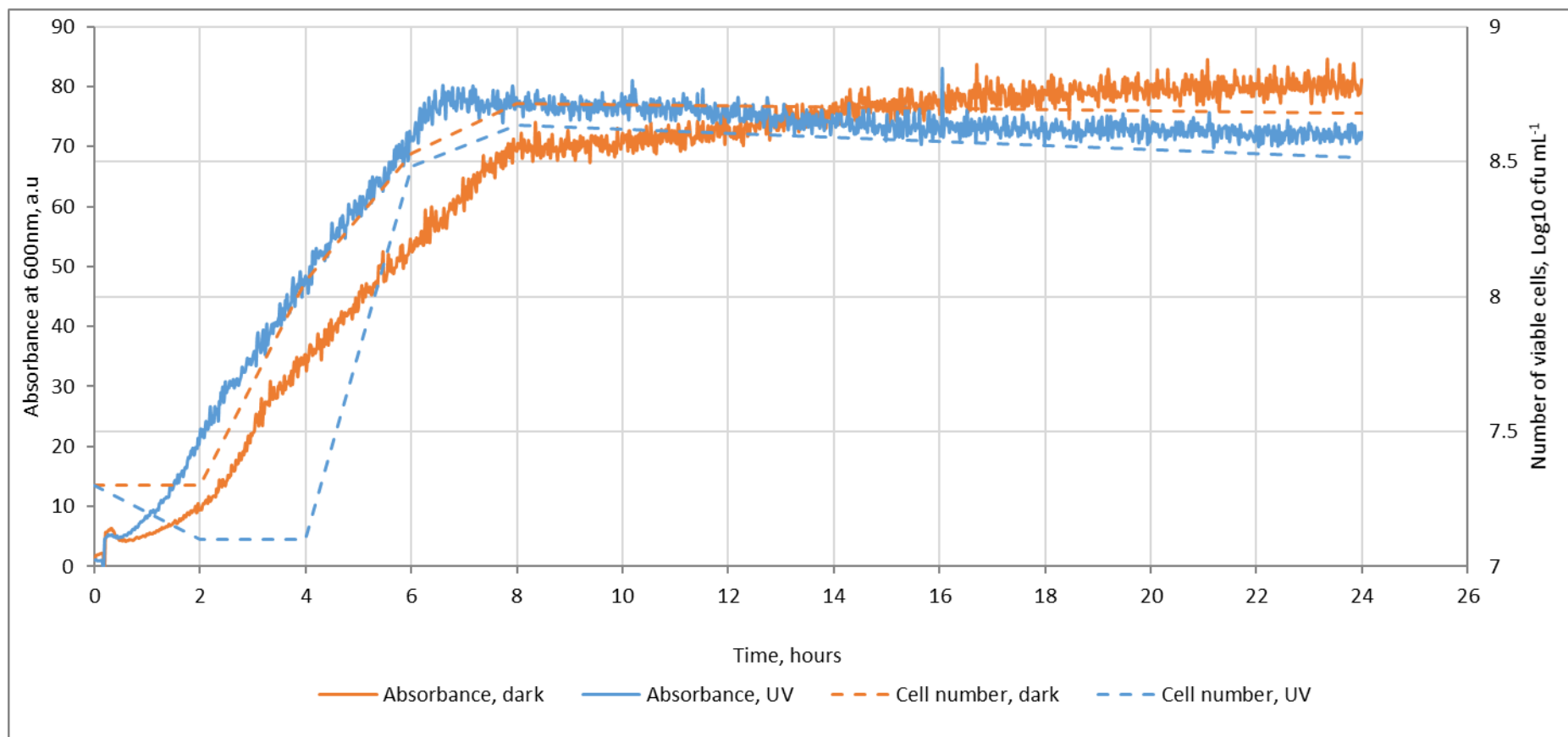
Figure 81: Changes in cell number and recorded absorbance at 600nm over 24 hours, with (blue) and without (orange) UV irradiation, for the first repeat. The absorbance of the suspension is indicated on the left-hand axis, while the number of viable cells is indicated on the truncated right-hand axis. The number of viable cells was similar between the irradiated and non-irradiated suspensions and despite small variate, the absorbance follows the growth dynamics.
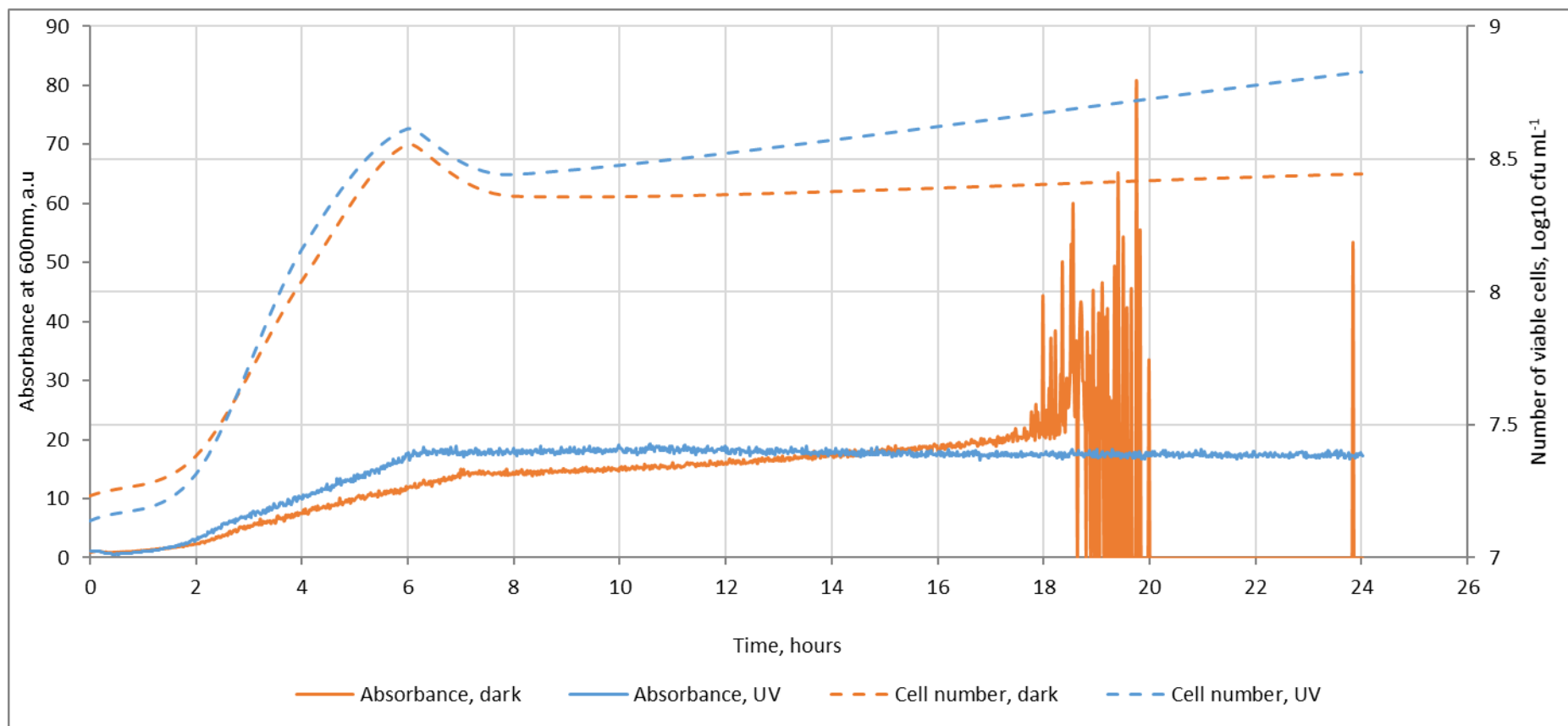
Figure 82: Changes in cell number and recorded absorbance at 600 nm over 24 hours, with (blue) and without (orange) UV irradiation, for the second repeat. The absorbance of the suspension is indicated on the left-hand axis, while the number of viable cells is indicated on the truncated right-hand axis. Similar to the first repeat, the number of viable cells was similar between the irradiated and non-irradiated suspensions. After around 18 hours, the spectrophotometry for the non-irradiated chamber began to detect large variations in absorbance. The source of the variation is unknown and as it cannot be shown that it is not an artefact or error of the instrument, data after 18 hours should be considered with caution.

Throughout these experiments, the UV irradiation did not exhibit bactericidal properties when the cells were in a nutrient-containing medium. Interestingly, similar findings have been reported by Jeon and Ha (2018), who found the bactericidal effects of UVA, UVB and UVC were lessened when peptone water was used as a medium, compared to phosphate buffered saline; this was ascribed to differences in absorption of the UV by the media. While this may be the case, consideration should also be given to other effects. For example, because UV causes cell death via DNA damage, the SOS response may be triggered in the cells (Abedi-Moghaddam *et al.*, 2004); the presence of nutrients may enable greater upregulation and expression of DNA repair mechanism genes such as RecA (Xu *et al.*, 2018), reducing the efficacy of the UV. This does not necessarily indicate that the UV is completely ineffective, but may suggest that bacteria are able to replicate faster than the UV causes inactivation.

This is especially salient when considering the UVA irradiation used in this experiment series. It has been shown that at lower doses, UVA damages cells rather than kills them; common effects are oxidative stress, protein damage and delayed metabolism. During favourable conditions, such as when presented with a nutrient-containing medium, cells may not become inactivated, rendering the UV treatment especially ineffective (Jeon and Ha, 2018). Indeed, the dose of UV required to inactivate bacteria is much higher with longer wavelengths than shorter wavelengths. In a review by Song *et al.* (2016), *E. coli* was treated with UV of various wavelengths and doses. The log reduction in viable cells was recorded and a dose-response calculated. The dose-response represents the dose of the UV wavelength required to reduce the viability of the cells by one log. It was found that there was a significant, strong positive correlation (R^2=0.808, p=0.008) between dose-response and irradiation wavelength, indicating that longer wavelengths required a much higher dosage to be as effective as shorter wavelengths (Figure 83).
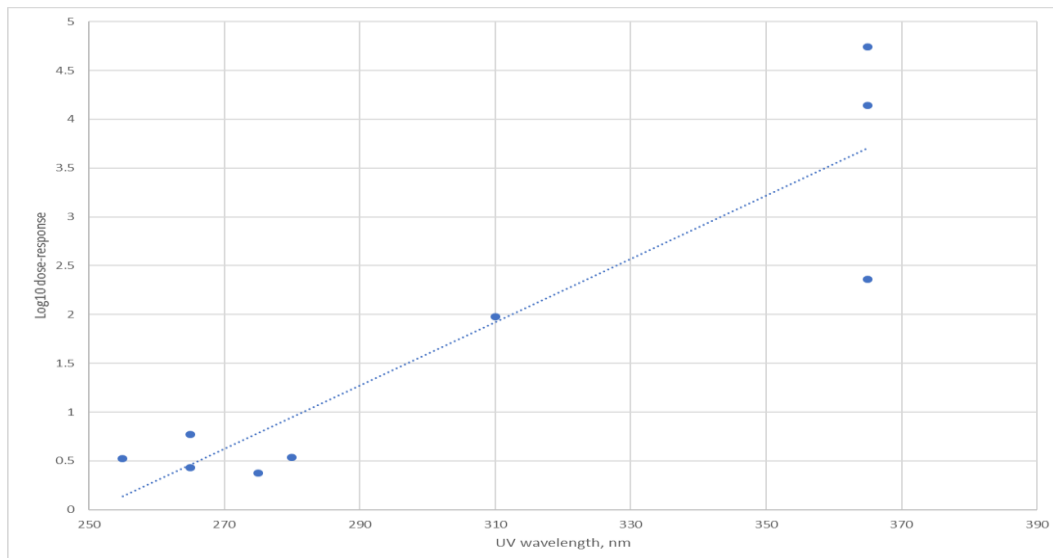
Figure 83: Relationship between UV wavelength and Log10 dose-response. A significant positive correlation was found ($R^2=0.809$, $p=0.008$). Shorter wavelengths in the UVC band have a lower dose-response than longer wavelengths in the UVB and UVA bands, indicating that a greater dosage is required to be effective when using longer-wave UV irradiation. Adapted from Song *et al.* (2016).

The growth analyser here showed potential for use as an approximation of cell number, in agreement with other authors (Stubbings *et al.*, 2004; Maia *et al.*, 2016). However, due to lack of evidence in detecting bacterial inactivation, it was not considered for further development during this project. A key limitation of the experiments here is the lack of experimental repeats; the experiments described in *sections 6.1.1.1, 6.1.2.1, 6.1.3.1 and 6.1.4.1* were not repeated, thus no statistical analyses could be performed. This can be attributed to the difficulty in performing parallel experiments and replicates and with the setup described, this would likely always be the case – repeat experiments would have to occur with either additional growth analysers or on separate occasions. What is clear is that *in situ* testing has multiple factors with complex dynamics. A successful *in situ* system must be able to measure the change in viability of the organisms; therefore, the inactivation source to be investigated must be efficacious enough to effect such a change. Future development of this method could address these issues by using more efficacious antimicrobials. Alternatively, a medium with lower nutrient concentration could be employed, which would not only increase UV permeability through the medium, but also reduce the replication rate,

allowing the effector to be detected (Shehata and Marr, 1971). Finally, a lower starting inoculum could be used to enable the action of an intervention to be discerned. Effectively, the UVA dosage used in this study was enough to activate titania and cause cell death via photocatalytic processes (demonstrated via the nanoparticle study in *section 6.1.4.2*), but not enough to cause cell death alone. Similar findings have been shown in the work of Clemente *et al.* (2019), which may indicate future promise for this method in the investigation the photocatalytic-antimicrobial properties of titania.

However, given current findings, the analyser was not deemed appropriate for the aims of this study; too many variables were unable to be controlled and too few replicates were possible. These are necessary for appropriate comparison of intervention/test and control. Furthermore, the experiments detailed in this section were only for the intervention of UV irradiation of planktonic cells – this inclusion of a photocatalytic surface would increase the number of variables (such as suspension volume, ROS diffusion distance, etc.) and add further complexity to the system.

6.2 – Resazurin assay

The resazurin assay detects the time taken for the dye resazurin to reduce to resorufin. This results in a colour change from blue to pink and a development of strong fluorescence. The shorter the time taken to detect a change, the more actively respiring microorganisms are present in the sample. Comparing the time taken to detect a change, or time-to-detection (TTD), of a test sample compared to a control sample can indicate the photocatalytic antimicrobial properties of the sample; if the control has a lower TTD than the test sample, all other parameters being equal, then the test sample can be considered to have fewer actively respiring microorganisms present. This can then be attributed to the photocatalytic antimicrobial properties.

While detection of the fluorescence is considered to be more sensitive than monitoring the colour change/absorbance (Rampersad, 2012), this may require more specialised equipment and is therefore less versatile and less easily adopted. In contrast, the colour change can either be assessed by eye (or imaging device such as a camera) and timer, simple spectrophotometer (with appropriate data logging software), or plate reader (with appropriate data logging and analysis software). These three measurement methods can be considered as 'tiers' of the test; assessing the colour change by eye acts as a basic screen for potentially photocatalytic surfaces and can be considered tier 1 – if the control has a lower TTD than the sample, the sample can be considered photocatalytically antimicrobial. Tier 2 of the tests would be considered a more sensitive screen than tier 1, facilitated by determining the TTD by spectrophotometer; improved sensitivity is achieved because the onset of the pink colour can be determined by monitoring the absorbance of the sample at $\lambda=570$ nm as opposed to judging the colour change by eye. Therefore, if the absorbance at $\lambda=570$ nm increases in the control sample before it increases in the test sample, the test sample can be considered to have fewer organisms present and therefore inferred to be photocatalytically antimicrobial. Tier 3 of the tests would be considered the most sensitive method and provides the most information; instead of acting

as a screen and differentiating between sample and control, tier 3 enables enumeration of the microorganisms present, in addition to easily incorporating more replicates for more reliable measurements. This would be achieved by comparing the TTD with a previously established standard curve of TTD for known bacterial loads.

6.2.1 – Method

6.2.1.1 – Preparation of reagents

A weight of 0.251 g resazurin sodium salt (Resazurin sodium salt powder, R7017, Merck, Gillingham) was mixed with 100 mL sterile distilled water to make a 10 mM solution. This stock solution was diluted 1:10 to make a 1 mM solution and then 1:2 to make a 0.5 mM solution (~0.01 % *w/v*) (Vazquez-Sanchez *et al.*, 2015). The resazurin solution was then sterilised via filtration using a 0.2 µm filter (Acrodisc Syringe Filter 0.2 µm, 4652, PALL, Port Washington).

Sterile saline at a concentration of 0.85 % *w/v* and sterile nutrient broth was prepared as described in *section 5.0.1*. A stock of "resazurin mix" was then prepared by aseptically combining the three ingredients (Table 6).

Table 6: Concentrations and accompanying volumes of reagents used to produce resazurin mix.

Material	Percentage by volume, %	Volume in one litre, mL
Sterile 0.85 % *w/v* saline	88.39	883.9
Sterile nutrient broth	10.49	104.9
Filtered 0.5 mM resazurin	1.12	11.2

A range of 'final' concentrations of resazurin (the concentration of resazurin with all other reagents during the detection step) have been reported in the literature, from 5 µM (Cai *et al.*, 2013) to 1800 µM (Corral *et al.*, 2013), but

typical concentrations used are around 100-120 µM (Khalifa *et al.*, 2013; Riss *et al.*, 2013; Munagala *et al.*, 2015)

The volumes and proportions detailed in Table 6 were used so that, for the spectrophotometer and plate reader-based assays, the 'final' concentration of resazurin would be ~4µM (~0.0001 % *w/v*), similar to Cai *et al.* (2013). This was selected to optimise the assay for the specific outcomes of this project; this concentration allowed less reagent to be used while maintaining effective detection, making the assay more cost-effective. Furthermore, the lesser-concentrated solution was more suited to the sensitivity of the spectrophotometer used in this setup.

This stock was dispensed aseptically into 100 mL volumes and kept refrigerated at 4 ^{0}C for a maximum of six months.

6.2.1.2 – Tier 1: assessment by eye of antimicrobial activity using resazurin

To determine whether tier 1 of the method could detect a reduction in viable microorganisms due to an intervention, the following experiment was performed.

Twelve 1 cm x 2 cm glass coupons were sterilised via autoclave at 121 °C for 20 minutes, after which six coupons were cleaned via isopropanol immersion and sonication as described in *section 4.0.1.* These six were then rinsed with sterile distilled water and left to air-dry. They were then coated with titanium dioxide via the reactive magnetron sputter deposition technique and annealed at 600 °C for 30 minutes, as described in *section 4.0.2* (Fisher *et al.*, 2014; Priha *et al.*, 2015; Ratova *et al.*, 2015). As in *section 5.0.3*, no additional sterilisation or disinfection protocol was performed on the coupons, to preserve coating integrity. However, the samples were handled aseptically after the annealing step, to reduce contamination.

Three each of the TiO_2-coated samples and glass samples were designated as the 'dark controls' for this experiment. Petri dishes containing the dark control samples were wrapped in aluminium foil (Aluchef premier foil, Terinex. Bedford) to prevent light ingress. The standard antimicrobial test was set up and performed as per *section 5.0.3.1*, except that instead of the tray being placed in a cooled incubator irradiated with fluorescent light, it was placed 30 cm below two 15 W, 365 nm UV lamps (UVP Blak-Ray UV Benchtop Lamp, Xx-15BLB, Fisher Scientific, Hampton) and irradiated for 24 hours, to activate the TiO_2 coatings.

After irradiation, each sample was removed and immersed in a sterile 5 mL 'bijou' bottle (Sterilin 129A Bijou Container, CON7522, SLS, Nottingham) containing 5 mL of resazurin mix, which was then vortex mixed for sixty seconds. To determine the number of viable cells present in the suspension, a typical dilution series was carried out. A volume of 0.5 mL was removed from the bottle and added to 4.5 mL of sterile saline, to give a 10^{-1} dilution. After agitation, 0.5 mL were transferred into a second bottle (10^{-2}) and the

process was repeated to 10^{-8}. To enumerate the cells, a Miles-Misra method was employed as per *section 6.1.1.1*.

Concurrently, the original bijou bottle, still containing the sample, was incubated at 37 °C in an orbital incubator at 180 rpm. The bijou bottles were inspected by eye for a colour change in the suspension every 60 minutes. Photographs were taken at t=0 h and after a change was observed.

6.2.1.3 – Tier 2: assessment by spectrometer of antimicrobial activity using resazurin

The second tier method uses the principle of the first, but instead of detecting the change in colour by eye, the intensity of absorbance of the resazurin reaction solution would be continuously measured at $\lambda=570$ nm. When the intensity of this absorbance increases, it signals the onset of the reduction of the resazurin to resorufin. The advantage of this method is that it does not a require a separate incubation step before assessing the colour change (as in tier 1), may improve reliability by continually monitoring for the reduction of resazurin to resorufin and can be used semi-quantitively to identify exactly when the reduction began to occur. This allows several samples to be compared against each other.

To validate this method, a system using a cuvette and spectrophotometer (connected to appropriate data-logging software) were used. Test samples and inocula were set up as per *section 6.2.1.2*. However, only two samples were used to demonstrate this test. One sample was a 1 cm x 2 cm uncoated glass coupon and the other sample was a 1 cm x 2 cm titanium dioxide-coated glass coupon, as per *section 6.2.1.2*. The inoculated titanium dioxide sample was irradiated with UV for 24 hours, according to all parameters described in *section 6.2.1.2,* with the inoculated uncoated glass coupon acting as a control.

After 24 hours, the coupons were immersed in 5 mL of sterile saline and vortex mixed for 60 seconds. After this, the resulting suspensions were diluted 10-fold eight times to a final dilution factor of 10^{-8}. The dilutions were then plated and enumerated as per the Miles-Misra technique described in *section 6.1.1.1.*

To determine whether the tier two test could detect a reduction in viability of bacteria, a spectrophotometer with data-logging software was used. A test rig similar to the one described in *sections 4.0.4.5, 6.1.1.1* and *6.1.5.1* was employed for this test. Two 45 mm x 45 mm x 42.5 mm cuvettes and magnetic stirrer beads were disinfected via washing and rinsing with 70 % ethanol solution, followed by rinsing with sterile water. The cuvettes were

filled with 31.67 mL of resazurin mix, fitted in bespoke cuvette holders and placed on magnetic stirrer plates, inside a large incubator set at 37 ^{0}C. Fibre optic patch cables were run from a tungsten-halogen incident light source to each cuvette holder and then to a spectrophotometer for each cuvette. The spectrophotometers were connected to a computer and data were collected and interpreted by Spectrasuite software. A volume of 3.33 mL of the original bijou that the test sample was recovered in was aseptically aliquoted and added to the cuvette – this was repeated for the non-irradiated control for the second cuvette. The use of these volumes allowed the concentration of the resazurin in the cuvette to be ~4 µM, as described in *section 6.2.1.1.* The magnetic stirrer plates were switched on at 400 rpm. The spectrophotometer software was previously calibrated against sterile resazurin mix and these files were loaded into the software, after which the intensity of the absorbance peak at λ=570 nm was monitored for 10 hours, with a reading taken once per minute. The change in absorbance was recorded and plotted as previously described in *section 6.1.5.1.*

After plotting, any differences in the time to detect the onset of the absorbance peak at λ=570 nm were determined by visual inspection of the chart. As this peak relates to the metabolism of present cells, onset of this peak was expected to be lower with increasing viable bacteria present.

6.2.1.4 – Tier 3: time-to-detection standard curve

The third tier of the resazurin method uses the principle of the second tier, but uses a microtiter plate instead of a cuvette and a plate reader instrument instead of a spectrophotometer. This allows many samples and replicates to be analysed simultaneously. As described, the TTD value obtained from a given sample can be compared to a standard curve of TTD against bacterial load, thus estimating actual viable microbial load of the sample. To this end, a standard curve of known bacterial load against the time taken to detect an increase in absorbance at λ=570 nm was produced.

A standardised washed cell suspension was prepared as per *section 5.0.2.3*. This suspension was serially diluted 1:10 eight times. A volume of 23.75 µL of each concentration was aliquoted into seven wells each of a 96-well microtiter plate (Sterilin 611U96 Clear Microtiter Plates, SLS, Nottingham). An equal volume of sterile saline was added to the remaining wells to act as a control.

A volume of 226.25 µL of resazurin mix was then added to each well of the plate. The microtiter plate was then loaded into the plate reader (FLUOstar Omega, BMG Labtech, Ortenberg). The plate reader was set to a temperature of 37 ^{0}C with double orbital shaking at 300 rpm. The absorbance of each well was measured at λ=570 nm every 7 mins for 24 hours and recorded by Omega data suite software (Omega and Mars, BMG Labtech, Ortenberg).

After 24 hours of monitoring, the data were imported into Microsoft Excel. The data were blank-corrected and then processed. Processing involved a series of Excel formulae that identified the TTD for each well in the microtiter plate, detailed further in *Appendix C.* Detection was logged when the absorbance in a specific well exceeded a critical value, which was the mean of the control values for that microtiter plate plus three standard deviations. A standard curve of TTD against the concentration of the initial inoculum was then produced.

6.2.1.5 – Tier 3: assessment by spectrometer and standard curve of antimicrobial activity using resazurin

After the standard curve was generated, the ability of the tier 3 test to determine photocatalytic antimicrobial effects was assessed using the photocatalytic samples described in *section 4.0.2.3* (molybdenum-doped, niobium-doped and undoped titania-coated glass coupons). These samples were assessed for photoactive antimicrobial properties using the standard antimicrobial test in *section 5.0.3.3* and using this method; the suspensions of cells from the coupons recovered at t=24 hours in *section 5.0.3.3* were used to assess the efficacy of this method. This was to allow comparison of antimicrobial effect determined by resazurin method with the standard antimicrobial test.

A volume of 226.25 µL of resazurin mix was aliquoted into each well of a sterile 96-well microtiter plate. This plate was kept in the dark until required. After the test coupons had been recovered into sterile saline at t=24 hours as previously described in *section 5.0.3.3*, a volume of 23.75 µL was aliquoted into four wells of the microtiter plate, such that each sample had four replicates on the microtiter plate.

The microtiter plate was then loaded into the plate reader. The plate was incubated, the absorbance measured and the data processed in the same manner described in *section 6.2.1.4*. After the TTD for each sample had been determined via the same processes as described, this was converted into a concentration for the initial inoculum using the equation obtained from the standard curve. The mean and standard deviation for the concentration of each sample type was calculated and was then compared to the corresponding cell number obtained via counting colonies on plates.

6.2.1.6 – Statistical analysis

Data were analysed for statistically significant differences, relationships and agreements as appropriate using IBM SPSS Statistics version 23. Data were analysed for normality using a Shapiro-Wilk test. Data that were not normally distributed were log-transformed to approximate a normal distribution. Normally distributed data was analysed using an ANOVA with post-hoc Tukey tests for pairwise comparison, or paired T-tests to identify the differences between groups. Data that were not normally distributed was analysed for differences between groups using a Kruskal-Wallis test with post-hoc Mann-Whitney U-tests for pairwise comparison, or Wilcoxon matched pairs tests to identify differences between groups. A Bonferroni correction was applied to reduce the familywise error rate as appropriate. Relationships between variables were investigated using linear regression models and Spearman's Rho correlation coefficients as appropriate. Agreement between measurement methods was assessed via intraclass correlation coefficient analysis. The alpha level for these tests was set to 0.05; differences, relationships and agreements were considered significant if $p<0.05$.

6.2.2 – Results and discussion

The results detailed below describe the implementation of the resazurin test after the coupons had been irradiated for 24 hours (Figure 84).
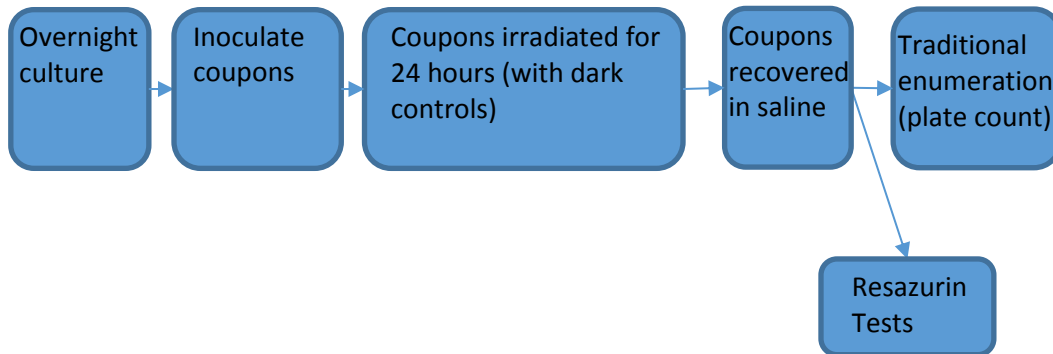
Figure 84: Flow chart describing the sequence of experimentation. Resazurin validation experiments took place after 24 hours of coupon irradiation.

6.2.2.1 – Tier 1: assessment by eye of antimicrobial activity using resazurin

Upon immersing the coupons into the resazurin mix after 24 hours irradiation, there was no immediate colour change. After 600 minutes, a colour change was observed in the bijoux containing in the non-irradiated coupons, but no colour change was observed in the bijous containing the irradiated coupons (Figure 85).
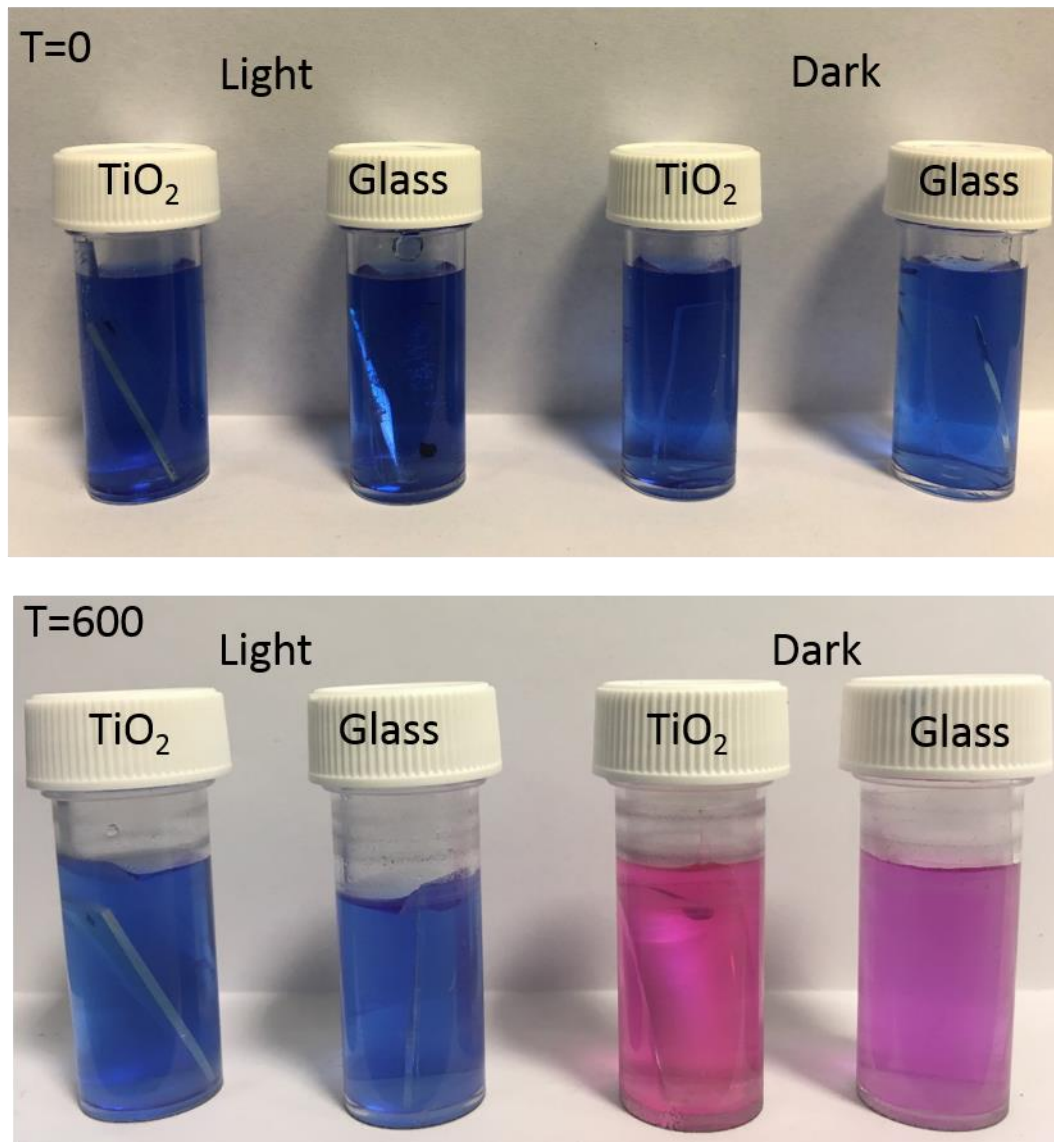
Figure 85: Colour change in the resazurin solution observed at time of recovery (T=0, top) and 600 minutes after immersion (t=600). The bijoux containing the non-irradiated coupons changed colour from blue to pink in response to the actively respiring bacteria present.

No colour change would indicate that there were no viable microorganisms present in suspension (or that there were so few that there was insufficient metabolic activity present to alter the colour of the resazurin). This was the case for both the titanium dioxide-coated samples and for the glass samples: UV irradiation is antimicrobial (Orlowska *et al.*, 2015) and any differentiation between the two surfaces in terms of antimicrobial activity could not be made in this case. However, for the non-irradiated samples, viable cells in the suspension were able to grow in the low concentration of nutrients present (via the diluted nutrient broth) in the resazurin reaction mix, thereby

decolourising the dye. In confirmation, few viable cells (between 10 and 100 cfu mL-1) were recovered from irradiated coupons, whereas significantly more cells ($p<0.001$) were recovered from the non-irradiated TiO_2 samples ($3.04\pm0.49\times10^5$ cfu mL^{-1}) and the non-irradiated glass samples ($2.78\pm0.77\times10^5$ cfu mL^{-1}), as shown in Figure 86.
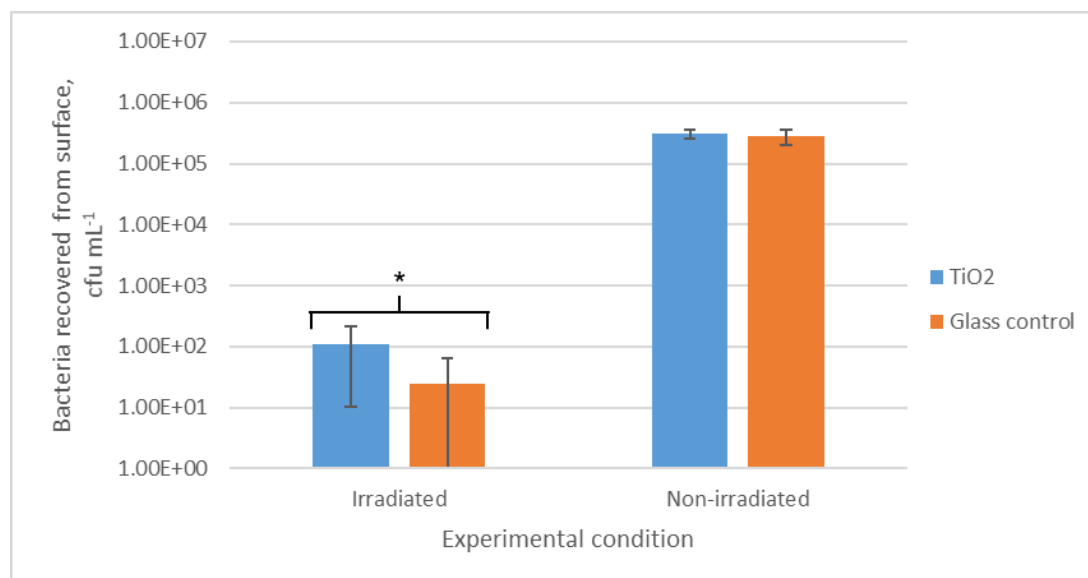
Figure 86: Viable cells recovered from each sample type 24 hours after inoculation. Brackets and * indicate significant differences from dark control ($p<0.001$). There were significantly fewer viable cells recovered from both irradiated titania and irradiated glass compared to the non-irradiated samples. N=6.

This indicates that the resazurin solution changed colour due to the presence of the viable cells. Few viable cells (up to 100 cfu mL^{-1}) were recovered from the irradiated samples and so the resazurin remained blue whereas many viable cells were recovered from the non-irradiated samples, causing the rezaurin to reduce to the pink/purple.

The chief advantage of this tier of the resazurin test is its simplicity and low cost. While only a qualitative method, it can identify reductions in cell number caused by an intervention using a simple redox dye and assessing a colour change by eye, with excellent agreement with established culture-and-count techniques. Furthermore, simple modifications such as including a digital automated camera with recording functions could make this test semi-automated and increase throughput (Borra *et al.*, 2009). Therefore, this test would be ideal as a first-stage screen for putative photocatalytic-antimicrobial

surfaces, usable by non-specialists from a variety of scientific and engineering backgrounds.

6.2.2.2 – Tier 2: assessment by spectrometer of antimicrobial activity using resazurin

The intensity of absorbance of the solution at λ=570 nm significantly increased with time for both the irradiated TiO_2 sample (r=0.99, p<0.001) and the non-irradiated glass sample (r=0.98, p<0.001) (Figure 87).
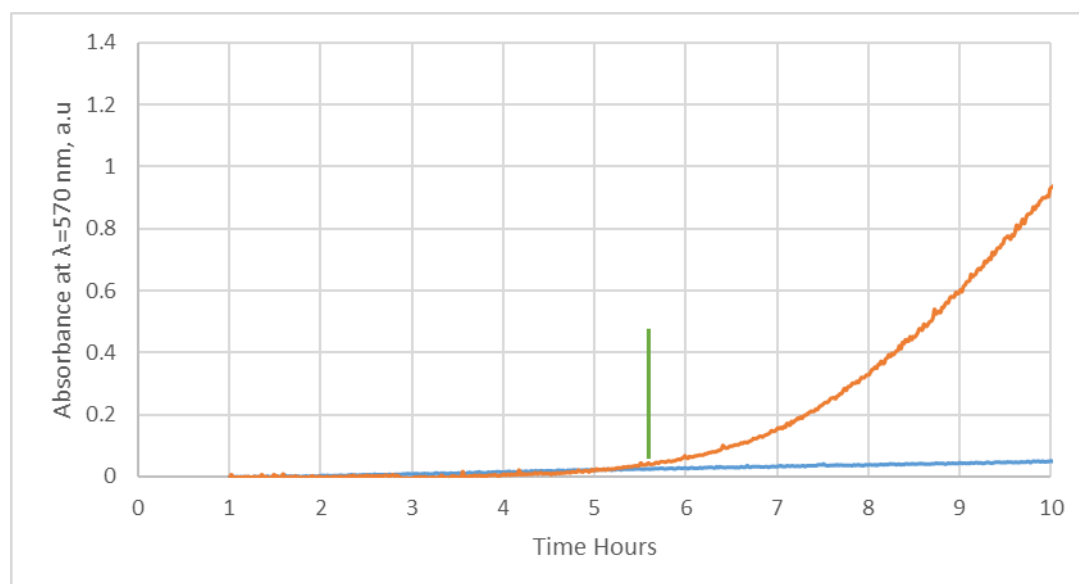
Figure 87: Absorbance of the resazurin mix at 570 nm for the irradiated sample (blue) and non-irradiated sample (orange). The vertical green line indicates the time when the intensity of absorbance for the non-irradiated sample exceeded the irradiated sample, known as the time-to-detection. In this case, it was around 5.5 hours.

This was expected, as resazurin will convert to resorufin under a variety of conditions, including exposure to light (Haggerty *et al.*, 2008). In this case, it is likely that the tungsten-halogen incident light source used in the spectrophotometer gave a small but significant background conversion. Despite this, a greater increase was seen in the non-irradiated glass sample.

Furthermore, the intensity of absorbance for the non-irradiated sample exceeded that for the irradiated sample at around t=5.5 hours, or 330 minutes, shown as the green line in Figure 87. This indicates that the time to detect an increase in absorbance was less in the non-irradiated sample. This is concordant with the number of viable microorganisms recovered from each sample, as more were recovered from the non-irradiated sample whereas any viable cells recovered from the irradiated sample were below the level of detection (Figure 88).
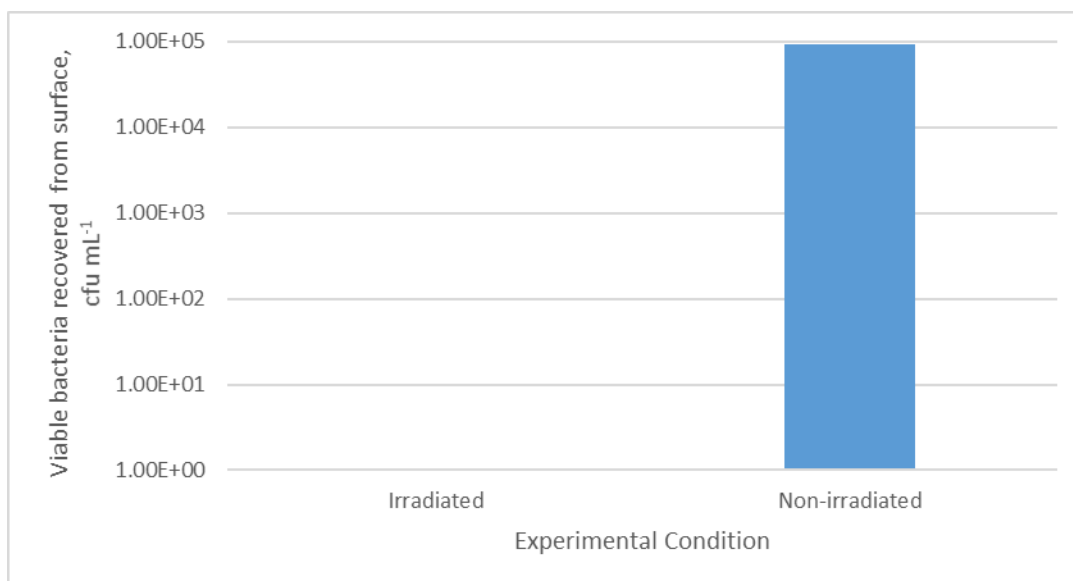
Figure 88: Number of viable bacteria recovered from the irradiated TiO₂ and non-irradiated glass surfaces. More viable microorganisms were recovered from the non-irradiated glass control sample than the irradiated TiO₂ test sample. N=1.

Therefore, it can be concluded that the greater magnitude of change and more rapid observation of change noticed in the non-irradiated sample, was due to the presence of more viable bacteria. This agrees with the results found for the tier 1 resazurin test. In contrast to the tier 1 test however, this test was more sensitive – a change was detected at 330 minutes compared with 600 for the tier 1 test, for similar cell numbers. This is likely due to measuring the absorbance at 570 nm as opposed to assessing colour change by eye; detecting the change in absorbance does not necessitate an observable colour change, which is a combination of the increasing absorbance at 570 nm and the decreasing absorbance at 600 nm. However, data for this experiment should be interpreted with caution, due to lack of experimental repeats.

Despite this, the tier 2 test may represent an improved sensitivity over the tier 1 test, as the tier 2 test permits semi-quantitative testing; two putative photocatalytic-antimicrobial surfaces can be assessed against a control and the TTD compared between them. As a shorter TTD is indicative of more viable cells, by inspecting the plot and determining the TTD, the surfaces can be compared in terms of reduction in cell number. Therefore, the surface with the greater TTD would have fewer viable cells and would therefore be the more photocatalytically antimicrobial.

Although more complex in setup and operation than tier 1, this tier represents advancements in terms of sensitivity and ability to semi-quantitatively describe the photocatalytic-antimicrobial potential of surfaces. However, the chief advantage of this test is the inexpensive and adaptable setup; the system used in this work was a modified version of the methylene blue test rig. As a key aim of the work was to develop rapid, simple tests suitable for non-microbiologists, this equipment was chosen as the setup (or similar setups used for methylene blue degradation tests) is likely to be familiar to research groups carrying out methylene blue tests and also minimise start-up costs for such groups.

While the results from this tier of the test are promising, the methodology presented here encountered some contamination issues – the experiment was performed four times, but only once did not experience contamination. The source of contamination was likely to cuvette and stirrer bead – the method of sterilisation (immersion in 70 % ethanol) may not have adequately inactivated all microorganisms present, thus when the broth was added, the adequate nutrients available permitted growth of the contaminant species in addition to the test organism. This could be ameliorated by using more effective disinfection and sterilisation protocols, including the use of an autoclave. However, these issues could dissuade the use of the tests by non-specialists and should be considered before implementation.

6.2.2.3 – Tier 3: time-to-detection standard curve

The time taken to detect the increase in absorbance of the λ=570 nm peak above the critical value significantly decreased with increasing inoculum load (Figure 89, R^2=0.952, p<0.001).
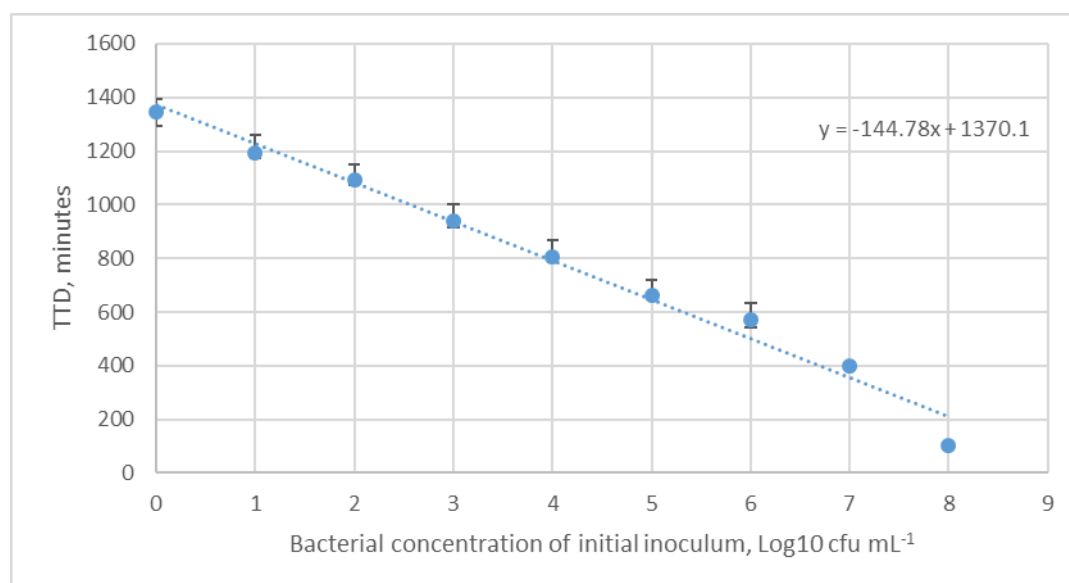
Figure 89: Standard curve of the initial inoculum concentration and the time taken for the absorbance to increase above the critical value. A significant strong linear relationship (R^2=0.952, p<0.001) was found between these variables. Data presented as medians and the 25th and 75th percentiles. N=20.

This is consistent with the findings for the other tiers of the resazurin test. A higher concentration of initial inoculum results in a shorter time-to-detection. This is because, if each cell has a specific metabolic potential, two identical cells will have an ideal combined metabolic capacity of twice the single cell. While cells from the same strain and culture may have variation in terms of metabolic capacity (Nikolic *et al.*, 2017), the relationship between Log10 inoculum concentration (cell number) and time-to-detection (metabolic capacity) was linear, as shown in Figure 89.

In other words, as TTD is related to the metabolic potential of the bacterial community present, it follows that the linear relationship observed is actually a representation of the metabolic needs of the bacterial community. Therefore, given similar cells, the number of bacteria present is represented; greater concentrations of cells lead to a greater concentration of respiratory and metabolic by-products, which therefore are more rapidly able to reduce resazurin to resorufin. This concurs with the work of Cai *et al.* (2013), who

similarly found that the time to detect the changes in the resazurin was related to the number of cells present. The relationship determined in this work had a function described by (19), where y is the TTD and x is the Log10 bacterial concentration of the initial inoculum.

$$y = -144.178x + 1370.1$$

<div align="right">(19)</div>

When rearranged for x, the function can be used to determine the Log10 initial inoculum concentration for an experimentally determined TTD, as shown in (20).

$$x = \frac{y - 1370.1}{-144.18}$$

<div align="right">(20)</div>

6.2.2.4 – Tier 3: assessment by spectrometer and standard curve of antimicrobial activity using resazurin

The concentration of viable cells recovered from the coupons was determined using the tier 3 resazurin method and traditional plate counting techniques. An intraclass correlation coefficient showed there was strong reliability and agreement between these methods (ICCC=0.939, 95% confidence interval=0.788-0.982, p<0.001). As can be seen in Figure 90, values reported via plate count were similar to values reported by the resazurin tier 3 method.

Figure 90: Agreement between enumeration via plate count techniques and the resazurin tier 3 method. TE: traditional enumeration; RT3: Tier 3 resazurin test. The majority of points are clustered at around 1x10^6 cfu mL^{-1}, due to the lack of strong bactericidal effects of the coatings. Nevertheless, significant strong agreement can be observed (ICCC=0.939, 95% CI=0.788-0.982, p<0.001). N=12.

When the data were grouped by sample type, there were few differences in number of cells detected between enumeration methods (Figure 91).

Figure 91: Agreement between the traditional culture and count technique and resazurin tier 3 technique. Brackets and * indicate a pair of measurements significantly different from each other (P<0.05). Significant differences in number of viable cells recovered were only noted for the TiO$_2$ L samples, but this small significant difference may not have noticeable real-world effects and should be extrapolated with caution. N=8 for TiO$_2$ L and D samples, 4 for Nb L and D samples and 2 for Mo L and D samples, due to limited sample numbers.

No significant differences in cell numbers were noticed between enumeration methods on any sample type, except for the irradiated titanium dioxide samples (t=-3.910, p=0.011). This may be related to variation in gene expression between cells (either via random mutation, or simply being at different points in their cell cycle), causing differences in metabolic potential between cells (Thattai and van Oudenaarden, 2004; Nikolic *et al.*, 2017). However, although the difference was statistically significant, it is very small, so extrapolating this to real-world differences should be considered with caution.

Similarly regarding variation in metabolic rate, when assessing the photocatalytic-antimicrobial properties of surfaces against different species, the metabolic rate of that organism must be considered; it will almost certainly differ to the model organism used in this study. As the reduction of resazurin to resorufin is dependent on not only the number of viable cells but also each cell's metabolic rate, it follows that a separate calibration curve must be produced for each model species of interest (Cai *et al.*, 2013). Therefore, future work could include the development of several standard curves for typical model and applied organisms of interest.

The photocatalytic treatment applied did not reduce the viability in most cases compared to control; only one sample (the irradiated molybdenum-doped titania) showed a reduction in viable cells after 24 hours treatment (as previously discussed in *section 5.1.2*). Moreover, the reduction was only ~2 Log_{10} cfu mL^{-1}, not complete eradication. While the detection of this reduction in viability is encouraging, the lack of further inactivation is concerning – given the studies on the mechanics of resazurin reduction; it is generally agreed that it is the NADH and other metabolism-associated cofactors within the cell that are responsible for reducing resazurin to resorufin in the intracellular environment (Candeias *et al.*, 1998; Pettit *et al.*, 2005; Cai *et al.*, 2013; Chen *et al.*, 2018).

This is important to note, due to the mechanism by which photocatalysts cause inactivation of microorganisms. Photocatalysts generate ROS, which then attack the cell membrane, causing membrane disruption, perforation, intracellular damage and leakage of intracellular components (Sunada *et al.*,

2003; Carp *et al.*, 2004; Fernández-Ibáñez *et al.*, 2009; Dalrymple *et al.*, 2010). The leakage of intracellular components can include metabolism-associated cofactors such as NADPH, NADH and $FADH_2$ (Koch-Nolte *et al.*, 2011); it could be speculated that this could lead to extracellular reduction of resazurin. This is particularly salient when considering low viable cell counts following a strong photocatalytic inactivation, as the mechanics of reduction may be different with low cell counts and may be more easily influenced by reduction from sources other than viable cells (Moyer and Campbell, 1963). The work of Munshi *et al.* (2014) identified changes in the background rate of the reduction of resazurin to resorufin by reaction with typical components of cell culture media, which must be considered, especially when attempting to enumerate small cell loads. This effect could be considered analogous to signal noise. Therefore, with low signal (few cells), noise may become an issue in determining the TTD with this assay. A counter to this argument is that, for the aims of this project, exact enumeration may not be necessary. If the viable cell load is reduced to the point that signal noise issues could become prominent, it could be assumed that the test surface has strong photocatalytic-antimicrobial properties.

However, while lysed or membrane-damage cells could leak metabolic cofactors into the extracellular environment (leading to post-death reduction of resazurin to resorufin and therefore inflated cell counts compared to culture-based assays), this study did not investigate this specifically and so evidence is limited. Due to the poor photocatalytic-antimicrobial capabilities of the samples, it is difficult to make conclusions on the sensitivity of this method over a range of bacterial concentrations after photocatalytic treatment. Testing a wider range of samples, with varying antimicrobial activity, would give greater confidence in the sensitivity and reproducibility of detection of the method; it has been shown that a for a given test assessing microbial viability, the reproducibility may vary with levels of reduction in viability (Parker *et al.*, 2018). Therefore, further studies should include positive control samples, with strong, known photocatalytic-antimicrobial properties, to assess the method over a range of conditions.

Despite these differences, all trends observed using culture-and-count techniques were also observed using the tier 3 resazurin method for the samples assessed. This indicates that the identification of the photocatalytic-antimicrobial capabilities of future samples would be straightforward. Indeed, such a method would be highly useful to engineering and research groups, being more rapid and long-term cost-effective, while requiring less expertise on the part of the operator than currently established tests. The use of resazurin for enumeration of microbial cells has been noted by other authors; it has shown good correlation with other metabolic assay tests such as XTT/MTT, whilst having considerable improvements such as reduced toxicity (to both the operator and sample cells), reduced costs, reduced time to perform the test and fewer steps, improving usability and making it an attractive alternative for microbial enumeration (Pettit *et al.*, 2005; Peeters *et al.*, 2008). It has also been shown to be more appropriate for photocatalytic-antimicrobial testing than LIVE/DEAD analysis (Cai *et al.*, 2013).

The use of resazurin for testing of photocatalytic-antimicrobial properties has been shown to be very effective (Lilja *et al.*, 2012; Cai *et al.*, 2014; Robertson *et al.*, 2015) and the findings of this study concur. In other studies, however, it is usually the fluorescence that is monitored. While more sensitive than assessment of colour or absorbance monitoring (Rampersad, 2012), fluorescence monitoring systems require the use of more specialised equipment and so are less suitable for adoption by surface engineering or non-specialist groups. The method presented here is rapid, requires less specialised equipment and can provide high-throughput quantitative results that can aid surface engineers assess the photocatalytic-antimicrobial activity of putative surfaces.

One criticism that can be made of all these methods is that they do not differentiate true photocatalytic-antimicrobial cell inactivation from other sources of cell inactivation. Indeed, when considering the results presented in *section 6.2.2.1* (tier 1) and *section 6.2.2.2* (tier 2), UV-irradiation was used to activate TiO_2-coated samples, to demonstrate photocatalytic reduction in number of viable cells; the effects of the irradiation and the photocatalyst may be conflated, due to similar reductions in viability observed between

glass samples and TiO$_2$-coated samples. However, a counter to this argument is that very few common tests can identify the method of cell inactivation and these tests may not be appropriate for non-specialists. Such tests may include using fluorescent dyes that bind solely to cells with damaged membranes (Kitaguchi *et al.*, 2006) and enumerating them, or visualising the inactivated cells using imaging techniques such as SEM, to investigate potential damage to the cell membrane (Kim *et al.*, 2013). While powerful, these and similar techniques can be expensive, require specialist equipment and training and are not easily scalable for high-throughput work, making them unsuitable and unattractive options for the intended application.

Although the inability to determine the cause of cell death may be considered a limitation, the 'gold standard' culture and count method is not able to determine this either, they simply enumerate viable cells. From this enumeration, appropriate inferences as to the cause of any reduction in viability can be made. All influencing variables must be appropriately controlled and secondary causes of cell death must be eliminated or minimised. As this is the case for the culture-and-count method, so it is for the resazurin method. Therefore, the resazurin enumeration can be considered a more rapid, simple alternative to the BS ISO test, suitable for non-specialists to undertake first-stage screenings of coatings for antimicrobial activity, or for more quantitative evaluation using the higher tier methods.

6.3 – Summary

In this chapter, two methods were explored for use in the rapid determination of the antimicrobial properties of antimicrobial coatings, with a focus on usability for non-specialists.

The first method, an *in situ* viability monitoring system based on the principles of optical density monitoring, was able to identify changes in absorbance and appropriately represent a growth curve. However, the inactivation strategies investigated did not reduce viability in the presence of nutrient media (likely due to the inactivation wavelength chosen), which was required to plot a growth curve. For this reason, the method was not considered for further investigation in this project, but could be developed further by identifying appropriate inactivation strategies, using a lower initial inoculum concentration, or a more nutrient-lean media.

The second method was a metabolism-based assay, based on three principles: that actively respiring bacteria produce reductive metabolic cofactors such as NADH, which reduce the metabolic dye resazurin causing a colour change from blue to pink; the speed of this change is related to the metabolic potential of the bacterial population present; the metabolic potential of a population of cells is proportional to the size of that population. Therefore, the size of the population and thus number of viable cells can be inferred from the time taken to detect the resazurin colour change.

The resazurin method was stratified into three tiers of tests, that represent qualitative, semi-quantitative and quantitative measurements, with increasing in complexity with each tier.

Tier 1 represents highly useable, simple test to rapidly screen putative surfaces. An automated camera with recording functions could be employed to further improve usability and throughput and semi-automate this qualitative method.

Tier 2 represents a semi-quantitative, semi-automated test that can be run overnight. This has improvements in usability over tier 1 due to ability to rank samples and ease of setup and ubiquity/flexibility of equipment. However,

this test may be more susceptible to contamination, due to additional equipment and manipulation steps.

Tier 3 tests showed excellent correlation with culture and count methods, as well as other high-throughput tests, used by other authors. When used with the calibrated standard curve, the method is fully quantitative, can assess many samples simultaneously at reduced cost to the traditional enumeration method and is better suited to non-specialists. The equipment requirements and setup may be considered higher than the previous tests, but improvements in throughput and automation are considerable advantages. Although some questions remain regarding low-cell number sensitivity, for the applications of this project, it is sufficient to ascertain that a large decrease in viability has occurred.

Future experiments could investigate the effects of highly-active photocatalytic-antimicrobial samples to validate the sensitivity of the method at low cell concentrations post-photocatalytic treatment.

Each tier of this test shows potential for further development and could find use in their intended application, which is a rapid, non-specialist method of identifying photocatalytic-antimicrobial properties of surface coatings.

OVERALL CONCLUSIONS and FUTURE WORK

The main aims of this project were to establish the antimicrobial effects of niobium-doped and molybdenum-doped titanium dioxide thin film photocatalysts and to identify, explore and develop suitable alternative tests to BS ISO 27447:2009 that could determine the photocatalytic-antimicrobial properties of photocatalytic titania coatings, with a focus on speed and usability for non-specialists. Reviewing the thesis, there were several sections: *i)*, an introduction to photocatalytic titania, *ii)*, description of the magnetron sputtering technique; *iii)*, description of the coating characterisation techniques; *iv)*, fabrication and characterising titania coatings and discussion of the findings; *v)*, determining the antimicrobial properties of titania coatings using traditional techniques and discussion of the findings; *vi)*, developing novel, rapid tests to identify antimicrobial properties of titania coatings. This chapter will highlight the key outcomes from, the experimental chapters and provide recommendations for future work.

7.0 – Conclusions

Photocatalytic titania coatings have been subject to extensive research over the past few years. They have excellent potential for many applications where self-sterilising properties would be beneficial: hospitals, food and beverage industries, hygienic domains and wastewater remediation, to name a few. Two key problems remain in the development of this technology: improving the visible-light activity of these coatings and determining the photocatalytic-antimicrobial properties in a cost-effective manner.

This project has attempted to ameliorate these issues with the following research:

- Fabrication of molybdenum- and niobium-doped titania thin film coatings.
- Characterisation of these coatings.
- Assessment of the photocatalytic-antimicrobial properties of these coatings.
- Identification and development of two alternative methods for determining photocatalytic-antimicrobial properties.
- Assessment of the agreement of the alternative method with the traditional method.

The conclusions of this research can be summarised as follows:

- Coatings deposited onto glass were much smoother than those deposited onto stainless steel coupons.
- Doping titania with molybdenum consistently promoted the rutile shift, leading to mainly anatase/rutile mixed phase coatings; doping with niobium inhibited the rutile shift and produced higher-quality anatase-only crystals.
- Molybdenum-doped titania showed significant activity under visible light irradiation on both glass and stainless steel.
- Photocatalytic-antimicrobial properties were observed for molybdenum-doped titania when irradiated and when not irradiated for the stainless steel samples, but only when irradiated for the glass

samples. The differences were ascribed to the differences in roughness and surface area between the coatings on glass and stainless steel. The glass coatings, being much smoother, had less adsorption and contact sites for the microorganisms and thus were less effective; inactivation of the organisms is closely related to number of contact sites. The differences in photocatalytic-antimicrobial properties were not observed when investigating the photocatalytic degradation of methylene blue, due to the much smaller size of the molecules compared with the cells and less dependence on available contact sites.

- The mechanism of molybdenum-based activity was suspected to be related to local pH changes facilitated by molybdenum trioxide cluster equilibria with the surrounding liquid.

- Poor photoactive and photocatalytic-antimicrobial properties were observed for the niobium-doped coatings, regardless of irradiation status. This was thought to be because of the formation of excessive charge recombination centres, as demonstrated in the literature.

- The methylene blue test may not be the most suitable test for the testing of visible-light photocatalysts. The dye molecules may absorb the visible-light photons, causing attenuation of the photons (so that they lack the energy to activate the photocatalyst), breakdown of the dye independently of the photocatalytic effects and the formation of dye radicals. These may become injected into the photocatalyst, which would artefactually increase activity, producing non-representative reports on efficacy.

- The optical density-based growth analyser method was able to approximate the viability dynamics of a bacterial population in suspension, but the presence of nutrient media made UVA irradiation interventions ineffective in reducing viability. This method is not recommended in its current form, because in this work, no inactivation or reduction was observed in viability to validate/measure using the growth analyser.

- The time to detect changes in colour and absorbance intensity at specific wavelengths in resazurin can be used to enumerate a population of cells in suspension.

- Three tiers of this test were identified and developed with different and increasing levels of sensitivity.

- The resazurin method is recommended for the testing of photocatalytic-antimicrobial properties as an alternative to traditional tests.

7.1 – Future work

Further to the work presented in this thesis, several questions remain; more studies are required to further develop this work. The recommendations for future work are as follows:

- Repeat activity experiments to clarify variability; intra- and inter-batch variability was observed, especially for the molybdenum-doped titania on glass coupons. Therefore, further developments would include producing more coatings, specifically Mo-doped titania coatings on glass coupons and further investigating the photoactivity and photocatalytic-antimicrobial properties.

- Combine molybdenum- and niobium-doped titania with a charge carrier material to investigate the effects of improved charge separation.

- Further explore the effects of surface roughness and surface area on the photocatalytic-antimicrobial properties of surface coatings, potentially by coating substrates of known varying roughness/surface area with doped titania.

- Use XPS to determine the electronic state of the doped molybdenum and niobium ions, to better elucidate their electron/hole acceptor/donator properties.

- Discern the mechanisms of activity of the non-irradiated molybdenum-doped titania – fluorescence lifetime spectroscopy and imaging with appropriate pH-sensitive probes could be used to determine local pH on molybdenum-doped titania coatings compared to pure titania. Substrates could be coated in a 'checkerboard' configuration to correlate any changes in local pH to specific coating compositions.

- Assess the photocatalytic activity of the coatings via alternative tests to methylene blue degradation, that is less reactive with visible light, less likely to artefactually improve photocatalytic performance and less affected by local pH. Alternative tests could include the degradation of colourless probe reactants such as acetone or acetic acid.

- Use samples with known, highly-active photocatalytic-antimicrobial activity to validate the low-cell-number sensitivity of the tier three resazurin method.
- Repeat the second tier of the resazurin method to obtain data for statistical analyses

APPENDICES

Appendix A

This appendix section pertains to *section 1.1.3* and contains a brief description of the experiments and public engagement work that complemented the work in the main thesis.

The experiments were performed outdoors on a west-facing wall of a 1970's Manchester building, located at 53.472058^0, -2.2402400^0. Initially, it was intended that six parallel trials would be used to investigate various self-cleaning, NOx abatement and antimicrobial properties, over a period of twelve months. This involved coating different materials with commercial photocatalytic titania and monitoring effects. The six trails were designed as follows:

1. Glass window panels were alternately coated with titania or left uncoated. Members of the public were asked to choose which panels were most clean by observation.
2. Stainless steel panels were alternately coated with titania or left uncoated. Photographs were taken every two months for twelve months.
3. Concrete panels were alternately painted with white paint containing active titania, white paint containing inactive titania, or left untreated. Member of the public were asked to choose which panels were most clean by observation.
4. Brickwork was alternately coated with a titania sol-gel or left uncoated. Photographs were taken every two months for twelve months.
5. Acetate film strips were coated with active titania or inactive titania and mounted to a wood backing board. These strips were posted to industrial partners every month for twelve months, who assessed the strips for evidence of NOx abatement.

6. Glass and stainless steel tiles were alternatively coated with active titania or left uncoated. Stone tiles were alternately painted with white paint containing active titania or white paint containing inactive titania. The tiles were swabbed every two months for twelve months; the swab extract was cultured on nutrient agar at 37 ^{0}C for 48 hours and on malt extract agar at 25 ^{0}C for one week. Colonies were counted on each plate and indicative species observed.

A poster detailing the intended experiments was produced and displayed at the 2nd Photocatalytic and Superhydrophilic Surfaces Workshop 2013, held in Manchester, UK (Figure 92).

Putting theory into practice: photoactive coatings on a Manchester wall

Antony Scimone, Joanna Verran & Peter Kelly, Manchester Metropolitan University, Manchester, UK

Introduction

Photoactive coatings have been well-characterised in laboratory settings, but fewer data are available that describe performance in outdoor trials, particularly over long time periods. In this study, a range of titanium dioxide coatings will be trialled, being applied to different substrates on a west-facing wall of a 1970s building in central Manchester (figure 1). Tests to determine self-cleaning capacity, antimicrobial properties and NOx abatement will be carried out over a 12 month period. The display will also be used as a vehicle for informing the public about the technology (figure 2).

Glass, stainless steel, concrete, and brickwork will be used as test substrates, being coated with TiO_2 in paint, sol-gel and thin film formats. Relative reflection and transmission of light will be measured to determine self-cleaning efficacy, sensitive films will be used to measure NOx abatement, and swabbing and culture of microbes will be used to assess antimicrobial activity. Results will be reported every two months for one year.

Figure 1: Diagram of west-facing wall.
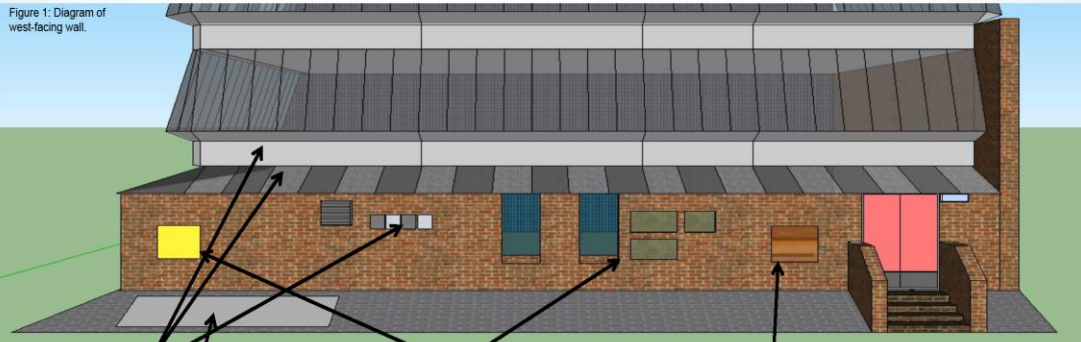
Self-cleaning

In addition to creating free radicals, photoactive coatings often exhibit superhydrophilic behaviour. Polar liquids such as water have a much larger spread on these surfaces, and thus occupy a greater area than on a non-superhydrophilic surface. The result of this is a phenomenon called 'sheeting' - liquid rolls off the surface in a continuous body as opposed to singular droplets (Chen *et al*, 2009). This carries away dirt and debris, cleaning the surface.

NOx Abatement

Nitrogen oxide and nitrogen dioxide are formed mainly during combustion in engines (Ângelo *et al*, 2013). Levels of these gases in the atmosphere, especially in cities, have raised human health concerns, in addition to causing acid rain (Wang *et al*, 2007). Hydroxyl radicals formed during the process shown in figure 3 are key to photoactive NOx abatement; gases are adsorbed on the surface of the substrate, where they react and are oxidised, towards nitrogen.

$$NO_{ads} + OH^{\cdot} \rightarrow HNO_2$$
$$HNO_2 + OH^{\cdot} \rightarrow NO_{2ads} + H_2O$$
$$NO_{2ads} + OH^{\cdot} \rightarrow NO_3^- + H^+$$
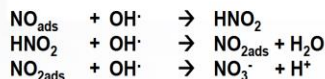
Microbiology

Photoactive TiO_2 has antimicrobial properties (figure 3). These properties are due to free radicals, produced by the process shown in figure 4. These highly reactive particles kill cells by oxidising the lipids within the cell membrane (Fernández-Ibánèz *et al*, 2009), causing the cell membrane to fail, ultimately resulting in cessation of respiration.
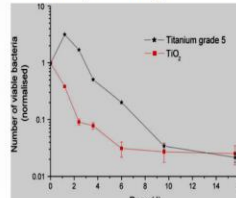
Figure 3: Number of viable bacteria recovered from photoactive and inert titania, as a function of UV dose in Joules (Lilja *et al*, 2012).
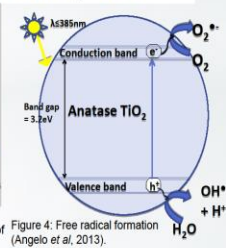
Figure 4: Free radical formation (Angelo *et al*, 2013).

Figure 2: Public information panel

Acknowledgements: The authors would like to thank the companies Cristal, Miba and NSG for their contributions to this project.

References

- Ângelo J, Andrade L, Madeira LM, Mendes A (2013). An overview of photocatalysis phenomena applied to NOx abatement. *Journal of Environmental Management*, (129), 522-539.
- Chen Y, Chen F & Zhang J (2009). Effect of surface fluorination on the photocatalytic an photo-induced hydrophilic properties of porous TiO_2 films. *Applied surface Science*, 255(16), pp 6290-6296
- Fernández-Ibáñèz P, Sichel C, Polo-López MI, de Cara-García M, Tello JC (2009). Photocatalytic disinfection of natural well water contaminated by *Fusarium solaniusing* $TiO2$ slurry in solar CPC photo-reactors. *Catalysis Today*, (144), 62-28.
- Wang H, Wu Z, Zhao W, Guan B (2007). Photocatalytic oxidation of nitrogen oxides using $TiO2$ loading on woven glass fabric. *Chemosphere*, (66), 185-190.

Corresponding author: Antony Scimone, ANTONY.SCIMONE@stu.mmu.ac.uk

Figure 92: Poster presented at PSS 2013. The poster details the experiments that were intended for the photocatalytic experiment wall.

256 | P a g e

During data collection, it became apparent that the experiments could not be completed as intended and the intended outcomes had to be adjusted. To this end, the public engagement components were focussed on and the number of other tests reduced. The two experiments that were used to highlight the potential of photocatalytic technology to the public were the experiments involving the glass panels and concrete panels.

For the glass panels, sixteen glass roof windows, sloping at an angle of 37^{0} to the horizontal, were alternately replaced with commercial self-cleaning glass panels that contained a TiO_2 coating (Pilkington Activeglass, NSG group, North Ormskirk) or left uncoated. Every two months for eight months, between 1-3pm on the 15th of that month, photographs were taken of the glass panels in order to visually compare accumulation of dirt (except during inclement weather, in which case the date was postponed until dry conditions emerged). The top-left, top-right, bottom-left and bottom-right of each panel was photographed. These were taken from inside the building looking outwards.

Members of the public were then asked if they could see a difference between pairs of matched photographs and if they could, which panel they thought was cleaner; pairs of matched photographs were labelled as "A-B", "C-D" and so on. Their responses were recorded in a tally chart.

For the concrete panels, eight concrete wall panels were cleaned using high-pressure water and then painted; three with an active TiO_2 paint, three with an inactive TiO_2 paint, with two were left unpainted as controls. Each panel was randomly assigned one of the treatments to reduce position bias. Photographs were taken after one month and after eight months.

After eight months, members of the public were then asked to rank the six painted panels in order of cleanliness, with 1 being most clean and 6 being least clean. The rankings were recorded in a table and counted. This experiment was conducted both in-person and using the photographic comparison via a social media platform.

For the glass panels, the titania-coated glass was cleaner by observation than ordinary glass at each time point (Figure 93).
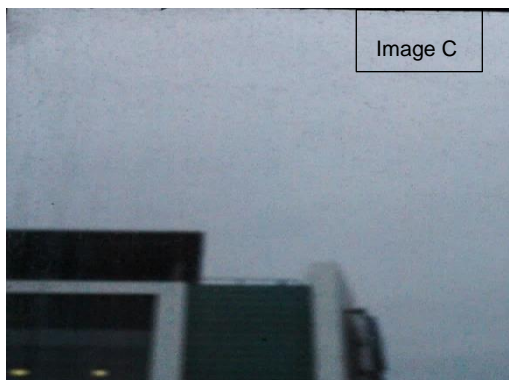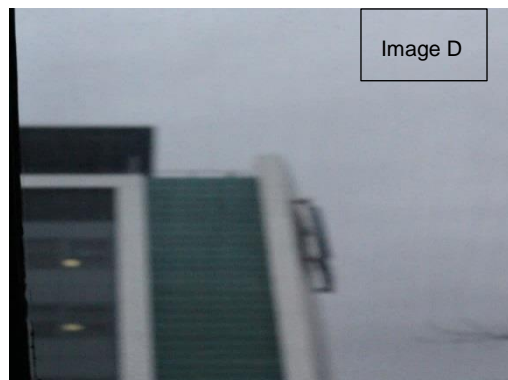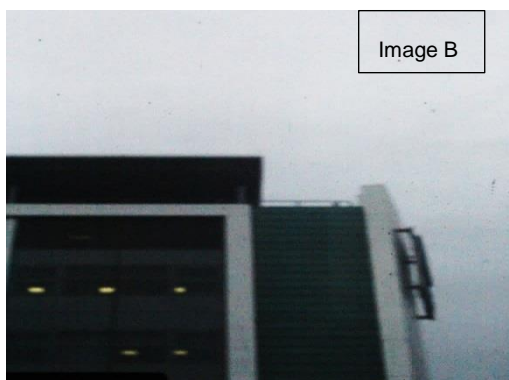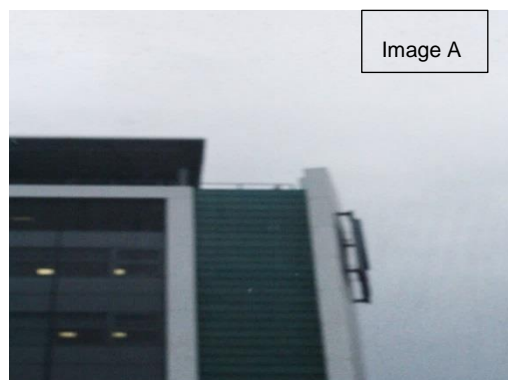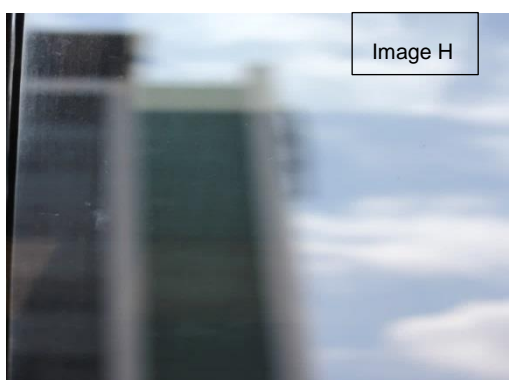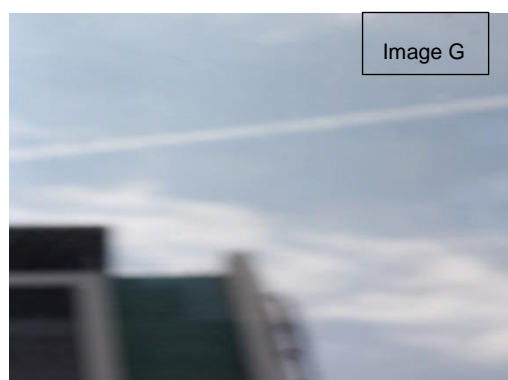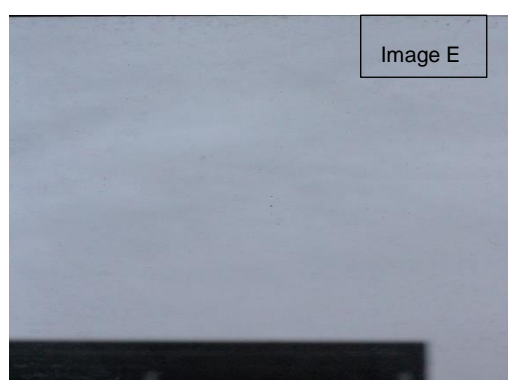
M	Ordinary glass	Titania-coated glass
2	Image C	Image D
4	Image B	Image A
6	Image H	Image G
8	Image F	Image E

Figure 93: Photographs taken from inside the building looking out, towards the John Dalton Tower building. The month is displayed on the left. The titania-coated glass appeared cleaner in each pair of images, at each time point.

The brightness of the photographs of the non-coated windows was increased using the in-built picture editor of Microsoft Word (Microsoft Word 365,

Microsoft, Reading); this was done so a comparison can be made between the coated and non-coated windows, as the non-coated windows had a 'smoked glass' effect.

These photographs were then used to develop a public engagement demonstration, where members of the public chose which window they thought looked cleaner. The demonstration consisted of four pairs of matched photographs similar to Figure 93. Thirty-seven participants were recruited from this event; more people chose the photoactive glass panel as looking cleaner than the matched uncoated glass panel (Table 7).

Table 7: Public responses when asked, "Which window is cleaner?" Images displaying the photoactive glass are indicated with a blue highlight. More participants selected the photocatalytic glass as appearing cleaner. N=37.

	Image Identifier							
	A	B	C	D	E	F	G	H
Number of Responses	30	7	3	34	3	34	27	10

These results indicate that by observation, photoactive glass windows appear cleaner than non-photoactive glass windows. The efficacy of the self-cleaning glass may have been improved somewhat by the degree of sloping, as this may have allowed rainwater to better 'sheet' along the glass, cleaning it more thoroughly than vertical self-cleaning glass. Furthermore, the public engagement aspects of this experiment were well received at the Manchester Science Festival and during ad-hoc participant recruitment, indicating simple observation as an alternative, inexpensive and relevant measurement method for self-cleaning surfaces.

For the concrete panels, the active and inactive titania panels appeared similar after one month, but the panels painted with the active titania paint appeared brighter than the panels painted with inactive titania after eight months (Figure 94), suggesting effective self-cleaning.

Figure 94: Photographs of the concrete panels after one month and after eight months. The panels treated with photocatalytic paint are labelled. The month is displayed on the left. The photocatalytic panels appear similar to the inactive painted panels at one month, but appear cleaner after eight months.

During the public engagement component of the experiment, forty-eight participants were recruited. When members of the public were asked to assess which panels appeared cleaner after eight months, twenty-five correctly chose all three photocatalytic panels as appearing cleaner, while twenty-three participants chose two correctly (Figure 95).
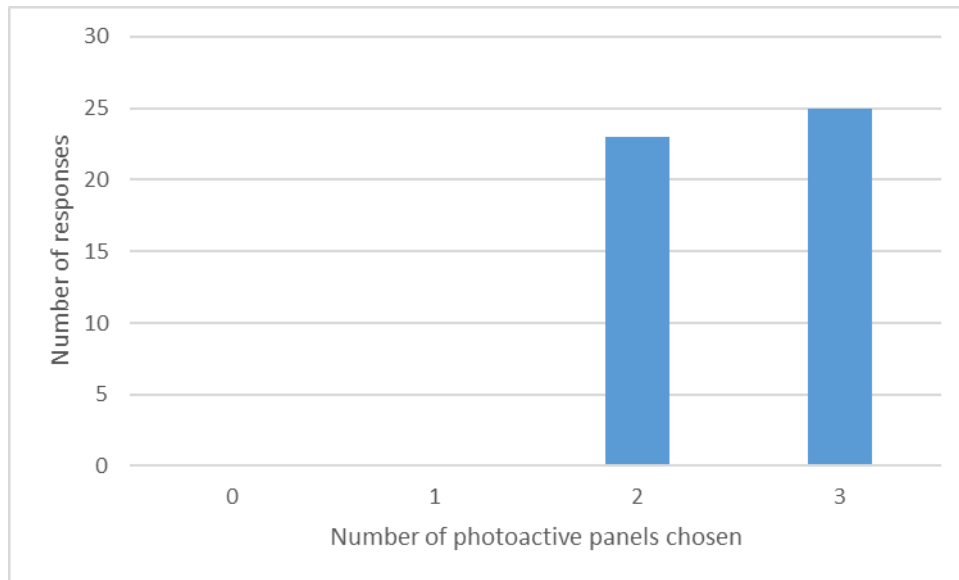
Figure 95: Number of participants who correctly identified 0, 1 , 2 or 3 photocatalytic concrete panels. All participants were able to identify either all three panels, or two out of three panels (N=48).

The results of this experiment indicate that active titania-containing paint can improve the appearance of cleanliness in concentrate building materials. Furthermore, similar to the glass panels already described, the public engagement aspects of this experiment were well received, both in person and using a social media online platform. This adds further evidence to suggest that, for the appearance of cleanliness, subjective observation by participants could be a relevant and inexpensive technique to assess self-cleaning surfaces.

In conclusion, the use of the photocatalytic wall was an excellent vehicle for public engagement. Participants were able to identify the photocatalytic self-cleaning glass and concrete panels via observation, evidencing the efficacy of the panels and suggesting that participant observation can be used to assess appearance of cleanliness of some self-cleaning materials.

Appendix B

This appendix section pertains to *section 4.1.3.3* and contains the hot stage XRD tables. This information provides details on the anatase – rutile weight fraction at each annealing temperature for each composition of the set 3 coating.

The first batch of undoped titania samples was crystalline as-deposited and, had the highest anatase-rutile weight fraction at ambient temperature, prior to hot stage investigation (Table 8).

The second batch of undoped titania samples developed anatase crystals with annealing, but no rutile crystals. Therefore a range of annealing temperatures from 330 ^{0}C – 600 ^{0}C could be recommended (Table 9).

The first (Table 10) and second (Table 11) batches of niobium-doped titania coatings exhibited similar properties to the second batch of undoped titania coatings.

The first batch of molybdenum-doped coatings did not exhibit crystallinity until the temperature reached 380 ^{0}C, which primarily consisted of the rutile phase – a very small amount of anatase was present (Table 12)

The second batch of molybdenum-doped samples displayed similar delayed crystallinity, developing anatase crystals at around 420 ^{0}C and rutile crystals at around 480 ^{0}C (Table 13).

Table 8: Peak intensity of anatase 101 and rutile 110 peaks and the ratio between the peak intensities for batch one titanium dioxide samples, by temperature.

Temperature, ^{0}C	Peak intensity, a.u		Weight ratio
	Anatase 101	Rutile 110	
25	2425	443	0.81
300	3031	950	0.72
310	3073	765	0.76
320	2985	914	0.72
330	2971	873	0.73
340	2787	881	0.72
350	2942	1071	0.69
360	3063	911	0.73
370	2917	787	0.75
380	2887	1062	0.68
390	2803	1017	0.69
400	2753	1052	0.67
410	2808	1061	0.68
420	2777	929	0.70
430	2914	928	0.71
440	2787	1180	0.65
450	3059	1005	0.71
460	3072	1130	0.68
470	3083	1278	0.66
480	2862	1325	0.63
490	2976	1332	0.64
500	3169	1406	0.64
510	3004	1589	0.60
520	3046	1445	0.63
530	3046	1630	0.60
540	3180	1444	0.64
550	3211	1387	0.65
560	3054	1508	0.62
570	3340	1519	0.64
580	3121	1644	0.60
590	3003	1614	0.60
600	2957	1507	0.61

Table 9: Peak intensity of anatase 101 and rutile 110 peaks and the ratio between the peak intensities for batch two titanium dioxide samples, by temperature.

Temperature ^{0}C	Peak intensity, a.u		Weight ratio
	Anatase 101	Rutile 110	
25	0	0	
300	3647	0	1.00
310	16244	0	1.00
320	22861	0	1.00
330	23931	0	1.00
340	23841	0	1.00
350	24162	0	1.00
360	24563	0	1.00
370	24611	0	1.00
380	25060	0	1.00
390	25237	0	1.00
400	25344	0	1.00
410	25596	0	1.00
420	26014	0	1.00
430	26171	0	1.00
440	26032	0	1.00
450	26378	0	1.00
460	26920	0	1.00
470	26432	0	1.00
480	27160	0	1.00
490	27246	0	1.00
500	27450	0	1.00
510	27162	0	1.00
520	27125	0	1.00
530	26996	0	1.00
540	27462	0	1.00
550	27100	0	1.00
560	26682	0	1.00
570	26266	0	1.00
580	26512	0	1.00
590	25620	0	1.00
600	25415	0	1.00

Table 10: Peak intensity of anatase 101 and rutile 110 peaks and the ratio between the peak intensities, for batch one niobium-doped titanium dioxide coatings, by temperature.

Temperature, ^{0}C	Peak intensity, a.u		Weight ratio
	Anatase 101	Rutile 110	
25	43	11	0.75
300	869	84	0.89
310	1999	0	1.00
320	1999	0	1.00
330	17018	0	1.00
340	30445	0	1.00
350	37435	0	1.00
360	38073	0	1.00
370	37897	0	1.00
380	38426	0	1.00
390	38461	0	1.00
400	37985	0	1.00
410	39094	0	1.00
420	38723	0	1.00
430	38087	0	1.00
440	38259	0	1.00
450	37666	0	1.00
460	37724	0	1.00
470	37969	0	1.00
480	37752	0	1.00
490	38053	0	1.00
500	37947	0	1.00
510	37745	0	1.00
520	36769	0	1.00
530	37470	0	1.00
540	36936	0	1.00
550	36311	0	1.00
560	34232	0	1.00
570	32096	0	1.00
580	31093	0	1.00
590	30334	0	1.00
600	29340	0	1.00

Table 11: Peak intensity of anatase 101 and rutile 110 peaks and the ratio between the peak intensities, for batch two niobium-doped titanium dioxide coatings, by temperature.

Temperature, ^{0}C	Peak intensity, a.u		Weight ratio
	Anatase 101	Rutile 110	
25	77	0	1.00
300	194	0	1.00
310	2471	0	1.00
320	17551	0	1.00
330	34272	0	1.00
340	37325	0	1.00
350	37807	0	1.00
360	38175	0	1.00
370	37560	0	1.00
380	37699	0	1.00
390	37708	0	1.00
400	37702	0	1.00
410	37174	0	1.00
420	36839	0	1.00
430	36758	0	1.00
440	36659	0	1.00
450	36987	0	1.00
460	36721	0	1.00
470	36526	0	1.00
480	35886	0	1.00
490	35674	0	1.00
500	35268	0	1.00
510	34737	0	1.00
520	34131	0	1.00
530	33944	0	1.00
540	32760	0	1.00
550	30694	0	1.00
560	29373	0	1.00
570	28743	0	1.00
580	28172	0	1.00
590	27673	0	1.00
600	27075	0	1.00

Table 12: Peak intensity of anatase 101 and rutile 110 peaks and the ratio between the peak intensities for batch one of the molybdenum-doped titanium dioxide samples, by temperature.

Temperature, ^{0}C	Peak intensity, a.u		Weight ratio
	Anatase 101	Rutile 110	
360	135	701	0.13
370	143	2694	0.04
380	618	4662	0.10
390	1114	6107	0.13
400	1369	6823	0.14
410	1182	7261	0.11
420	1464	7601	0.13
430	1319	8210	0.11
440	1387	8482	0.11
450	1261	8809	0.10
460	1234	9400	0.09
470	1079	9752	0.08
480	1005	10119	0.07
490	876	10505	0.06
500	757	10932	0.05
510	579	11621	0.04
520	504	12710	0.03
530	488	13192	0.03
540	313	13940	0.02
550	454	14714	0.02
560	469	15419	0.02
570	543	15481	0.03

Table 13: Peak intensity of anatase 101 and rutile 110 peaks and the ratio between the peak intensities, for batch two of the molybdenum-doped titanium dioxide coatings, by temperature.

Temperature, ^{0}C	Peak intensity, a.u		Weight ratio
	Anatase 101	Rutile 110	
430	1121	102	0.90
440	2938	0	1.00
450	3097	0	1.00
460	3040	0	1.00
470	3414	0	1.00
480	3756	58	0.98
490	3995	421	0.88
500	4729	845	0.82
510	5302	1424	0.75
520	6051	1617	0.75
530	6573	1885	0.73
540	7235	2379	0.71
550	7999	2678	0.70
560	8696	2833	0.71
570	9437	3032	0.71
580	10195	3164	0.72
590	10734	3184	0.73
600	11188	3246	0.73

Appendix C

This appendix section pertains to *sections 6.2.1.4* and *6.2.1.5* – the details of the Microsoft Excel formulae used during processing of the tier three resazurin method are detailed here. The raw data from the plate reader were pasted into a Microsoft Excel sheet. The data were blank-corrected by subtracting the absorbance of the control at each time point. The data were then pasted into a second sheet, where an 'IF table' was used to determine whether the absorbance at each time point had risen by the critical value (the mean plus three standard deviations of the blank wells). The formula used in the IF table is given by (21):

$$=IF(\textit{sample absorbance cell range}>(\textit{blank mean}$$
$$\textit{absorbance}+(3*\textit{blank standard deviation})),1,0)$$

<div align="right">(21)</div>

The text in italics was replaced with the cell coordinates, i.e., B1-B10, C2, etc. This formula reports a '1' if the absorbance had increased by at least the critical value and a '0' if not. An excerpt from an IF table is shown in Figure 96.

After this, a VLOOKUP table was used to determine at what time point, if any, the absorbance exceeded the critical value, for each sample. The formula used in the VLOOKUP table is given by (22):

$$=VLOOKUP(1,IF \textit{ table range}, \textit{time column}$$
$$\textit{range}, FALSE)$$

<div align="right">(22)</div>

This formula searches the IF table for '1' and reports the corresponding value in the time column if it is found. It was required that five sequential 'hits' occur in order to report the time value as the TTD; this reduced anomalous or stochastic triggering. The mean and standard deviation of the TTD for each bacterial load was determined and a regression analysis performed in order to generate a standard curve and equation.

Figure 96: An excerpt from an IF table. The red '0' values indicate that, at that time for that well, the absorbance was below the critical value of the mean of the blank plus 3 standard deviations. Green '1' values indicate the critical value had been exceeded and a critical event had been observed. The time of sampling is shown in the right-hand column – this is read by the VLOOKUP table (Figure 97).

On the right-hand side of the IF table, is the time in minutes at which the wells were sampled. The VLOOKUP table searched the IF table and reported the time at which a critical event occurred (Figure 97).

	A	B	C	D	E	F	G	H	I	J	K	L	M	N	O	P	Q	R	S
1	Cell suspension concentration (CFU/ml)	1.00E+06						1.00E+07						1.00E+08					
2	Well ID	Sample X1	Sample X2	Sample X3	Sample X4	Sample X5	Sample X6	Sample X1	Sample X2	Sample X3	Sample X4	Sample X5	Sample X6	Sample X1	Sample X2	Sample X3	Sample X4	Sample X5	Sample X6
3	Time (mins)	786	808	786	808	779	794	632	662	654	654	662	662	537	537	544	551	573	573

Figure 97: Excerpt from a VLOOKUP table. The VLOOKUP table inspected the IF table for a critical event and reports the time from the right-most column.

In this manner, investigation of the data was semi-automated, greatly reducing operator load and enabling the use of larger datasets than would be feasible for a candidate rapid test (as large datasets would take longer to interpret manually).

REFERENCES

Abedi-Moghaddam, N., Bulić, A., Henderson, L. and Lam, E. (2004) 'Survival of *Escherichia coli* to UV Irradiation During Exponential and Stationary Phases of Growth.' *Journal of Experimental Microbiology and Immunology*, 5(1), pp. 44-49.

Akbarzadeh, R., Umbarkar, S. B., Sonawane, R. S., Takle, S. and Dongare, M. K. (2010) 'Vanadia–Titania Thin Films for Photocatalytic Degradation of Formaldehyde in Sunlight.' *Applied Catalysis A: General*, 374(1–2), pp. 103-109.

Alivehmas, T., Louhi, M. and Sandholm, M. (1991) 'Automation of the Resazurin Reduction Test Using Fluorometry of Microtitration Trays.' *Journal of Veterinary Medicine B: Infectious Diseases and Veterinary Public Health*, 38(5), pp. 358-372.

Allen, N. S., Edge, M., Sandoval, G., Verran, J., Stratton, J. and Maltby, J. (2005) 'Photocatalytic Coatings for Environmental Applications.' *Photochemistry and Photobiology*, 81(1), pp. 279-290.

Allen, N. S., Edge, M., Verran, J., Stratton, J., Maltby, J. and Bygott, C. (2008) 'Photocatalytic Titania Based Surfaces: Environmental Benefits.' *Polymer Degradation and Stability*, 93(9), pp. 1632-1646.

Angelo, J., Andrade, L., Madeira, L. M. and Mendes, A. (2013) 'An Overview of Photocatalysis Phenomena Applied to NOx Abatement.' *Journal of Environmental Management*, 129, pp. 522-539.

Arbiol, J., Cerdà, J., Dezanneau, G., Cirera, A., Peiró, F., Cornet, A. and Morante, J. R. (2002) 'Effects of Nb Doping on the TiO_2 Anatase-to-Rutile Phase Transition.' *Journal of Applied Physics*, 92(2), pp. 853-861.

Ashokkumar, S. and Adler-Nissen, J. (2011) 'Evaluating Non-Stick Properties of Different Surface Materials for Contact Frying.' *Journal of Food Engineering*, 105(3), pp. 537-544.

Atkins, P. and de Paula, J. (2014) *Atkins' Physical Chemistry.* 10th ed., Oxford: Oxford Univeristy Press.

Bakardjieva, S., Šubrt, J., Štengl, V., Dianez, M. J. and Sayagues, M. J. (2005) 'Photoactivity of Anatase–Rutile TiO_2 Nanocrystalline Mixtures Obtained by Heat Treatment of Homogeneously Precipitated Anatase.' *Applied Catalysis B: Environmental*, 58(3–4), pp. 193-202.

Banat, I. M., Franzetti, A., Gandolfi, I., Bestetti, G., Martinotti, M. G., Fracchia, L., Smyth, T. J. and Marchant, R. (2010) 'Microbial Biosurfactants Production, Applications and Future Potential.' *Applied Microbiology and Biotechnology*, 87(2), pp. 427-444.

Banerjee, S., Dionysiou, D. D. and Pillai, S. C. (2015) 'Self-Cleaning Applications of TiO_2 by Photo-Induced Hydrophilicity and Photocatalysis.' *Applied Catalysis B: Environmental*, 176-177, pp. 396-428.

Banyamin, Z. (2014) *Novel Photovoltaic Solar Power Generating Diode.* Doctor of Philosophy. Manchester Metropolitan University.

Batzill, M. (2011) 'Fundamental Aspects of Surface Engineering of Transition Metal Oxide Photocatalysts.' *Energy & Environmental Science*, 4(9), pp. 3275-3286.

Baudart, J., Guillaume, C., Mercier, A., Lebaron, P. and Binet, M. (2015) 'Rapid Quantification of Viable *Legionella* in Nuclear Cooling Tower Waters Using Filter Cultivation, Fluorescent *in situ* Hybridization and Solid-Phase Cytometry.' *Journal of Applied Microbiology*, 118(5), pp. 1238-1249.

Beerens, H. (1998) 'Bifidobacteria as Indicators of Faecal Contamination in Meat and Meat Products: Detection, Determination of Origin and Comparison with *Escherichia coli*.' *International Journal of Food Microbiology*, 40(3), pp. 203-207.

Berman, D., Erdemir, A. and Sumant, A. V. (2013) 'Few Layer Graphene to Reduce Wear and Friction on Sliding Steel Surfaces.' *Carbon*, 54, pp. 454-459.

Bindell, J. B. (1992) '2.2 - SEM: Scanning Electron Microscopy.' *In* Brundle, C. R. (ed.) *Encyclopedia of Materials Characterization*. Boston: Butterworth-Heinemann, pp. 70-84.

Binnig, G., Quate, C. F. and Gerber, C. (1986) 'Atomic Force Microscope.' *Physical Review Letters*, 56(9), pp. 930-933.

Bogdan, J., Zarzynska, J. and Plawinska-Czarnak, J. (2015) 'Comparison of Infectious Agents Susceptibility to Photocatalytic Effects of Nanosized Titanium and Zinc Oxides: A Practical Approach.' *Nanoscale Research Letters*, 10, p. 15.

Borra, R. C., Lotufo, M. A., Gogioti, S. M., Barros, F. d. M. and Andrade, P. M. (2009) 'A Simple Method to Measure Cell Viability in Proliferation and Cytotoxicity Assays.' *Brazilian Oral Research*, 23(3), pp. 255-262.

Boulos, L., Prevost, M., Barbeau, B., Coallier, J. and Desjardins, R. (1999) 'LIVE/DEAD BacLight : Application of a New Rapid Staining Method for Direct Enumeration of Viable and Total Bacteria in Drinking Water.' *Journal of Microbiological Methods*, 37(1), pp. 77-86.

Bouroushian, M. and Kosanovic, T. (2012) 'Characterization of Thin Films by Low Incidence X-Ray Diffraction.' *Crystal Structure Theory and Applications*, 1(3), pp. 35-39.

Bräuer, G., Szyszka, B., Vergöhl, M. and Bandorf, R. (2010) 'Magnetron Sputtering – Milestones of 30 Years.' *Vacuum*, 84(12), pp. 1354-1359.

Breault, T. M. and Bartlett, B. M. (2012) 'Lowering the Band Gap of Anatase-Structured TiO_2 by Coalloying with Nb and N: Electronic Structure and Photocatalytic Degradation of Methylene Blue Dye.' *The Journal of Physical Chemistry C*, 116(10), pp. 5986-5994.

British Standards Institution. (2009) BS ISO 27447:2009 - Fine ceramics (advanced ceramics, advanced technical ceramics) - Test method for antibacterial activity of semiconducting photocatalytic materials.

British Standards Institution. (2010) BS ISO 10678:2010 - Fine ceramics (advanced ceramics, advanced technical ceramics) - Determination of photocatalytic activity of surfaces in an aqueous medium by degradation of methylene blue.

Brook, L. A., Evans, P., Foster, H. A., Pemble, M. E., Steele, A., Sheel, D. W. and Yates, H. M. (2007) 'Highly Bioactive Silver and Silver/Titania Composite Films Grown by Chemical Vapour Deposition.' *Journal of Photochemistry and Photobiology A: Chemistry*, 187(1), pp. 53-63.

Brown, S., Santa Maria, J. P., Jr. and Walker, S. (2013) 'Wall Teichoic Acids of Gram-Positive Bacteria.' *Annual Review of Microbiology*, 67, pp. 313-336.

Bruscolini, F., Paolucci, D., Rosini, V., Sabatini, L., Andreozzi, E. and Pianetti, A. (2015) 'Evaluation of Ultraviolet Irradiation Efficacy in an Automated System for the Aseptic Compounding Using Challenge Test.' *International Journal for Quality in Health Care*, 27(5), pp. 412-417.

Buchrieser, C. and Kaspar, C. W. (1993) 'An Improved Direct Viable Count for the Enumeration of Bacteria in Milk.' *Internatinal Journal of Food Microbiology*, 20(4), pp. 227-237.

Byrne, J. A., Dunlop, P. S., Hamilton, J. W., Fernandez-Ibanez, P., Polo-Lopez, I., Sharma, P. K. and Vennard, A. S. (2015) 'A Review of Heterogeneous Photocatalysis for Water and Surface Disinfection.' *Molecules*, 20(4), pp. 5574-5615.

Caballero, L., Whitehead, K. A., Allen, N. S. and Verran, J. (2009) 'Inactivation of *Escherichia coli* on Immobilized TiO_2 Using Fluorescent Light.' *Journal of Photochemistry and Photobiology A: Chemistry*, 202(2–3), pp. 92-98.

Caballero, L., Whitehead, K. A., Allen, N. S. and Verran, J. (2014) 'Photocatalytic Inactivation of *Escherichia coli* Using Doped Titanium Dioxide under Fluorescent Irradiation.' *Journal of Photochemistry and Photobiology A: Chemistry*, 276, pp. 50-57.

Cady, P., Dufour, S. W., Shaw, J. and Kraeger, S. J. (1978) 'Electrical Impedance Measurements: Rapid Method for Detecting and Monitoring Microorganisms.' *Journal of Clinical Microbiology*, 7(3), pp. 265-272.

Cai, Y., Strømme, M. and Welch, K. (2013) 'Bacteria Viability Assessment After Photocatalytic Treatment.' *3 Biotech*, 4(2), pp. 149-157.

Cai, Y., Strømme, M. and Welch, K. (2014) 'Disinfection Kinetics and Contribution of Reactive Oxygen Species When Eliminating Bacteria with TiO_2 Induced Photocatalysis.' *Journal of Biomaterials and Nanobiotechnology*, 5(3), pp. 200-209.

Camera-Roda, G. and Santarelli, F. (2007) 'Optimization of the Thickness of a Photocatalytic Film on the Basis of the Effectiveness Factor.' *Catalysis Today*, 129, pp. 161-168.

Campbell, D. (1970) *Handbook of Thin Film Technology, edited by Leon I. Maissel and Reinhard Glang.* New York: McGraw-Hill.

Candeias, L. P., MacFarlane, D. P. S., McWhinnie, S. L. W., Maidwell, N. L., Roeschlaub, C. A., Sammes, P. G. and Whittlesey, R. (1998) 'The Catalysed NADH Reduction of Resazurin to Resorufin.' *Journal of the Chemical Society, Perkin Transactions 2*, (11), pp. 2333-2334.

Cao, S., Liu, B., Fan, L., Yue, Z., Liu, B. and Cao, B. (2014) 'Highly Antibacterial Activity of N-Doped TiO_2 Thin Films Coated on Stainless Steel Brackets under Visible Light Irradiation.' *Applied Surface Science*, 309, pp. 119-127.

Carp, O., Huisman, C. L. and Reller, A. (2004) 'Photoinduced Reactivity of Titanium Dioxide.' *Progress in Solid State Chemistry*, 32(1–2), pp. 33-177.

Cassar, L. (2011) 'Photocatalysis of Cementitious Materials: Clean Buildings and Clean Air.' *MRS Bulletin*, 29(5), pp. 328-331.

Chen, J. and Poon, C. S. (2009) 'Photocatalytic Construction and Building Materials: From Fundamentals to Applications.' *Building and Environment*, 44(9), pp. 1899-1906.

Chen, J. L., Steele, T. W. J. and Stuckey, D. C. (2018) 'Metabolic Reduction of Resazurin; Location Within the Cell for Cytotoxicity Assays.' *Biotechnology and Bioengineering*, 115(2), pp. 351-358.

Chen, M. and Chu, J. W. (2011) 'NOx Photocatalytic Degradation on Active Concrete Road Surface — From Experiment to Real-Scale Application.' *Journal of Cleaner Production*, 19(11), pp. 1266-1272.

Chen, Y. and Dionysiou, D. D. (2006) 'Correlation of Structural Properties and Film Thickness to Photocatalytic Activity of Thick TiO_2 Films Coated on Stainless Steel.' *Applied Catalysis B: Environmental*, 69, pp. 24-33.

Choi, H., Stathatos, E. and Dionysiou, D. D. (2007) 'Photocatalytic TiO_2 Films and Membranes for the Development of Efficient Wastewater Treatment and Reuse Systems.' *Desalination*, 202(1), pp. 199-206.

Choi, J., Park, H. and Hoffmann, M. R. (2010) 'Effects of Single Metal-Ion Doping on the Visible-Light Photoreactivity of TiO_2.' *Journal of Physical Chemistry C*, 114(2), pp. 783-792.

Chow, P. P. (1991) 'II-3 - Molecular Beam Epitaxy.' *In* Vossen, J. L. and Kern, W. (eds.) *Thin Film Processes.* San Diego: Academic Press, pp. 133-175.

Chun, H. D., Kim, J. S., Yoon, S. M. and Kim, C. G. (2001) 'Physical Properties and Photocatalytic Performance of TiO_2 Coated Stainless Steel Plate.' *Korean Journal of Chemical Engineering*, 18(6), pp. 908-913.

Clemente, A., Ramsden, J. J., Wright, A., Iza, F., Morrissey, J. A., Li Puma, G. and Malik, D. J. (2019) '*Staphylococcus aureus* Resists UVA at Low Irradiance But Succumbs in the Presence of TiO_2 Photocatalytic Coatings.' *Journal of Photochemistry and Photobiology B: Biology*, 193, pp. 131-139.

Codd, G. A., Morrison, L. F. and Metcalf, J. S. (2005) 'Cyanobacterial Toxins: Risk Management for Health Protection.' *Toxicology and Applied Pharmacology*, 203(3), pp. 264-272.

Corral, M. J., González, E., Cuquerella, M. and Alunda, J. M. (2013) 'Improvement of 96-well Microplate Assay for Estimation of Cell Growth and Inhibition of *Leishmania* with Alamar Blue.' *Journal of Microbiological Methods*, 94(2), pp. 111-116.

Cosemans, P., Zhu, X., Celis, J. P. and Van Stappen, M. (2003) 'Development of Low Friction Wear-Resistant Coatings.' *Surface and Coatings Technology*, 174–175, pp. 416-420.

Cottineau, T., Bealu, N., Gross, P. A., Pronkin, S. N., Keller, N., Savinova, E. R. and Keller, V. (2013) 'One Step Synthesis of Niobium Doped Titania Nanotube Arrays to Form (N, Nb) Co-Doped TiO_2 with High Visible Light Photoelectrochemical Activity.' *Journal of Materials Chemistry A*, 1(6), pp. 2151-2160.

Craig, S. and Harding, G. L. (1981) 'Effects of Argon Pressure and Substrate Temperature on the Structure and Properties of Sputtered Copper Films.' *Journal of Vacuum Science and Technology*, 19(2), pp. 205-215.

Dalrymple, O. K., Stefanakos, E., Trotz, M. A. and Goswami, D. Y. (2010) 'A Review of the Mechanisms and Modeling of Photocatalytic Disinfection.' *Applied Catalysis B: Environmental*, 98(1-2), pp. 27-38.

Dargahi, Z., Asgharzadeh, H. and Maleki-Ghaleh, H. (2018) 'Synthesis of Mo-doped TiO_2/Reduced Graphene Oxide Nanocomposite for Photoelectrocatalytic Applications.' *Ceramics International*, 44(11), pp. 13015-13023.

Dastider, S. G., Barizuddin, S., Yuksek, N. S., Dweik, M. and Almasri, M. F. (2015) 'Efficient and Rapid Detection of Salmonella Using Microfluidic Impedance Based Sensing.' *Journal of Sensors*, 2015, pp. 1-8.

Davis, C. (2014) 'Enumeration of Probiotic Strains: Review of Culture-Dependent and Alternative Techniques to Quantify Viable Bacteria.' *Journal of Microbiological Methods*, 103, pp. 9-17.

De Paoli, P. (2005) 'Bio-Banking in Microbiology: from Sample Collection to Epidemiology, Diagnosis and Research.' *FEMS Microbiology Reviews*, 29(5), pp. 897-910.

Delcour, A. H. (2009) 'Outer Membrane Permeability and Antibiotic Resistance.' *Biochimica et biophysica acta*, 1794(5), pp. 808-816.

Deshpandey, C. V. and Bunshah, R. F. (1991) 'II-2 - Evaporation Processes.' *In* Vossen, J. L. and Kern, W. (eds.) *Thin Film Processes*. San Diego: Academic Press, pp. 79-132.

Devi, L. G. and Murthy, B. N. (2008) 'Characterization of Mo-Doped TiO_2 and its Enhanced Photocatalytic Activity under Visible Light.' *Catalysis Letters*, 125(3), pp. 320-330.

Di Paola, A., Marcì, G., Palmisano, L., Schiavello, M., Uosaki, K., Ikeda, S. and Ohtani, B. (2002) 'Preparation of Polycrystalline TiO_2 Photocatalysts

Impregnated with Various Transition Metal Ions: Characterization and Photocatalytic Activity for the Degradation of 4-Nitrophenol.' *The Journal of Physical Chemistry B*, 106(3), pp. 637-645.

Diebold, U. (2002) 'The Surface Science of Titanium Dioxide.' *Surface Science Reports*, 48(1), pp. 53-229.

Ditta, I. B., Steele, A., Liptrot, C., Tobin, J., Tyler, H., Yates, H. M., Sheel, D. W. and Foster, H. A. (2008) 'Photocatalytic Antimicrobial Activity of Thin Surface Films of TiO_2, CuO and TiO_2/CuO dual layers on *Escherichia coli* and bacteriophage T4.' *Applied Microbiology and Biotechnology*, 79(1), p. 127.

Donoso, M. G., Méndez-Vilas, A., Bruque, J. M. and González-Martin, M. L. (2007) 'On the Relationship Between Common Amplitude Surface Roughness Parameters and Surface Area: Implications for the Study of Cell–Material Interactions.' *International Biodeterioration & Biodegradation*, 59(3), pp. 245-251.

Driscoll, J. A., Brody, S. L. and Kollef, M. H. (2007) 'The Epidemiology, Pathogenesis and Treatment of *Pseudomonas aeruginosa* Infections.' *Drugs*, 67(3), pp. 351-368.

Dunlop, P. S. M., Sheeran, C. P., Byrne, J. A., McMahon, M. A. S., Boyle, M. A. and McGuigan, K. G. (2010) 'Inactivation of Clinically Relevant Pathogens by Photocatalytic Coatings.' *Journal of Photochemistry and Photobiology A: Chemistry*, 216(2-3), pp. 303-310.

Eden, R. and Eden, G. (1984) *Impedance Microbiology.* Hertfordshire: Research Studies Press.

Euan, M. (1996) 'The Development of a Prototype High-Speed Stylus Profilometer and its Application to Rapid 3D Surface Measurement.' *Nanotechnology*, 7(1), p. 37.

Fabrega, J., Fawcett, S. R., Renshaw, J. C. and Lead, J. R. (2009) 'Silver Nanoparticle Impact on Bacterial Growth: Effect of pH, Concentration, and Organic Matter.' *Environmental Science & Technology*, 43(19), pp. 7285-7290.

Farahani, N., Kelly, P. J., West, G., Ratova, M., Hill, C. and Vishnyakov, V. (2011) 'Photocatalytic Activity of Reactively Sputtered and Directly Sputtered Titania Coatings.' *Thin Solid Films*, 520(5), pp. 1464-1469.

Feng, H. E. and Le-cheng, L. (2004) 'Degradation Kinetics and Mechanisms of Phenol in Photo-Fenton Process.' *Journal of Zhejiang University SCIENCE*, 5(2), pp. 198-205.

Fernández-Ibáñez, P., Sichel, C., Polo-López, M. I., de Cara-García, M. and Tello, J. C. (2009) 'Photocatalytic Disinfection of Natural Well Water Contaminated by *Fusarium solani* Using TiO_2 Slurry in Solar CPC Photo-Reactors.' *Catalysis Today*, 144(1-2), pp. 62-68.

Filho, A. I., Silva, R. V. d., Oliveira, P. G. B. d., Martins, J. B. R., Bose Filho, W. W. and Strangwood, M. (2017) 'Influence of Niobium and Molybdenum on Mechanical Strength and Wear Resistance of Microalloyed Steels.' *Materials Research*, 20, pp. 1029-1034.

Fischer, T. W., Wigger-Alberti, W. and Elsner, P. (1999) 'Direct and Non-Direct Measurement Techniques for Analysis of Skin Surface Topography.' *Skin Pharmacology and Physiology*, 12(1-2), pp. 1-11.

Fisher, L., Ostovapour, S., Kelly, P., Whitehead, K. A., Cooke, K., Storgards, E. and Verran, J. (2014) 'Molybdenum-Doped Titanium Dioxide Photocatalytic Coatings for Use as Hygienic Surfaces: the Effect of Soiling on Antimicrobial Activity.' *Biofouling*, 30(8), pp. 911-919.

Foster, H. A., Ditta, I. B., Varghese, S. and Steele, A. (2011) 'Photocatalytic Disinfection Using Titanium Dioxide: Spectrum and Mechanism of Antimicrobial Activity.' *Applied Microbiology and Biotechnology*, 90(6), pp. 1847-1868.

Foster, H. A., Sheel, D. W., Sheel, P., Evans, P., Varghese, S., Rutschke, N. and Yates, H. M. (2010) 'Antimicrobial activity of titania/silver and titania/copper films prepared by CVD.' *Journal of Photochemistry and Photobiology A: Chemistry*, 216(2-3), pp. 283-289.

Fox, M. A. and Dulay, M. T. (1993) 'Heterogeneous Photocatalysis.' *Chemical Reviews*, 93(1), pp. 341-357.

Fu, G. F., Vary, P. S. and Lin, C. T. (2005) 'Anatase TiO_2 Nanocomposites for Antimicrobial Coatings.' *Journal of Physical Chemistry B*, 109(18), pp. 8889-8898.

Fujishima, A. and Honda, K. (1972) 'Electrochemical Photolysis of Water at a Semiconductor Electrode.' *Nature*, 238(5358), pp. 37-38.

Fujishima, A. and Zhang, X. T. (2006) 'Titanium Dioxide Photocatalysis: Present Situation and Future Approaches.' *Comptes Rendus Chimie*, 9(5-6), pp. 750-760.

Fujishima, A., Rao, T. N. and Tryk, D. A. (2000) 'Titanium Dioxide Photocatalysis.' *Journal of Photochemistry and Photobiology C: Photochemistry Reviews*, 1(1), pp. 1-21.

Fujishima, A., Zhang, X. and Tryk, D. (2008) 'TiO_2 Photocatalysis and Related Surface Phenomena.' *Surface Science Reports*, 63(12), pp. 515-582.

Fuster-Valls, N., Hernández-Herrero, M., Marín-de-Mateo, M. and Rodríguez-Jerez, J. J. (2008) 'Effect of Different Environmental Conditions on the Bacteria Survival on Stainless Steel Surfaces.' *Food Control*, 19(3), pp. 308-314.

Garcia, J. A., Martinez, A., Lerga, B., Rico, M. and Fuentes, G. G. (2006) 'Decorative Coatings by PVD on Ceramics.' *Boletín de la Sociedad Española de Cerámica y Vidrio (1983)*, 45(4), pp. 255-258.

Garciaarmesto, R., Prieto, M., Otero, A., Encinas, J. P., Garcialopez, L. and Moreno, B. (1994) 'Assessment of the Microbiological Quality of Raw Ewes Milk by Rapid Colorimetric Methods.' *Netherlands Milk and Dairy Journal*, 48(2), pp. 99-110.

Gardecka, A. J., Goh, G. K. L., Sankar, G. and Parkin, I. P. (2015) 'On the Nature of Niobium Substitution in Niobium-Doped Titania Thin Films by

AACVD and its Impact on Electrical and Optical Properties.' *Journal of Materials Chemistry A*, 3(34), pp. 17755-17762.

Gautier, C., Moulard, G., Chatelon, J. P. and Motyl, G. (2001) 'Influence of Substrate Bias Voltage on the *in situ* Stress Measured by an Improved Optical Cantilever Technique of Sputtered Chromium Films.' *Thin Solid Films*, 384(1), pp. 102-108.

Gelover, S., Gomez, L. A., Reyes, K. and Teresa Leal, M. (2006) 'A Practical Demonstration of Water Disinfection Using TiO_2 Films and Sunlight.' *Water Research*, 40(17), pp. 3274-3280.

Genzer, J. and Efimenko, K. (2006) 'Recent Developments in Superhydrophobic Surfaces and Their Relevance to Marine Fouling: a Review.' *Biofouling*, 22(5), pp. 339-360.

Gerhardts, A., Hammer, T. R., Balluff, C., Mucha, H. and Hoefer, D. (2012) 'A Model of the Transmission of Micro-Organisms in a Public Setting and its Correlation to Pathogen Infection Risks.' *Journal of Applied Microbiology*, 112(3), pp. 614-621.

Gogniat, G., Thyssen, M., Denis, M., Pulgarin, C. and Dukan, S. (2006) 'The Bactericidal Effect of TiO_2 Photocatalysis Involves Adsorption onto Catalyst and the Loss of Membrane Integrity.' *FEMS Microbiology Letters*, 258(1), pp. 18-24.

Goldstein, J. I., Newbury, D. E., Michael, J. R., Ritchie, N. W. M., Scott, J. H. J. and Joy, D. C. (2018) *Scanning Electron Microscopy and X-Ray Microanalysis.* 4 ed., New York: Springer.

González-Pinzón, R., Haggerty, R. and Myrold, D. D. (2012) 'Measuring Aerobic Respiration in Stream Ecosystems Using the Resazurin-Resorufin System.' *Journal of Geophysical Research: Biogeosciences*, 117(G00N06), pp. 1-10.

Guo, J., Gan, Z., Lu, Z., Liu, J., Xi, J., Wan, Y., Le, L., Liu, H., Shi, J. and Xiong, R. (2013) 'Improvement of the Photocatalytic Properties of TiO_2 by (Fe+Mo) Co-Doping - a Possible Way to Retard the Recombination Process.' *Journal of Applied Physics*, 114(10), p. 104903.

Gutbrod, K. and Zollfrank, C. (2013) 'The Photocatalytic Properties of Ti–Mo Oxides Prepared by a Simple Sol–Gel Route.' *Journal of Sol-Gel Science and Technology*, 66(1), pp. 112-119.

Haggerty, R., Argerich, A. and Martí, E. (2008) 'Development of a "Smart" Tracer for the Assessment of Microbiological Activity and Sediment-Water Interaction in Natural Waters: the Resazurin-Resorufin System.' *Water Resources Research*, 44(4),

Hanaor, D. A. H. and Sorrell, C. C. (2011) 'Review of the Anatase to Rutile Phase Transformation.' *Journal of Materials Science*, 46(4), pp. 855-874.

Haque, S. M., Shinde, D. D., Misal, J. S., Bhattacharyya, D. and Sahoo, N. K. (2014) 'Study of Optical Properties of Asymmetric Bipolar Pulse DC Magnetron Sputtered Ta_2O_5 Thin Film as a Function of Oxygen Content in Deposition Ambient.' *AIP Conference Proceedings*, 1591(1), pp. 858-860.

He, K., Chen, N. F., Wang, C. J., Wei, L. S. and Chen, J. K. (2018) 'Method for Determining Crystal Grain Size by X-Ray Diffraction.' *Crystal Research and Technology*, 53(2), p. 6.

Hedges, A. J. (2002) 'Estimating the Precision of Serial Dilutions and Viable Bacterial Counts.' *International Journal of Food Microbiology*, 76(3), pp. 207-214.

Herrmann, J. M. (1999) 'Heterogeneous Photocatalysis Fundamentals and Applications.' *Catalysis Today*, 53(1), pp. 115-129.

Herrmann, J. M. (2010) 'Photocatalysis Fundamentals Revisited to Avoid Several Misconceptions.' *Applied Catalysis B: Environmental*, 99(3-4), pp. 461-468.

Hirano, M. and Matsushima, K. (2006) 'Photoactive and Adsorptive Niobium-Doped Anatase (TiO_2) Nanoparticles: Influence of Hydrothermal Conditions on their Morphology, Structure, and Properties.' *Journal of the American Ceramic Society*, 89(1), pp. 110-117.

Hoffmann, M. R., Martin, S. T., Choi, W. and Bahnemann, D. W. (1995) 'Environmental Applications of Semiconductor Photocatalysis.' *Chemical Reviews*, 95(1), pp. 69-96.

Hou, Y.-Q., Zhuang, D.-M., Zhang, G., Zhao, M. and Wu, M.-S. (2003) 'Influence of Annealing Temperature on the Properties of Titanium Dioxide Thin Film.' *Applied Surface Science*, 218(1), pp. 98-106.

Hu, C., Guo, J., Qu, J. and Hu, X. (2007) 'Photocatalytic Degradation of Pathogenic Bacteria with AgI/TiO_2 under Visible Light Irradiation.' *Langmuir*, 23(9), pp. 4982-4987.

Hubálek, Z. (2003) 'Protectants Used in the Cryopreservation of Microorganisms.' *Cryobiology*, 46(3), pp. 205-229.

Hüsken, G., Hunger, M. and Brouwers, H. J. H. (2009) 'Experimental Study of Photocatalytic Concrete Products for Air Purification.' *Building and Environment*, 44(12), pp. 2463-2474.

Iancu, A. T., Logar, M., Park, J. and Prinz, F. B. (2015) 'Atomic Layer Deposition of Undoped TiO_2 Exhibiting P-Type Conductivity.' *ACS Applied Materials & Interfaces*, 7(9), pp. 5134-5140.

Inagaki, M., Nonaka, R., Tryba, B. and Morawski, A. W. (2006) 'Dependence of photocatalytic activity of anatase powders on their crystallinity.' *Chemosphere*, 64(3), pp. 437-445.

Irie, H., Watanabe, Y. and Hashimoto, K. (2003) 'Carbon-Doped Anatase TiO_2 Powders as a Visible-Light Sensitive Photocatalyst.' *Chemistry Letters*, 32(8), pp. 772-773.

Ismail, A. A. and Bahnemann, D. W. (2011) 'Mesoporous titania photocatalysts: preparation, characterization and reaction mechanisms.' *Journal of Materials Chemistry*, 21(32), pp. 11686-11707.

Jack, J. J. (1977) 'Modified Resazurin Test for Milk.' *Agriculture in Northern Ireland*, 51(9), pp. 254-256.

Jacobsen, A. E. (1949) 'Titanium Dioxide Pigments: Correlation between Photochemical Reactivity and Chalking.' *Industrial & Engineering Chemistry*, 41(3), pp. 523-526.

Japanese Standards Association. (2000) JIS Z 2801:2000 - Antimicrobial Products - Test for Antimicrobial Activity and Efficacy.

Jehn, H. A. (1992) 'Decorative Coatings.' *In* Gissler, W. and Jehn, H. A. (eds.) *Advanced Techniques for Surface Engineering. Eurocourses: Mechanical and Materials Science.* Vol. 1. Dordrecht: Springer, pp. 359-370.

Jeon, M. J. and Ha, J. W. (2018) 'Efficacy of UV-A, UV-B, and UV-C Irradiation on Inactivation of Foodborne Pathogens in Different Neutralizing Buffer Solutions.' *LWT - Food Science and Technology*, 98, pp. 591-597.

Joshi, B. N., Yoon, H., van Hest, M. and Yoon, S. S. (2013) 'Niobium-Doped Titania Photocatalyst Film Prepared via a Nonaqueous Sol-Gel Method.' *Journal of the American Ceramic Society*, 96(8), pp. 2623-2627.

Joya, Y. F., Liu, Z. and Wang, T. (2011) 'Characterization and Antibacterial Functions of Ag–TiO_2 and W–TiO_2 Nanostructured Thin Films Prepared by Sol-Gel/Laser-Induced Technique.' *Applied Physics B*, 105(3), pp. 525-536.

Kafizas, A., Kellici, S., Darr, J. A. and Parkin, I. P. (2009) 'Titanium Dioxide and Composite Metal/Metal Oxide Titania Thin Films on Glass: A Comparative Study of Photocatalytic Activity.' *Journal of Photochemistry and Photobiology A: Chemistry*, 204(2–3), pp. 183-190.

Kaleji, B. K., Sarraf-Mamoory, R. and Fujishima, A. (2012) 'Influence of Nb Dopant on the Structural and Optical Properties of Nanocrystalline TiO_2 Thin Films.' *Materials Chemistry and Physics*, 132(1), pp. 210-215.

Kaleji, B. K., Hosseinabadi, N. and Fujishima, A. (2013) 'Enhanced Photo-Catalytic Activity of TiO_2 Nanostructured Thin Films under Solar Light by Sn and Nb Co-Doping.' *Journal of Sol-Gel Science and Technology*, 65(2), pp. 195-203.

Kaleji, B. K., Fariman, N. A. and Hosseinabadi, N. (2017) 'Fabrication of Nb/V Co-Doped TiO_2 Thin Films and Study of Structural, Optical and Photocatalytic Properties.' *International Journal of Nano Dimension*, 8(3), pp. 265-273.

Kamisaka, H., Hitosugi, T., Suenaga, T., Hasegawa, T. and Yamashita, K. (2009) 'Density Functional Theory Based First-Principle Calculation of Nb-Doped Anatase TiO_2 and its Interactions With Oxygen Vacancies and Interstitial Oxygen.' *The Journal of Chemical Physics*, 131(3), p. 034702.

Kelly, P. J. and Arnell, R. D. (2000) 'Magnetron Sputtering: A Review of Recent Developments and Applications.' *Vacuum*, 56(3), pp. 159-172.

Kelly, P. J. and Zhou, Y. (2006) 'Zinc Oxide-Based Transparent Conductive Oxide Films Prepared by Pulsed Magnetron Sputtering from Powder Targets: Process Features and Film Properties.' *Journal of Vacuum Science & Technology A: Vacuum, Surfaces, and Films*, 24(5), pp. 1782-1789.

Kelly, P. J., West, G. T., Ratova, M., Fisher, L., Ostovarpour, S. and Verran, J. (2014) 'Structural Formation and Photocatalytic Activity of Magnetron

Sputtered Titania and Doped-Titania Coatings.' *Molecules*, 19(10), pp. 16327-16348.

Kepner, R. L. and Pratt, J. R. (1994) 'Use of Fluorochromes for Direct Enumeration of Total Bacteria in Envrinomental Samples: Past and Present.' *Microbiological Reviews*, 58(4), pp. 603-615.

Khalifa, R. A., Nasser, M. S., Gomaa, A. A., Osman, N. M. and Salem, H. M. (2013) 'Resazurin Microtiter Assay Plate Method for Detection of Susceptibility of Multidrug Resistant *Mycobacterium tuberculosis* to Second-Line Anti-Tuberculous Drugs.' *Egyptian Journal of Chest Diseases and Tuberculosis*, 62(2), pp. 241-247.

Khan, H. and Berk, D. (2014) 'Synthesis, Physicochemical Properties and Visible Light Photocatalytic Studies of Molybdenum, Iron and Vanadium Doped Titanium Dioxide.' *Reaction Kinetics, Mechanisms and Catalysis*, 111(1), pp. 393-414.

Khan, H., Jiang, Z. and Berk, D. (2018) 'Molybdenum Doped Graphene/TiO_2 Hybrid Photocatalyst for UV/Visible Photocatalytic Applications.' *Solar Energy*, 162, pp. 420-430.

Kim, D. J., Hahn, S. H., Oh, S. H. and Kim, E. J. (2002) 'Influence of Calcination Temperature on Structural and optical Properties of TiO_2 Thin Films Prepared by Sol–Gel Dip Coating.' *Materials Letters*, 57(2), pp. 355-360.

Kim, S.-J., Kim, D.-K. and Kang, D.-H. (2016) 'Using UVC Light-Emitting Diodes at Wavelengths of 266 to 279 Nanometers To Inactivate Foodborne Pathogens and Pasteurize Sliced Cheese.' *Applied and Environmental Microbiology*, 82(1), p. 11.

Kim, S., Ghafoor, K., Lee, J., Feng, M., Hong, J., Lee, D.-U. and Park, J. (2013) 'Bacterial Inactivation in Water, DNA Strand Breaking, and Membrane Damage Induced by Ultraviolet-Assisted Titanium Dioxide Photocatalysis.' *Water Research*, 47(13), pp. 4403-4411.

Kitaguchi, A., Yamaguchi, N. and Nasu, M. (2006) 'Simultaneous Enumeration of Viable Enterobacteriaceae and *Pseudomonas* spp. Within Three Hours by Multicolor Fluorescence i*n situ* Hybridization with Vital Staining.' *Journal of Microbiological Methods*, 65(3), pp. 623-627.

Klaysri, R., Ratova, M., Praserthdam, P. and Kelly, P. J. (2017) 'Deposition of Visible Light-Active C-Doped Titania Films via Magnetron Sputtering Using CO_2 as a Source of Carbon.' *Nanomaterials*, 7(5), p. 113.

Klein, L. C. (1991) 'III-4 - Sol-Gel Coatings.' *In* Vossen, J. L. and Kern, W. (eds.) *Thin Film Processes*. San Diego: Academic Press, pp. 501-522.

Koch-Nolte, F., Fischer, S., Haag, F. and Ziegler, M. (2011) 'Compartmentation of NAD^+-Dependent Signalling.' *FEBS Letters*, 585(11), pp. 1651-1656.

Koch, A. (1981) 'Growth Measurement.' *In* Gerhardt, P., Murray, R., Costilow, R., Nester, E., Wood, W., Krieg, N. and Phillips, G. (eds.) *Manual of Methods for General Bacteriology*. Washington, DC: American Society for Microbiology, pp. 191-197.

Kozlov, D., Bavykin, D. and Savinov, E. (2003) 'Effect of the Acidity of TiO_2 Surface on Its Photocatalytic Activity in Acetone Gas-Phase Oxidation.' *Catalysis Letters*, 86(4), pp. 169-172.

Kühn, K. P., Chaberny, I. F., Massholder, K., Stickler, M., Benz, V. W., Sonntag, H.-G. and Erdinger, L. (2003) 'Disinfection of Surfaces by Photocatalytic Oxidation with Titanium Dioxide and UVA Light.' *Chemosphere*, 53(1), pp. 71-77.

Kusumaningrum, H. D., Riboldi, G., Hazeleger, W. C. and Beumer, R. R. (2003) 'Survival of Foodborne Pathogens on Stainless Steel Surfaces and Cross-Contamination to Foods.' *International Journal of Food Microbiology*, 85(3), pp. 227-236.

Kuwana, E., Liang, F. and Sevick-Muraca, E. M. (2004) 'Fluorescence Lifetime Spectroscopy of a pH-Sensitive Dye Encapsulated in Hydrogel Beads.' *Biotechnology Progress*, 20(5), pp. 1561-1566.

Lahmar, A., Assaf, A., Durand, M. J., Jouanneau, S., Thouand, G. and Garnier, B. (2016) 'Factors Influencing Adhesion of Submicrometer Thin Metal Films: A Critical Review.' *Reviews of Adhesion and Adhesives*, 4(1), pp. 47-68.

Lang, X. J., Chen, X. D. and Zhao, J. C. (2014) 'Heterogeneous Visible Light Photocatalysis for Selective Organic Transformations.' *Chemical Society Reviews*, 43(1), pp. 473-486.

Lasek, J., Yu, Y. H. and Wu, J. C. S. (2013) 'Removal of NOx by Photocatalytic Processes.' *Journal of Photochemistry and Photobiology C: Photochemistry Reviews*, 14, pp. 29-52.

Lee, C., Wei, X. D., Kysar, J. W. and Hone, J. (2008) 'Measurement of the Elastic Properties and Intrinsic Strength of Monolayer Graphene.' *Science*, 321(5887), pp. 385-388.

Lee, D. Y., Park, J. H., Kim, Y. H., Lee, M. H. and Cho, N. I. (2014) 'Effect of Nb Doping on Morphology, Crystal Structure, Optical Band Gap Energy of TiO_2 Thin Films.' *Current Applied Physics*, 14(3), pp. 421-427.

Li, C., Hsieh, J. H., Hung, M. T. and Huang, B. Q. (2015) 'The Deposition and Microstructure of Amorphous Tungsten Oxide Films by Sputtering.' *Vacuum*, 118, pp. 125-132.

Li, C. X., Zhang, D., Jiang, Z. H., Yao, Z. P. and Jia, F. Z. (2011) 'Mo-Doped Titania Films: Preparation, Characterization and Application for Splitting Water.' *New Journal of Chemistry*, 35(2), pp. 423-429.

Li Puma, G., Salvadó-Estivill, I., Obee, T. N. and Hay, S. O. (2009) 'Kinetics Rate Model of the Photocatalytic Oxidation of Trichloroethylene in Air Over TiO_2 Thin Films.' *Separation and Purification Technology*, 67(2), pp. 226-232.

Li, S., Cai, J., Wu, X., Zheng, F., Lin, X., Liang, W., Chen, J., Zheng, J., Lai, Z., Chen, T. and Zhu, L. (2014) 'Fabrication of positively and negatively charged, double-shelled, nanostructured hollow spheres for photodegradation of cationic and anionic aromatic pollutants under sunlight irradiation.' *Applied Catalysis B: Environmental*, 160–161, pp. 279-285.

Liao, C. H. and Shollenberger, L. M. (2003) 'Survivability and Long-Term Preservation of Bacteria in Water and in Phosphate-Buffered Saline.' *Letters in Applied Microbiology*, 37(1), pp. 45-50.

Lilja, M., Forsgren, J., Welch, K., Astrand, M., Engqvist, H. and Strømme, M. (2012) 'Photocatalytic and Antimicrobial Properties of Surgical Implant Coatings of Titanium Dioxide Deposited Though Cathodic Arc Evaporation.' *Biotechnology Letters*, 34(12), pp. 2299-2305.

Lin, C. P., Chen, H., Nakaruk, A., Koshy, P. and Sorrell, C. C. (2013) 'Effect of Annealing Temperature on the Photocatalytic Activity of TiO_2 Thin Films.' *Energy Procedia*, 34, pp. 627-636.

Liu, H., Lu, Z., Yue, I., Liu, J., Gan, Z., Shu, C., Zhang, T., Shi, J. and Xiong, R. (2011) '(Mo+N) Codoped TiO_2 for Enhanced Visible-Light Photoactivity.' *Applied Surface Science*, 257(22), pp. 9355-9361.

Liu, H. L. and Yang, T. C. K. (2003) 'Photocatalytic Inactivation of *Escherichia coli* and *Lactobacillus helveticus* by ZnO and TiO_2 Activated with Ultraviolet Light.' *Process Biochemistry*, 39(4), pp. 475-481.

Liu, X., Jiang, R. and Liu, S. (2010) 'Preparation, Charaterization, and Photocatalytic Activity of TiO_2/Mo-TiO_2.' *Chinese Journal of Catalysis*, 31(11), pp. 1381-1387.

Lopez, L., Daoud, W. A., Dutta, D., Panther, B. C. and Turney, T. W. (2013) 'Effect of Substrate on Surface Morphology and Photocatalysis of Large-Scale TiO_2 Films.' *Applied Surface Science*, 265, pp. 162-168.

Lorenz, K., Bauer, S., Gutbrod, K., Guggenbichler, J. P., Schmuki, P. and Zollfrank, C. (2011) 'Anodic TiO_2 Nanotube Layers Electrochemically Filled with MoO_3 and their Antimicrobial Properties.' *Biointerphases*, 6(1), pp. 16-21.

Low, J. X., Cheng, B. and Yu, J. G. (2017) 'Surface Modification and Enhanced Photocatalytic CO_2 Reduction Performance of TiO_2: A Review.' *Applied Surface Science*, 392, pp. 658-686.

Lu, X., Zhao, T., Gao, X., Ren, J., Yan, X. and La, P. (2018a) 'Investigation of Mo-, Pt-, and Rh-doped rutile TiO2 based on first-principles calculations.' *AIP Advances*, 8(7), p. 075014.

Lu, X. F., Zhao, T. T., Gao, X., Ren, J. Q., Yan, X. B. and La, P. Q. (2018b) 'Investigation of Mo-, Pt-, and Rh-doped rutile TiO2 based on first-principles calculations.' *AIP Advances*, 8(7), p. 10.

Luidalepp, H., Berger, S., Joss, O., Tenson, T. and Polacek, N. (2016) 'Ribosome Shut-Down by 16S rRNA Fragmentation in Stationary-Phase *Escherichia coli*.' *Journal of Molecular Biology*, 428(10, Part B), pp. 2237-2247.

Luppens, S. B. I., Reij, M. W., van der Heijden, R. W. L., Rombouts, F. M. and Abee, T. (2002) 'Development of a Standard Test To Assess the Resistance of *Staphylococcus aureus* Biofilm Cells to Disinfectants.' *Applied and Environmental Microbiology*, 68(9), pp. 4194-4200.

Luttrell, T., Halpegamage, S., Tao, J., Kramer, A., Sutter, E. and Batzill, M. (2014) 'Why is Anatase a Better Photocatalyst than Rutile? - Model Studies on Epitaxial TiO_2 Films.' *Scientific Reports*, 4, p. 4043.

Ma, X. G., Wu, Y., Lu, Y. H., Xu, J., Wang, Y. J. and Zhu, Y. F. (2011) 'Effect of Compensated Codoping on the Photoelectrochemical Properties of Anatase TiO_2 Photocatalyst.' *Journal of Physical Chemistry C*, 115(34), pp. 16963-16969.

Mahalingam, T., Selvakumar, C., Ranjith Kumar, E. and Venkatachalam, T. (2017) 'Structural, Optical, Morphological and Thermal Properties of TiO_2–Al and TiO_2–Al_2O_3 Composite Powders by Ball Milling.' *Physics Letters A*, 381(21), pp. 1815-1819.

Maia, M. R. G., Marques, S., Cabrita, A. R. J., Wallace, R. J., Thompson, G., Fonseca, A. J. M. and Oliveira, H. M. (2016) 'Simple and Versatile Turbidimetric Monitoring of Bacterial Growth in Liquid Cultures Using a Customized 3D Printed Culture Tube Holder and a Miniaturized Spectrophotometer: Application to Facultative and Strictly Anaerobic Bacteria.' *Frontiers in Microbiology*, 7, pp. 1381-1381.

Mamane, H., Ducoste, J. J. and Linden, K. G. (2006) 'Effect of Particles on Ultraviolet Light Penetration in Natural and Engineered Systems.' *Applied Optics*, 45(8), pp. 1844 - 1856.

Mathews, N. R., Morales, E. R., Cortés-Jacome, M. A. and Toledo Antonio, J. A. (2009) 'TiO_2 Thin Films – Influence of Annealing Temperature on Structural, Optical and Photocatalytic Properties.' *Solar Energy*, 83(9), pp. 1499-1508.

Matteucci, F., Cruciani, G., Dondi, M. and Raimondo, M. (2006) 'The Role of Counterions (Mo, Nb, Sb, W) in Cr-, Mn-, Ni- and V-Doped Rutile Ceramic Pigments: Part 1. Crystal Structure and Phase Transformations.' *Ceramics International*, 32(4), pp. 385-392.

Mattsson, A., Leideborg, M., Larsson, K., Westin, G. and Österlund, L. (2006) 'Adsorption and Solar Light Decomposition of Acetone on Anatase TiO_2 and Niobium Doped TiO_2 Thin FIlms.' *Journal of Physical Chemistry B*, 110(1), pp. 1210-1220.

Matz, C., Bergfeld, T., Rice, S. A. and Kjelleberg, S. (2004) 'Microcolonies, Quorum Sensing and Cytotoxicity Determine the Survival of *Pseudomonas aeruginosa* Biofilms Exposed to Protozoan Grazing.' *Environmental Microbiology*, 6(3), pp. 218-226.

McEvoy, J. G., Cui, W. and Zhang, Z. (2013) 'Degradative and Disinfective Properties of Carbon-Doped Anatase–Rutile TiO_2 Mixtures under Visible Light Irradiation.' *Catalysis Today*, 207, pp. 191-199.

McFeters, G. A., Pyle, B. H., Lisle, J. T. and Broadaway, S. C. (1999) 'Rapid Direct Methods for Enumeration of Specific, Active Bacteria in Water and Biofilms.' *Symposium Series (Society for Applied Microbiology*, 85(28), pp. 193-200.

Mengyue, Z., Shifu, C. and Yaowu, T. (1995) 'Photocatalytic Degradation of Organophosphorus Pesticides Using Thin Films of TiO$_2$.' *Journal of Chemical Technology & Biotechnology*, 64(4), pp. 339-344.

Michalow, K. A., Flak, D., Heel, A., Parlinska-Wojtan, M., Rekas, M. and Graule, T. (2012) 'Effect of Nb Doping on Structural, Optical and Photocatalytic Properties of Flame-Made TiO$_2$ Nanopowder.' *Environmental Science and Pollution Research*, 19(9), pp. 3696-3708.

Miles, A. A., Misra, S. S. and Irwin, J. O. (1938) 'The Estimation of the Bactericidal Power of the Blood.' *The Journal of Hygiene*, 38(6), pp. 732-749.

Mills, A. (2012) 'An Overview of the Methylene Blue ISO Test for Assessing the Activities of Photocatalytic Films.' *Applied Catalysis B: Environmental*, 128, pp. 144-149.

Mills, A. and LeHunte, S. (1997) 'An Overview of Semiconductor Photocatalysis.' *Journal of Photochemistry and Photobiology A: Chemistry*, 108, pp. 1-35.

Mills, A. and O'Rourke, C. (2011) 'Adsorption and Destruction of Methylene Blue by Semiconductor Photocatalysis.' *Green*, 1(1), pp. 105-113.

Mills, A., Hill, C. and Robertson, P. K. J. (2012) 'Overview of the Current ISO Tests for Photocatalytic Materials.' *Journal of Photochemistry and Photobiology A: Chemistry*, 237, pp. 7-23.

Mills, A., Wells, N. and O'Rourke, C. (2016) 'Correlation Between the Photocatalysed Oxidation of Methylene Blue in Solution and the Reduction of Resazurin in a Photocatalyst Activity Indicator Ink (Rz Paii).' *Journal of Photochemistry and Photobiology A: Chemistry*, 330, pp. 86-89.

Mills, A., Wells, N., MacKenzie, J. and MacDonald, G. (2017) 'Kinetics of Reduction of a Resazurin-Based Photocatalytic Activity Ink.' *Catalysis Today*, 281(1), pp. 14-20.

Monteagudo, J. M., Durán, A., Martín, I. S. and García, S. (2014) 'Ultrasound-Assisted Homogeneous Photocatalytic Degradation of Reactive Blue 4 in Aqueous Solution.' *Applied Catalysis B: Environmental*, 152–153, pp. 59-67.

Møretrø, T., Heir, E., Mo, K. R., Habimana, O., Abdelgani, A. and Langsrud, S. (2010) 'Factors Affecting Survival of Shigatoxin-Producing *Escherichia coli* on Abiotic Surfaces.' *International Journal of Food Microbiology*, 138(1–2), pp. 71-77.

Mowry, S. and Ogren, P. J. (1999) 'Kinetics of Methylene Blue Reduction by Ascorbic Acid.' *Journal of Chemical Education*, 76(7), p. 970.

Moyer, R. H. and Campbell, J. J. R. (1963) 'Mechanism of Resazurin Reduction in Milk of Low Bacterial Content.' *Journal of Dairy Science*, 46(9), pp. 897-906.

Mu, W., Herrmann, J.-M. and Pichat, P. (1989) 'Room Temperature Photocatalytic Oxidation of Liquid Cyclohexane into Cyclohexanone Over Neat and Modified TiO$_2$.' *Catalysis Letters*, 3(1), pp. 73-84.

Munagala, G., Yempalla, K. R., Singh, S., Sharma, S., Kalia, N. P., Rajput, V. S., Kumar, S., Sawant, S. D., Khan, I. A., Vishwakarma, R. A. and Singh, P. P. (2015) 'Synthesis of New Generation Triazolyl- and Isoxazolyl-Containing 6-Nitro-2,3-Dihydroimidazooxazoles as Anti-TB Agents: *in vitro*, Structure-Activity Relationship, Pharmacokinetics and *in vivo* Evaluation.' *Organic & Biomolecular Chemistry*, 13(12), pp. 3610-3624.

Munshi, S., Twining, R. C. and Dahl, R. (2014) 'Alamar Blue Reagent Interacts with Cell-Culture Media Giving Different Fluorescence Over Time: Potential for False Positives.' *Journal of Pharmacological and Toxicological Methods*, 70(2), pp. 195-198.

Murashita, S., Kawamura, S. and Koseki, S. (2017) 'Inactivation of Nonpathogenic *Escherichia coli*, *Escherichia coli* O157:H7, *Salmonella enterica Typhimurium*, and *Listeria monocytogenes* in Ice Using a UVC Light-Emitting Diode.' *Journal of Food Protection*, 80(7), pp. 1198-1203.

Musil, J., Vlcek, J. and Baroch, P. (2006) 'Magnetron Discharges for Thin Films Plasma Processing.' *In* Pauleau, Y. (ed.) *Materials Surface Processing by Directed Energy Techniques*. Oxford: Elsevier, pp. 67-110.

Nakaruk, A., Ragazzon, D. and Sorrell, C. C. (2010) 'Anatase–Rutile Transformation Through High-Temperature Annealing of Titania Films Produced by Ultrasonic Spray Pyrolysis.' *Thin Solid Films*, 518(14), pp. 3735-3742.

Nakata, K. and Fujishima, A. (2012) 'TiO_2 Photocatalysis: Design and Applications.' *Journal of Photochemistry and Photobiology C: Photochemistry Reviews*, 13(3), pp. 169-189.

Natori, H. and Kobayashi, K. T. M. (2009) 'Fabrication and Photocatalytic Activity of TiO_2/MoO_3 Particulate Films.' *Journal of Oleo Science*, 58(4), pp. 203-211.

Nguyen, N. H., Wu, H.-Y. and Bai, H. (2015) 'Photocatalytic Reduction of NO_2 and CO_2 using Molybdenum-Doped Titania Nanotubes.' *Chemical Engineering Journal*, 269, pp. 60-66.

Nikolic, N., Schreiber, F., Dal Co, A., Kiviet, D. J., Bergmiller, T., Littmann, S., Kuypers, M. M. M. and Ackermann, M. (2017) 'Cell-to-Cell Variation and Specialization in Sugar Metabolism in Clonal Bacterial Populations.' *PLOS Genetics*, 13(12), p. e1007122.

Niu, X. Y., Yan, W. J., Zhao, H. L. and Yang, J. K. (2018) 'Synthesis of Nb Doped TiO_2 Nanotube/Reduced Graphene Oxide Heterostructure Photocatalyst with High Visible Light Photocatalytic Activity.' *Applied Surface Science*, 440, pp. 804-813.

Nixon, M. C. and Lamb, A. B. (1945) 'Resazurin Test for Grading Raw Milk.' *Canadian Journal of Comparative Medicine and Veterinary Science*, 9(1), pp. 18-23.

Ohno, T., Sarukawa, K., Tokieda, K. and Matsumura, M. (2001) 'Morphology of a TiO_2 Photocatalyst (Degussa, P-25) Consisting of Anatase and Rutile Crystalline Phases.' *Journal of Catalysis*, 203(1), pp. 82-86.

Ohtani, B., Prieto-Mahaney, O. O., Li, D. and Abe, R. (2010) 'What is Degussa (Evonik) P25? Crystalline Composition Analysis, Reconstruction from Isolated Pure Particles and Photocatalytic Activity Test.' *Journal of Photochemistry and Photobiology A: Chemistry*, 216(2), pp. 179-182.

Orlowska, M., Koutchma, T., Kostrzynska, M. and Tang, J. (2015) 'Surrogate Organisms for Pathogenic O157:H7 and Non-O157 *Escherichia coli* Strains for Apple Juice Treatments by UV-C Light at Three Monochromatic Wavelengths.' *Food Control*, 47, pp. 647-655.

Osan, J., Szaloki, I., Ro, C. U. and Van Grieken, R. (2000) 'Light Element Analysis of Individual Microparticles Using Thin-Window EPMA.' *Mikrochimica Acta*, 132(2-4), pp. 349-355.

Oxford English Dictionary. (2017) *Defnition of Photocatalysis in English*. [Online] [Accessed on 18.04.17] https://en.oxforddictionaries.com/definition/photocatalysis

Ozawa, K., Emori, M., Yamamoto, S., Yukawa, R., Yamamoto, S., Hobara, R., Fujikawa, K., Sakama, H. and Matsuda, I. (2014) 'Electron–Hole Recombination Time at TiO_2 Single-Crystal Surfaces: Influence of Surface Band Bending.' *The Journal of Physical Chemistry Letters*, 5(11), pp. 1953-1957.

Page, K., Wilson, M. and Parkin, I. P. (2009) 'Antimicrobial Surfaces and their Potential in Reducing the Role of the Inanimate Environment in the Incidence of Hospital-Acquired Infections.' *Journal of Materials Chemistry*, 19(23), p. 3819.

Pal, A., Pehkonen, S. O., Yu, L. E. and Ray, M. B. (2007) 'Photocatalytic Inactivation of Gram-Positive and Gram-Negative Bacteria using Fluorescent Light.' *Journal of Photochemistry and Photobiology A: Chemistry*, 186(2–3), pp. 335-341.

Pan, J. H. and Lee, W. I. (2006) 'Preparation of Highly Ordered Cubic Mesoporous WO_3/TiO_2 Films and Their Photocatalytic Properties.' *Chemistry of Materials*, 18(3), pp. 847-853.

Parker, A. E., Hamilton, M. A. and Goeres, D. M. (2018) 'Reproducibility of Antimicrobial Test Methods.' *Scientific Reports*, 8(1), p. 12531.

Parsons, R. (1991) 'II-4 - Sputter Deposition Processes.' *In* Vossen, J. L. and Kern, W. (eds.) *Thin Film Processes*. San Diego: Academic Press, pp. 177-208.

Paz, Y. and Heller, A. (1997) 'Photo-Oxidatively Self-Cleaning Transparent Titanium Dioxide Films on Soda Lime Glass: The Deleterious Effect of Sodium Contamination and its Prevention.' *Journal of Materials Research*, 12(10), pp. 2759-2766.

Peeters, E., Nelis, H. J. and Coenye, T. (2008) 'Comparison of Multiple Methods for Quantification of Microbial Biofilms Grown in Microtiter Plates.' *Journal of Microbiological Methods*, 72(2), pp. 157-165.

Pelaez, M., Nolan, N. T., Pillai, S. C., Seery, M. K., Falaras, P., Kontos, A. G., Dunlop, P. S. M., Hamilton, J. W. J., Byrne, J. A., O'Shea, K., Entezari, M. H. and Dionysiou, D. D. (2012) 'A Review on the Visible Light Active

Titanium Dioxide Photocatalysts for Environmental Applications.' *Applied Catalysis B: Environmental*, 125, pp. 331-349.

Pérez-Rodríguez, F., Posada-Izquierdo, G. D., Valero, A., García-Gimeno, R. M. and Zurera, G. (2013) 'Modelling Survival Kinetics of *Staphylococcus aureus* and *Escherichia coli* O157:H7 on Stainless Steel Surfaces Soiled with Different Substrates under Static Conditions of Temperature and Relative Humidity.' *Food Microbiology*, 33(2), pp. 197-204.

Peternel, I. T., Koprivanac, N., Božić, A. M. L. and Kušić, H. M. (2007) 'Comparative Study of UV/TiO_2, UV/ZnO and Photo-Fenton Processes for the Organic Reactive Dye Degradation in Aqueous Solution.' *Journal of Hazardous Materials*, 148(1–2), pp. 477-484.

Pettit, R. K., Weber, C. A., Kean, M. J., Hoffmann, H., Pettit, G. R., Tan, R., Franks, K. S. and Horton, M. L. (2005) 'Microplate Alamar Blue Assay for *Staphylococcus epidermidis* Biofilm Susceptibility Testing.' *Antimicrobial Agents and Chemotherapy*, 49(7), pp. 2612-2617.

Poelman, H., Tomaszewski, H., Poelman, D., Depla, D. and De Gryse, R. (2004) 'Effect of the Oxygen Deficiency of Ceramic TiO_2-x Targets on the Deposition of TiO_2 Thin Films by DC Magnetron Sputtering.' *Surface and Interface Analysis*, 36(8), pp. 1167-1170.

Priha, O., Raulio, M., Cooke, K., Fisher, L., Hill, C., Hylkinen, S., Kelly, P., Navabpour, P., Ostovarpour, S., Tapani, K., Tattershall, C., Vehviläinen, A.-K., Verran, J. and Storgårds, E. (2015) 'Microbial Populations on Brewery Filling Hall Surfaces – Progress Towards Functional Coatings.' *Food Control*, 55, pp. 1-11.

Puddu, V., Choi, H., Dionysiou, D. D. and Puma, G. L. (2010) 'TiO_2 Photocatalyst for Indoor Air Remediation: Influence of Crystallinity, Crystal Phase, and UV Radiation Intensity on Trichloroethylene Degradation.' *Applied Catalysis B: Environmental*, 94(3–4), pp. 211-218.

Rampersad, S. N. (2012) 'Multiple Applications of Alamar Blue as an Indicator of Metabolic Function and Cellular Health in Cell Viability Bioassays.' *Sensors* 12(9), pp. 12347-12360.

Rao, H., Lu, Z., Liu, X., Ge, H., Zhang, Z., Zou, P., He, H. and Wang, Y. (2016) 'Visible Light-Driven Photocatalytic Degradation Performance for Methylene Blue with Different Multi-Morphological Features of ZnS.' *RSC Advances*, 6(52), pp. 46299-46307.

Ratova, M. (2013) *Enhanced Properties of Photocatalytic Titania Thin Films via Doping During Magnetron Sputter Deposition.* Doctor of Philosophy. Manchester Metropolitan University.

Ratova, M., Kelly, P. J., West, G. T. and Iordanova, I. (2013) 'Enhanced Properties of Magnetron Sputtered Photocatalytic Coatings via Transition Metal Doping.' *Surface and Coatings Technology*, 228, pp. S544-S549.

Ratova, M., Redfern, J., Verran, J. and Kelly, P. J. (2018) 'Highly Efficient Photocatalytic Bismuth Oxide Coatings and their Antimicrobial Properties under Visible Light Irradiation.' *Applied Catalysis B: Environmental*, 239, pp. 223-232.

Ratova, M., West, G. T., Kelly, P. J., Xia, X. and Gao, Y. (2015) 'Synergistic Effect of Doping with Nitrogen and Molybdenum on the Photocatalytic Properties of Thin Titania Films.' *Vacuum*, 114, pp. 205-212.

Ratova, M., Marcelino, R., de Souza, P., Amorim, C. and Kelly, P. (2017) 'Reactive Magnetron Sputter Deposition of Bismuth Tungstate Coatings for Water Treatment Applications under Natural Sunlight.' *Catalysts*, 7(10), p. 283.

Ren, G. G., Hu, D. W., Cheng, E. W. C., Vargas-Reus, M. A., Reip, P. and Allaker, R. P. (2009) 'Characterisation of Copper Oxide Nanoparticles for Antimicrobial Applications.' *International Journal of Antimicrobial Agents*, 33(6), pp. 587-590.

Riss, T., Moravec, R., Niles, A., Duellman, S., Benink, H., Worzella, T. and Minor, L. (2013) 'Cell Viability Assays.' *In* Sittampalam, G., Coussens, N., Brimabombe, K., Grossman, A., Arkin, M., Auld, D., Austin, C., Baell, J., Bejcek, B., Caaveiro, J., Chung, T., GDahlin, J., Devanaryan, V., Foley, T., Glicksman, M., Hall, M., Haas, J., Inglese, J., Iverson, P., Kahl, S., Kales, S., Lal-Nag, M., Li, Z., McGee, J., McManus, O., Riss, T., Trask, O., Weidner, J., Wildey, M., Zia, M. and Xu, X. (eds.) *Assay Guidance Manual [Internet]*. Bethesda, MD: Eli Lilly & Company and the National Center for Advancing Translational Sciences,

Ro, C. U., Osán, J. and Van Grieken, R. (1999) 'Determination of Low-Z Elements in Individual Environmental Particles Using Windowless EPMA.' *Analytical Chemistry*, 71(8), pp. 1521-1528.

Ro, C. U., Kim, H. and Van Grieken, R. (2004) 'An Expert System for Chemical Speciation of Individual Particles Using Low-Z Particle Electron Probe X-Ray Microanalysis Data.' *Analytical Chemistry*, 76(5), pp. 1322-1327.

Robertson, J. M. C., Sieberg, C. and Robertson, P. K. J. (2015) 'The Influence of Microbial Factors on the Susceptibility of Bacteria to Photocatalytic Destruction.' *Journal of Photochemistry and Photobiology A: Chemistry*, 311, pp. 53-58.

Rochkind, M., Pasternak, S. and Paz, Y. (2015) 'Using Dyes for Evaluating Photocatalytic Properties: A Critical Review.' *Molecules*, 20(1), pp. 88-110.

Rossnagel, S. M. (1991) 'II-1 - Glow Discharge Plasmas and Sources for Etching and Deposition.' *In* Vossen, J. L. and Kern, W. (eds.) *Thin Film Processes.* San Diego: Academic Press, pp. 11-77.

Roy, S., Hegde, M. S. and Madras, G. (2009) 'Catalysis for NOx Abatement.' *Applied Energy*, 86(11), pp. 2283-2297.

Rtimi, S., Pulgarin, C., Robyr, M., Aybush, A., Shelaev, I., Gostev, F., Nadtochenko, V. and Kiwi, J. (2017) 'Insight Into the Catalyst/Photocatalyst Microstructure Presenting the Same Composition but Leading to a Variance in Bacterial Reduction under Indoor Visible Light.' *Applied Catalysis B: Environmental*, 208, pp. 135-147.

Saar-Dover, R., Bitler, A., Nezer, R., Shmuel-Galia, L., Firon, A., Shimoni, E., Trieu-Cuot, P. and Shai, Y. (2012) 'D-Alanylation of Lipoteichoic Acids

Confers Resistance to Cationic Peptides in Group B *Streptococcus* by Increasing the Cell Wall Density.' *PLOS Pathogens*, 8(9), p. e1002891.

Saito, T., Iwase, T., Horie, J. and Morioka, T. (1992) 'Mode of Photocatalytic Bactericidal Action of Powdered Semiconductor TiO_2 on mutans streptococci.' *Journal of Photochemistry and Photobiology B: Biology*, 14(4), pp. 369-379.

Samsonov, G. V. (1968) *Handbook of the Physicochemical Properties of the Elements.* New York: IFI-Plenum.

Sauer, T., Cesconeto Neto, G., José, H. J. and Moreira, R. F. P. M. (2002) 'Kinetics of Photocatalytic Degradation of Reactive Dyes in a TiO_2 Slurry Reactor.' *Journal of Photochemistry and Photobiology A: Chemistry*, 149(1–3), pp. 147-154.

Sawatsky, H. (2004) *A Decorative and Protective System for Wares.* Society for Imaging Science and Technology.

Sayılkan, F., Asiltürk, M., Tatar, P., Kiraz, N., Şener, Ş., Arpaç, E. and Sayılkan, H. (2008) 'Photocatalytic Performance of Sn-Doped TiO_2 Nanostructured Thin Films for Photocatalytic Degradation of Malachite Green Dye under UV and VIS-Lights.' *Materials Research Bulletin*, 43(1), pp. 127-134.

Scherrer, P. (1918) 'Bestimmung der Grosse und der Inneren Struktur von Kolloidteilchen Mittels Rontgenstrahlen.' *Mathematisch-Physikalische Klasse*, 2, pp. 98-100.

Seery, M. K., George, R., Floris, P. and Pillai, S. C. (2007) 'Silver Doped Titanium Dioxide Nanomaterials for Enhanced Visible Light Photocatalysis.' *Journal of Photochemistry and Photobiology A: Chemistry*, 189(2-3), pp. 258-263.

Shankar, M. V., Cheralathan, K. K., Arabindoo, B., Palanichamy, M. and Murugesan, V. (2004) 'Enhanced Photocatalytic Activity for the Destruction of Monocrotophos Pesticide by $TiO_2/H\beta$.' *Journal of Molecular Catalysis A: Chemical*, 223(1–2), pp. 195-200.

Sharifi, S., Behzadi, S., Laurent, S., Forrest, M. L., Stroeve, P. and Mahmoudi, M. (2012) 'Toxicity of Nanomaterials.' *Chemical Society Reviews*, 41(6), pp. 2323-2343.

Shehata, T. E. and Marr, A. G. (1971) 'Effect of Nutrient Concentration on the Growth of *Escherichia coli*.' *Journal of Bacteriology*, 107(1), pp. 210-216.

Shi, H., Magaye, R., Castranova, V. and Zhao, J. (2013) 'Titanium Dioxide Nanoparticles: A Review of Current Toxicological Data.' *Particle and Fibre Toxicology*, 10, p. 15.

Shie, J. S., Chou, B. C. S. and Chen, Y. M. (1995) 'High Performance Pirani Vacuum Gauge.' *Journal of Vacuum Science & Technology A*, 13(6), pp. 2972-2979.

Silhavy, T. J., Kahne, D. and Walker, S. (2010) 'The Bacterial Cell Envelope.' *Cold Spring Harbor Perspectives in Biology*, 2(5), p. a000414.

Silley, P. and Forsythe, S. (1996) 'Impedance Microbiology — A Rapid Change for Microbiologists.' *Journal of Applied Bacteriology*, 80(3), pp. 233-243.

Simões, M., Simões, L. C. and Vieira, M. J. (2010) 'A Review of Current and Emergent Biofilm Control Strategies.' *LWT - Food Science and Technology*, 43(4), pp. 573-583.

Singh, A., Pyle, B. H. and McFeters, G. A. (1989) 'Rapid Enumeration of Viable Bacteria by Image Analysis.' *Journal of Microbiological Methods*, 10, pp. 91-101.

Sirelkhatim, A., Mahmud, S., Seeni, A., Kaus, N. H. M., Ann, L. C., Bakhori, S. K. M., Hasan, H. and Mohamad, D. (2015) 'Review on Zinc Oxide Nanoparticles: Antibacterial Activity and Toxicity Mechanism.' *Nano-Micro Letters*, 7(3), pp. 219-242.

Smits, M., Huygh, D., Craeye, B. and Lenaerts, S. (2014) 'Effect of Process Parameters on the Photocatalytic Soot Degradation on Self-Cleaning Cementitious Materials.' *Catalysis Today*, 230, pp. 250-255.

Song, K., Mohseni, M. and Taghipour, F. (2016) 'Application of Ultraviolet Light-Emitting Diodes (UV-LEDs) for Water Disinfection: A Review.' *Water Research*, 94, pp. 341-349.

Sperelakis, N. (2012) *Cell Physiology Source Book: Essentials of Membrane Biophysics.* 4th ed., London: Academic Press.

Spurr, R. A. and Myers, H. (1957) 'Quantitative Analysis of Anatase-Rutile Mixtures with an X-Ray Diffractometer ' *Analytical Chemistry*, 29(5), pp. 760-762.

Sreedhar, M., Brijitta, J., Reddy, I. N., Cho, M., Shim, J., Bera, P., Joshi, B. N. and Yoon, S. S. (2017) 'Dye Degradation Studies of Mo-Doped TiO_2 Thin Films Developed by Reactive Sputtering.' *Surface and Interface Analysis*, 50(2), pp. 171-179.

Statham, P. J. (2002) 'Limitations to Accuracy in Extracting Characteristic Line Intensities from X-Ray Spectra.' *Journal of Research of the National Institute of Standards and Technology*, 107(6), pp. 531-546.

Stubbings, W. J., Bostock, J. M., Ingham, E. and Chopra, I. (2004) 'Assessment of a Microplate Method for Determining the Post-Antibiotic Effect in *Staphylococcus aureus* and *Escherichia coli*.' *Journal of Antimicrobial Chemotherapy*, 54(1), pp. 139-143.

Subasri, R., Tripathi, M., Murugan, K., Revathi, J., Rao, G. V. N. and Rao, T. N. (2010) 'Investigations on the Photocatalytic Activity of Sol–Gel Derived Plain and Fe^{3+}/Nb^{5+}-Doped Titania Coatings on Glass Substrates.' *Materials Chemistry and Physics*, 124(1), pp. 63-68.

Sunada, K., Watanabe, T. and Hashimoto, K. (2003) 'Studies on Photokilling of Bacteria on TiO_2 Thin Film.' *Journal of Photochemistry and Photobiology A: Chemistry*, 156(1-3), pp. 227-233.

Terada, A., Yuasa, A., Tsuneda, S., Hirata, A., Katakai, A. and Tamada, M. (2005) 'Elucidation of Dominant Effect on Initial Bacterial Adhesion onto

Polymer Surfaces Prepared by Radiation-Induced Graft Polymerization.' *Colloids and Surfaces B: Biointerfaces*, 43(2), pp. 99-107.

Thattai, M. and van Oudenaarden, A. (2004) 'Stochastic Gene Expression in Fluctuating Environments.' *Genetics*, 167(1), pp. 523-530.

The IARC Monographs Working Group on the Evaluation of Carcinogenic Risks to Humans. (2010) *Carbon Black, Titanium Dioxide, and Talc* Vol. 93. Lyon: World Health Organization International Agency for Research on Cancer.

Thornton, J. A. (1974) 'Influence of Apparatus Geometry and Deposition Conditions on the Structure and Topography of Thick Sputtered Coatings.' *Journal of Vacuum Science and Technology*, 11(4), pp. 666-670.

Toney, M. F. (1992) '4.1 - XRD: X-Ray Diffraction.' *In Encyclopedia of Materials Characterization*. Boston: Butterworth-Heinemann, pp. 198-213.

Toyoda, M., Nanbu, Y., Nakazawa, Y., Hirano, M. and Inagaki, M. (2004) 'Effect of Crystallinity of Anatase on Photoactivity for Methyleneblue Decomposition in Water.' *Applied Catalysis B: Environmental*, 49(4), pp. 227-232.

Uyanga, E., Gibaud, A., Daniel, P., Sangaa, D., Sevjidsuren, G., Altantsog, P., Beuvier, T., Lee, C. H. and Balagurov, A. M. (2014) 'Structural and Vibrational Investigations of Nb-Doped TiO_2 Thin Films.' *Materials Research Bulletin*, 60, pp. 222-231.

van Grieken, R., Marugán, J., Sordo, C. and Pablos, C. (2009a) 'Comparison of the Photocatalytic Disinfection of *E. coli* Suspensions in Slurry, Wall and Fixed-Bed Reactors.' *Catalysis Today*, 144(1), pp. 48-54.

van Grieken, R., Marugán, J., Sordo, C., Martínez, P. and Pablos, C. (2009b) 'Photocatalytic Inactivation of Bacteria in Water using Suspended and Immobilized Silver-TiO_2.' *Applied Catalysis B: Environmental*, 93(1-2), pp. 112-118.

van Grieken, R., Marugán, J., Pablos, C., Furones, L. and López, A. (2010) 'Comparison Between the Photocatalytic Inactivation of Gram-Positive *E. faecalis* and Gram-Negative *E. coli* Faecal Contamination Indicator Microorganisms.' *Applied Catalysis B: Environmental*, 100(1–2), pp. 212-220.

Vassen, R., Stuke, A. and Stover, D. (2009) 'Recent Developments in the Field of Thermal Barrier Coatings.' *Journal of Thermal Spray Technology*, 18(2), pp. 181-186.

Vazquez-Sanchez, D., Cabo, M. L. and Rodriguez-Herrera, J. J. (2015) 'Antimicrobial Activity of Essential Oils against *Staphylococcus aureus* Biofilms.' *Food and Science Technology Internatinal*, 21(8), pp. 559-570.

Venkatasubramanian, R., Srivastava, R. S. and Misra, R. D. K. (2008) 'Comparative Study of Antimicrobial and Photocatalytic Activity in Titania Encapsulated Composite Nanoparticles with Different Dopants.' *Materials Science and Technology*, 24(5), pp. 589-595.

Verdier, T., Coutand, M., Bertron, A. and Roques, C. (2014) 'Antibacterial Activity of TiO_2 Photocatalyst Alone or in Coatings on *E. coli*: The Influence of Methodological Aspects.' *Coatings*, 4(3), p. 670.

Verran, J. (2002) 'Biofouling in Food Processing: Biofilm or Biotransfer Potential?' *Food and Bioproducts Processing*, 80(4), pp. 292-298.

Verran, J., Sandoval, G., Allen, N. S., Edge, M. and Stratton, J. (2007) 'Variables Affecting the Antibacterial Properties of Nano and Pigmentary Titania Particles in Suspension.' *Dyes and Pigments*, 73(3), pp. 298-304.

Vroom, J. M., De Grauw, K. J., Gerritsen, H. C., Bradshaw, D. J., Marsh, P. D., Watson, G. K., Birmingham, J. J. and Allison, C. (1999) 'Depth Penetration and Detection of pH Gradients in Biofilms by Two-Photon Excitation Microscopy.' *Applied and Environmental Microbiology*, 65(8), pp. 3502-3511.

Wang, H., Wu, Z., Zhao, W. and Guan, B. (2007) 'Photocatalytic Oxidation of Nitrogen Oxides using TiO_2 Loading on Woven Glass Fabric.' *Chemosphere*, 66(1), pp. 185-190.

Wang, S., Bai, L. N., Sun, H. M., Jiang, Q. and Lian, J. S. (2013) 'Structure and Photocatalytic Property of Mo-Doped TiO_2 Nanoparticles.' *Powder Technology*, 244, pp. 9-15.

Westwood, W. D. (2003) *Sputter Deposition.* New York: AVS.

Whitehouse, D. J. (2000) 'Surface Characterization and Roughness Measurement in Engineering.' *In* Malacara-Hernández, D. and Rastogi, P. K. (eds.) *Photo-Mechanics*. Berlin: Springer, pp. 413-461.

Wilke, K. and Breuer, H. D. (1999) 'The Influence of Transition Metal Doping on the Physical and Photocatalytic Properties of Titania.' *Journal of Photochemistry and Photobiology A: Chemistry*, 121(1), pp. 49-53.

Wilks, S. A., Michels, H. and Keevil, C. W. (2005) 'The Survival of *Escherichia coli* O157 on a Range of Metal Surfaces.' *International Journal of Food Microbiology*, 105(3), pp. 445-454.

Wilks, S. A., Michels, H. T. and Keevil, C. W. (2006) 'Survival of *Listeria monocytogenes* Scott A on Metal Surfaces: Implications for Cross-Contamination.' *International Journal of Food Microbiology*, 111(2), pp. 93-98.

Windischmann, H. (1992) 'Intrinsic Stress in Sputter-Deposited Thin Films.' *Critical Reviews in Solid State and Materials Sciences*, 17(6), pp. 547-596.

Wu, M. C., Lin, T. H., Chih, J. S., Hsiao, K. C. and Wu, P. Y. (2017) 'Niobium Ddoping Induced Morphological Changes and Enhanced Photocatalytic Performance of Anatase TiO_2.' *Japanese Journal of Applied Physics*, 56(4), p. 6.

Xia, Y. N. and Whitesides, G. M. (1998) 'Soft Lithography.' *Angewandte Chemie - International Edition*, 37(5), pp. 550-575.

Xu, L., Zhang, C., Xu, P. and Wang, X. C. (2018) 'Mechanisms of Ultraviolet Disinfection and Chlorination of *Escherichia coli*: Culturability, Membrane

Permeability, Metabolism, and Genetic Damage.' *Journal of Environmental Sciences*, 65, pp. 356-366.

Xu, M. C., Gao, Y. K., Moreno, E. M., Kunst, M., Muhler, M., Wang, Y. M., Idriss, H. and Woll, C. (2011) 'Photocatalytic Activity of Bulk TiO_2 Anatase and Rutile Single Crystals using Infrared Absorption Spectroscopy.' *Physical Review Letters*, 106(13), p. 4.

Yan, X., Ohno, T., Nishijima, K., Abe, R. and Ohtani, B. (2006) 'Is Methylene Blue an Appropriate Substrate for a Photocatalytic Activity Test? A Study with Visible-Light Responsive Titania.' *Chemical Physics Letters*, 429(4), pp. 606-610.

Yang, J., Gao, M. Z., Jiang, S. B., Huo, X. J. and Xia, R. (2018) 'Hysteretic Phase Transformation of Two-Dimensional TiO_2.' *Materials Letters*, 232, pp. 171-174.

Yao, M., Chen, J., Zhao, C. and Chen, Y. (2009) 'Photocatalytic Activities of Ion Doped TiO_2 Thin Films when Prepared on Different Substrates.' *Thin Solid Films*, 517(21), pp. 5994-5999.

Yin, M., Liu, X., Hu, L., Xu, L. and He, J. (2016) 'Effects of Nb Doping on Microstructure and Photocatalytic Properties of TiO_2 Thin Film.' *Desalination and Water Treatment*, 57(15), pp. 6910-6915.

Yoon, K. Y., Byeon, J. H., Park, J. H. and Hwang, J. (2007) 'Susceptibility Constants of *Escherichia coli* and *Bacillus subtilis* to Silver and Copper Nanoparticles.' *Science of the Total Environment*, 373(2–3), pp. 572-575.

Yoon, Y. H., Lee, S. Y., Gwon, J. G., Cho, H. J., Wu, Q., Kim, Y. H. and Lee, W. H. (2018) 'Photocatalytic Performance of Highly Transparent and Mesoporous Molybdenum-Doped Titania Films Fabricated by Templating Cellulose Nanocrystals.' *Ceramics International*, 44(14), pp. 16647-16653.

Yoong, L. S., Chong, F. K. and Dutta, B. K. (2009) 'Development of Copper-Doped TiO_2 Photocatalyst for Hydrogen Production under Visible Vight.' *Energy*, 34(10), pp. 1652-1661.

Yu, J. C., Ho, W. K., Yu, J. G., Yip, H., Wong, P. K. and Zhao, J. C. (2005) 'Efficient Visible-Light-Induced Photocatalytic Disinfection on Sulfur-Doped Nanocrystalline Titania.' *Environmental Science & Technology*, 39(4), pp. 1175-1179.

Yu, X., Wang, C. B., Liu, Y., Yu, D. Y. and Xing, T. Y. (2006) 'Recent Developments in Magnetron Sputtering.' *Plasma Science & Technology*, 8(3), pp. 337-343.

Zaleska, A. (2008) 'Doped TiO_2 - A Review.' *Recent Patents on Engineering*, 2(1), pp. 157-164.

Zarrin, S. and Heshmatpour, F. (2018) 'Photocatalytic Activity of TiO_2/Nb_2O_5/PANI and TiO_2/Nb_2O_5/RGO as New Nanocomposites for Degradation of Organic Pollutants.' *Journal of Hazardous Materials*, 351, pp. 147-159.

Zhou, J., Wu, Z. and Liu, Z. (2008) 'Influence and Determinative Factors of Ion-to-Atom Arrival Ratio in Unbalanced Magnetron Sputtering Systems.'

Journal of University of Science and Technology Beijing, Mineral, Metallurgy, Material, 15(6), pp. 775-781.

Zhou, Z., Zhao, Z. G., Wu, J. and Cai, Q. (2005) 'New Method to Measure the Total Amount of Bacteria in Raw Milk.' *SPIE Proceedings: Optics in Health Care and Biomedical Optics: Diagnostics and Treatment II*, 5630, pp. 447-451.

Zollfrank, C., Gutbrod, K., Wechsler, P. and Guggenbichler, J. P. (2012) 'Antimicrobial Activity of Transition Metal Acid MoO_3 Prevents Microbial Growth on Material Surfaces.' *Materials Science and Engineering: C*, 32(1), pp. 47-54.